THE ELECTROCHEMISTRY OF 2D HEXAGONAL BORON NITRIDE

A. F. KHAN

PhD 2018

THE ELECTROCHEMISTRY OF 2D HEXAGONAL BORON NITRIDE

AAMAR FAROOQ KHAN

A thesis submitted in partial fulfilment of the requirements of the Manchester Metropolitan University for the degree of Doctor of Philosophy

2018

School of Science and the Environment
Division of Chemistry and Environmental Science
Manchester Metropolitan University

Abstract

Since the discovery of the unique physical properties of graphene, research has intensified in the field of two-dimensional (2D) nanomaterial electrochemistry. Indeed, newly emerging 2D materials such as 2D-hexagonal boron nitride (2D-hBN) have the potential to transform the field of electrochemistry when implemented as a next generation electrode material. This thesis reports on the electrochemical applicability of utilising 2D-hBN, previously considered non-electroactive, as a novel electrode material. Also considered is the effect of the fabrication process of 2D-hBN when employed towards a range of electrochemical applications.

Chapter 1 gives an overview of the general electrochemical concepts that concern this thesis. Chapter 2 offers an insight into recent 2D materials electrochemistry literature regarding, first, graphene and then 2D-hBN. From this, successive chapters follow the development and investigation of 2D-hBN, formed *via* differing synthesis techniques, thus enabling a truer reflection of 2D-hBN as an electrode material to be achieved.

Chapter 3 details the relevant experimental information and the full physicochemical characterisation of the different 2D-hBN materials employed within this thesis. Chapters 4 and 5 utilise surfactant-free (pristine) 2D-hBN, where pristine 2D-hBN is 'electrically wired' upon a suitable electrode surface. Chapter 4 reveals for the first time that pristine 2D-hBN gives rise to beneficial electrochemical behaviour towards the oxygen reduction reaction (ORR) when immobilised upon a graphitic substrate. Chapter 5 explores pristine 2D-hBN towards a biological approach in the sensing of dopamine (DA) and its common interferents ascorbic acid (AA) and uric acid (UA). Pristine 2D-hBN exhibits a beneficial electrocatalytic effect towards the detection of dopamine when immobilised upon a graphitic

substrate. This observed beneficial effect upon the utilisation of pristine 2D-hBN has not previously been reported in the literature when supported upon any electrode. Both chapters implement 'mass coverage' studies of 2D-hBN, an often overlooked parameter within the literature

Chapters 6 and 7 utilise surfactant-exfoliated 2D-hBN and compare the effect of the fabrication process of 2D-hBN (pristine *vs.* surfactant-exfoliated) upon the observed electrochemistry towards the ORR, capacitance applications and the sensing of dopamine, *via* a dropcasting electrode modification approach. Chapter 6 explores surfactant-exfoliated 2D-hBN towards the ORR and capacitance applications for the first time. The surfactant-exfoliated 2D-hBN nanosheets are immobilised upon graphitic screen-printed electrodes (SPEs) with 'mass coverage' studies performed and the observed electrochemical response is compared to the surfactant-free pristine 2D-hBN approach. Chapter 7 explores surfactant-exfoliated 2D-hBN as a potential electrochemical sensing platform towards the electroanalytical sensing of dopamine (DA) in the presence of the common interferents, ascorbic acid (AA) and uric acid (UA) for the first time. Surfactant exfoliated 2D-hBN is electrically wired *via* a drop-casting modification process onto SPEs and the observed electrochemical response is compared to the surfactant-free (pristine) 2D-hBN approach. The performance of these surfactant-exfoliated 2D-hBN modified SPEs are critically evaluated upon the implementation of 'mass coverage studies.

Chapter 8 explores for the first time a low cost and reproducible approach for producing 2D Hexagonal Boron Nitride (2D-hBN) electrochemical screen-printed platforms (hBN-SPEs). These novel hBN-SPEs are explored as a potential electrocatalyst towards the ORR. This fabrication approach is compared to the drop

casting technique of pristine and surfactant-exfoliated 2D-hBN utilised towards the ORR, thus offering an alternative approach.

This thesis demonstrates for the first time that 2D-hBN is electroactive when immobilised upon a graphitic substrate towards a range of applications. It is also shown that fabrication process in the production of 2D-hBN can affect the observed electrochemistry, thus control experiments must be undertaken to truly understand the impact of this material.

Aims and Objectives

The aim of this thesis is to explore 2D-hexagonal boron nitride (2D-hBN) as an electrode material towards energy applications and as a sensor platform. The objectives of this work are described in greater detail below.

Objectives:

1) Understand how the supporting (electrode) substrate interaction affects the electrochemical performance of surfactant-free (pristine) 2D-hBN utilised in the oxygen reduction reaction and as a sensor platform.

2) Establish the impact and effects that surfactants have on the electrochemical performance of 2D-hBN utilised towards the oxygen reduction reaction, capacitance and sensing applications, given that they are used routinely in the fabrication of 2D materials.

3) Produce a novel carbon electrode incorporating the characterised 2D-hBN, through the development of desirable inks for screen-printing to produce a mass producible and large surface electrode area composite.

Acknowledgements

I would like to thank Professor Craig Banks for gifting me this opportunity and for all the support, knowledge and guidance he has afforded me over the last three years. Our chance encounter on Oxford road helped begin this journey and it is incredible how something so important began in such an unexpected manner. I am truly grateful. Furthermore, I would like to offer a special thank you to Dr. Dale Brownson, Dr. Edward Randviir, Dr. Christopher Foster and Dr. Michael Down. All of whom have offered fantastic expertise and support, helping me develop my skills as an electrochemist. This support was not only limited to academia. Indeed, the guidance they showed in my difficult and challenging moments was invaluable, making this period of my life one I will dearly remember.

I would also like to extend my thanks to all members of the Banks Research group, who helped make my time enjoyable and memorable.

Finally, the completion of my studies would not have been possible without the countless sacrifices made by my grandfather Hajji Jalal Khan, grandmother Akbar Jan, father Iqbal Khan, mother Naseem Khan and uncle Lal Khan, in addition to the love and support offered by my entire family, for which I am forever grateful. It is unto them, as only proper, I dedicate this thesis.

Table of Contents

Abstract i

Aims and Objectives iv

Acknowledgements v

List of Tables x

List of Figures xiii

Chapter 1 : General Electrochemistry 1

1.1 Introduction to Electrochemistry 1

1.1.1 Faradaic Processes 3

1.1.2 Mass Transport 6

1.1.3 Reactions Controlled by the Rate of Electron Transfer 10

1.2 Electrochemical Methodologies 12

1.2.1 Cyclic Voltammetry 12

1.2.2 Differential Pulse Voltammetry 20

1.2.3 Supercapacitors 26

1.2.4 Electroanalysis 29

1.2.5 Redox Probes 31

1.3 Electrode Materials 32

1.3.1 Carbon Materials 34

Chapter 2 : 2D Materials in Electrochemistry 39

2.1 Graphene 39

2.1.1 2D Hexagonal Boron Nitride (2D-hBN) 44

Chapter 3 : Experimental Section 49

3.1 Experimental Details 49

3.2 Electrode Materials Utilised 50

3.2.1 Screen-Printed Electrodes (SPEs) 50

3.2.2 GC and BDD Electrodes 51

3.2.3 EPPG Electrode 51

3.2.4 Gold and Platinum Electrodes 51

3.2.5 Electrode Preparation 51

3.2.6 Electrode Modification 52

3.3 Physical/Chemical Characterisation Techniques 54

3.3.1 Scanning Electron Microscopy (SEM), Transition Electron Microscopy (TEM) AND Energy Dispersive X-ray (EDX) Spectroscopy 54

3.3.2 Raman Spectroscopy 54

3.3.3 X-ray Photoelectron Spectroscopy (XPS) 55

3.3.4 X-ray Diffraction (XRD) 56

3.3.5 White Light Profilometry (WLP) 56

3.3.6 Ultraviolet-Visible Spectroscopy (UV-VIS) 56

3.4 2D Hexagonal Boron Nitride (2D-hBN) Utilised: Details and Characterisation 56

3.4.2 Pristine (Surfactant-Free) 2D-hBN 56

3.4.2. Pristine (Surfactant-Free) 2D-hBN Characterisation 57

3.4.3 Surfactant-Exfoliated 2D-hBN 68

3.4.3.1 Surfactant-Exfoliated 2D-hBN Characterisation 69

3.4.4 2D-hBN Nanopowder 79

3.4.4.1 2D-hBN Nanopowder Characterisation 79

Chapter 4 : Pristine 2D Hexagonal Boron Nitride (2D-hBN) Explored as a Potential Electrocatalyst for the Oxygen Reduction Reaction 84

4.1. Introduction 85

4.2 Experimental Details 88

4.3 Results and Discussion 90

4.4 Conclusions 128

Chapter 5 : Pristine 2D Hexagonal Boron Nitride (2D-hBN) Explored for the Electrochemical Sensing of Dopamine 130

5.1 Introduction 130

5.2 Results and Discussion 137

5.3 Conclusions 158

Chapter 6 : Surfactant-Exfoliated 2D Hexagonal Boron Nitride (2D-hBN): role of surfactant upon the electrochemical reduction of oxygen and capacitance applications 160

6.1 Introduction 160

6.2 Experimental Details 163

6.3 Results and Discussion 165

6.3.2 Exploring 2D-hBN as a Capacitive Material 177

6.4 Conclusions 197

Chapter 7 : Surfactant-Exfoliated 2D hexagonal Boron Nitride (2D-hBN) Explored as a Potential Electrochemical Sensor for Dopamine: surfactants significantly influence sensor capabilities 199

7.1.1 Introduction 200

7.2 Results and Discussion 205

7.3 Conclusions 225

Chapter 8 : 2D Hexagonal Boron Nitride Screen-Printed Electrode Platforms Explored Towards the Oxygen Reduction Reaction 227

8.1 Introduction 227

8.2 Experimental Details 230

8.3 Results and Discussion 231

8.4 Conclusions 240

Chapter 9 : Conclusions and Future Work 242

9.1 Overall Conclusions 242

9.2 Suggestions for Future Work 245

References 248

List of Tables

Table 1.1: variation of ΔE_p with ψ at 298 K. Reproduced with permission from Ref.[10] 18

Table 3.1: A summary depicting the composition of pristine 2D-hBN dried from ethanol suspension onto Si(111) following analysis of XPS spectra. Note that the analysis includes data from the 2D-hBN, the ethanol residue, and a proportion of the surface region of the Si(111) wafer including the native surface oxide. 62

Table 3.2: A summary depicting the composition of surfactant-exfoliated 2D-hBN layer dried from sodium cholate suspension onto Si(111), following analysis of XPS spectra. Note that the analysis includes data from the 2D-hBN and the sodium cholate residue. 76

Table 3.3: A summary depicting the composition of 2D-hBN, following analysis of XPS spectra. 83

Table 4.1: Analysis of voltammograms presented in Figure 4.3. Table exhibits the effects of increasing voltammetric cycle number upon the 'cathodic peak current' (μA) and 'cathodic peak potential' (V) when utilising a 162 ng pristine 2D-hBN modified SPE. 95

Table 4.2: Comparison of 2D nanomaterials that have been utilised for the ORR.. 124

Table 5.1: A comparison of various electrode materials utilised towards the detection of DA in the presence of UA and AA. ***Key:*** *AuNP@MoS_2, Gold nanoparticle modified molybdenum disulfide; AuNPs–β-CD–Graphene, Gold nanoparticles–β-cyclodextrin–graphene; 2D-hBN, 2D hexagonal boron nitride; GC, Glassy carbon electrode; CPE, Carbon paste electrode; functionalised graphene synthesised by solvothermal reduction of colloidal dispersions of graphite oxide;*

UA, Uric Acid; AA, Ascorbic Acid DPV, Differential Pulse Voltammetry; SWV, Square Wave Voltammetry. 135

Table 6.1: Analysis of voltammograms presented in Figure 6.4. Table exhibits the effects of increasing voltammetric cycle number upon the 'cathodic peak current' (μA) and 'cathodic peak potential' (V) when utilising a 37.5 ng surfactant-exfoliated 2D-hBN, 324 ng pristine 2D-hBN and 10 μg sodium cholate modified SPE. 171

Table 6.2: A summary of the effect of increasing mass immobilisation of pristine 2D-hBN, surfactant-exfoliated 2D-hBN and sodium cholate modified SPEs upon capacitance μF. Note, capacitance values were obtained from cyclic voltammograms 182

Table 6.3: A summary of the effect of increasing mass immobilisation of pristine 2D-hBN (75 ng), surfactant-exfoliated 2D-hBN (75 ng) and sodium cholate (20 μg) upon SPEs towards; capacitance (C_{WE}) μF, specific capacitance (C_S) F g^{-1}, areal capacitance (C_A) μF cm^{-2} and volumetric capacitance (C_V) F cm^{-3}. The current is held at 5.0 μA throughout. Note capacitance measurements are obtained from charge/discharge profiles 190

Table 6.4: A summary of the effect of increasing mass immobilisation of pristine 2D-hBN (7.5 - 75 ng), surfactant-exfoliated 2D-hBN (7.5 – 75 ng) and sodium cholate (2 -20 μg) modified SPEs towards capacitance (C_{WE}) μF, areal capacitance (C_A) μF cm^{-2}, volumetric capacitance (C_V) F cm^{-3} and specific capacitance (C_S) F g^{-1} . The current is held at 5.0 μA throughout. Note, capacitance values were obtained from charge/discharge profiles. 196

Table 7.1: A comparison of various 2D materials utilised towards the detection of DA. ***Key:*** *PtNP@MoS2, Platinum nanoparticle modified molybdenum disulfide;AuNP@MoS_2, GNS-CNTs/MoS_2, Molybdenum disulfide flowers placed on*

graphene nanosheets and multiwalled carbon nanotubes; MoS_2-RGO, Molybdenum disulphide – reduced graphene oxide; Gold nanoparticle modified molybdenum disulfide; AuNPs–β-CD–Graphene, Gold nanoparticles–β-cyclodextrin–graphene; 2D-hBN, 2D hexagonal boron nitride; GC, Glassy carbon electrode; CPE, Carbon paste electrode; functionalised graphene synthesised by solvothermal reduction of colloidal dispersions of graphite oxide; UA, Uric Acid; AA, Ascorbic Acid DPV, Differential Pulse Voltammetry; SWV, Square Wave Voltammetry......203

Table 7.2: Tabulated data shown from Figure 7.2. 210

List of Figures

Figure 1.1: A typical three electrode system with a basal plane pyrolytic graphite electrode (WE), platinum wire counter electrode (CE) and a saturated calomel reference electrode (RE). Reproduced from Ref.[5] 3

Figure 1.2: An illustration of the Nernst diffusion layer. Reproduced from Ref.[5] 10

Figure 1.3: Triangular potential waveform utilised for linear sweep and cyclic voltammetry. Reproduced from Ref.[5] 12

Figure 1.4: Typical cyclic voltammograms exhibiting the peak position E_p and peak height I_p (A) and (B) illustrates cyclic voltammograms for reversible (a), quasi reversible (b) and irreversible (c) electron transfer. Reproduced from Ref.[5].....14

Figure 1.5: Effect of capacitative and Faradaic current following the application of a potential step. Reproduced from Ref.[5] 21

Figure 1.6: Differential pulse voltammetry waveform of pulses superimposed on a staircase. Reproduced from ref.[5].....22

Figure 1.7: Differential pulse voltammetry; voltammetric profiles of ΔI vs. staircase potential. Reproduced from Ref.[5] 23

Figure 1.8: (A) Cyclic and (B) differential pulse voltammograms 0.1 mM and 0.1 mM ascorbic acid acetaminophen in acetate buffer solution (pH 4.0) on the surface of various electrodes; unmodified carbon paste electrode (solid line), CNT–carbon paste electrode (dotted line) and multi-walled carbon nanotube/thionine modified electrode (dashed line). Sweep rate was 100 mV s^{-1}. Reproduced from Ref.[5] 25

Figure 1.9: a) Image of a commercially available slab of HOPG. b) Schematic of a side on view of a HOPG surface, which highlights its edge plane and basal plane and like- sites/defects which exhibit contrasting behaviours in terms of electrochemical activity c) A representation of a HOPG surface illustrating the discrete basal plane

and edge plane islands. d) A typical STM image of a HOPG surface with the corresponding fragment of the graphene structure superimposed. Reproduced with permission from Ref.[5] 35
Figure 1.10: represents the structure of the GC. Reproduced from Ref.[5] 37
Figure 1.11: Typical SPEs consisting of a graphite working electrode, (WE, 3mm diameter), a graphite counter electrode, (CE) and an Ag/AgCl reference electrode (RE). In this example 2D-hBN can be readily immobilised upon SPEs.....38
Figure 2.1 Illustrates the structure of 2D-hBN. 45
Figure 2.2 The molecular orbital structure of 2D-hBN is illustrated. 46
Figure 3.1: A schematic representation of the process utilised to produce the hBN-SPEs reported herein. 53
Figure 3.2: Typical TEM images of commercially procured pristine 2D-hBN deposited onto a holey carbon film supported upon a Cu TEM grid (A), and at a higher magnification (B). Scale bars are 200 nm (A) and 100 nm (B). Images obtained using a 200 kV primary beam under bright-field conditions. 58
Figure 3.3: Typical SEM images for: unpolished SPE (A); polished SPE (B); unpolished SPE with 324 ng pristine 2D-hBN (C) and a further magnified version (E); polished SPE with 324 ng pristine 2D-hBN (D) and a further magnified version (F). Pristine 2D-hBN platelets are evident in images C-F as small, disc-like shapes approximately 200 nm in size. 60
Figure 3.4: Curve fitted XPS spectra of pristine 2D-hBN deposited upon a Si (111) wafer. (A) illustrates XPS spectra of the B atom and spectra (B) is that of the N atom. 61
Figure 3.5: Typical SEM image (A) for pristine 2D-hBN immobilised upon a silicon substrate, where the red box shows the target of the EDX analysis. The SEM was

obtained at ×20,000 magnification. An acceleration voltage of 25.00 kV and a working distance of 14.4 mm were utilised. Part (B) illustrates the accompanying EDX spectrum of pristine 2D-hBN and analysis of this is shown in the inset table..64

Figure 3.6: XRD spectra of the pristine 2D-hBN deposited onto a glass slide between 5 and 45 2θ, exhibiting a characteristic peak at 26.7°.....65

Figure 3.7: A typical Raman spectra (A) obtained for 2D-hBN (solid line) immobilised upon a supporting silicon wafer. The dotted line depicts the Raman spectra of the silicon substrate upon which 2D-hBN is deposited. Image (B) shows the Raman mapping of an unmodified (bare) SPE and (C) is that of a 324 ng 2D-hBN modified SPE. Raman intensities for B and C were recorded at 1366 cm^{-1}. Figure C shows several areas, appearing as black dots, that are indicative of pristine 2D-hBN immobilisation given that the Raman intensities were recorded at the wavenumber corresponding to the peak observed in A. 67

Figure 3.8 Schematic illustrating the structure of sodium cholate and its encapsulation of 2D-hBN.....68

Figure 3.9: Typical TEM images of surfactant-exfoliated 2D-hBN deposited onto a holey carbon film supported upon a Cu TEM grid (A), and at a higher magnification (B). Scale bars are 100 nm (A) and 200 nm (B). Images obtained using a 200 kV primary beam under bright-field conditions; (C), typical Raman spectra obtained for surfactant-exfoliated 2D-hBN (solid line) immobilised upon a supporting silicon wafer. (D) Typical SEM images for an SPE modified with 37.5ng surfactant-exfoliated 2D-hBN. 2D-hBN platelets are evident as small, disc-like shapes approximately 200 nm in size. 71

*Figure 3.10: A typical UV-visible absorption spectra of surfactant-exfoliated 2D-hBN nanosheets, where the inset shows the corresponding plot of $\varepsilon^{1/2}/\lambda$ vs. $1/\lambda$. *72

Figure 3.11: XPS survey spectrum for a sample of the surfactant-exfoliated 2D-hBN following deposition onto a Si (111) wafer. 74

Figure 3.12: Curve fitted XPS spectra of surfactant-exfoliated 2D-hBN deposited upon a Si (111) wafer. (A) illustrates XPS spectra of the B atom and spectra (B) is that of the N atom. 75

Figure 3.13: XRD spectra of the surfactant-exfoliated 2D-hBN deposited onto a glass slide between 20 and 45 2θ, exhibiting a characteristic peak at 26.7°. 77

Figure 3.14: SEM image (A) of surfactant-exfoliated 2D-hBN immobilised on a SPE along with EDX elemental analysis highlighting the underlying SPE carbon support (B, in green), boron (C, in red) and nitrogen (D, in purple) coverage of image A respectively......78

Figure 3.15: A typical Raman spectra (A) obtained for the commercially procured 2D-hBN (solid line) immobilised upon a supporting silicon wafer. (B) Typical TEM images of the 2D-hBN deposited onto a holey carbon film supported upon a Cu TEM grid. Scale bars are 200 nm. Images obtained using a 200 kV primary beam under bright-field conditions. (C) XRD spectra of the 2D-hBN, exhibiting characteristic peaks at 26.7°, 41.56° and 44.38°.....80

Figure 3.16: XPS survey spectrum (A) for a sample of the 2D-hBN. Curve fitted XPS spectra of the2D- hBN nanopowder. (B) illustrates XPS spectra of the B atom and spectra (C) is that of the N atom.....82

Figure 4.1: Typical cyclic voltammograms (A) recorded in 1 mM $[Ru(NH_3)_6]^{2+/3+}$ / 0.1 M KCl with pristine 2D-hBN masses of: 10.8, 21.6, 32.4, 43.2, 54, 162 and 324 ng immobilised upon SPEs. The dotted line represents an unmodified (bare) SPE. Also shown are the analysis of the voltammograms presented in Figure 4.1A in the form of peak-to-peak separation (ΔE_P) vs. mass of pristine 2D-hBN (B), 'reduction

cathodic wave current' against mass of pristine 2D-hBN (C) and 'reduction cathodic wave current density' against mass of pristine 2D-hBN (D) . Scan rate: 100 mV s^{-1} (vs. SCE). 91

Figure 4.2: Typical cyclic voltammograms (A) recorded in 1 mM $[Ru(NH_3)_6]^{2+/3+}$ / 0.1 M KCl with pristine 2D-hBN mass of 324 ng immobilised upon SPEs. Also shown are analysis of the voltammograms presented in Figure 4.2A in the form of 'reduction cathodic wave current' vs. 'square root scan rate' (B) and 'log reduction cathodic wave curren't vs. 'log of scan rate' (C). Scan rates present in (A): 15, 25, 50, 75, 100, 150, 200 and 400 mV s^{-1} (vs. SCE). 93

Figure 4.3: Cyclic voltammograms recorded in 1 mM $[Ru(NH_3)_6]^{2+/3+}$ / 0.1 M KCl using a 162 ng pristine 2D-hBN modified SPE. Repeat scans were performed up to 100 cycles. Scan rate: 100 mV s^{-1} (vs. SCE)......94

Figure 4.4: Typical cyclic voltammograms (A) recorded in 1 mM $[Ru(NH_3)_6]^{2+/3+}$ / 0.1 M KCl with pristine 2D-hBN masses of: 10.8, 21.6, 32.4, 43.2, 54, 162 and 324 ng immobilised upon a GC electrode. The dotted line represents an unmodified (bare) GC electrode. Also shown are the analysis of the voltammograms presented in Figure 4.4A in the form 'reduction cathodic wave current' against 'mass of 2D-hBN' (B). Scan rate: 100 mV s^{-1} (vs. SCE)......96

Figure 4.5: Typical cyclic voltammograms (A) recorded in 1 mM $[Ru(NH_3)_6]^{2+/3+}$ / 0.1 M KCl with pristine 2D-hBN masses of: 10.8, 21.6, 32.4, 43.2, 54, 162 and 324 ng immobilised upon a BDD electrode. The dotted line represents an unmodified (bare) BDD electrode. Also shown are the analysis of the voltammograms presented in Figure 4.5 A in the form 'reduction cathodic wave current' against 'mass of pristine 2D-hBN' (B). Scan rate: 100 mV s^{-1} (vs. SCE)......97

Figure 4.6: Typical cyclic voltammograms (A) recorded in 1 mM $[Ru(NH_3)_6]^{2+/3+}$ / 0.1 M KCl with pristine 2D-hBN masses of: 10.8, 21.6, 32.4, 43.2, 54, 162 and 324 ng immobilised upon a EPPG electrode. The dotted line represents an unmodified (bare) EPPG electrode. Also shown are the analysis of the voltammograms presented in Figure 4.6A in the form 'reduction cathodic wave' current 'against mass of pristine 2D-hBN' (B). Scan rate: 100 mV s^{-1} (vs. SCE)......98

Figure 4.7: Cyclic voltammograms recorded in 0.1 M H_2SO_4 solution for SPEs modified with varying amounts of pristine 2D-hBN. Modifications; (A) 0, (B) 108, (C) 216, (D) 324 ng. Scan rate: 20 (black), 40 (red), 60 (blue), 80 (green) and 100 mV s^{-1} (pink) (vs. SCE)......100

Figure 4.8: The difference in anodic and cathodic current density for unmodified and pristine 2D- hBN modified SPEs taken at +0.06 V vs. scan rate (mV s^{-1}) (see Figure 4.7). The slope of the linear regression indicates the value of double layer capacitance (C_{dl})......101

Figure 4.9: Cyclic voltammograms recorded in 0.1 M H_2SO_4 solution for a GC electrode modified with varying amounts of pristine 2D-hBN. Modifications; (A) 0, (B) 108, (C) 216, (D) 324 ng. Scan rate: 20 (black), 40 (red), 60 (blue), 80 (green) and 100 mV s^{-1} (pink) (vs. SCE)......102

Figure 4.10: The difference in anodic and cathodic current density for an unmodified and 2D-hBN modified GC electrode taken at +0.06 V vs. scan rate (mV s^{-1}) (see Figure 4.9). The slope of the linear regression indicates the value of double layer capacitance (C_{dl})......103

Figure 4.11: White light profilometry, giving surface topography maps of an unmodified GC electrode (A), a polished SPE (B) and an unpolished SPE (C). Also shown (D, E and F) are the respective electrodes (GC/polished SPE/unpolished

SPE) following modification with 108 ng pristine 2D-hBN. It is evident that the surface roughness significantly increases with pristine 2D-hBN immobilisation upon unpolished SPEs in comparison to the same conditions when utilising a polished or initially smooth substrate. 105

Figure 4.12: Cyclic voltammetry scan rate study recorded in oxygen saturated 0.1 M H_2SO_4 utilising an unmodified SPE (A). Scan rates: 15, 25, 50, 75, 100, 150, 200 and 400 mV s^{-1} (vs. SCE). Also shown are plots of peak height vs. square root scan rate (B) and log peak height vs. log of scan rate (C). 106

Figure 4.13: Cyclic voltammetry scan rate study recorded in oxygen saturated 0.1 M H_2SO_4 utilising an unmodified GC electrode. Scan rates: 10, 25, 50, 75, 100, 200 and 400 mV s^{-1} (vs. SCE). 107

Figure 4.14: Cyclic voltammetry scan rate study recorded in an oxygen saturated 0.1 M H_2SO_4 utilising an unmodified BDD electrode. Scan rates: 25, 50, 100, and 200 mV s^{-1} (vs. SCE). 108

Figure 4.15: Typical cyclic voltammograms recorded in oxygen saturated 0.1 M H_2SO_4 with an unmodified SPE (A) and a 108 ng pristine 2D-hBN modified SPE (B). The dotted line depicts a deoxygenated SPE equivalent in each case. Scan rates: 15, 25, 50, 75, 100, 150, 200 and 400 mV s^{-1} (vs. SCE)......109

Figure 4.16: Typical cyclic voltammograms recorded in oxygen saturated 0.1 M H_2SO_4 using a 108 ng pristine 2D-hBN (A) and a 324 ng pristine 2D-hBN (B) modified GC electrode. The dotted line depicts a deoxygenated GC electrode equivalent in each case. Scan rates: 10, 25, 50, 75, 100, 200 and 400 mV s^{-1} (vs. SCE). 110

Figure 4.17: Typical cyclic voltammograms recorded in oxygen saturated 0.1M H_2SO_4 using a pristine 108 ng 2D-hBN (A) and a pristine 324 ng 2D-hBN (B)

modified BDD electrode. The dotted line depicts a deoxygenated equivalent BDD electrode in each case. Scan rates: 25, 50, 100 and 200 mV s^{-1} (vs. SCE)......111

Figure 4.18: Typical cyclic voltammogram (A) recorded in oxygen saturated 0.1 M H_2SO_4 with a 108 ng pristine 2D-hBN modified SPE. The dotted line depicts a deoxygenated unmodified SPE. Also shown are analysis of the peaks presented in Figure 4.18A in the form of 'peak height' vs 'square root scan rate' (B) and 'log peak height' vs. 'log of scan rate' (C). Scan rates: 15, 25, 50, 75, 100, 150, 200 and 400 mV s^{-1} (vs. SCE).....112

Figure 4.19: Typical cyclic voltammograms recorded in an oxygen saturated 0.1 M H_2SO_4 solution using unmodified (black line), 54 ng (red line), 108 ng (blue line), 216 ng (green line) and 324 ng (pink line) pristine 2D-hBN modified SPEs. Shown in the inset is analysis of cyclic voltammograms obtained in an oxygen saturated 0.1 M H_2SO_4 solution in the form of a plot of oxygen reduction peak potential vs. mass of pristine 2D-hBN electrically wired upon SPEs. Scan rate: 100 mV s^{-1} (vs. SCE)...114

Figure 4.20: Cyclic voltammograms recorded in an oxygen saturated 0.1 M H_2SO_4 solution using unmodified (A) and 324 ng pristine 2D-hBN modified SPEs (B). The 'solid line' depicts an unpolished SPE and the 'dashed line' illustrates the response of a polished SPE. Scan rate: 100 mV s^{-1} (vs. SCE). 116

Figure 4.21: Illustrates Tafel plots for unmodified (A), 108 (B), 216 (C) and 324 ng (D) pristine 2D-hBN modified SPEs. 118

Figure 4.22: Typical cyclic voltammograms (A) recorded in in oxygen saturated 0.1 M H_2SO_4 for an unmodified and a 108, 216 and 324 ng pristine 2D-hBN modified gold electrode. The dotted line represents a deoxygenated unmodified gold electrode. Scan rate: 100 mV s^{-1} (vs. SCE). Also shown are the analysis of the voltammograms at different scan rates in the form of oxygen reduction potential vs mass of pristine

2D-hBN deposited upon a gold electrode (B). Scan rates: 10, 50, 100 and 200 mV s^{-1} (vs. SCE). 125

Figure 4.23: Typical cyclic voltammograms (A) recorded in in oxygen saturated 0.1 M H_2SO_4 for unmodified and a 108, 216 and 324 ng pristine 2D-hBN modified platinum electrode. The dotted line represents a deoxygenated unmodified (bare) platinum electrode. Scan rate: 100 mV s^{-1} (vs. SCE). Also shown are the analysis of the voltammograms at different scan rates in the form of oxygen reduction potential vs. mass of pristine 2D-hBN deposited upon a platinum electrode (B). Scan rates: 10 mV s^{-1}, 50 mV s^{-1} 100 mV s^{-1} and 200 mV s^{-1} (vs. SCE). 126

Figure 5.1: Structures of DA (A), AA (B) and UA (C) are shown.[122-124] 132

Figure 5.2: Typical cyclic voltammograms recorded in a 1 mM DA solution (PBS, pH 7.4) utilising a bare/unmodified SPE (green), GC (red) and BDD (blue) electrode. The dashed line depicts respective pH 7.4 PBS blanks. Scan rate: 100 mV s^{-1} (vs. SCE). 138

*Figure 5.3: Typical cyclic voltammograms recorded in (A) 1 mM DA and (B) 1 mM ascorbic acid, pH 7.4 PBS with unmodified SPEs (black) and pristine 2D-hBN modified electrodes. Masses of modification as follows: 108 (blue), 216 (green) and 324 ng (red) immobilised. The dashed line represents the PBS blank respectively. Analysis of the cyclic voltammograms is presented in the form of plot (C) illustrating oxidation potential of DA (black square) and AA (red circle) vs. mass of pristine 2D-hBN immobilised and plot (D) depicting peak current of DA (black square) and AA (red circle) vs. mass of pristine 2D-hBN immobilised. Scan rate: 100 mV s^{-1} (vs. SCE). Each data point (C and D) is the average and standard deviation (*N = 3*).*..139

Figure 5.4: Typical cyclic voltammograms (A) recorded in 1 mM DA (PBS pH 7.4) using an unmodified GC electrode (black) and a GC electrode following

*modification with various pristine 2D-hBN masses of 108 (blue), 216 (green) and 324 ng (red). The dashed line depicts the PBS blank for the GC electrode. Analysis of cyclic voltammograms for the unmodified and pristine 2D-hBN modified GC electrode is presented in the form of plot (B) illustrating DA oxidation potential vs. mass of pristine 2D-hBN deposited, and plot (C) depicting peak current vs. mass of pristine 2D-hBN immobilised upon a GC electrode. Scan rate: 100 mV s^{-1} (vs. SCE). Each data point (B and C) is the average and standard deviation (*N = *3).*.....142

Figure 5.5: Typical cyclic voltammograms recorded in 1 mM DA (black) and 1 mM AA (red) pH 7.4 PBS. The response of the unmodified SPEs are utilised in (A) and 324 ng pristine 2D-hBN modified SPEs in (B).The 'dashed line' depicts the blank response in the absence of the analyte. Scan rate: 100 mV s^{-1} (vs. SCE). 148

Figure 5.6: Typical DPVs obtained utilising unmodified SPEs (A) and 108 ng pristine 2D-hBN modified SPEs (B) by adding aliquots of DA at concentrations in the range of 3 – 75 μM into a 0.1 mM AA solution (pH 7.4 PBS); the dotted line represents 0.1 mM AA. Analytical curve (C) obtained utilising unmodified (red) and 108 ng pristine 2D-hBN modified SPEs (black) corresponding to the anodic peak current for the oxidation of DA over the concentration range. Also shown is the correlation/curve (D) utilising unmodified (red) and 108 ng pristine 2D-hBN modified SPEs (black) corresponding to the anodic peak potential for the oxidation of DA and how this changes over the concentration range. Conditions as follows: E-*pulse, 20 mV;* t-*pulse, 200 ms; equivalent scan rate, 10 mV s^{-1}; (vs. SCE). Each data point (C and D) is the average and standard deviation (*N = *3).* 150

Figure 5.7: Typical cyclic voltammograms recorded in 1 mM UA in pH 7.4 PBS utilising an unmodified SPE (black) and SPEs following modification with pristine 2D-hBN masses of 108 (blue), 216 (green) and 324 ng (red). The dashed line depicts

*the PBS blank. Analysis of cyclic voltammograms for the unmodified and pristine 2D-hBN modified SPE's is presented in the form of plot (B) illustrating UA oxidation potential vs. mass of pristine 2D-hBN and plot (C) depicting peak current vs. mass of pristine 2D-hBN immobilised upon a SPE. Scan rate: 100 mV s^{-1} (vs. SCE). Each data point (B and C) is the average and standard deviation (*N = *3).* 152

Figure 5.8: Typical cyclic voltammograms (A) recorded in 0.5 mM DA and 0.5 mM UA (PBS pH 7.4) with an unmodified SPE (black) and pristine 2D-hBN modified SPEs at masses of 108 (blue), 216 (green) and 324 ng (red). Figure B depicts voltammograms recorded in 0.5 mM DA and 0.5 mM UA (in a pH 5 acetate buffer) at an unmodified SPE (black) and a 324 ng (red) pristine 2D-hBN modified SPE. Scan rate: 100 mV s^{-1} (vs. SCE). 153

Figure 5.9: Typical DPVs (A, C, E and G) recorded by adding aliquots of DA at concentrations in the range of 3–75 μM (in 0.1 mM UA in pH 5.0 acetate buffer) utilising an unmodified SPE and a SPE following modification with 108, 216 and 324 ng pristine 2D-hBN. Dotted line represents 0.1 mM UA blank. Additionally, corresponding analytical curves of the simultaneous oxidation of DA (black squares) and UA (red circle) over the concentration ranges utilising unmodified SPEs (Figure B) and 108 ng (Figure D), 216 ng (Figure F), 324 ng (Figure H) pristine 2D-hBN modified SPEs are shown. Conditions as follows: E-pulse, 20 mV; t-pulse, 200 ms; equivalent scan rate, 10 mV s^{-1}; (vs. SCE). Each data point (B, D, F and H) is the average and standard deviation (N = 3). 156

Figure 6.1: Typical cyclic voltammograms recorded in an oxygen saturated 0.1 M H_2SO_4 solution using unmodified (black line), 37.5 ng surfactant-exfoliated 2D-hBN (red line) and 10 μg sodium cholate (on its own as a control, blue line) modified SPEs**.** Shown in the inset is analysis of the cyclic voltammograms in the form of a

plot of oxygen reduction potential vs. mass of 2D-hBN (red squares) and sodium cholate (blue triangles) electrically wired upon SPEs. The green circle depicts an unmodified (bare) SPE. Scan rate: 100 mV s^{-1} (vs. SCE).....166

Figure 6.2: Typical cyclic voltammograms (A) recorded in nitrogen saturated 0.1 M H_2SO_4 solution using unmodified (black line), 37.5 ng surfactant-exfoliated 2D-hBN (red line) and 10 µg sodium cholate (blue line) modified SPEs. Also shown are cyclic voltammograms (B) recorded in nitrogen saturated 0.1 M H_2SO_4 with unmodified (black line), 54 ng (red line), 108 ng (blue line), 216 ng (green line) and 324 ng (pink line) pristine 2D-hBN modified SPEs. Scan rate: 100 mV s^{-1} (vs. SCE). 167

Figure 6.3: Cyclic voltammograms recorded in 0.1 M H2SO4 using; (A) an unmodified SPE, (B) a 37.5 ng surfactant-exfoliated 2D-hBN modified SPE, (C) a 10 µg sodium cholate modified SPE and (D) a 324 ng pristine 2D-hBN modified SPE. Repeat scans were performed up to 10 cycles. Scan rate: 100 mV s^{-1} (vs. SCE). ...170

Figure 6.4: Illustrates Tafel plots for unmodified (A), 7.5 (B), 15 (C), 37.5 (D) and 75 ng (E) surfactant-exfoliated 2D-hBN modified SPEs.....172

Figure 6.5: Illustrates Tafel plots for unmodified (A), 2 (B), 4 (C), 10 (D) and 20 µg (E) sodium cholate modified SPEs. 173

Figure 6.6: Typical cyclic voltammograms recorded in 0.1 M H_2SO_4 with surfactant-exfoliated 2D-hBN masses of: 7.5 (red line), 15 (yellow line), 37.5 (blue line) and 75ng (green line) immobilised upon SPEs (A). Sodium cholate masses of: 2.0 (red line), 4.0 (yellow line), 10.0 (blue line) and 20.0 µg (green line) immobilised upon SPEs (B). Pristine 2D-hBN masses of: 7.5 (red line), 15 (yellow line), 37.5 (blue line) and 75ng (green line) immobilised upon SPEs (C). In all cases, the black line represents an unmodified (bare) SPE. Scan rate: 100 mV s^{-1}. 178

*Figure 6.7: Typical cyclic voltammograms (A) recorded in 0.1 M H_2SO_4 with unmodified (black line) and 75 ng pristine 2D-hBN (green line), 75 ng surfactant-exfoliated 2D-hBN (red line) and 20 µg sodium cholate (blue line) modified SPEs. Scan rate: 100 mV s^{-1}. (B) Analysis of voltammograms (Figure 6.5) illustrates the effects of SPEs modified with masses of pristine 2D-hBN (green) and surfactant-exfoliated 2D-hBN (red), mass range: 7.5, 15, 37.5 and 75 ng along with sodium cholate (blue) mass range: 2, 4, 10 and 20 µg vs. the capacitance (µF). (C) Typical charge/discharge profiles recorded in 0.1 M H_2SO_4 with unmodified (black) 75 ng pristine 2D-hBN (green), 75 ng surfactant-exfoliated 2D-hBN (red) and 20 µg sodium cholate (blue) modified SPEs. (D) Analysis of charge/discharge profiles illustrates the effects of SPEs modified with masses of pristine 2D-hBN (green) and surfactant-exfoliated 2D-hBN (red), mass range: 7.5, 15, 37.5 and 75 ng along with sodium cholate (blue) mass range: 2, 4, 10 and 20 µg, vs. the capacitance (µF). ..*180

Figure 6.8: Capacitance circuits for the three-capacitor system, A) in parallel and B) in series.....183

Figure 6.9: Evaluation of the capacitance of the supercapacitor integrated into a parallel circuit for 100 µF 185

Figure 6.10: Evaluation of the capacitance of the supercapacitor integrated into a parallel circuit for 200 µF. 186

Figure 6.11: Evaluation of the capacitance of the supercapacitor integrated into a parallel circuit for 620 µF. 187

Figure 6.12: Capacitance retention 500 life cycle test obtained from charge/discharge profiles in 0.1M H_2SO_4 utilising a 75 ng pristine 2D-hBN, 75 ng surfactant-exfoliated 2D-hBN and 10 µg sodium cholate modified SPE, at a current of 5.0 µA. 191

Figure 6.13: Typical charge/discharge profiles recorded in 0.1 M H_2SO_4 with a 7.5 ng surfactant-exfoliated 2D-hBN modified SPE. Note the average slope of the charge profile relates to 0.015329 V s^{-1} (N=3) at a current of 5.0 µA. 194

Figure 7.1: Typical TEM image of surfactant-exfoliated 2D-hBN after deposition onto a holey carbon film supported upon a Cu TEM grid (A). Also shown are typical cyclic voltammograms recorded in pH 7.4 PBS with (B) 1 mM DA, (C) 1 mM AA and (D) 1mM UA when utilising unmodified SPEs (black), and 150 ng surfactant exfoliated 2D-hBN (red) and 40 µg sodium cholate (blue) modified SPEs. The dashed line represents the blank PBS respectively. Scan rate: 100 mV s^{-1} (vs. SCE). Note that full coverage study data of the modified electrodes is presented in Figure 7.2 and Table 7.2 206

Figure 7.2: Analysis of the cyclic voltammograms of 7.5 – 300 ng surfactant-exfoliated 2D-hBN and (separately) 2 – 80 µg sodium cholate modified SPEs is presented in the form of plot (A), illustrating the oxidation potential of DA (circle), AA (inverted triangle) and UA (square) vs. mass of surfactant- exfoliated 2D-hBN immobilised (red) and equivalently oxidation potential of DA (circle), AA (inverted triangle) and UA (square) vs. mass of sodium cholate immobilised (blue). Plot (B) depicts the peak current of DA (circle), AA (inverted triangle) and UA (square) vs. mass of surfactant-exfoliated 2D-hBN immobilised (red) and equivalently peak current of DA (circle), AA (inverted triangle) and UA (square) vs. mass sodium cholate immobilised (blue). In plots A and B, the black circle, inverted triangle and square represent the unmodified SPE towards DA, AA and UA respectively. Scan rate: 100 mV s^{-1} (vs. SCE). Each data point (A and B) is the average and standard deviation (N = 3). 208

Figure 7.3: **A:** Typical cyclic voltammograms recorded in 0.5 mM DA and 0.5 mM AA (PBS pH 7.4) using an unmodified (black), 150 ng surfactant-exfoliated 2D-hBN (red) and 40 µg sodium cholate (blue) modified SPEs. **B:** Voltammograms recorded in 0.5 mM DA and 0.5 mM UA (PBS pH 7.4) at unmodified (black), 150 ng surfactant-exfoliated 2D-hBN (red) and 40 µg sodium cholate (blue) modified SPEs. A and B were recorded utilising a scan rate of 100 mV s^{-1} (vs. SCE). **C:** Typical DPVs obtained by adding aliquots of DA at concentrations in the range of 3 – 75 µM into a 0.1 mM AA solution (pH 7.4 PBS) utilising a 150 ng surfactant-exfoliated 2D-hBN modified SPE; the dashed line represents 0.1 mM AA with no DA present. **D:** Analytical curves corresponding to the anodic peak current for the oxidation of DA over the concentration range studied, obtained utilising unmodified and surfactant-exfoliated 2D-hBN (mass range: 7.5 – 300 ng) modified SPEs. DPV conditions: E-pulse, 20 mV; t-pulse, 10 mV s^{-1}; (vs. SCE). Each data (D) is the average deviation (N = 3) 214

Figure 7.4: Typical DPVs (A) for the simultaneous detection of DA and AA utilising unmodified/bare SPEs by adding aliquots of DA at concentrations in the range of 3 – 75 µM into a 0.1 mM AA solution (pH 7.4 PBS); the dashed line represents the 0.1 mM AA scan in the absence of DA. (B) illustrates typical DPVs for the simultaneous detection of DA and UA utilising unmodified SPEs by adding aliquots of DA at concentrations in the range of 3 – 75 µM into a 0.1 mM UA solution (pH 7.4 PBS); the dashed line represents 0.1 mM UA scan in the absence of DA. Conditions as follows: E-*pulse, 20 mV;* t-*pulse, 200 ms; equivalent scan rate, 10 mV* s^{-1}*; (vs. SCE).* 217

Figure 7.5: DPVs obtained utilising (A), 40 µg sodium cholate modified SPEs by adding aliquots of DA at concentrations in the range of 3 – 75 µM into a 0.1 mM AA

solution (pH 7.4 PBS); the dashed line represents 0.1 mM AA scan in the absence of DA. Analytical curves (B) obtained utilising unmodified and sodium cholate modified SPEs of masses ranging from 2 – 80 µg corresponding to the anodic peak current for the oxidation of DA over the concentration range. Conditions as follows: E-*pulse, 20 mV;* t-*pulse, 200 ms; equivalent scan rate, 10 mV* s^{-1}*; (vs. SCE). Each data point (B) is the average and standard deviation (N = 3).*.....219

Figure 7.6: DPVs obtained utilising (A), 150 ng surfactant-exfoliated modified SPEs by adding aliquots of DA at concentrations in the range of 3 – 75 µM into a 0.1 mM UA solution (pH 7.4 PBS); the dashed line represents 0.1 mM UA. Analytical curves (B) obtained utilising unmodified and surfactant- exfoliated 2D-hBN modified SPEs of masses ranging from 7.5 – 300 ng corresponding to the anodic peak current for the oxidation of DA over the concentration range. (C) analytical curves obtained utilising unmodified and surfactant-exfoliated 2D-hBN modified SPEs of masses ranging from 7.5 – 300 ng corresponding to the anodic peak current for the oxidation of UA over the concentration range. Conditions as follows: E-*pulse, 20 mV;* t-*pulse, 200 ms; equivalent scan rate, 10 mV* s^{-1}*; (vs. SCE). Each data point (B and C) is the average and standard deviation (N = 3).* 221

Figure 7.7: DPVs obtained utilising (A), 40 µg sodium cholate modified SPEs by adding aliquots of DA at concentrations in the range of 3 – 75 µM into a 0.1 mM UA solution (pH 7.4 PBS); the dashed line represents 0.1 mM UA. Analytical curves (B) obtained utilising unmodified and sodium cholate modified SPEs of masses ranging from 2 – 80 µg corresponding to the anodic peak current for the oxidation of DA over the concentration range. (C) analytical curves obtained utilising unmodified and sodium cholate modified SPEs of masses ranging from 2 – 80 µg corresponding to the anodic peak current for the oxidation of UA over the concentration range.

Conditions as follows: E-*pulse, 20 mV;* t-*pulse, 200 ms; equivalent scan rate, 10 mV* s^{-1}*; (vs. SCE). Each data point (B and C) is the average and standard deviation (N = 3).* 223

Figure 8.1: Typical cyclic voltammograms recorded in an oxygen saturated 0.1 M H_2SO_4 *solution using unmodified (black line), 1% 2D-hBN (blue line), 5% 2D-hBN (red line), 10% 2D-hBN (green line) and 15% 2D-hBN (pink line) incorporated SPEs. Shown in the inset is analysis of the cyclic voltammograms in the form of a plot of oxygen reduction potential vs. % incorporation of 2D-hBN. Scan rate: 100 mV* s^{-1} *(vs. SCE).*.....232

Figure 8.2: Typical SEM images for SPE with 1% 2D-hBN (A), 5% 2D-hBN (B), 10% 2D-hBN (C) and 15% 2D-hBN (D). 2D-hBN platelets are evident as disc-like shapes approximately 200 nm in size......234

Figure 8.3: Analysis of cyclic voltammograms obtained in an oxygen saturated 0.1 M H_2SO_4 *solution in the form of a plot of oxygen reduction peak current vs. incorporated 2D-hBN % (A), peak current vs. mass of pristine 2D-hBN (B) and peak current vs. mass of surfactant-exfoliated 2D-hBN deposited upon SPEs, recorded in oxygen saturated 0.1 M* H_2SO_4*. Scan rate: 100 mV* s^{-1} *(vs. SCE). Each data point (A, B & C) is the average and standard deviation (*N = *3).* 237

Figure 8.4: Illustrates Tafel plots for unmodified (A), 1 (B), 5 (C), 10 (D) and 15% (E) hBN-SPEs. 238

Chapter 1 : General Electrochemistry

This chapter introduces general concepts in electrochemistry, enabling a greater understanding and appreciation of this subject. The ensuing chapters apply these concepts when exploring 2D-hexagonal boron nitride (2D-hBN) as a potential electrode material.

1.1 Introduction to Electrochemistry

Electrochemical and electroanalytical techniques are concerned with the interaction between electricity and chemistry, enabling specific electrical quantities such as current, potential or charge to be measured and thus related to chemical reactions.[1, 2] The field of electrochemistry has an array of applications including: fuel cells, batteries, electroanalytical sensors and solar power. Therefore, the beneficiaries of electrochemistry are both the scientific community and wider population.

Unlike most areas of chemistry in which bulk solutions are utilised for measurements, electrochemical processes occur at the electrode-solution interface and require a minimum two electrode conducting system with a contacting electrolyte solution, thus allowing the formation of an electrochemical cell.[3, 4] Electroanalytical techniques pay attention to the processes and dynamics that affect the movement of charge across the interface between an electrode (electronic conductor) and an electrolyte (ionic conductor).[1] Moreover, the two electrodes are known as the working electrode (which responds to the target analyte(s)) and the reference electrode (which upholds a constant potential and is independent to the composition of the electrolyte solution).[1]

Electrochemical cells can be considered one of galvanic or electrolytic.[1] In the first case (galvanic cells), a spontaneous chemical reaction at the electrodes of the cell occurs, whereby chemical energy converts into electrical energy. Whereas in the case of electrolytic cells, a non-spontaneous chemical reaction occurs at the electrodes, upon which electrical energy from an external source converts into chemical energy.[1]

The two main types of electroanalytical techniques utilised (differing through the electrical signal used for quantification) are potentiostatic (dynamic technique) and potentiometric (equilibrium technique) measurements.[1] In the case of the potentiostatic technique, the potential (static) is controlled (not zero current 'situations') and the current is measured when considering the charge transfer occurring between the electrode and solution. Whereas upon considering the potentiometric technique, the measured parameter is the potential applied across the membrane of an electrode, with the system remaining in equilibrium upon the utilisation of an external source (static at zero current 'situations'). Upon the implementation of the potentiostatic technique, the electron-transfer reaction is driven by the electrode potential, enabling the measurement of current to be achieved.[3] This corresponds to the rate at which electrons are transferred across the electrode-solution interface.[3] This technique is the focus of this thesis.

Furthermore, the potentiostatic method commonly employs a three electrode system, upon the utilisation of an auxiliary (counter) electrode.[1,3] The implementation of a counter electrode in combination with a working electrode, allows for a current to be passed through the solution and measured. As a result, the potential of the working electrode can be measured against the reference electrode,

which is stable, since the current will not pass through it.[3] Figure 1.1 illustrates a traditional three electrode system in electroanalytical experiments

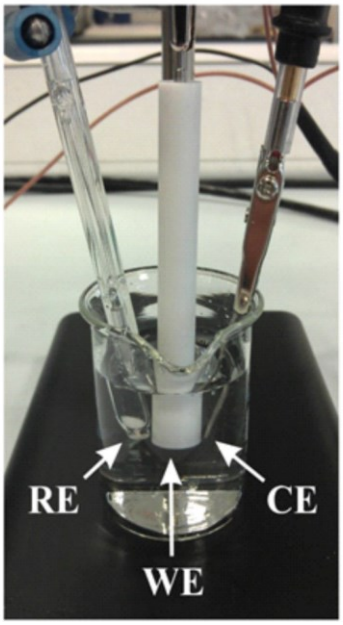

Figure 1.1: A typical three electrode system with a basal plane pyrolytic graphite electrode (WE), platinum wire counter electrode (CE) and a saturated calomel reference electrode (RE). Reproduced from Ref.[5]

1.1.1 Faradaic Processes

The two types of processes that occur at electrodes are known as Faradaic and non-Faradaic processes.[1, 4] A Faradaic process describes the transfer of charge across the electrode-solution interface, leading to an oxidation or reduction and is governed by Faraday's law shown in equation (1.1).[1]

$$eq = \frac{Q}{F} \qquad (1.1)$$

This reveals the amount of chemical reaction instigated by the current flow, is proportional to that of the electricity passed.[1] Where *eq* are the chemical equivalents of the reactants that are oxidised or reduced, Q, is the charge that is transferred across the electrode-solution interface and is given by $Q = it$ (for a stable current) or $Q = \int_0^t idt$ (for an unstable current) where i is the current, t, is the time and F, is the Faraday constant (96485.38 coulombs mol^{-1}).[1, 6]

A non-Faradaic process is somewhat different, since there is no charge transfer across the electrode-solution interface for an oxidation or reduction reaction to occur.[1] However applications such as capacitors can emanate from this process, since altering the potential of the electrode or the solution composition, can result in non-Faradaic processes such as desorption and adsorption taking place at the interface of the electrode, therefore an external capacitive current is able to flow.[1, 3] It is noted, both Faradaic and non-Faradaic processes ensue upon the initiation of electrode reactions.

The implementation of potential-controlled techniques allows for the obtention of a Faradaic current response, which is related to the concentration of the analyte under investigation. Thus, monitoring the electron transfer of a redox couple allows such responses to be measured:[1, 6]

$$O + ne^- \leftrightarrow R \qquad (1.2)$$

where O and R are the oxidised and reduced species respectively, of the redox couple. This reaction will take place in a potential region which enables the electron transfer to be kinetically or thermodynamically favourable. Furthermore thermodynamically controlled systems relate the potential of the electrode to the

activity of the species at the surface, where a_O and a_R denote the activities of the oxidised and reduced forms respectively on the electrode surface, in accordance with the Nernst equation:[1-4, 7]

$$E = E^0 - \frac{RT}{nF} \ln \frac{a_R}{a_O} \quad (1.3)$$

where E^o is the standard potential for the redox reaction, R is the universal gas constant (8.314 J K^{-1} mol^{-1}), T is the temperature (in Kelvin), n is the number of electrons transferred in the reaction, and F is the Faraday constant (96485.38 C mol^{-1}). In ideal highly dilute aqueous solutions, (whereby the ions do not interact with each other), it is assumed that the activity is equal to concentration. Leading to the Nernst equation being expressed in the following form:[1, 3, 7]

$$E = E^0 - \frac{RT}{nF} ln \frac{C_R}{C_O} \quad (1.4)$$

where C_O and C_R are the concentrations of the oxidised and reduced species respectively (on the electrode surface). Resultantly, at a temperature of 298 K and since ln (x) = 2.3log(x) equation (1.4) is further expressed as:[1, 3]

$$E = E^0 - \frac{0.059}{n} \, log \frac{C_R}{C_O} \quad (1.5)$$

From the said Faradaic processes, a plot of current *vs*. potential results in the obtention of a voltammogram (discussed later). Furthermore, characteristics such as the shape and magnitude of the voltammogram corresponds to the Faradaic and non-

Faradaic processes exhibited in the reaction of the electrode. The background charge current (non-Faradaic) and Faradaic current form the overall current observed.[7]

1.1.2 Mass Transport

Reactions that occur in the electrode-solution interface, can be influenced or dominated by mass transport (the rate at which an analyte moves towards the surface of an electrode) and thus affect the rate of reaction.[2, 3] There are three forms of mass transport that influence a reaction:[1, 3, 6, 8]

- Diffusion – movement of charged and uncharged particles from a region of higher concentration to regions of lower concentration, hence the influence of concentration gradient between the electrode surface and solution.
- Convection – the mechanically forced movement of a solution species to the electrode *via* stirring, gas flow, vibration and pumping (forced convection). In addition, a second type of convection, natural convection, is created by minimal density or thermal differences, whereby a solution is mixed in a random and unpredictable manner.
- Migration – the movement of ionic species in the liquid phase towards an oppositely charged electrode. Thus, an electrostatic effect arises owed to the application of voltage on the electrodes, creating a charged interface (the said electrodes). Hence any charged or partially charged ions heading towards that interface will be repelled or attracted by its electrostatic forces.

When applying a voltammetric technique in an experimental setup, the mass transport can be controlled so that only one factor from those stated above (usually diffusion) is present. Diffusion is favoured since it ensures the transfer of electroactive species occurs at a reproducible rate, (corresponding to the

concentration of the analyte in the bulk solution), without utilising any mechanical methodologies.[8] Forced convection can be reduced upon abandoning techniques involving stirring and electrode rotation. In the case of migration, utilising a supporting electrolyte (not electroactive in the potential region of the analyte investigated) negates its effect. Indeed, with a concentration greatly superior to that of the target analyte (100 times higher), the supporting electrolyte reduces the electric field between the two electrodes and thus offsets the potential gradient. It is noted, the resistance of a solution can be reduced upon the utilisation of said electrolyte.[1, 6]

Flux (*J*), which is defined as the number of molecules penetrating a specific unit area of an electrode over an imaginary plane, is the measurement of mass transport within an electrochemical system. The units of flux correspond to mol s^{-1} cm^{-2}. Diffusional flux (mass transport specific to diffusion) which describes the flux of an electroactive species from solution to the electrode can be quantified utilising Fick's 1st law:[1, 3, 4]

$$J(x,t) = -D\left[\frac{\partial C(x,t)}{\partial x}\right] \qquad (1.6)$$

where, $J(x,t)$ is the flux of the species at time *t*, and distance *x*, in mol s^{-1} cm^{-2}. $\frac{\partial C(x,t)}{\partial x}$ is the concentration gradient (at time *t*, and distance *x*) in mol cm^{-3} cm^{-1} and *D* is the diffusion coefficient. The negative sign suggests the concentration gradient is moving from a high to low concentration gradient.[1, 4, 6] It is also noted that the smaller the molecule, the larger the diffusion coefficient is. Thus, the relationship between distance and time to the concentration results in the formation of Fick's 2nd law:[1, 4, 6]

$$\frac{\partial C}{\partial t} = D\frac{\partial^2 C}{\partial x^2} \quad (1.7)$$

Previously, Fick's 1st law demonstrated the proportionality of flux in relation to the concentration gradient slope, when diffusion is the only mode of mass transport considered. The Nernst-Planck equation considers both migration and convection (previously discounted) along with diffusion in relation to flux, and is shown below:[1, 3, 6]

$$J(x,t) = -D\frac{\partial C(x,t)}{\partial x} - \frac{zFDC(x,t)}{RT}\frac{\partial \varphi(x,t)}{\partial x} + C(x,t)V(x,t) \quad (1.8)$$

where, D is the diffusion coefficient, $\frac{\partial C(x,t)}{\partial x}$ is the concentration gradient at time (t) and distance (x), $\frac{\partial \varphi(x,t)}{\partial x}$ is the potential gradient, z is the charge of the electroactive species and $V(x,t)$ is the hydrodynamic velocity in aqueous media. It is noted, the equations above are specifically utilised for one dimension.[1, 3, 6]

The magnitude of the current i, and its relationship with flux, J, is shown by the following expression:[1-4, 6]

$$i = -nAFJ \quad (1.9)$$

where, n is the number of electrons, A is the electrode area and F is the Faraday's constant (96,485.33 C mol^{-1}). Incorporating equation (1.6) with equation (1.9) results in the formation of equation (1.10) which exhibits the relationship between

the concentration gradient of an electroactive species and the diffusion induced current.

$$i = -nFAD\frac{\partial C(x,t)}{\partial x} \quad (1.10)$$

The inhibition of migration and convection as a mode of mass transport leaves only diffusion to take place. The particles must pass through the Nernst diffusional layer (formed by the electrochemical technique utilised), which is illustrated in Figure 1.2. It is observed that beyond the diffusional layer, δ, the solution is well mixed resulting in the concentration of the electroactive species remaining at a constant bulk value. However, as the analyte moves through the diffusion layer, the diffusional mass transport mode dominates (concentration changes occur in this zone only) and natural convection is no longer prevalent, due to the rigid electrode surface. It is noted, the size of said diffusion layers is in the order of tens to hundreds of micrometres and this can be affected by scan rate, v since the thickness of the diffusion layer, increases as a function of time, *t*. Thus the 2 dimensional diffusion layer can be calculated from:[4]

$$\delta = \sqrt{2Dt} \quad (1.11)$$

Where: $t = \frac{RT}{Fv}$ (1.12)

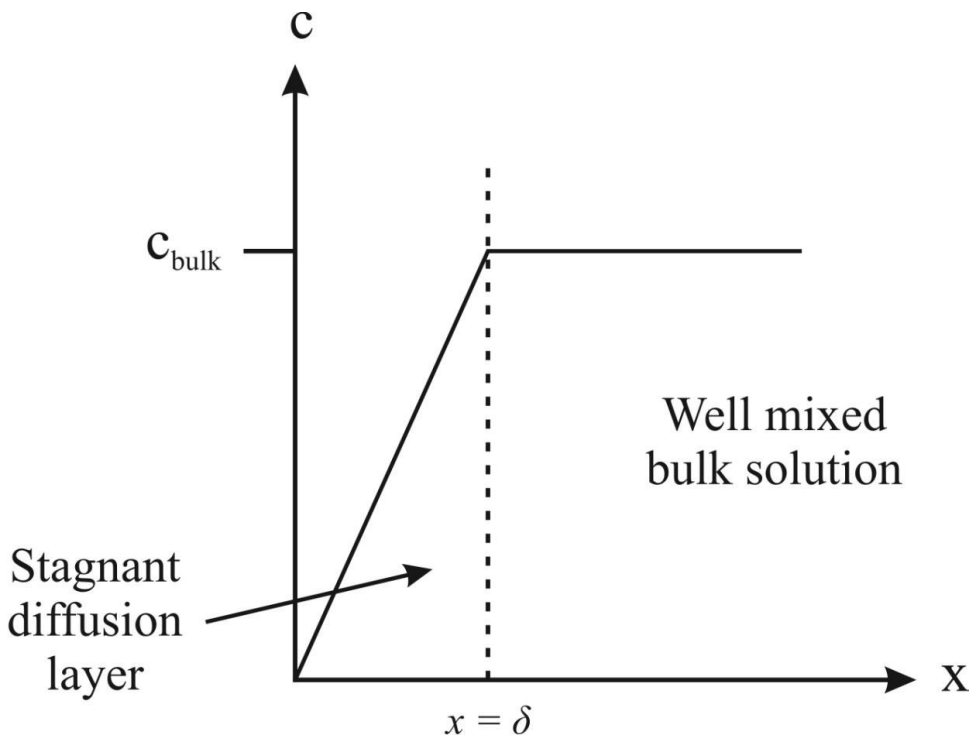

Figure 1.2: An illustration of the Nernst diffusion layer. Reproduced from Ref.[5]

1.1.3 Reactions Controlled by the Rate of Electron Transfer

The relation between current and potential differs when mass transport is observed to be fast, as a result the reaction is controlled by the rate at which the electron transfer takes place. This occurs between the conduction bands of oxidised and reduced species. The rate of reduction, V_{red} is given by:[3]

$$V_{Red} = k_{Red} C^{O}(0,t) \quad (1.13)$$

The rate of oxidation, V_{Ox} is the reverse form of equation (1.13):

$$V_{Ox} = k_{Ox} C^{R}(0,t) \quad (1.14)$$

where C^O and C^R are concentrations of the oxidised and reduced species respectively, with k_{Ox} and k_{Red} being the heterogeneous rate constants for the oxidation and reduction half-cells respectively. The Butler-Volmer equations below express this further.[3]

$$k_{Red} = k^0 \exp[\frac{-\alpha nF(E - E^0)}{RT}] \quad (1.15)$$

$$k_{Ox} = k^0 \exp[\frac{(1-\alpha)nF(E - E^0)}{RT} \quad (1.16)$$

where k^0 is the standard heterogeneous rate constant (cm s^{-1}), corresponding to the reaction speed between an analyte and the electrode material utilised. Furthermore, α is the transfer coefficient which describes the symmetry of a free energy curve with regards to products and reactants (an α value of 0.5 is noted for a symmetrical curve).[3]

In addition, equations (1.13) and (1.14) illustrate that upon changing the applied potential, there is an exponential effect on the electron transfer rate of oxidation and reduction half cells. Thus, positive and negative potentials speed up the formation of oxidation and reduction products, respectively. The equations stated correspond to a system in which no current passes, thus the addition of flux, j where $j = k_{red}[C_{ox}] - k_{ox}[C_{red}]$, yields the following expression upon the incorporation of equation (1.15) and (1.16):

$$j = k^0_{red} \exp[\frac{-\alpha nF(E-E^0)}{RT}][C_{Ox}] - k^0_{Ox} \exp[\frac{(1-\alpha)nF(E-E^0)}{RT}][C_{Red}] \quad (1.17)$$

1.2 Electrochemical Methodologies

1.2.1 Cyclic Voltammetry

The most prominently utilised voltammetric technique to record qualitative and quantitative information with regards to electrochemical reactions is cyclic voltammetry.[1, 3] Since it is a rapid method, it is used as a tool to comprehend the properties of electroactive species under investigation such as the heterogeneous electron-transfer reactions, thermodynamics, adsorption processes and coupled electrochemical reactions.[1, 3] Upon the use of this technique, the potential of the working electrode is linearly swept between two values at a fixed rate (scan rate, v (mV s^{-1})) E_1 and E_2 and reversed back to E_1 within a triangular waveform (Figure 1.3). This differs to linear sweep voltammetry which sweeps the potential from E_1 to E_2 only.[4, 9]

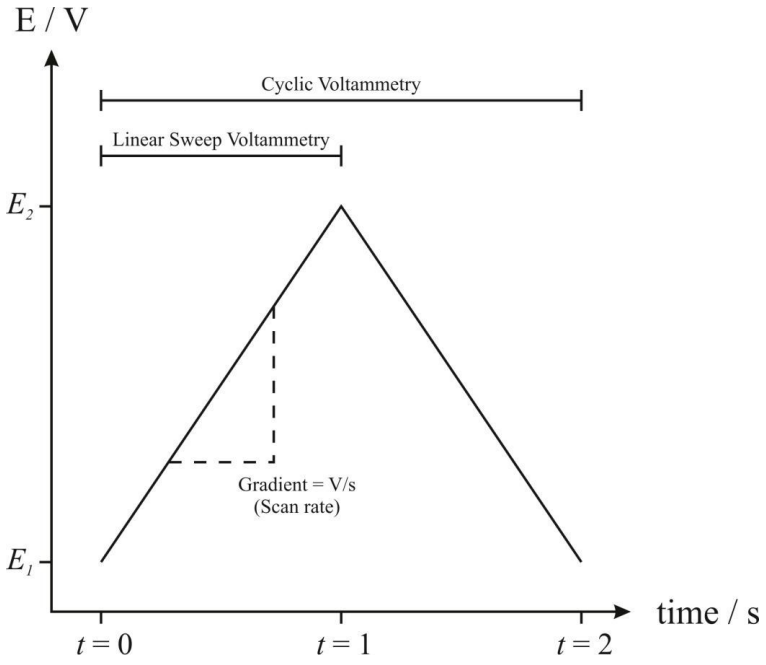

Figure 1.3: Triangular potential waveform utilised for linear sweep and cyclic voltammetry. Reproduced from Ref.[5]

The cyclic voltammetric technique enables single or multiple cycles to be carried out. In addition, the applied voltage utilising a potentiostat, allows the corresponding current to be measured. Thus, a plot of current *vs*. potential (voltage) reveals a cyclic voltammogram. A typical cyclic voltammogram for a 1mM potassium ferrocyanide (II) / 0.1 M KCl solution utilising a boron-doped diamond (BDD) working electrode, a saturated calomel reference electrode (SCE) and a platinum counter electrode is shown in Figure 1.4A. It is apparent a potential of -0.2 V is where the scan initiates, in which a non-faradaic process is in operation. However, as the potential is swept more positive towards the characteristic potential for said redox probe, a faradaic process becomes prominent, whereby the anodic current increases until a peak is reached, at this point the Fe (II) ions, which are on the surface of the working electrode begin to deplete, resulting in the formation of a symmetrical peak. Upon reversing the potential at +0.8 V, a non-faradaic process is again observed until a potential of +0.3 V is reached. At this point, the Fe (III) ions generated at the surface of the working electrode upon the initial potential sweep, are reduced (Fe (II)) back into the electrode solution interface forming a second peak.

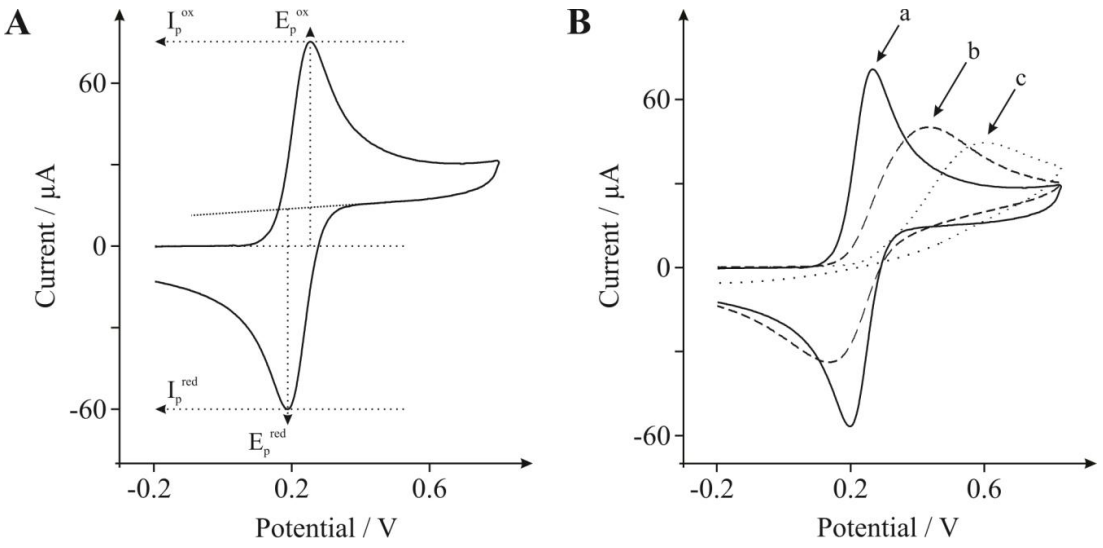

Figure 1.4: Typical cyclic voltammograms exhibiting the peak position E_p and peak height I_p (A) and (B) illustrates cyclic voltammograms for reversible (a), quasi reversible (b) and irreversible (c) electron transfer. Reproduced from Ref.[5]

It is noted that it is possible to distinguish if the redox process observed in a cyclic voltammogram, is reversible, quasi-reversible and irreversible when the distance between the two identifiable peaks is considered. This is dependent upon the processes being / not being controlled solely by mass transport. The above scenarios are illustrated in Figure 1.4B

The peak separation (ΔE_p) between two peak potentials (at 298 K) for a reversible redox couple, (where the rate of charge transfer is faster than the rate of mass transport) is given by:[7]

$$\Delta E_p = E_{pa} - E_{pc} = 0.057/n \qquad (1.18)$$

where n is the number of electrons within the half-reaction. Furthermore, when analysing a reversible system, (for a one electron transfer process) the ΔE_p should be 57 mV at 298 K where the peak potentials are independent of the scan rate implemented. The case for a quasi-reversible system differs. Here, two peaks of the redox couple are still present, however the ΔE_p is greater than 57 mV suggesting the peak potentials are dependent on the scan rate.[4] In addition, the standard reduction potential for a redox couple is shown by the following equation:

$$E^0 = \frac{E_{pa} + E_{pc}}{2} \qquad (1.19)$$

The case of an irreversible system (in which electron transfer is slow) differs further, the peaks of the redox couple increasingly separate and reduce in size. The peak potential for said system is given by:

$$E_p = E^0 - \frac{RT}{\alpha n' F}\left[0.78 - ln\left(\frac{k^0}{D^{\frac{1}{2}}}\right) + ln\left(\frac{\alpha n' F v}{RT}\right)^{1/2}\right] \qquad (1.20)$$

where υ is the voltammetric scan rate utilised, α is the transfer coefficient and n' is the number of electrons involved in the charge-transfer step. The, E_p potential is higher than that of E^0, with the over potential related to k^0 (the standard heterogenous rate constant) and α. Furthermore, the E_p is larger when the value of αn decreases resulting in the voltammogram obtained to become more irreversible.

Aside from obtaining quantitative information in the form of peak position with regards to a voltammogram, the peak current can also be found. There is a proportional relationship between the peak current and the concentration of the analyte under investigation and the anodic and cathodic peak currents are equal for a

reversible redox system. Thus the Randles-Ševčík equation for a reversible system gives:[1, 2, 4]

$$i_p = 0.446FA[C]_{bulk}\sqrt{\frac{FDv}{RT}} \quad (1.21)$$

Leading to (at 298 K):

$$I_p = (2.69 \times 10^5)n^{3/2}ACD^{1/2}v^{1/2} \quad (1.22)$$

When considering a quasi-reversible system, the value 2.65×10^5 replaces the constant in equation (1.22). The case of the irreversible system differs in that, α (transfer coefficient) is introduced and the value of the constant alters further. The equation (at 298 K) is given by:

$$i_p = 2.99 \times 10^5 \sqrt{\alpha}AD^{1/2}[C]_{bulk}v^{1/2} \quad (1.23)$$

where F is the Faraday constant, A is the electrode area (in cm^2), n is the number of electrons transferred in the redox process, D is the diffusion coefficient of the electroactive species (in $cm^2\ s^{-1}$), C is their concentration (in mol cm^{-3}) and v is the applied scan rate (in $V\ s^{-1}$).

Reversible and irreversible processes are governed by mass transport and charge transfer. The rate electron of transfer kinetics is measured by the heterogeneous rate constant, k^0. Whereas, the mass transport coefficient, m_T, measures the rate of mass transport by:[4]

$$m_T = \frac{D}{\delta} \quad (1.24)$$

where, δ is the diffusion layer thickness calculated upon the utilisation of equations (1.11) and (1.12). The heterogeneous rate constant, k^0can be calculated for quasi-reversible systems and the implementation of the Nicholson method enables the estimate of the k^0 utilising the following equation:[10]

$$\psi = k^0 \left[\frac{\pi D n v F}{RT}\right]^{-1/2} \quad (1.25)$$

where ψ is the kinetic parameter, *D*, the diffusion coefficient, *n*, the number of electrons involved in the process, *F*, the Faraday constant, *v*, the scan rate, *R*, the gas constant, and *T* the temperature. The kinetic parameter is tabulated in Table 1.1, as a function of peak-to-peak separation (ΔE_p) at a set temperature (298 K) for a one-step, one electron process.

ψ	$(\Delta E_p)(n)/\,mV$
20	61
7	63
6	64
5	65
4	66
3	68
2	72
1	84
0.75	92
0.50	105
0.35	121
0.25	141
0.10	212

Table 1.1: variation of ΔE_p with ψ at 298 K. Reproduced with permission from Ref.[10]

The function of (ΔE_p)which fits Nicholson's data, for practical usage, instead of producing a working curve is given by:[11, 12]

$$\psi = -\frac{(-0.628+0.0021X)}{(1-0.017X)} \tag{1.26}$$

where $X = \Delta E_p$ is used to determine ψ as a function of ΔE_p from the experimentally obtained voltammetry. From this, a plot of ψ against $\left[\frac{\pi DnvF}{RT}\right]^{-1/2}$ is produced

graphically enabling, k^0 (the standard heterogeneous rate transfer constant), to be found.. However if the value of ΔE_p shown in the Nicholson table is greater than 212 mV, the Klinger Kochi equation is utilised:[13]

$$k^0 = \left[2.18\left(\frac{D\alpha nFv}{RT}\right)^{1/2}\right] exp\left[\frac{-\alpha^2 nF(\Delta E_p)}{RT}\right] \quad (1.27)$$

where the α value corresponds to 0.5 and the remaining constants are equal to those described in equation (1.25).

The distinction between fast and slow electrode kinetics is related to the rate of mass transport, thus calculating the mass transport coefficient and heterogeneous rate constant enables the identification of a reversible or irreversible system by the following:

$k^0 \gg m_T$ (reversible) (1.28)

$k^0 \ll m_T$ (irreversible) (1.29)

The Matsuda and Ayabe parameter Λ, enables the transition limits between reversible and irreversible systems to be defined:[14]

$$\Lambda = \frac{k^0}{\left(\frac{FDv}{RT}\right)^{1/2}} \quad (1.30)$$

Thus, allowing the Matsuda Ayabe ranges to be determined (see below), where α corresponds to 0.5 for reversible, quasi-reversible and irreversible systems at 298 K.

Reversible	$\Lambda \geq 15$	$\Lambda \geq 0.3\ \upsilon^{1/2}$ cm s^{-1}
Quasi-reversible	$15 > \Lambda > 10^{-3}$	$0.3\ \upsilon^{1/2} > k^0 > 2 \times 10^{-5}\ \upsilon^{1/2}$ cm s^{-1}
Irreversible	$\Lambda \leq 10^{-3}$	$k^0 \leq 2 \times 10^{-5}\ \upsilon^{1/2}$ cm s^{-1}

1.2.2 Differential Pulse Voltammetry

Voltammetry is a technique concerned with applying a potential step leading to a pulse of current response which decays with time upon the consumption of electroactive species near the surface of the working electrode. Furthermore a faradaic process (I_F) superimposes together with a capacitive input (I_C) occurring as a result of double layer charge.[5] This double layer charging effect is eliminated rapidly, within microseconds and is illustrated in Figure 1.5 The Cottrell Equation describes the relationship of current in a reversible system, where $I \propto t^{-1/2}$ and in the case of charge, Q, is $Q \infty t^{-1/2}$.[5] The capacitative current deteriorates upon the application of a step in potential leading to the current being sampled. This is carried out upon the implementation of pulse widths.[5]

Differential pulse voltammetry (DPV) eliminates the capacitative input through subtraction, whereby the difference between two currents before the end of the pulse and prior to its application are measured.[5] These waveform pulses are illustrated in Figure 1.6 when superimposed on a staircase.

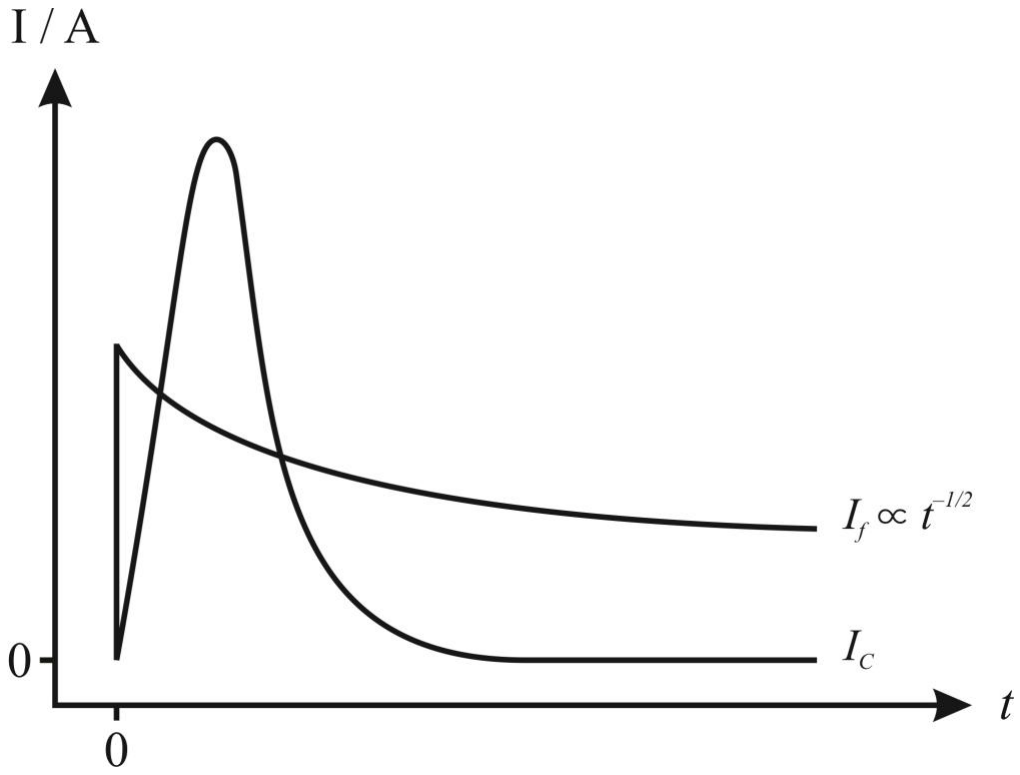

Figure 1.5: Effect of capacitative and Faradaic current following the application of a potential step. Reproduced from Ref.[5]

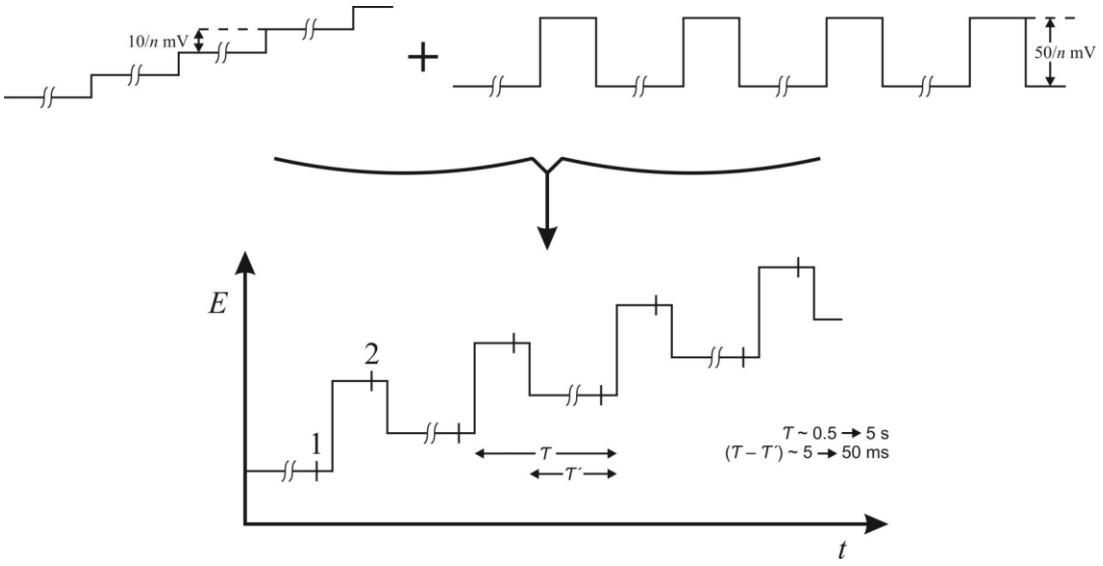

Figure 1.6: Differential pulse voltammetry waveform of pulses superimposed on a staircase. Reproduced from ref.[5]

Furthermore, a base potential in the staircase is employed and the pulse is shorter than the staircase wave form by 10 times.[5] Moreover, the difference between the two currents that are sampled enables a plot *vs.* staircase potential to be formed.[5] This results in a waveform in the shape of a peak, which is depicted in Figure 1.7.

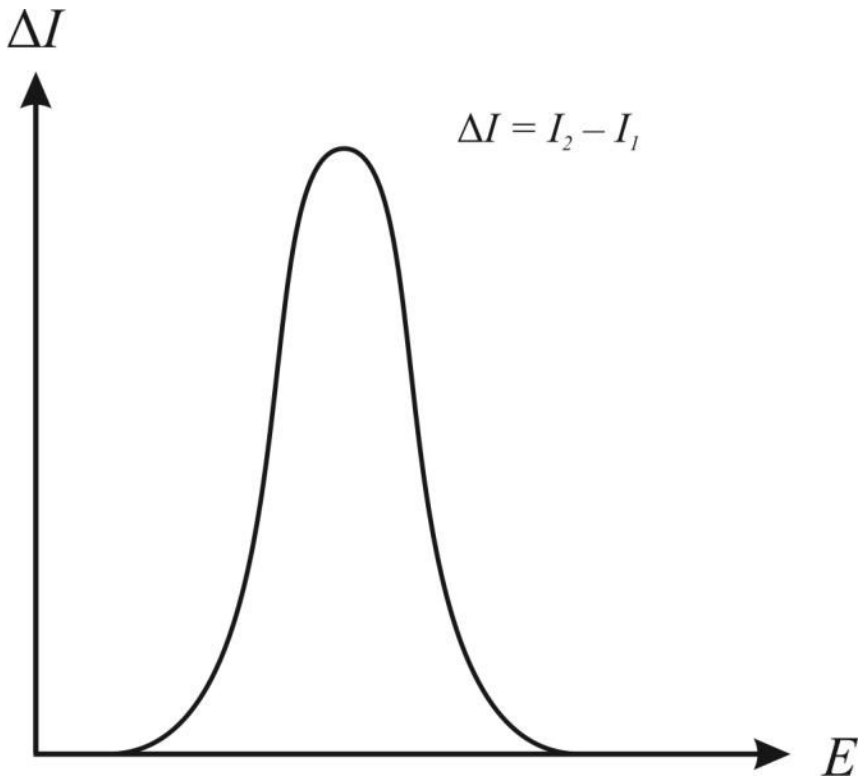

Figure 1.7: Differential pulse voltammetry; voltammetric profiles of ΔI vs. *staircase potential. Reproduced from Ref.*[5]

When considering a reversible system, the potential of the peak is given by: $E_p = E_{1/2} - \Delta E/2$ where $\Delta E$is the pulse amplitude. The current can be found with the following expression :[5]

$$I_p = \frac{nFAD^{1/2}C}{\pi^{1/2}t^{1/2}}\left(\frac{1-\alpha}{1+\alpha}\right) \quad (1.31)$$

Where the value of α, is given by:

$$\alpha = \exp(nF\Delta E/2RT) \quad (1.32)$$

Since DPV is effective in eliminating non-faradaic capacitative contrbutions *via* subtraction, it is utilised to resolve voltammetric signatures (typically cyclic voltammetry) which are close in terms of peak potential and difficult to distinguish.[5] Thus the implementation of DPV offers de-convoluted peak shaped responses which are easy to quantify. An example of this is illustrated in Figure 1.8, for the simultaneous detection of acetaminophen and ascorbic acid, whose voltammteric signals often overlap. Figure 1.8A exhibits a modified electrode response using cyclic voltammetry, whereas in Figure 1.8B differential pulse voltammetry is utilised. It is clear, when utilising DPV, two sharp, resolved peaks are apparent, whereas the cyclic voltammograms in Figure 1.8A are more convoluted and less distinguishable. Thus the utilisation of DPV enables the accurate simultaneous detection of acetaminophen and ascorbic acid to be accomplished.[15]

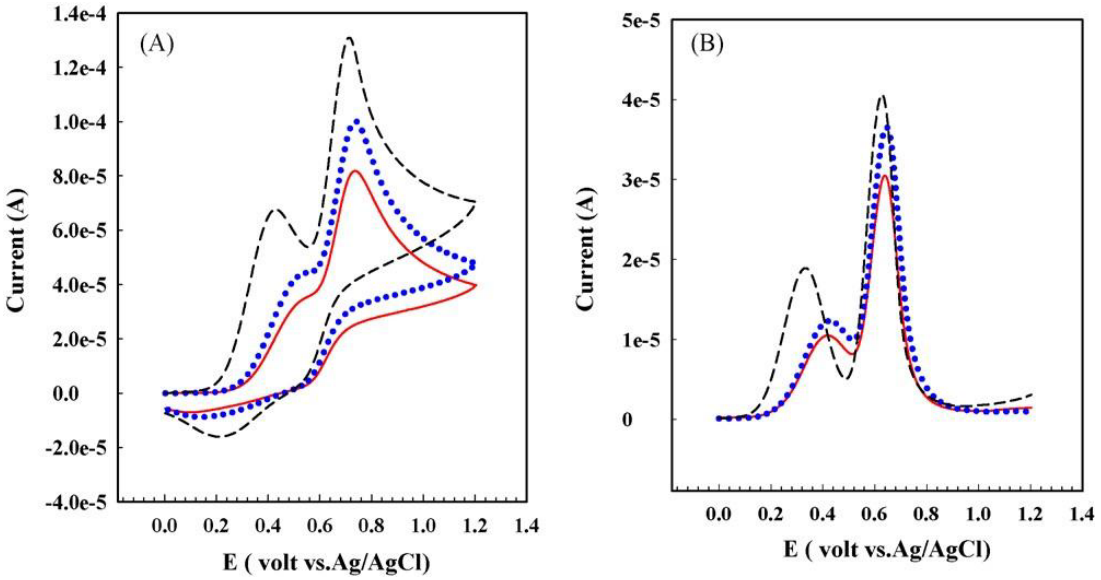

Figure 1.8: (A) Cyclic and (B) differential pulse voltammograms 0.1 mM and 0.1 mM ascorbic acid acetaminophen in acetate buffer solution (pH 4.0) on the surface of various electrodes; unmodified carbon paste electrode (solid line), CNT–carbon paste electrode (dotted line) and multi-walled carbon nanotube/thionine modified electrode (dashed line). Sweep rate was 100 mV s^{-1}. Reproduced from Ref.[5]

It is noted these responses are a result of increasing pulse amplitude. However, this correspondingly increases peak width, therefore ΔE values over 100 mV are seen as not feasible.[5] This means the electrochemical parameters must be optimised appropriately. Leading to the expression for the half-width at half height, $W_{1/2}$; where $W_{1/2} = 3.52RT/nF$ which results in a value of 90.4 mV where n = 1 at 298 K.[5] hence peak separations of 50 mV can be resolved with this technique. Furthermore, DPV has a detection limit of 10^{-7} M.[5]

1.2.3 Supercapacitors

Supercapacitors, also referred to as electrical double-layer capacitors, are energy storage devices.[16, 17] Within supercapacitors, energy is stored between the electrode/electrolyte interface *via* the accumulation of electrostatic ions on the electrode.[16, 17] The charge separation at the electrode/electrolyte interface is described by the Helmholtz model[18] whereby an electrode of surface area S (m^2) becomes polarised.[16] As a result, oppositely charged ions diffuse *via* the electrolyte forming a layer that is parallel to the electrode surface resulting in a neural charge. This build-up of charge is known as the electrical double layer.[16, 17] Furthermore, as the distance (d) between the ions and the electrode increases, there is a reduction in the potential within the vicinity of the electrode. Thus the Helmholtz-double layer can be seen as the electrical capacitor of capacitance, C_H and is given by:[16]

$$C_H = \varepsilon_0 \times \varepsilon_r \times \frac{S}{d} \tag{1.33}$$

where ε_0 is the vacuum permittivity ($\varepsilon_0 = 8.854 \times 10^{-12}\ F/m$), ε_r is the relative permittivity of the dielectric electrolyte, s is the surface area of an electrode and d is the effective thickness of the Helmholtz-double layer.[16]

However, the Helmholtz model disregards factors such as diffusion of ions. Thus, Stern devised a model which implements a diffuse model of the electrical double layer, in which there is an exponential decrease in potential from the surface of the electrode to the bulk solution and combined this with the Helmholtz model. This model also considered the hydrodynamic movement of the ionic species in the diffuse layer and the build-up of ions on electrode surface.[16] Furthermore these two

layers are equal to two capacitors in series, and the total capacitance C_{DL} is given by:[16]

$$\frac{1}{C_{DL}} = \frac{1}{C_H} + \frac{1}{C_D} \quad (1.34)$$

where C_H, is the Helmholtz layer and C_D, is the diffuse layer.

A supercapacitor contains two electrodes in contact with a current collector, separated by a thin isolation membrane impregnated with an electrolyte solution. Upon charging a supercapacitor, positive ions are attracted to the electrons at the cathode and the negative ions are attracted to the anode due to the vacancy of electrons, resulting in the obtention of a balanced charge.[16] Such attraction leads to the formation of capacitance between the ions and electrode surface. Thus, a supercapacitor which contains two electrodes is equal to two capacitors in series and the capacitance (C) is given by:[16]

$$\frac{1}{C} = \frac{1}{C_+} + \frac{1}{C_-} \quad (1.35)$$

where C, C_+ and C_- are the capacitance (where Farad = Coulomb/Volt), of the overall device, the positive electrode and negative electrode respectively.[16]

Furthermore, in order to compare the performance of various electrode materials, the gravimetric method is implemented to obtain a specific capacitance (C_s) and the calculation is given by:[16]

$$C_s = \frac{C}{m_1} \tag{1.36}$$

where C, is the capacitance (F) of the material and m_1 is the total mass (g) of the material.

It is important to also consider the electrolyte of choice, which can be organic, a liquid salt or an aqueous solution (applied in this thesis). The selection of electrolyte is based upon its ionic conductivity and the electrochemical stability window.[16, 17] Common aqueous electrolytes include acids and alkalis such as H_2SO_4 and KOH respectively. These solutions are often utilised due to their high conductivity in comparison to the organic alternative, resulting in improved power performance. Though, limitations include a low operating voltage (*ca.*1.0 V) due to the narrow electrochemical stability window of water (*ca.* 1.23 V).[16] However these solutions are used in the literature due to the ease of implementation and thus are highly beneficial to benchmark the system under investigation.[16]

1.2.4 Electroanalysis

Electroanalysis is the analytical division of electrochemistry in which electrochemical techniques are utilised to reveal the concentrations of specific target analytes within a given medium. Cyclic voltammetry and differential pulse voltammetry (stated earlier in this chapter), are the foremost utilised techniques for analysis in this thesis. Indeed, when considering an analyte, the voltammetric peak height (I_p) is attained at a certain voltammetric potential (E_p) from an oxidation or reduction reaction and an example of this is the benchmarked redox system, hexaammineruthenium (III) chloride. Upon utilisation of this system it is likely an increase in the concentration of the analyte corresponds to an increase in peak height and this relationship is known as the analytical linear range. There are two parameters utilised to benchmark electrochemical devices for their electroanalytical qualities. These are the analytical linear range and the statistical limit of detection (LOD). The analytical linear range is described as the linear relationship between the analyte concentration and peak height. Here, an analyte concentration increment results in an equal increment to the corresponding peak height. Additionally, the peak height in relation to concentration cannot be as easily realised when outside of this linear range. The linearity is measured through the regression (R^2) of the data points for a plot of peak height *vs*. concentration. The R^2 value can range between 1 and 0 for linear and non-linear curves respectively, though, within electroanalysis, R^2 values between 0.96 and 0.99 are viable. The second parameter often utilised to benchmark an electroanalytical system is the limit of detection (LOD). The LOD is described as the minimum value of the signal from the measured species which differs greatly to the blank signal. The LOD can be calculated *via*:

$$LOD = \frac{\overline{y_D} - \overline{y_B}}{q_1} = K_{D^{sb}}/q_1 \quad (1.37)$$

where $\overline{y_D}$ is the signal value and $\overline{y_B}$ is the mean blank signal, K_D is the factor implemented in accordance to the confidence statistical level. The K_D value is denoted as 3 leading to the 3 sigma method.[5] Furthermore, an LOD value can be obtained upon forming a repeatable, statistically viable calibration plot *via* the following equation:

$$LOD = 3Sb/m \quad (1.38)$$

where *Sb* is the standard deviation of the blank and *m* is the gradient of the calibration curve. A high quality calibration plot can lead to a low detection limit for the target analyte due the *Sb* value being small.

Finally, the working electrode utilised can be modified with different materials to improve electrochemical performance and thus electroanalysis. Indeed, much attention has turned towards modifying common substrates utilising state of the art 2D materials such as graphene, in order to obtain improved electrochemical performance in the sensing of analytes and the investigation of other key systems. More recently, research has deviated towards the exploration of other novel 2D materials such as 2D hexagonal Boron Nitride; this is further explored later in this thesis.

1.2.5 Redox Probes

To benchmark an electrochemical system upon the utilisation of the cyclic voltammetric technique (section 1.2.1), an inner or outer-sphere redox probe must be chosen. When utilising pyrolytic graphite or glassy carbon substrates, as is focused upon in this thesis, a wide variety of redox probes including hexaammineruthenium (III) chloride and potassium ferrocyanide (II) can be utilised as benchmarking tools.[19]

An outer-sphere redox probe such as hexaammineruthenium (III) chloride, is noted as *surface insensitive* since the k^0 is not influenced by varying factors including: the ratio between the surface oxygen and carbon, uncharged adsorbates (monolayer coating) on the surface of the electrode, *i.e.* surface cleanliness or specific adsorption to surface groups.[20] Moreover, the surface *i.e*. the electrode, does not involve any chemical or catalytic mechanism interactions such as an adsorption step.[20] Thus the electrode acts as a sink of electrons resulting in outer-sphere redox probes being mainly utilised to understand the electronic structure of materials due to the density of electronic states near the Fermi level.[20]

Whereas inner-sphere redox probes, such as potassium ferrocyanide (II) are noted as *surface sensitive* since the k^0 is influenced by factors such as the electrode surface, *i.e.* its chemistry and microstructure. Indeed, if the surface is affected by impurities or adsorbates, electro-catalytic interactions can become inhibited. Furthermore, these interactions can also be dependent upon oxygenated species being present or absent, to give favourable or unbeneficial electrochemical effects.[20, 21] As a result, such systems are highly influenced by the surface state and structure such that a surface interaction is required and being catalysed or inhibited by specific

interactions with surface functional groups (adsorption sites) rather than the density of electronic states due to these systems having high reorganisation energies.[20, 21]

1.3 Electrode Materials

The choice of working electrode is heavily relied upon when forming an electrochemical cell for electroanalytical experiments, due to the processes that occur on its surface.[2] A variety of electrode materials are available and noble metals such as gold and platinum are often utilised. These metallic electrodes offer favourable electron rate kinetics, with a large potential range. However, upon the utilisation of metallic electrodes, oxide films can form on the surface which can affect conductivity and also increase the background current. Furthermore, due to the high cost of metallic electrodes, their use as disposable electrodes becomes redundant.[5]

Carbon based electrode materials, which are readily available, easily modified and relatively chemically inert, offer a cheap alternative in comparison to the expensive metallic electrodes. Common carbon electrodes are manufactured from materials such as highly ordered pyrolytic graphite (HOPG), glassy carbon (GC), carbon fibres, boron-doped diamond (BDD) and single and multi-walled carbon nanotubes (SWCNTs and MWCNTs respectively).[22] Furthermore, not only are these carbon electrodes cheap relative to metallic electrodes, they offer a large potential window and a low background current. However the electron rate kinetics of carbon materials are slower than that of the metallic counterparts due to the way the species are oriented upon the surface. It is also noted, that carbon electrodes contain a sp^2 hybridised six-membered aromatic ring, though the ratios of edge and basal plane

sites differ with each electrode. Moreover, when considering edge and basal sites, it is noted edge sites offer a faster rate kinetics in comparison to basal plane sites.[22]

In this thesis, there were many forms of carbon which were utilised, most notably the BDD, the GC and pyrolytic graphite.

1.3.1 Carbon Materials

Due to its electron configuration having a small energy difference between the s-orbital and p-orbitals, carbon atoms can form many allotropes and those common to it include graphite and diamond. Graphite, which has a hexagonal structure, is made up of stacked graphene layers which are held together by Van der Waals forces. The carbon atoms in graphite are arranged in a sp^2 hybridised trigonal structure.[22] Whereas, the sp^3 hybridised covalently bonded structure of diamond arranges its atoms in a tetrahedral configuration.[22]

When implementing graphite as an electrode, a common material utilised is highly ordered pyrolytic graphite (HOPG). The HOPG material can be cut and modified to have either the edge plane (EPPG) or the basal plane(BPPG) as the surface, which offers "fast" and "slow" electron transfer kinetics respectively.[23, 24] EPPG electrodes can offer advantages over the BPPG electrodes, since the edge planes of an EPPG electrode are highly reactive allowing for low detection limits, high sensitivity and improved signal to noise ratio to be obtained.[23, 24] Though the BPPG electrode is the same material, the orientation of this material can affect the performance. A full schematic of the edge and basal plane sites is shown within Figure 1.9.

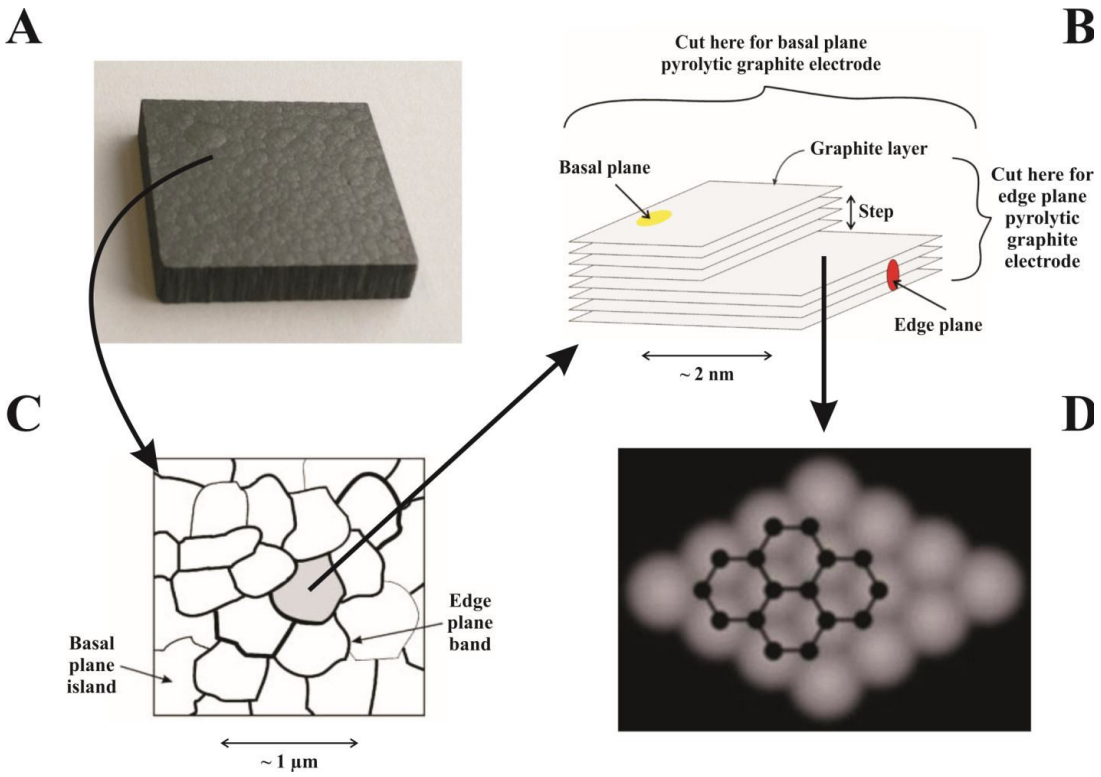

Figure 1.9: a) Image of a commercially available slab of HOPG. b) Schematic of a side on view of a HOPG surface, which highlights its edge plane and basal plane and like- sites/defects which exhibit contrasting behaviours in terms of electrochemical activity c) A representation of a HOPG surface illustrating the discrete basal plane and edge plane islands. d) A typical STM image of a HOPG surface with the corresponding fragment of the graphene structure superimposed. Reproduced with permission from Ref.[5]

Due to its insulating properties, diamond is not considered a good electrode material. However the introduction of boron, which is an electron acceptor, increases the conductivity of diamond, thus forming the boron doped diamond electrode (BDD).[25] Boron doping levels can range from 10^{19} to 10^{21} atoms/cm^3.[25] Furthermore organic compounds do not interact with the BDD resulting in the absence adsorbed by-products upon its surface when a redox reaction occurs, thus further reactions of electroactive species in the solution can occur owing to the absence of surface

pollution. Advantages of the BDD include a wide potential window for electrochemical procedures, low background currents and high stability in aggressive media.[25] The orbital structure of diamond is sp^3 and is therefore inert, boron doping is implemented since it acquires low charge carrier activation energy. The resulting BDD structure gives an electron configuration of $1s^2$ and four $2sp^3$ (hybrid orbitals). This hybridisation enables the formation of four strong covalent bonds with an additional four carbon atoms (each sharing two electrons) in a tetrahedron configuration.

A further carbon material utilised as an electrode is glassy carbon (GC). Properties of a GC include its surface having no defects and minimal impurities, a low permeability and it is non-porous.[26] The production method utilising a polymer define the said characteristics of the GC and it is described as a non-graphitising carbon since it is unable to be transformed into crystalline graphite at very high temperatures.[26] Furthermore, the GC has a 'ribbon' like structure (Figure 1.10) in which the aromatic rings are twisted and cross linked with covalent bonds, thus the GC contains sp^2 and sp^3 structures and is the sp^3 configuration that gives it the high strength, hardness and resistance to chemical attack.

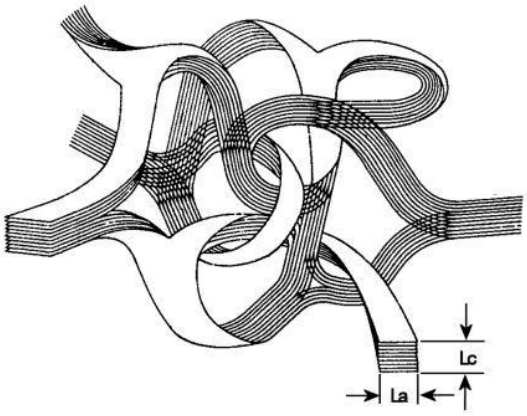

Figure 1.10: represents the structure of the GC. Reproduced from Ref.[5]

A hindrance to current electrochemical methods is the rigorous electrode preparation techniques which results in an electrode surface with no reactive sites, grain boundaries and adsorbed species upon it. Furthermore, the expense of metallic electrodes and some carbon electrodes such as EPPG and BPPG has resulted in the need to find a cheaper alternative. Due to the reasons stated, electrochemical experiments are difficult to transfer in the field which require disposable platforms with no pre-treatment or recourse. Thus, an electrode which was disposable and easily mass-producible whilst offering good performance was necessary. As a results screen-printed electrodes (SPEs) were produced. These SPEs are low cost, able to be mass produced, lightweight and require no pre-treatment or recourse.[27] An SPE contains an on-board working counter and reference electrode. Screen-printed carbon electrodes are fabricated using a thixotropic fluid such as a carbon ink.[27] A carbon ink is usually a specifically tailored mixture of graphite, carbon black, solvents, and polymeric binders.[27] The working and counter electrode are usually graphitic and the reference electrode is an Ag/AgCl paste. A detailed description of the manufacturing process is described in section 3.2.6. Figure 1.11 depicts an image of a typical SPE.

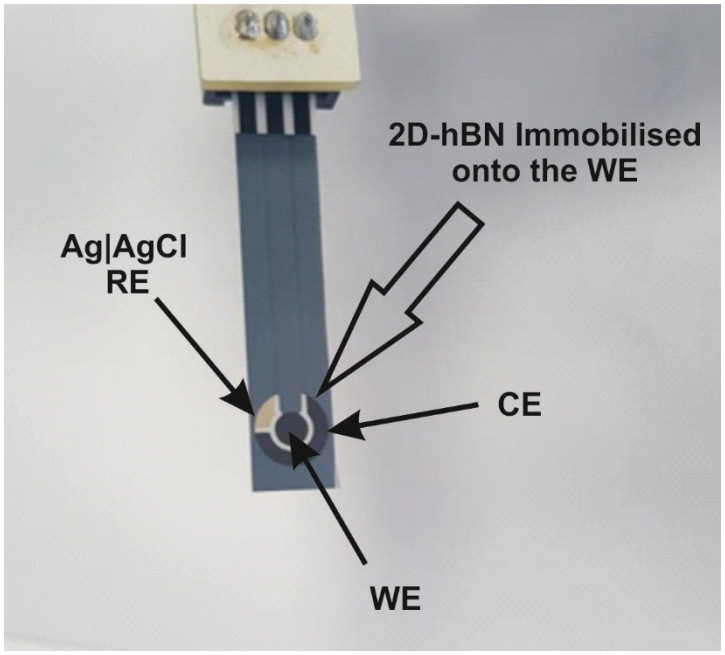

Figure 1.11: Typical SPEs consisting of a graphite working electrode, (WE, 3mm diameter), a graphite counter electrode, (CE) and an Ag/AgCl reference electrode (RE). In this example 2D-hBN can be readily immobilised upon SPEs.

Chapter 2 : 2D Materials in Electrochemistry

This chapter explores the unique properties of 2D materials and their utilisation in electrochemistry. First considered is the literature reports concerning graphene, which leads towards the exploration of newly emerging 2D materials such as 2D-hexagonal boron nitride (2D-hBN), the focus of this thesis.

It is noted that the field of 2D-hBN electrochemistry is continuously moving forward and work within this thesis has been published in peer-reviewed journals. Thus the work in this thesis has contributed and influenced the direction of future work within the literature. As a result the literature presented within this chapter focuses on work published prior to 2014 in order to not pre-empt the novel work performed throughout this thesis which has contributed to the understanding of 2D-hBN electrochemistry. It is noted within this thesis, following chapters introduce new literature as and when it occurred post 2014.

2.1 Graphene

Since the physical properties of graphene were reported in 2005 by Geim and Novoselov,[33] research has intensified in the field of two-dimensional (2D) nanomaterials. Graphene is described as a single (2D) carbon layer of graphite and there have many reports of graphene discovery prior to the pioneering work of Geim and Novoselov.[28, 29] However the findings from these studies were observational and failed to describe any of graphene's distinguishing properties.[28, 29] Thus Geim and Novoselov were the first to report the isolation of graphene and its physical properties.[33]

Graphene, which has a hexagonal structure containing sp^2 hybridized atoms,[30] is the foundation of all graphitic carbon materials.[31] Materials such as carbon nanotubes, ('rolled up' graphene sheets) and graphite (layered graphene sheets) are based upon a single layer of graphene.[32] Geim and Novoselov first isolated and characterised pristine graphene in 2005[33, 34] utilising the 'scotch tape method'.[34]

This material has gained great interest and further to the initial report of the properties of graphene, [34] newly reported properties include an optical transparency of 97.7%,[35] electron mobility of 200,000 $cm^2\ V^{-1}\ S^{-1}$,[35] a thermal conductivity of 5000 $Wm^{-1}\ K^{-1}$.[35] Furthermore graphene has a surface area of 2630 $m^2\ g^{-1}$,[35] a breaking strength of 42 N m^{-1} and an elastic modulus of 0.25 TPa.[35]

It is clear graphene is an exciting material and it has been utilised in electrochemical investigations, with literature studies showing the beneficial effects of this material towards energy storage and conversion.[36, 37] In theory, graphene has many properties which make it suitable for electrochemical applications including a large surface area (2630 $m^2\ g^{-1}$) which is greater than that of graphite (*ca.* 10 $m^2\ g^{-1}$) and double that of CNTs (1315 $m^2\ g^{-1}$).[38] Graphene's electrical conductivity (64 mS cm^{-1}) is another favourable aspect of this material and it is approximately 60 times greater than that of SWCNTs.[39, 40] It has also been found that this beneficial conductivity is stable at high temperatures, which is highly sought for many applications. Moreover graphene has an ultra-high electron mobility (200,000 $cm^2\ V^{-1}\ s^{-1}$), whereas the electron mobility in silicon 200 times smaller.[36]

Graphene can fabricated via a range of methodologies including; mechanical exfoliation, which utilises a slab of HOPG (see chapter 1) and the "scotch tape" method is employed.[41, 42] This method is direct, simple and produces graphene of

high structural and electronic quality within a very low cost. However, this methodology can be delicate and time consuming (hours) forming low yields.[40, 41] Furthermore, the said method has poor reproducibly and contamination is prevalent upon the utilisation of the adhesive tape.[40, 41] The mechanical exfoliation, "scotch tape method" was implemented in the fundamental research of graphene,[34] which in turn enabled high quality single layer graphene sheets to be obtained, with little lattice defect density and domain sizes ranging from 500 Å to 10 μm.[40, 41] Another method utilised in the fabrication of graphene is chemical exfoliation.[30, 43] Chemical exfoliation involves the dispersion and exfoliation of graphite in organic solvents or through the use of surfactant complexes. This technique is direct, simple, offering large-scale production at low-cost.[30, 43] Furthermore, in comparison to the mechanical exfoliation methodology, chemical exfoliation offers a high yield. Thus, it is seen as much more practical given a liquid is handled.[30, 43] However, it can be time-consuming to produce (hours), with the resulting product sometimes impure and at risk of contamination from the surfactant or solvents utilised. The said technique has frequently been applied to general graphene research for modified substrates.[30, 43] Though, the resulting product often contains multiple layered graphene incorporated with structural defects originating from the fabrication process with domain sizes ranging from 500 Å up to 1500 Å.[30, 43] Aside from the methodologies stated in fabrication of graphene, a common technique utilised in electrochemistry is the formation of graphene oxide via the reduction of graphite oxide.[30, 36, 42] This technique is implemented upon the exfoliation of graphite leading to its oxidation. Subsequently graphite oxide is reduced to form graphene oxide.[29, 35, 41] Thus, the stated method, which has facile scalability, produces high yields at low cost, with excellent processability and practicability due to the production of a liquid.

However, this production method of graphene is indirect and a large number of structural defects are found upon its implemention.[29, 35, 41] Moreover, disruptions to the electronic structure of graphene can be caused due to impurities with the reduction of graphene often incomplete.[29, 35, 41] The Graphene oxide produced is usually multiple layered incorporated with structural defects originating from the fabrication process with domain size ranging from 500 Å up to 1500 Å.[29, 35, 41] Chemical vapour deposition (CVD) is another technique utilised in the fabrication of graphene.[42, 44, 45] This method forms graphene primarily from hydrocarbon gas under variable pressures and temperatures.[42, 44, 45] Thus enabling large-scale graphene production of high quality with uniform films to obtained.[42, 44, 45] A disadvantage of CVD is that it requires high operating temperatures with a high cost. Furthermore, the production process is often complicated with variable yields obtained.[42, 44, 45] CVD graphene fabrication is utilised as a tool for fundamental graphene research since high quality single layer graphene sheets are obtained with little lattice defect density.[42, 44, 45] Though, graphene can be tailored to contain specific defects and impurities where these are required for beneficial implementation in given devices. Layer thickness and domain sizes are thus variable.

When utilising graphene in electrochemical procedures, solution-based fabrication approaches are favoured due to the ease of handling and the high yields obtained. This method involves the dispersion of graphene into a solvent, which is then drop-cast and immobilised upon a surface following evaporation. This technique is facile, however drawbacks include surface instability, reproducibility, coverage issues and the quality of the graphene remaining, where multilayer graphene may exist, i.e. graphite. Thus post-application characterisation of the

graphene is required for clarity. Nevertheless, this fabrication approach is a viable means to investigate the electrochemical properties of graphene.

Graphene applied in the field of electroanalysis has had a plethora of research carried out, with many reports citing graphene as a beneficial electrode material,[46, 47] which acts as a catalyst in electrochemical reactions. Conversely, it has been demonstrated that surfactants were the basis of the observed electrocatalysis towards many target analytes.[48, 49] This is due to the production method used to form graphene, as the liquid based phase process utilises surfactants.[32] Moreover, the structure of graphene is such that the electron density is minimal due to the structure being a single layer basal plane of graphite, thus slow electron kinetics are observed. It is found that the initial slow electrode kinetics of single layer graphene improve as the number of layers of graphene increase, thus the response becomes similar to that of graphite. Furthermore, it has been suggested that graphene does not act as an electrocatalyst when carrying out electrochemical experiments towards different analytes due the exposed basal plane.

Brownson *et al.*[48] investigated the utilisation of surfactant–free (pristine) graphene immobilised upon EPPG and BPPG electrodes towards a range of redox probes. Their report found pristine graphene exhibited slow electron transfer towards the electrochemical probes studied, effectively blocking the underlying electron transfer of the supporting electrode substrate.[48] This effect was explained due to the large basal and low edge plane content of graphene.[48] It was also shown the 'mass coverage' of pristine graphene significantly affected the electron transfer rate, with improvements observed upon increasing layering.[48]

The fabrication process utilised in the production of graphene has been shown to affect the observed electrochemical response towards model solutions. [49-51]

Previous studies employed a surfactant-exfoliation methodology utilising sodium cholate[49-51] and it was illustrated the surfactant (sodium cholate) was electroactive when modified onto SPEs.[49] It was surmised that the electrochemical response was due to the oxidation of cyclohexanol (hydroxyl groups), *via* an equal proton/electron transfer process. Thus, the surfactant utilised in the exfoliation of graphene was found to contribute and in some cases dominate the observed electrochemical response. Therefore, these studies suggested when fabricating graphene with a surfactant-exfoliation methodology, the electrochemical response should not be assumed to be due solely to graphene itself, but rather due to the effect of surfactant (sodium cholate) incorporated which can *contribute to* and *dominate* the electrochemical response. [49-51]

Due to its adsorptive properties graphene has been utilised as a support for DNA oligonucleotides, characteristic of Alzheimer's disease.[32] Thus, upon these oligonucleotides binding with DNA strands that are linked with Alzheimer's disease, the electrode surface is blocked. Therefore, from carrying out impedence studies, it can be determined whether Alzheimer's disease is present in a sample due the differences observed in impedance.[32] Hence, this technique may have the potential for application towards many other diseases. Additionally, the use of defected graphene via oxygenated functional groups may become more prominent in electrochemistry due the increase in edge-plane sites, resulting in improved electrode kinetics.[32]

2.1.1 2D Hexagonal Boron Nitride (2D-hBN)

Attention has recently turned towards utilising other novel 2D materials towards electroanalytical applications. Indeed, 2D transition-metal-dichalcogenide (TMD) nanosheets, such as MoS_2, TiS_2, TaS_2, WS_2, $MoSe_2$, and WSe_2, have been

extensively researched due to their observed catalytic activity and low cost in comparison to noble metals.[52-55] However a lesser researched 2D material is crystalline hexagonal boron nitride (2D-hBN), a 2D material comprising equal boron and nitrogen atoms arranged in a similar hexagonal structure in crystalline form to that of graphene (thus referred to as 'white graphene').[56] The structure of 2D-hBN is presented in Figure 2.1.[58]

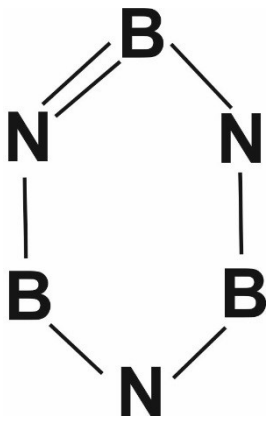

Figure 2.1 Illustrates the structure of 2D-hBN.

In addition, the molecular orbital diagram of 2D-hBN is also shown in Figure 2.2.[57,58]

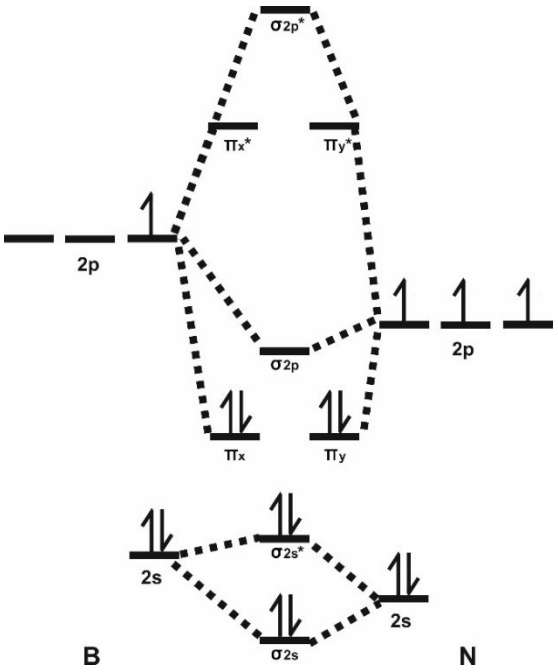

Figure 2.2 The molecular orbital structure of 2D-hBN is illustrated.

2D-hBN is found in amorphous and crystalline forms,[59] with crystalline 2D-hBN containing strong σ bonds and weak van der Waals forces,[60] resulting in a range of favourable thermal, mechanical, and chemical properties.[61] It is noted that the bonding of 2D-hBN is covalent[60] and the electrons in the σ bond are localised towards nitrogen,[60] whereas the π bonding present involves an empty p-orbital of boron and a filled p-orbital of nitrogen, with the nitrogen π electrons delocalised.[60] Such an electronic structure allows 2D-hBN to be a good insulator in its solid form, with 2D-hBN having a large band gap of 5.5 eV, significantly greater than the zero bandgap of graphene .[62] These properties have made 2D-hBN an excellent composite and dielectric material.[60]

The fabrication of 2D-hBN can occur via many routes, such as those described in the production of graphene, with similar advantages and disadvantages observed upon the implementation of these processes. Indeed 2D-hBN has been

fabricated by a range of techniques including: ball milling,[63] mechanical cleavage,[64] ultrasonic vibration which separates the layers of bulk h-BN (a method utilised in this thesis), high-energy electron beam irradiation[65] and the reaction of boric acid and urea.[66] Furthermore, Chemical vapour deposition (CVD) is a route often utilised to synthesise large-area 2D-hBN.[67, 68] In this thesis, as described previously when considering graphene, the 2D-hBN utilised in electrochemical procedures follows mainly a solution-based fabrication approach due to the ease of handling and the high yields obtained.

Due to the reported insulating properties of 2D-hBN, it is often considered non-electroactive and therefore its utilisation in electrochemical applications has not been prominent. However, there have been some reports of its employment towards electroanalytical applications. Uosaki *et al.*[69] experimentally investigated the ORR and immobilised 2D-hBN upon gold substrates/electrodes. Their work demonstrated an excellent 2D-hBN|gold interaction due to the binding of the 2D-hBN monolayer with transition metal surfaces given that the N-p_z and B-p_z orbitals of 2D-hBN mix with d_z^2 metal orbitals.[69] Thus upon modification of a gold electrode with 2D-hBN, the potential required for the ORR was reduced by *ca.* 0.27 V compared to a bare gold electrode (although unfortunately the modified electrode followed the two electron pathway, producing H_2O_2).[69] This example shows that 2D-hBN potentially possesses an electrocatalytic behaviour towards the ORR on this substrate. However, gold is a precious metal with a high cost, making it an expensive substrate and therefore not highly desirable in the design, commercialisation and mass-production of fuel cells.[69] their report also considered the immobilisation of 2D-hBN upon a glassy carbon based substrate and observed little (*no real*) electrocatalytic effect towards the ORR.[69] Furthermore, the utilisation of 2D-hBN in PEM fuel cells been

reported, in which a 2D-hBN membrane allows protons through whilst simultaneously reducing fuel crossover.[70] This effect is highly desirable and may help to improve fuel cell lifetime. However, the report does not consider that 2D-hBN *per se* may be useful as a catalytic material for fuel cell cathodes. In this regard, there have been limited investigations of 2D-hBN as an electrode material. Lyalin *et al*.[71] found *via* density functional theory (DFT) calculations that an inert 2D-hBN monolayer can become catalytically active upon nitrogen doping, whilst Studt *et al.*[72] explored the effects of nitrogen doped graphene towards the ORR with DFT calculations and found the intermediates involved in the reaction bind to the carbon atom next to the nitrogen dopant.

Thus, this thesis explores the viability of 2D-hBN as an electrode material utilising various electrode substrates, towards a range of applications and considers the effect of the fabrication process upon the observed electrochemistry.

Chapter 3 : Experimental Section

This chapter details the general experimental conditions applied throughout this thesis. It is noted, where the conditions reported herein alter, specific chapter experimental sections are implemented. Within these specific chapter experimental sections, the detail of any additional experimental conditions utilised are given.

3.1 Experimental Details

All chemicals utilised were of analytical grade and were used as received from Sigma-Aldrich without any further purification. All solutions were prepared with deionised water of resistivity not less than 18.2 MΩ cm and (when necessary) were vigorously degassed prior to electrochemical measurements with high purity, oxygen free nitrogen.

Voltammetric measurements were performed using an ‘Autolab PGSTAT 101` (Metrohm Autolab, The Netherlands) potentiostat which was controlled by Nova software version 1.11 for Windows 7. All measurements were conducted, using a conventional three electrode system and were performed at a temperature of 297 K (± 2/3 K). The working electrode utilised was variable (vide infra, Chapters 3.2 and 3.4) and unless otherwise stated a platinum wire and a saturated calomel electrode (SCE) (Radiometer, Copenhagen, Denmark) were used to complete the circuit as auxiliary/counter and reference electrodes, respectively.

3.2 Electrode Materials Utilised

3.2.1 Screen-Printed Electrodes (SPEs)

The screen-printed graphite electrodes (SPEs) utilised throughout this work consisted of a graphite working electrode, a graphite counter electrode and an Ag/AgCl reference electrode. The SPEs, which have a 3 mm diameter working electrode, were fabricated in-house with appropriate stencil designs using a microDEK 1760RS screen-printing machine (DEK, Weymouth, UK). This SPE design has been previously reported by the Banks group.[73-75] Unless stated otherwise, where SPEs have been used within this work, it is to be assumed the on-board Ag/AgCl reference and carbon counter electrodes were removed and replaced with an external SCE reference and Pt counter electrodes respectively. The SPEs have been electrochemically characterised previously and exhibit a heterogeneous electron transfer rate constant, k^{o}_{eff}, of *ca.* 1.08×10^{-3} cm s^{-1} using 1 mM hexaammineruthenium (III) chloride/0.1 M KCl.[76] The reproducibility and repeatability of the fabricated batches of electrodes were explored through comparison of cyclic voltammetric responses using 1 mM $Ru(NH_3)_6^{2+/3+}$ in 0.1 M KCl supporting electrolyte. Analysis of the voltammetric data revealed the % relative standard deviation (% RSD) to correspond to no greater than 0.82 % (N = 20) and 0.76 % (N = 3) for the reproducibility and repeatability of the fabricated SPEs (for use in electroanalysis).[77] Unless stated otherwise, SPE fabrication was performed by Dr. Christopher Foster, Manchester Metropolitan University.

3.2.2 GC and BDD Electrodes

Glassy carbon (GC) (3 mm diameter, BAS, USA) and Boron-doped diamond (BDD) (3 mm diameter, BAS, USA) working electrodes were also utilised, which were obtained commercially.

3.2.3 EPPG Electrode

The edge plane pyrolytic graphite (EPPG) working electrode (Le Carbone, Ltd. Sussex, U.K.) was machined to possess a 4.9 mm diameter, with the disc face parallel to the edge plane, as required, from a slab of highly ordered pyrolytic graphite (HOPG) (highest grade available: SPI-2, which is equivalent to Union Carbide's ZYA grade, with a lateral grain size, La of 1–10 μm and 0.4 ± 0.1° mosaic spread).

3.2.4 Gold and Platinum Electrodes

Gold (Au 3 mm diameter, BAS, USA) and platinum (Pt 3 mm diameter, BAS, USA) working electrodes were also utilised, which were obtained commercially.

3.2.5 Electrode Preparation

SPEs were single-use only and thus were new when utilised and disposed of after use. Whereas GC, BDD, EPPG, Au and Pt electrodes were reused before the beginning of each experiment and were first polished using diamond suspension in a spray format (Kemet international Ltd.).[1] The diamond particle size was decreased from 1 to 0.25 μm. Upon carrying out each polishing step the electrode was washed

to remove any microparticles attained from the diamond spray and sonicated in water to remove diamond particles.

3.2.6 Electrode Modification

Where liquid suspensions of 2D hexagonal Boron Nitride (2D-hBN) (or appropriate control solutions) were utilised a drop-casting method was used to immobilise the given material onto the supporting electrode material of choice. For example, pristine 2D-hBN modified electrodes were prepared by drop-casting aliquots of an ethanol suspension containing pristine flakes of 2D-hBN onto the required working electrode with a micropipette. After 30 minutes the ethanol completely evaporated (at ambient temperature) and the modified electrodes were ready for use.

Where h-BN nanopowder was incorporated into screen-printed electrodes (SPEs), the screen-printing process depicted in Figure 3.1 was utilised to fabricate these hBN-SPEs.

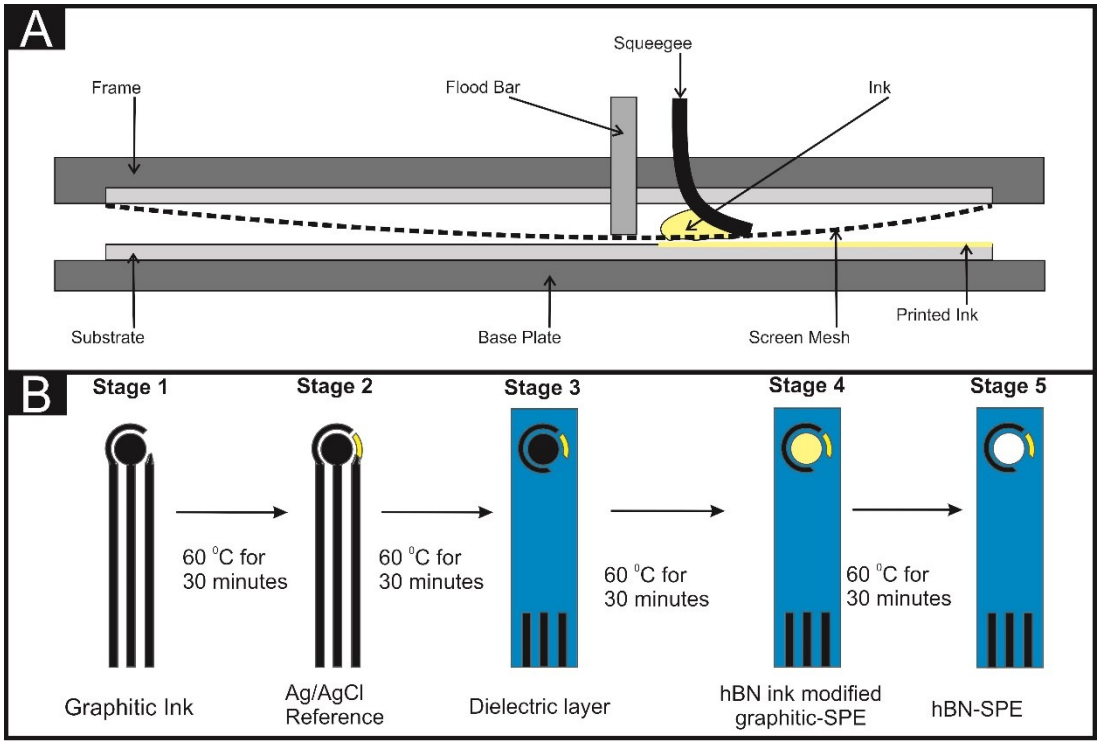

Figure 3.1: A schematic representation of the process utilised to produce the hBN-SPEs reported herein.

In detail, the in-house fabrication of screen-printed graphite electrodes (with the dimensions of 41 mm long × 7 mm wide) containing a graphite working electrode (3.1 mm diameter), a graphite counter electrode and an Ag/AgCl reference electrode were performed using suitable stencil designs using a microDEK1760RS screen-printing machine (DEK, Weymouth, UK). This SPE design has been previously reported.[73, 74, 78] For experimental continuity, the SPE's on-board Ag/AgCl reference and carbon counter electrodes were removed and replaced with an external SCE reference and Pt counter electrodes respectively. hBN-SPEs were prepared by incorporating the commercially procured 2D-hBN (used as received from Sigma Aldrich), into the SPE ink (product code: C2000802P2). The 2D-hBN was

incorporated into the SPEs according to weight % of M_P and M_I, where M_P is the mass of particulate and M_I is the mass of the carbon-graphite ink formulation utilised in the printing process. The weight per cent of M_P and M_I typically varied in the range of 0–15%. For the fabrication of the hBN-SPEs, 2D-hBN was screen-printed on top of the working electrode and cured (60 °C for 30 minutes).[79]

3.3 Physical/Chemical Characterisation Techniques

3.3.1 Scanning Electron Microscopy (SEM), Transition Electron Microscopy (TEM) AND Energy Dispersive X-ray (EDX) Spectroscopy

Scanning electron microscopy (SEM) images and surface element analysis were obtained using a JEOL JSM-5600LV model equipped with an energy-dispersive X-ray (EDX) for the EDX microanalysis. Transmission electron microscopy (TEM) images were obtained using a 200 kV primary beam under conventional bright-field conditions.

Unless stated otherwise, SEM, EDX analysis performed by Dr. Hayley Andrews, Manchester Metropolitan University. TEM analysis was performed by Professor Graham Smith, Chester University, England.

3.3.2 Raman Spectroscopy

Raman spectroscopy was performed using a 'Renishaw InVia' spectrometer with a confocal microscope (×50 objective) spectrometer with an argon laser (514.3 nm excitation) at a very low laser power level (0.8 mW) to avoid any heating effects. Spectra were recorded using a 10 second exposure time for 3 accumulations. The

Raman mapping was performed using a 'Thermo Scientific DXR Raman Microscope' with laser (532 nm excitation).

3.3.3 X-ray Photoelectron Spectroscopy (XPS)

X-ray photoelectron spectroscopy (XPS) was used to analyse the electrode surface and its oxygenated groups. XPS data was acquired using a bespoke ultra-high vacuum system fitted with a Specs GmbH Focus 500 monochromated Al Kα X-ray source, Specs GmbH PHOIBOS 150 mm mean radius hemispherical analyser with 9-channeltron detection, and a Specs GmbH FG20 charge neutralising electron gun. Survey spectra was acquired over the binding energy range 1100 – 0 eV using a pass energy of 50 eV and high resolution scans were made over the C 1s and O 1s lines using a pass energy of 20 eV. Under these conditions the full width at half maximum of the Ag $3d_{5/2}$ reference line is *ca*. 0.7 eV. In each case, the analysis was an area-average over a region approximately 1.4 mm in diameter on the sample surface, using the 7 mm diameter aperture and lens magnification of ×5. The energy scale of the instrument was calibrated according to ISO standard 15472, and the intensity scale was calibrated using an in-house method traceable to the UK National Physical Laboratory. Finally, data was quantified using Scofield photoelectric cross sections corrected for the energy dependencies of the electron attenuation lengths and the instrument transmission. Data interpretation was carried out using CasaXPS software v2.3.16. Unless stated otherwise, XPS experiments and analysis were performed by Professor Graham Smith, Chester University, England.

3.3.4 X-ray Diffraction (XRD)

The XRD was performed using a "X'pert powder PANalytical model" with a copper source of K_{α} radiation of 1.54 Å and $K_{ß}$ radiation of 1.39 Å, using a thin sheet of nickel with an absorption edge of 1.49 Å to absorb $K_{ß}$ radiation.

3.3.5 White Light Profilometry (WLP)

White light profilometry was carried out using a ZeGage 3D Optical Surface Profiler, manufactured by Zygo.

3.3.6 Ultraviolet-Visible Spectroscopy (UV-VIS)

An Agilent 8453 UV-visible Spectroscopy System (equipped with a tungsten lamp assembly, G1315A, 8453 for absorption between 250 nm and 1500 nm and a deuterium lamp, 2140-0605 for absorption between 200 nm and 400 nm) was used to obtain the absorption spectroscopy. The absorption spectra was analysed using the UV-Visible ChemStation software. A Quartz cell with a path length of 1 cm was utilised.

3.4 2D Hexagonal Boron Nitride (2D-hBN) Utilised: Details and Characterisation

3.4.2 Pristine (Surfactant-Free) 2D-hBN

The 2D-hBN utilised was commercially obtained from 'Graphene Supermarket' (Reading, MA, USA) and is known as 'Boron Nitride Pristine Flakes' comprised entirely of pristine 2D-hBN nanoscale crystals dispersed in ethanol (5.4 mg L^{-1}) that have not been oxidised, reduced or chemically modified in anyway

and are free from surfactants.[80] These are fabricated *via* a liquid exfoliation procedure using ethanol and water in appropriate composition to produce a highly stable suspension. The 2D-hBN platelets have an average particle size (lateral) of *ca*. 50–200 nm, a thickness of between 1–5 monolayers (in solution) and a purity (in the dry phase) of >99%.[80]

3.4.2. Pristine (Surfactant-Free) 2D-hBN Characterisation

The physicochemical characterisation of the pristine 2D-hBN utilised in this work is provided through TEM, SEM, XPS, EDX, XRD and Raman spectroscopy. Typical TEM images are depicted in Figure 3.2 where it can be observed that pristine 2D-hBN platelets have an average (lateral) particle size of *ca*. 200 nm, which is in agreement with the commercial manufacturer.[80]

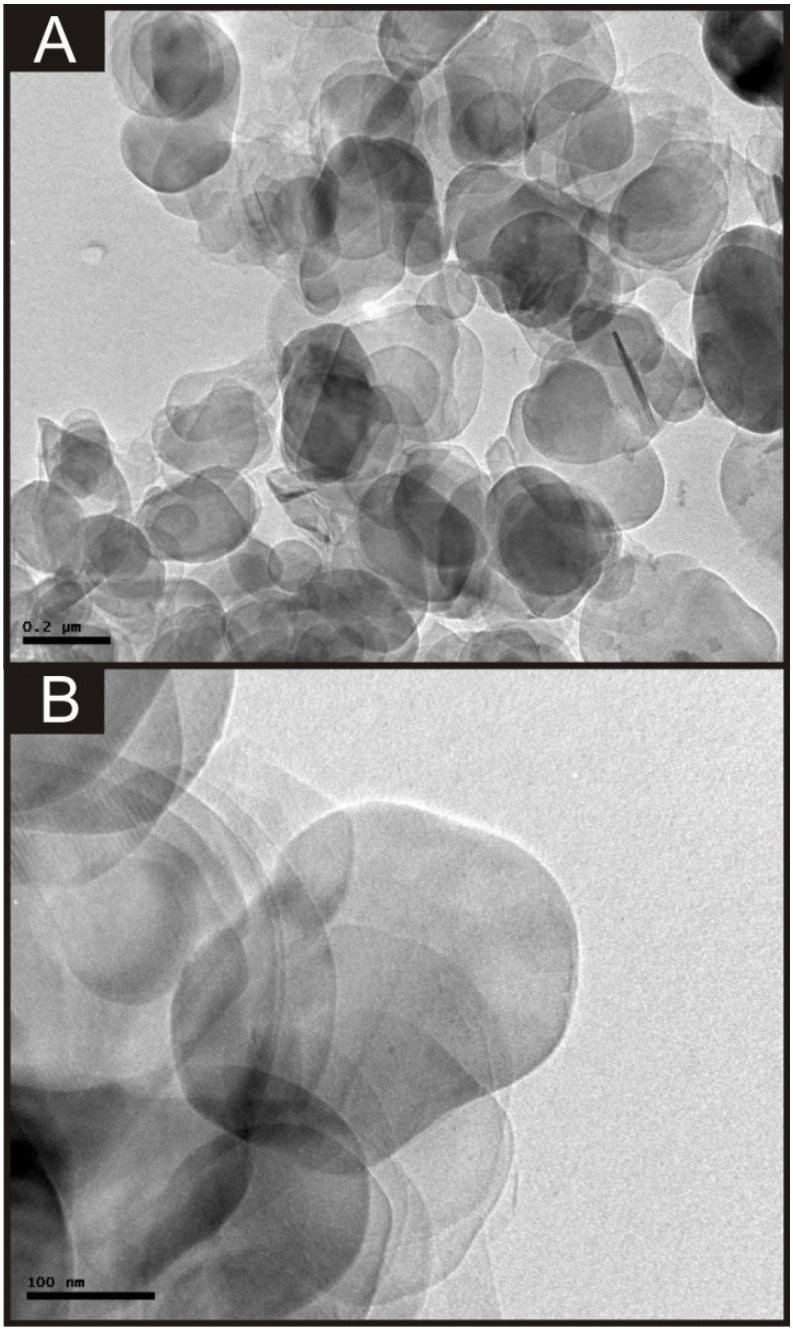

Figure 3.2: Typical TEM images of commercially procured pristine 2D-hBN deposited onto a holey carbon film supported upon a Cu TEM grid (A), and at a higher magnification (B). Scale bars are 200 nm (A) and 100 nm (B). Images obtained using a 200 kV primary beam under bright-field conditions.

Furthermore, SEM images were obtained to assess how the pristine 2D-hBN platelets prefer to reside upon SPE surfaces. SPEs were utilised as a model electrode surface due to the ease at which they can be adapted and placed into an SEM instrument, unlike the alternative carbon electrodes (such as GC), utilised in this study. The said alternative carbon electrodes are expensive and must be mechanically altered in order to be utilised within an SEM instrument. Whereas SPEs are cheap, disposable and thus more readily employed within SEM characterisation.

Figure 3.3A and 3.3B displays the surface morphology of an unpolished and polished SPE. It is clear that the polishing process reduces the number of contours and ridges of the SPE (evident in Figure 3.3A) to a comparatively smooth electrode surface (as observed within Figure 3.3B). Figure 3.2C-F shows how the surface morphology changes when the pristine 2D-hBN is immobilised upon the SPE surface. In Figure 3.3C (unpolished SPE), the pristine 2D-hBN platelets are visible as discs that collect preferentially around contours and ridges upon the SPE surface. Conversely, Figure 3.3D (polished SPE) shows the platelets collecting in similar areas, but also indicates large areas of underlying substrate where the platelets have not rested because the surface is apparently not suitable to 2D-hBN interaction, leading us to infer that pristine 2D-hBN prefers to reside upon a rougher electrode surface. This is an interesting concept occurring following the modification of electrode surfaces with pristine 2D-hBN and the implications of this are considered later.

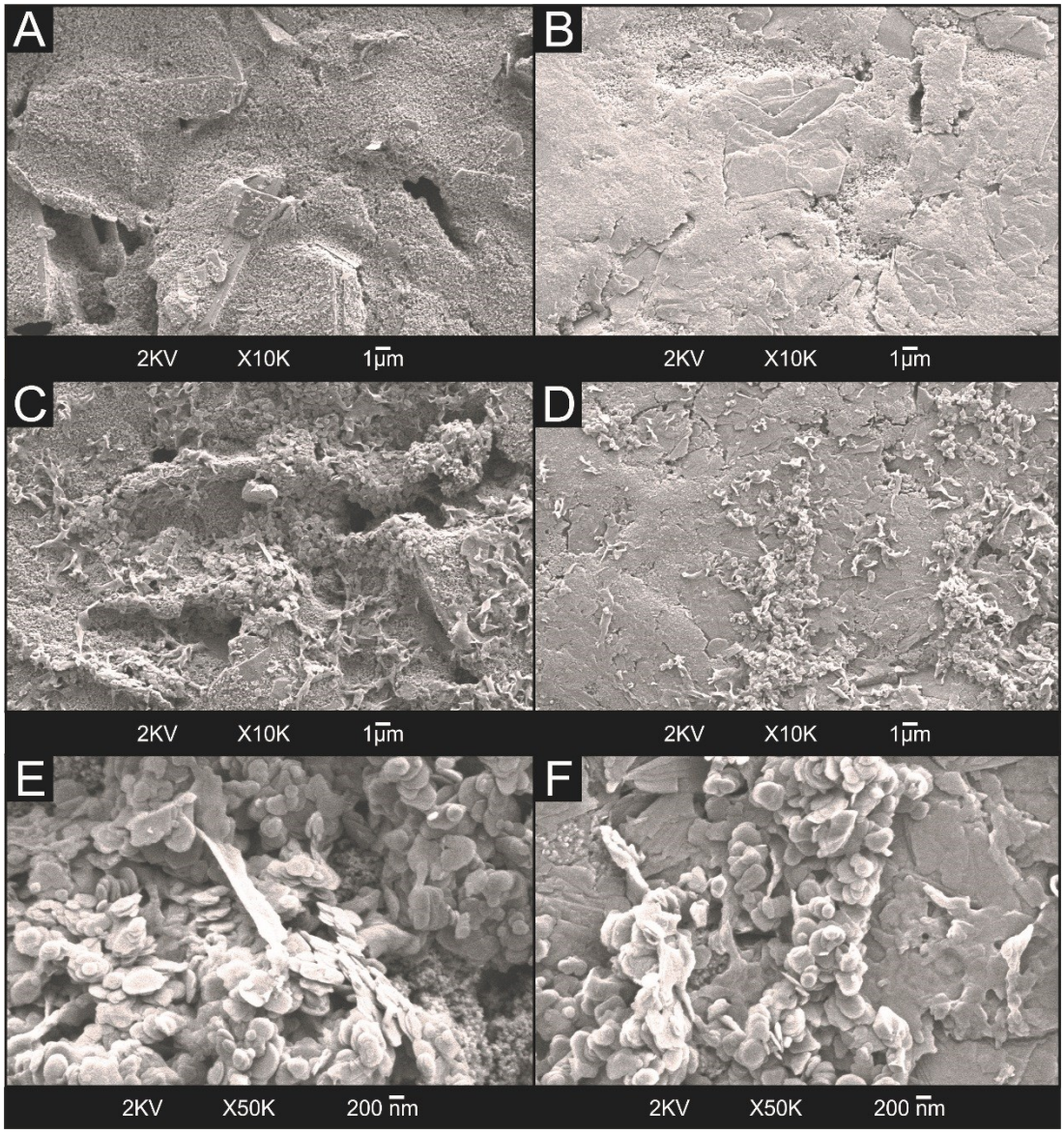

Figure 3.3: Typical SEM images for: unpolished SPE (A); polished SPE (B); unpolished SPE with 324 ng pristine 2D-hBN (C) and a further magnified version (E); polished SPE with 324 ng pristine 2D-hBN (D) and a further magnified version (F). Pristine 2D-hBN platelets are evident in images C-F as small, disc-like shapes approximately 200 nm in size.

XPS analysis was next performed on the pristine 2D-hBN and is depicted in Figure 3.4. Note that the analysis was conducted on a thin layer of pristine 2D-hBN, dried from an ethanol suspension on a Si(111) substrate and therefore the results include contributions from the underlying Si wafer, its surface oxide and any

adventitious contaminants as well as from the 2D-hBN and the ethanol residue. The XPS spectra showed the presence of a single component at 190.8 eV in the B 1s spectrum and the N 1s spectrum exhibited a main peak at 398.4 eV, with both in good agreement to previous literature.[67] A weak (minor) component in the N 1s spectrum at *ca*. 400.2 eV was evident and most likely originated from atmospheric contamination on the underlying silicon (Si) (111) substrate. Thus, the results are fully consistent with pristine 2D-hBN immobilised upon a Si (111) substrate. The stoichiometry of 1:1 for B:N is noted and the binding energies for the B 1s and N 1s photoelectron peaks agree well with the expected values for pristine 2D-hBN.

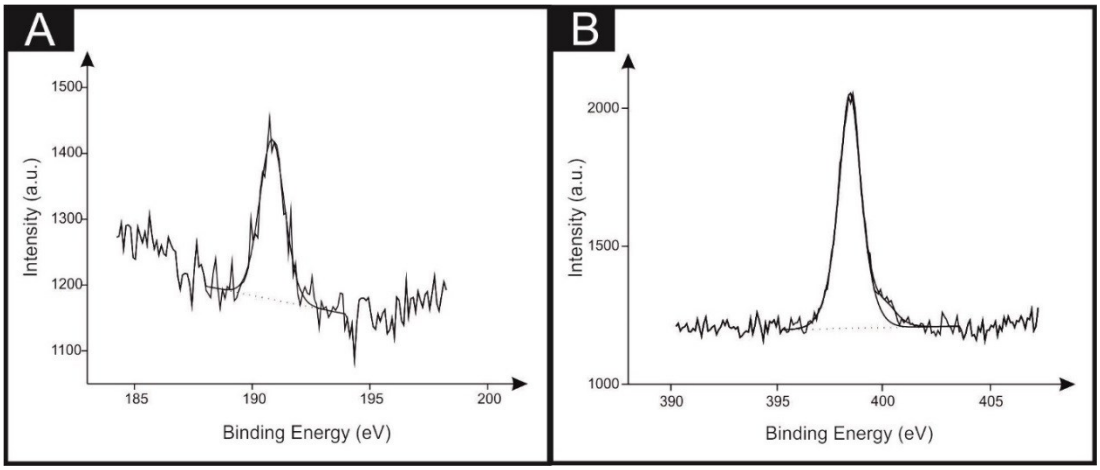

Figure 3.4: Curve fitted XPS spectra of pristine 2D-hBN deposited upon a Si (111) wafer. (A) illustrates XPS spectra of the B atom and spectra (B) is that of the N atom.

Table 3.1 exhibits the full surface composition of the dried ethanol suspension of pristine 2D-hBN on Si(111) from the XPS analysis. The C and O present are likely a result of residuals from the ethanol used to disperse the pristine 2D-hBN. The presence of a C-O component in the C 1s spectrum (not shown) confirmed this. The Na and Ca were attributed to the concentration of organic Na- and Ca-containing

contaminants in the ethanol. The Si and a proportion of the O originated form the Si (111) wafer substrate, which typically has thin surface oxide of approximately 1.5 nm thickness. The XPS analysis confirmed the presence of stoichiometric pristine 2D-hBN in the commercially obtained material.

Element	Atom % Concentration
Na 1s	2.9
O 1s	21.2
N 1s	3.5
Ca 2p	0.5
C 1s	44.7
B 1s	3.7
Si 2p	23.5

Table 3.1: A summary depicting the composition of pristine 2D-hBN dried from ethanol suspension onto Si(111) following analysis of XPS spectra. Note that the analysis includes data from the 2D-hBN, the ethanol residue, and a proportion of the surface region of the Si(111) wafer including the native surface oxide.

It has previously been shown that metallic impurities in carbon nanotubes can contribute to the electrocatalysis seen at some nanotube-modified electrodes.[24] Thus, it is important to consider the possible presence of metallic impurities for the case of pristine 2D-hBN, which if present, may contribute to the response observed towards the ORR. EDX analysis was performed on a single platelet of pristine 2D-hBN (see Figure 3.5) to further establish its elemental composition, where it was indicated to

be comprised of 11.40% atomic boron and 9.93% atomic nitrogen. This is in agreement with the XPS obtained that shows the stoichiometry between B:N is *ca.* 1:1. Further scrutiny of the EDX data reveals a 78.67% contribution/component of atomic Silicon (Si), which as discussed above originates from the substrate upon which pristine 2D-hBN is immobilised. This confirms that there are no impurities within the commercially obtained samples, therefore the response is not dominated by such metallic constituents, but rather is due solely to that of the pristine 2D-hBN present.

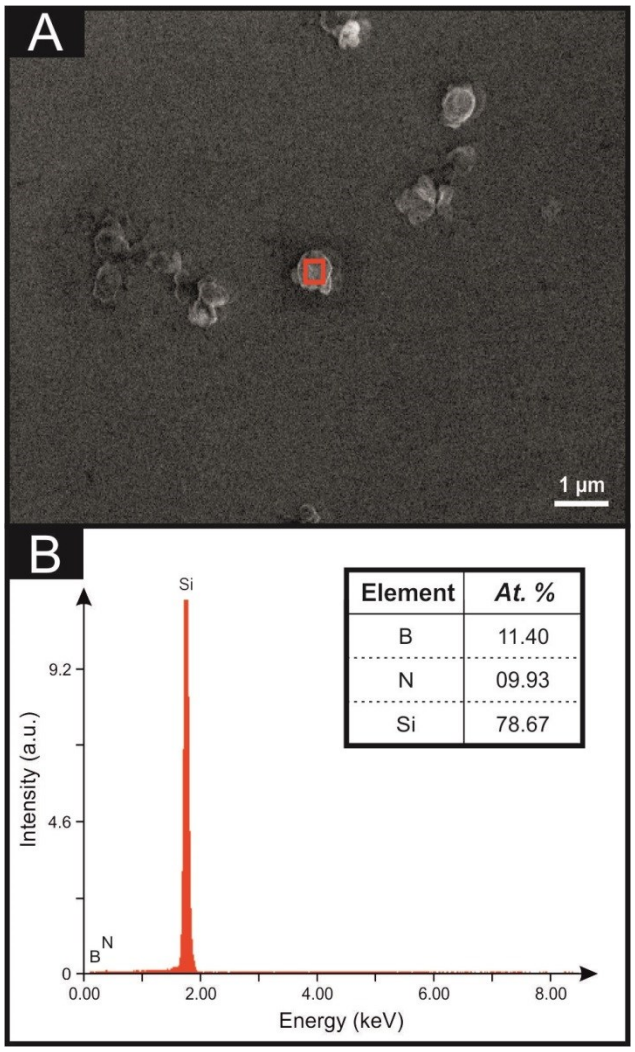

Figure 3.5: Typical SEM image (A) for pristine 2D-hBN immobilised upon a silicon substrate, where the red box shows the target of the EDX analysis. The SEM was obtained at ×20,000 magnification. An acceleration voltage of 25.00 kV and a working distance of 14.4 mm were utilised. Part (B) illustrates the accompanying EDX spectrum of pristine 2D-hBN and analysis of this is shown in the inset table.

XRD was performed on the pristine 2D-hBN with corresponding spectra depicted in Figure 3.6, indicating that 2D-hBN crystals are oriented in the (002) direction with a characteristic peak observed at 26.7°, in agreement with an independent literature report.[81]

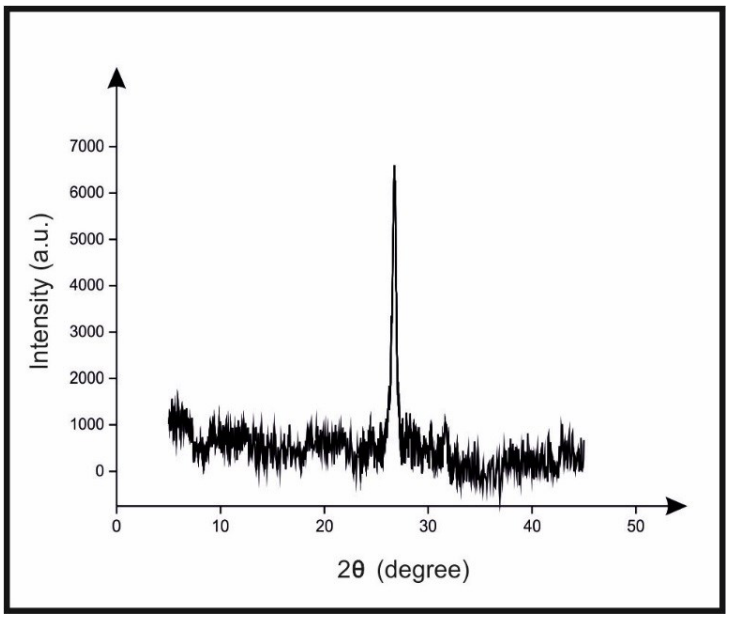

Figure 3.6: XRD spectra of the pristine 2D-hBN deposited onto a glass slide between 5 and 45 2θ, exhibiting a characteristic peak at 26.7°.

Finally, the commercially procured pristine 2D-hBN was characterised using Raman spectroscopy. Figure 3.7A shows Raman spectra of immobilised pristine 2D-hBN upon a silicon wafer, which gives rise to a characteristic Raman peak at 1366 cm^{-1}, which is due to the E_{2g} phonon mode.[82] This is in good agreement to an independent literature report,[82] indicating that the immobilised sample upon the silicon wafer consists of *ca*. 2 – 4 layers of pristine 2D-hBN. Note however, it is not possible to observe the Raman peak of pristine 2D-hBN upon graphitic electrodes due to overlapping signals occurring between pristine 2D-hBN and graphite. Hence, the pristine 2D-hBN modified electrode cannot be referred to the in terms of the number layers immobilised upon it, but rather the mass of pristine 2D-hBN that has been immobilised each time. Next, several masses of pristine 2D-hBN were immobilised upon SPEs. These modified SPEs were characterised using Raman

spectroscopy (mapping) to ensure full electrode coverage of 2D-hBN. Figures 3.7B and 3.7C show Raman map comparisons of an unmodified and a 324 ng pristine 2D-hBN modified SPE. Figure 3.7B shows a smooth / uniform surface, yet Figure 3.7C shows several areas, appearing as black dots (and generally has a darker grey background intensity), that are indicative of pristine 2D-hBN immobilisation given that the Raman intensities were recorded at the wavenumber corresponding to the peak observed in Figure 3.7A. The Raman maps indicate a significant coverage of *ca*. 2 layer (thin layer) pristine 2D-hBN on the electrode surface (with some areas that are darker in colour (higher Raman intensity) indicating occasional thicker regions ($\geq 2 - 4$ layers).[27] It is clear that following pristine 2D-hBN modification *via* drop casting, a complete coverage is achieved and thus the electrochemical profiles associated with pristine 2D-hBN modified electrodes are due to the pristine 2D-hBN and not the underlying electrode surface.

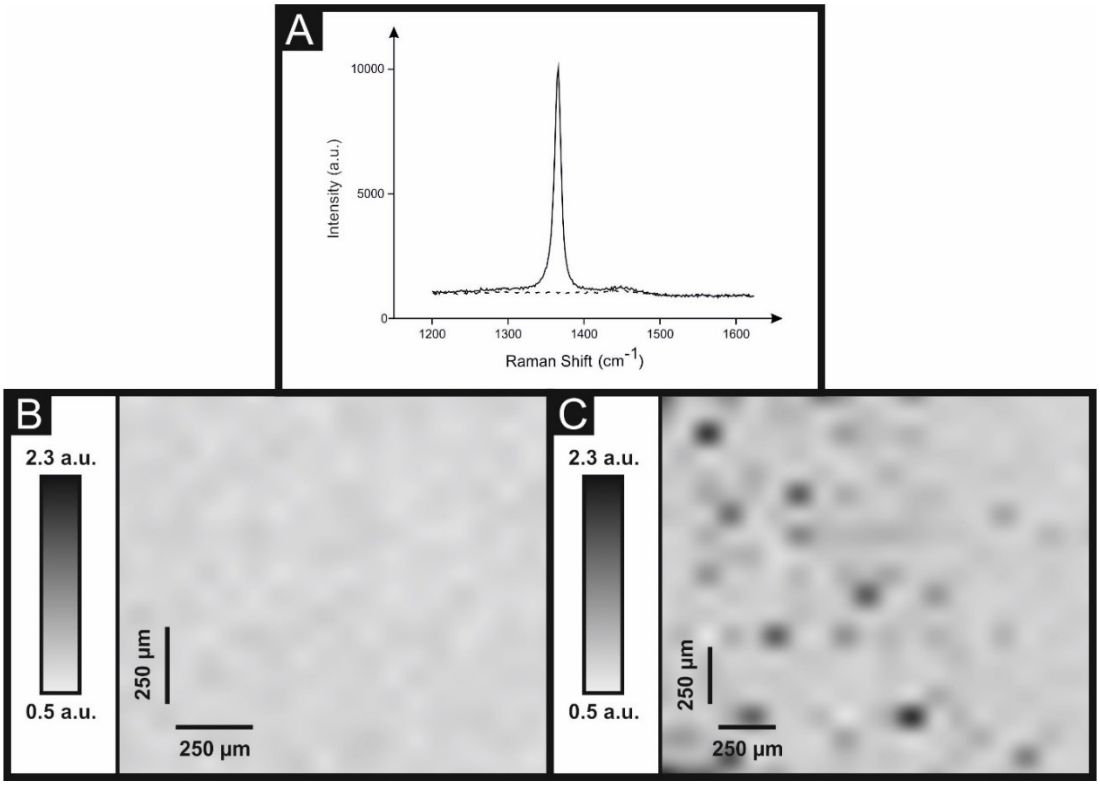

Figure 3.7: A typical Raman spectra (A) obtained for 2D-hBN (solid line) immobilised upon a supporting silicon wafer. The dotted line depicts the Raman spectra of the silicon substrate upon which 2D-hBN is deposited. Image (B) shows the Raman mapping of an unmodified (bare) SPE and (C) is that of a 324 ng 2D-hBN modified SPE. Raman intensities for B and C were recorded at 1366 cm^{-1}. Figure C shows several areas, appearing as black dots, that are indicative of pristine 2D-hBN immobilisation given that the Raman intensities were recorded at the wavenumber corresponding to the peak observed in A.

In summary, physicochemical characterisation indicates that the material exhibits the characteristic features of highly pure pristine 2D-hBN (no metallic impurities present), whilst comprising an average particle size (lateral) of *ca*. 200 nm and flake thickness of 2-4 layers. The drop-casting procedure appears to be an adequate method to apply/immobilise the pristine 2D-hBN upon an electrode substrate in order to 'electrically wire to' and explore its electrochemical

properties/performance, providing uniform/full coverage across the electrode surface when immobilised.

3.4.3 Surfactant-Exfoliated 2D-hBN

The surfactant-exfoliated 2D-hBN utilised herein was fabricated in-house. Utilising a method reported previously by Kurapati *et al.*;[83] bulk Boron Nitride was procured from Sigma Aldrich (used as received), after which it was sonicated in an aqueous solution (water, pH 5.6) containing sodium cholate, to induce liquid phase exfoliation. A schematic illustrating an ordered surfactant (sodium cholate)-monolayer on 2D-hBN, with the structure of sodium cholate also shown in Figure 3.8. It is clear from its structure, the sodium cholate contains hydroxyl groups which may exhibit electroactive behaviour.

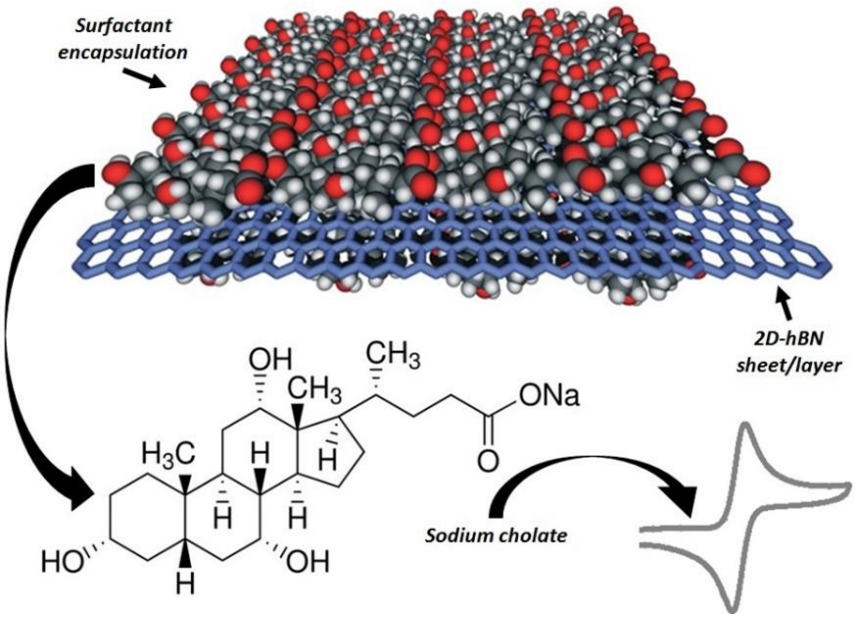

Figure 3.8 Schematic illustrating the structure of sodium cholate and its encapsulation of 2D-hBN.

The 2D-hBN utilised throughout this work was synthesised *via* a surfactant based liquid exfoliation, sonication and centrifugation methodology. Liquid exfoliation was performed by adding bulk h-BN powder into an aqueous solution of sodium cholate hydrate (SC: concentration, 6 g/L) contained within a 100 mL beaker. The resulting dispersion of bulk h-BN comprised a concentration of 30 g L^{-1}. This dispersion was then sonicated in a sonication bath (Ultrawave, UK) (60 % Amplitude) for 1 hour, prior to a centrifugation step that was performed at 5000 rpm for 90 minutes. Following centrifugation, the corresponding supernatant was discarded and the resulting sediment was re-agitated/dispersed into aqueous SC (2 g/L, 100 mL). Next, the said re-agitated sediment underwent sonication in a sonication bath (Ultrawave, UK) (60 % Amplitude) for a further 5 hours. Upon completion of the sonication treatment, the solution was separated into 20 mL aliquots before each sample was centrifuged at 2000 rpm for 90 mins (separately). The sediment from this process contained un-exfoliated h-BN and was consequently discarded, with the remaining supernatant being subjected to a further centrifugation period at 5000 rpm for 90 minutes. Finally, the forthcoming supernatant was removed and found to contain the 2D-hBN nanosheets that are utilised herein. The resultant product comprised surfactant (sodium cholate) exfoliated 2D-hBN nanosheets sodium cholate (2 g L^{-1}) in an aqueous solution. Note that where surfactant control experiments were utilised, a 2 g L^{-1} solution of sodium cholate was prepared and utilised in the absence of 2D-hBN (*i.e.* 2D material *not* present).

3.4.3.1 Surfactant-Exfoliated 2D-hBN Characterisation

2D hexagonal boron nitride nanosheets (2D-hBN) were fabricated as described in the section 3.4.3 via surfactant exfoliation of bulk hexagonal boron nitride.

Characterisation of the fabricated 2D-hBN was performed using TEM, SEM, XPS, XRD, EDX, UV-visible spectroscopy and Raman spectroscopy applied to provide a thorough physicochemical characterisation of the surfactant-exfoliated 2D-hBN. First considered is the structural characterisation of surfactant-exfoliated 2D-hBN with TEM. Typical TEM images are depicted in Figure 3.9A and B where it can be observed that surfactant-exfoliated 2D-hBN platelets have an average (lateral) particle size of *ca*. 200 nm, which is in agreement to an independent literature report utilising the same fabrication methodology.[80] It is also clear from the TEM images that the surfactant-exfoliated 2D-hBN exists in single layers.

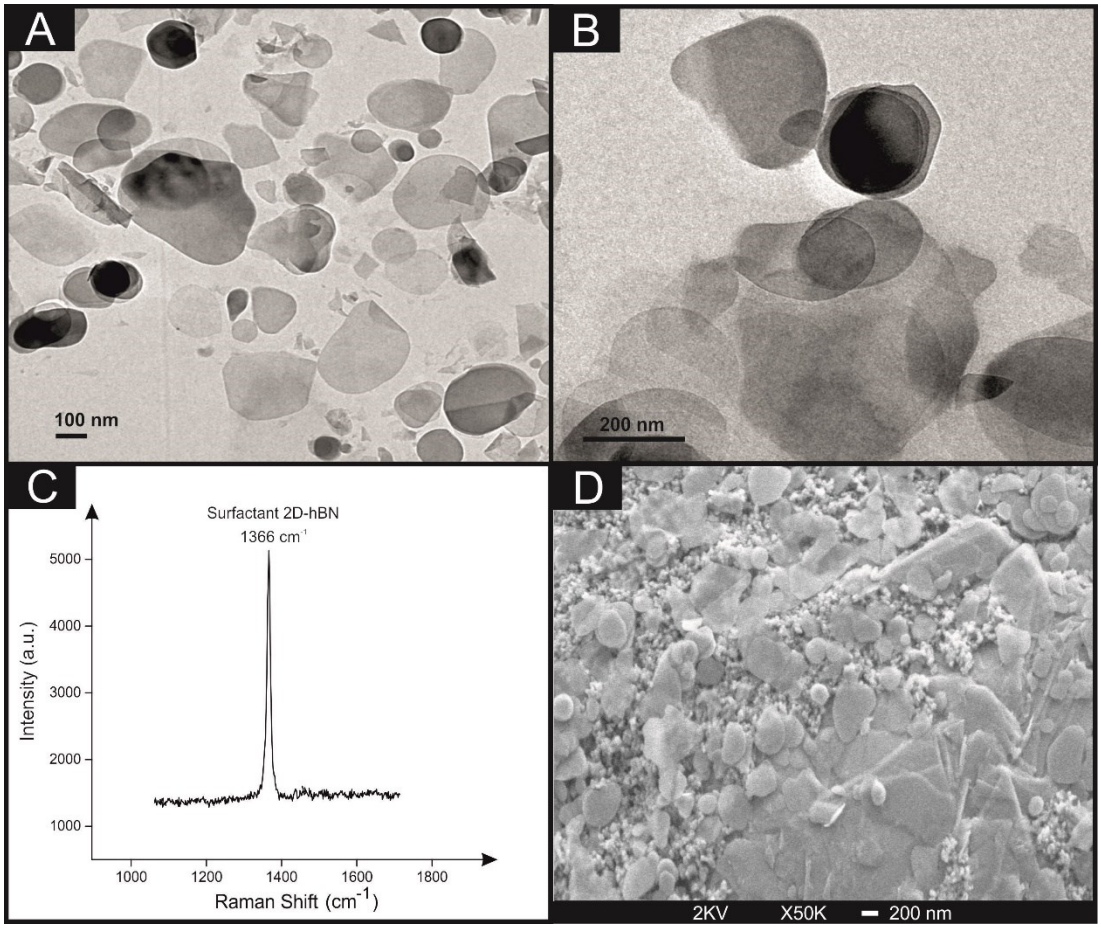

Figure 3.9: Typical TEM images of surfactant-exfoliated 2D-hBN deposited onto a holey carbon film supported upon a Cu TEM grid (A), and at a higher magnification (B). Scale bars are 100 nm (A) and 200 nm (B). Images obtained using a 200 kV primary beam under bright-field conditions; (C), typical Raman spectra obtained for surfactant-exfoliated 2D-hBN (solid line) immobilised upon a supporting silicon wafer. (D) Typical SEM images for an SPE modified with 37.5ng surfactant-exfoliated 2D-hBN. 2D-hBN platelets are evident as small, disc-like shapes approximately 200 nm in size.

To investigate the layer thickness of surfactant-exfoliated 2D-hBN in solution, the UV-visible absorption spectrum methodology was employed (Figure 3.10), where an optical band gap value of 5.61 eV was found, indicating that 2–4 layer 2D-hBN is present in solution.[67] This is also in good agreement with previous literature utilising the same fabrication methodology.[83]

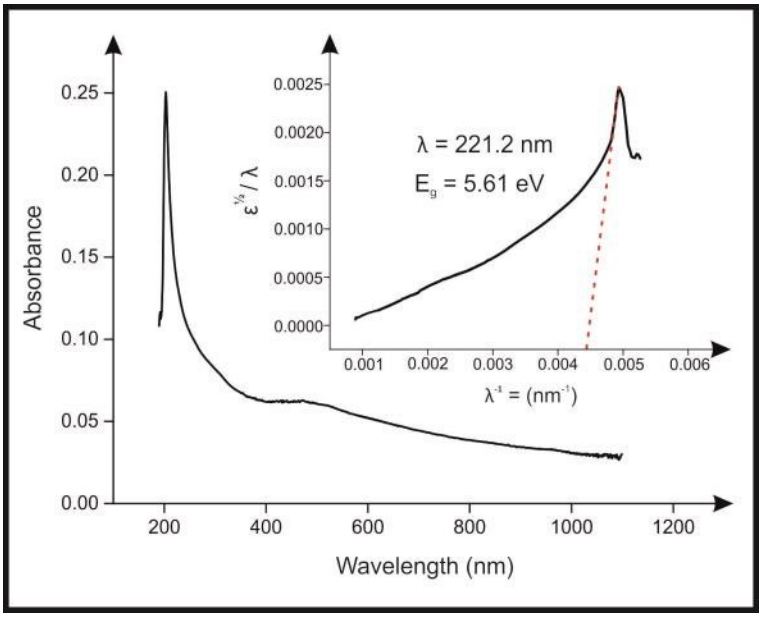

Figure 3.10: A typical UV-visible absorption spectra of surfactant-exfoliated 2D-hBN nanosheets, where the inset shows the corresponding plot of $\varepsilon^{1/2}/\lambda$ vs. $1/\lambda$.

The Tauc equation: $\omega^2\varepsilon = (h\omega - E_g)^2$ was utilised to determine the optical band gap E_g for surfactant-exfoliated 2D-hBN.[84] Where ε is the optical absorbance, h is Planck's constant, and $\omega = 2\pi/\lambda$ is the angular frequency of the incident radiation (λ is the wavelength). Thus, a plot of $\varepsilon^{1/2}/\lambda$ versus $1/\lambda$ results in a straight line at the absorption range. Hence, the intersection point with the x axis is $1/\lambda_g$ (λ_g is defined as the gap wavelength). Finally, the optical band gap can be calculated utilising the equation $E_g = hc/\lambda_g$.[67] Consequently, Figure 3.10 illustrates the surfactant-exfoliated 2D-hBN exhibits an absorption peak at 203 nm and a plot of $\varepsilon^{1/2}/\lambda$ *vs.* $1/\lambda$ can be constructed (inset Figure 3.10). Therefore, the calculated gap wavelength (λ_g) relates to 221.2 nm, with a corresponding optical band gap of 5.61 eV indicating that 2-4 layer 2D-hBN is present in solution.[67]

Figure 3.9C shows a typical Raman spectra of the surfactant-exfoliated 2D-hBN, which gives rise to a characteristic Raman peak at 1366 cm^{-1}.[85] The Raman

peak is due to the E_{2g} phonon mode and agrees well with prior literature reporting the fabrication of 2D-hBN.[82] Full width at half maximum (FWHM) peak analysis of the Raman spectra (Figure 3.9C) exhibits a value that corresponds to 12.1 cm^{-1}, which upon comparison to a recent report by Tran *et al.*[85] indicates that few to multilayer surfactant-exfoliated 2D-hBN is present. Furthermore, SEM imaging (Figure 3.9D) was obtained to assess how the 2D-hBN platelets prefer to reside upon the screen-printed electrode (SPEs) surfaces.

XPS analysis was next performed on the surfactant-exfoliated 2D-hBN and is depicted in Figure 3.11. Note that the analysis was conducted on a thin layer of 2D-hBN, dried from a sodium cholate suspension on a Si (111) wafer fragment. The Si (111) wafer was sputter cleaned (prior to 2D-hBN deposition) using argon ions, in-situ, within the vacuum of the XPS instrument to remove surface contaminants, thus allowing for the layer composition of surfactant-exfoliated 2D-hBN to be calculated.

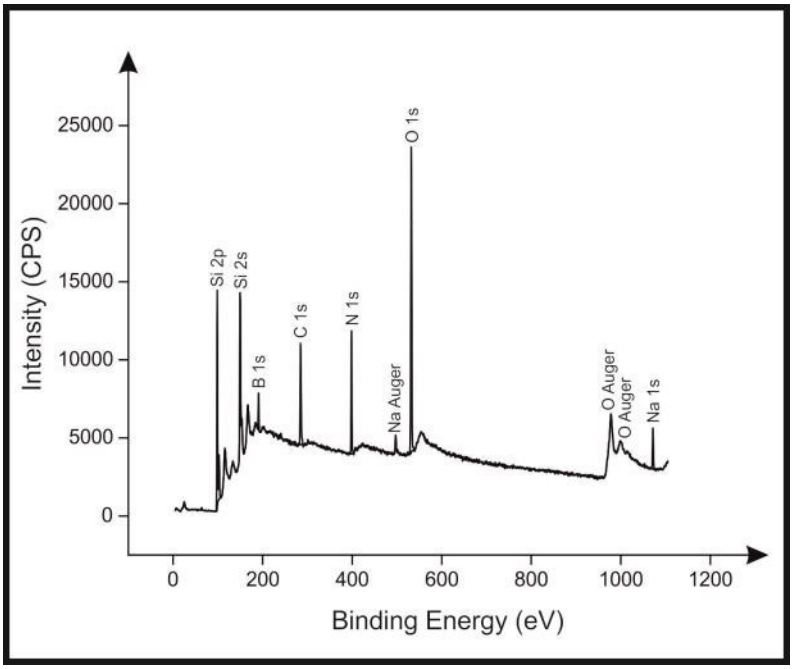

Figure 3.11: XPS survey spectrum for a sample of the surfactant-exfoliated 2D-hBN following deposition onto a Si (111) wafer.

The XPS spectra showed the presence of a single component at 191.1 eV in the B 1s spectrum and the N 1s spectrum exhibited a main peak at 398.7 eV (Figure 3.11), both in good agreement to previous literature.[83] The stoichiometry of 1:1 for B:N is noted and the binding energies for the B 1s and N 1s photoelectron peaks agree well with the expected values for 2D-hBN.

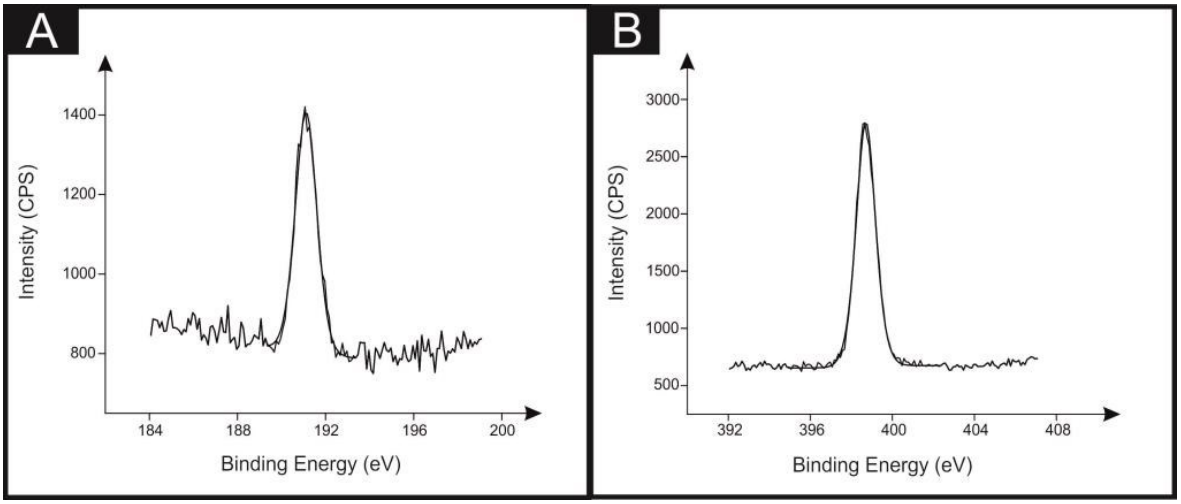

Figure 3.12: Curve fitted XPS spectra of surfactant-exfoliated 2D-hBN deposited upon a Si (111) wafer. (A) illustrates XPS spectra of the B atom and spectra (B) is that of the N atom.

Table 3.2 exhibits the full surface composition of the dried surfactant-exfoliated 2D-hBN layer on Si (111) from the XPS analysis. The C and O present are a result of residuals from the sodium cholate surfactant used to disperse the 2D-hBN. The presence of a C-O component in the C 1s spectrum confirmed this, with the Na attributed to the sodium of the cholate structure (Figure 3.11).

Element	Atom % Layer composition
O 1s	26.4
C 1s	31.4
Na 1s	2.8
B 1s	19.8
N 1s	19.6

Table 3.2: A summary depicting the composition of surfactant-exfoliated 2D-hBN layer dried from sodium cholate suspension onto Si(111), following analysis of XPS spectra. Note that the analysis includes data from the 2D-hBN and the sodium cholate residue.

XRD was performed on the surfactant-exfoliated 2D-hBN with corresponding spectra depicted in Figure 3.13. It is observed *via* XRD that surfactant-exfoliated 2D-hBN crystals are oriented in the (002) direction with a characteristic peak observed at 26.7°, in agreement with an independent literature report.[81] Note, the high background observed in Figure 3.13 is due to the thin film coating of the material, whereby the scattering of the supporting substrate gives rise to background interference.

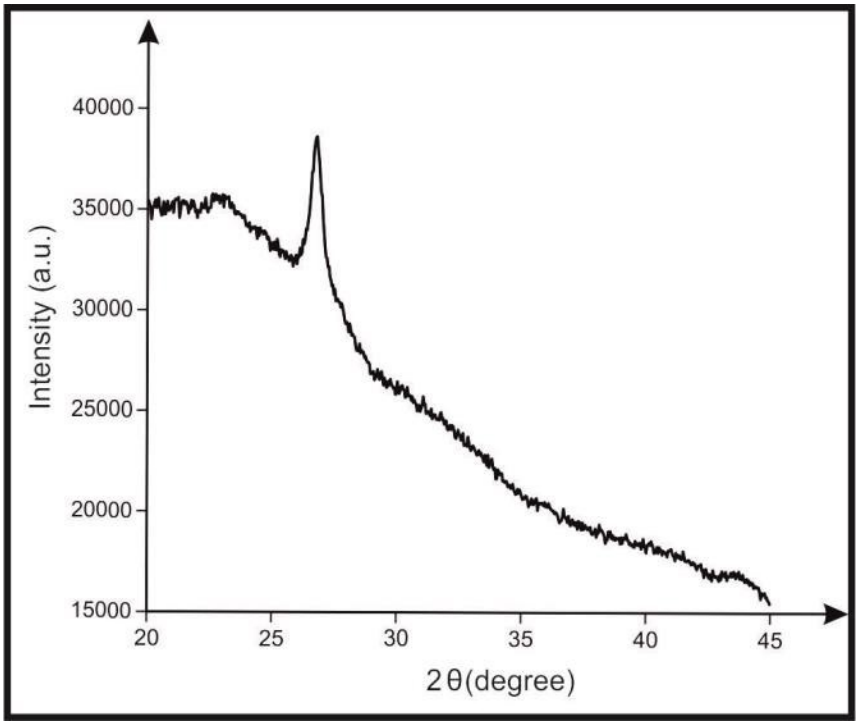

Figure 3.13: XRD spectra of the surfactant-exfoliated 2D-hBN deposited onto a glass slide between 20 and 45 2θ, exhibiting a characteristic peak at 26.7°.

EDX mapping analysis was performed to offer insight into the elemental composition of the area shown in Figure 3.14. Analysis of the EDX map shows uniform distribution of B and N atoms with a ratio (1:1) of 20.12% At. and 18.81% At. B:N respectively and this composition correlates with expected values for surfactant-exfoliated 2D-hBN.[86]

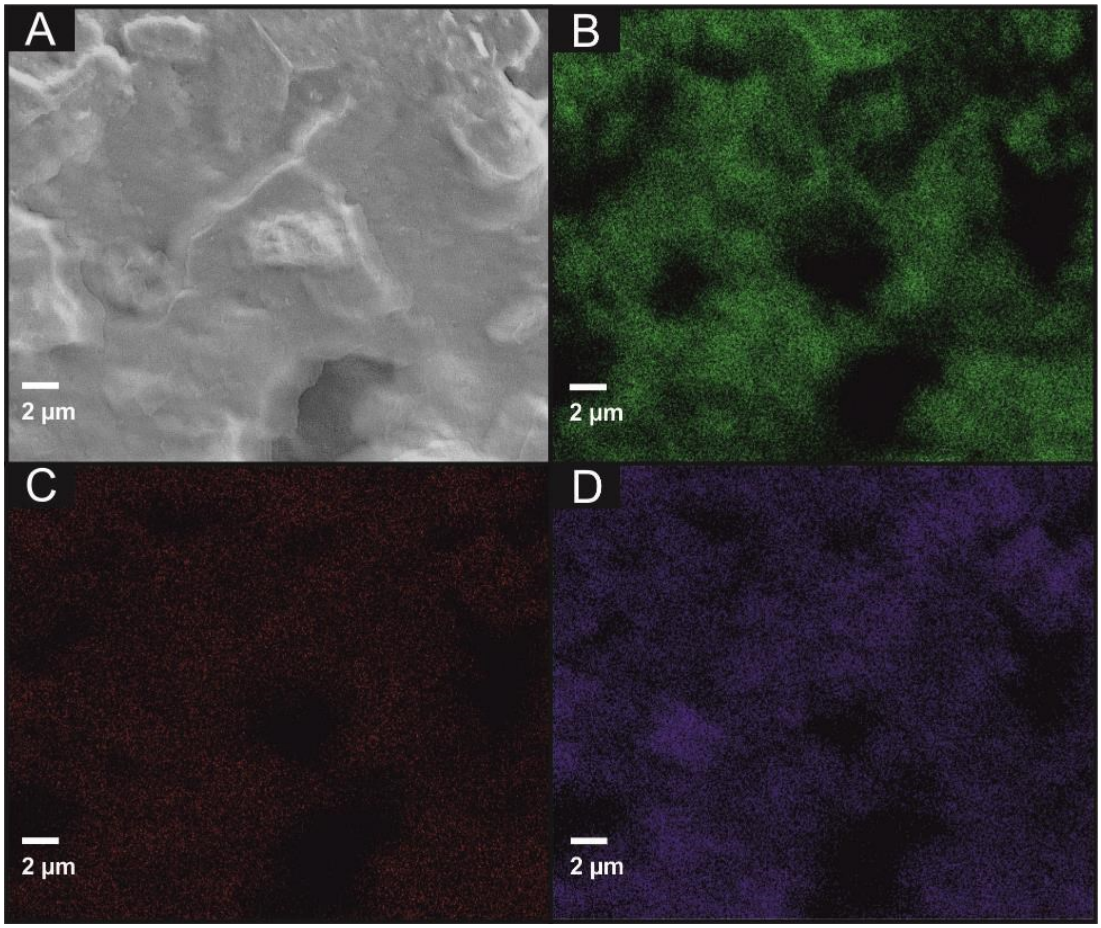

Figure 3.14: SEM image (A) of surfactant-exfoliated 2D-hBN immobilised on a SPE along with EDX elemental analysis highlighting the underlying SPE carbon support (B, in green), boron (C, in red) and nitrogen (D, in purple) coverage of image A respectively.

3.4.4 2D-hBN Nanopowder

The 2D-hBN nanopowder utilised was commercially obtained from Sigma Aldrich (used as received) and is known as 'Boron Nitride nanopowder' comprised entirely 2D-hBN nanopowder.

3.4.4.1 2D-hBN Nanopowder Characterisation

TEM, XRD, XPS and Raman spectroscopy were utilised to provide a comprehensive physicochemical characterisation of the commercially procured 2D-hBN. Figure 3.14A shows a typical Raman spectra of the 2D-hBN, which gives rise to a characteristic Raman peak at 1366 cm^{-1}.[85] The Raman peak is due to the E_{2g} phonon mode and agrees well with prior literature.[82]

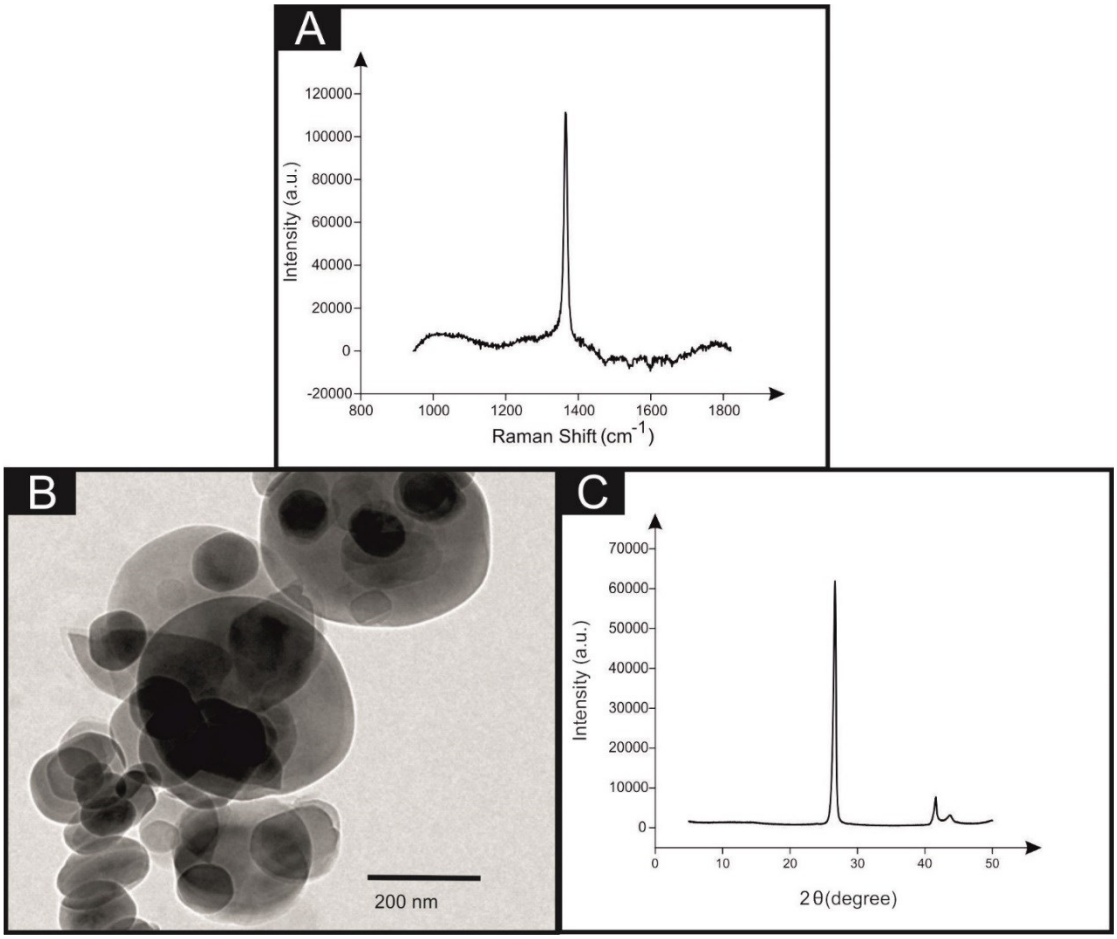

Figure 3.15: A typical Raman spectra (A) obtained for the commercially procured 2D-hBN (solid line) immobilised upon a supporting silicon wafer. (B) Typical TEM images of the 2D-hBN deposited onto a holey carbon film supported upon a Cu TEM grid. Scale bars are 200 nm. Images obtained using a 200 kV primary beam under bright-field conditions. (C) XRD spectra of the 2D-hBN, exhibiting characteristic peaks at 26.7°, 41.56° and 44.38°.

A TEM image is shown in Figure 3.14B and indicates that the 2D-hBN has an average particle size (lateral) of *ca*. 100-300 nm. It is also evident, that the 2D-hBN exists in an agglomerated form, due to the black regions exhibited in the TEM. The XRD (Figure 3.14C) indicates that the 2D-hBN is oriented in the 002, 100 and 101 plane, with a characteristic peaks observed at 26.70° 41.56° and 44.38° respectively, which is in agreement with previous literature.[81 87] Here it is noted that

the background is less prominent in comparison to Figure 3.12 which is due to the quantity of this material being such that a powder was analysed as opposed to a thin film which results in a reduction in background interference/noise.

XPS was also performed and the resultant spectra (see Figure 3.15) showed the presence of a single component at 190.8 eV in the B 1s spectrum, with the N 1s spectrum exhibiting a main peak at 398.4 eV; both are in good agreement to previous literature.[83] The stoichiometry of 1:1 for B:N is noted and the binding energies for the B 1s and N 1s photoelectron peaks agree well with the expected values for 2D-hBN.

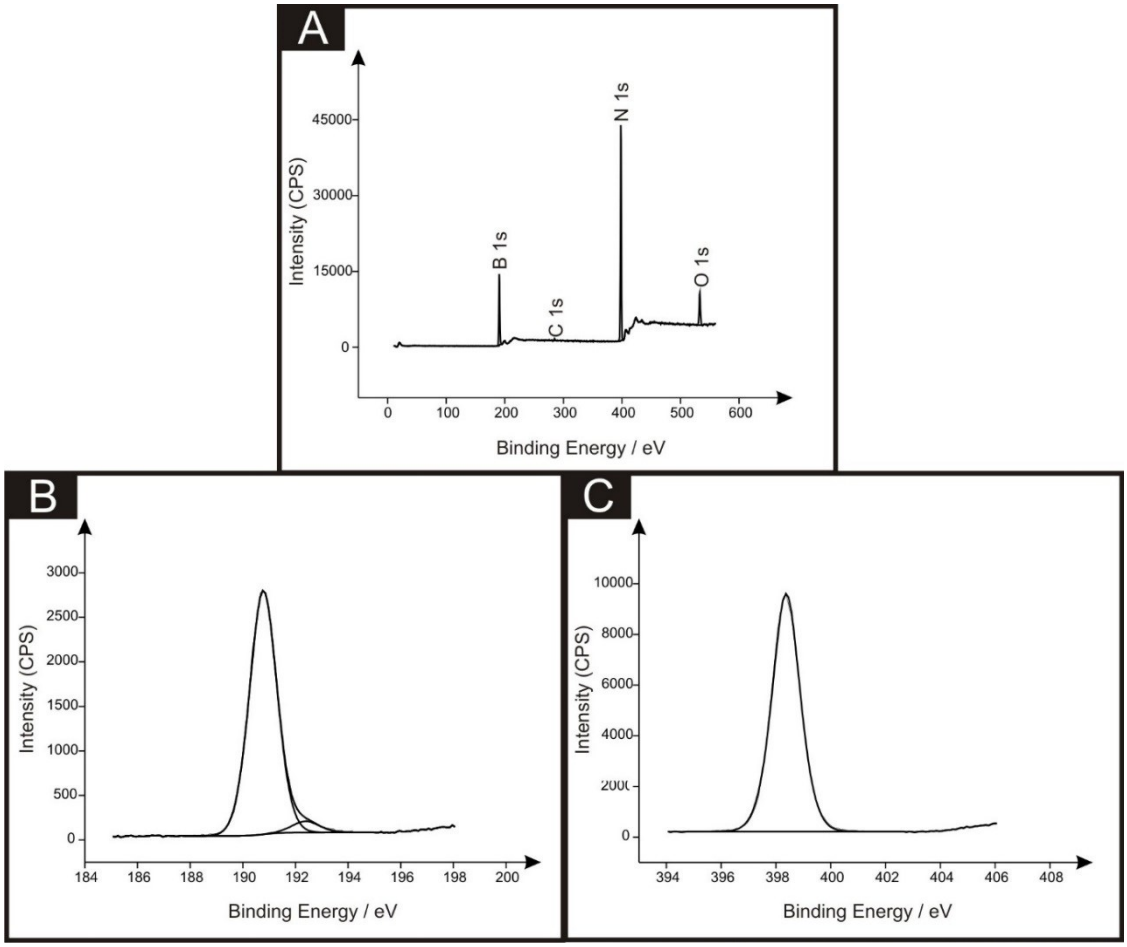

Figure 3.16: XPS survey spectrum (A) for a sample of the 2D-hBN. Curve fitted XPS spectra of the2D- hBN nanopowder. (B) illustrates XPS spectra of the B atom and spectra (C) is that of the N atom.

Table 3.3 exhibits the full surface composition obtained from the XPS analysis of the 2D-hBN (when supported on Si (111)).

Element	Atom % Layer composition
O 1s	5.54
C 1s	0.78
B 1s	50.02
N 1s	43.66

Table 3.3: A summary depicting the composition of 2D-hBN, following analysis of XPS spectra.

Chapter 4 : Pristine 2D Hexagonal Boron Nitride (2D-hBN) Explored as a Potential Electrocatalyst for the Oxygen Reduction Reaction

In this chapter, surfactant-free (pristine) crystalline 2D hexagonal Boron Nitride (2D-hBN) (see chapter 3.4.2) is explored as a potential electrocatalyst towards the oxygen reduction reaction (ORR) when electrically wired *via* a drop-casting approach upon a range of carbon based electrode surfaces; namely, glassy carbon (GC), boron-doped diamond (BDD), and screen-printed graphitic electrodes (SPEs). The ORR is considered in acidic conditions and the performance of unmodified and pristine 2D-hBN modified electrodes are critically evaluated, with coverage studies implemented (commonly neglected in the literature) in order to ascertain the true impact of this novel nanomaterial. The behaviour of 2D-hBN towards the ORR is shown to be highly dependent upon both the underlying carbon substrate and the coverage/mass utilised. This chapter reveals for the first time that pristine 2D-hBN gives rise to beneficial electrochemical behaviour towards the ORR when immobilised on a graphic substrate. This chapter contains work that has been peer-reviewed and published in the academic literature.[1]

[1] A. F. Khan, E. P. Randviir, D. A. C. Brownson, X. Ji, G. C. Smith and C. E. Banks, *Electroanalysis*, 2017, **29**, 622-634.

4.1. Introduction

As the availability of natural energy resources depletes, it has become increasingly important to find alternative means of energy production.[37] The most common alternatives to fossil fuels are renewable sources such as hydroelectric power[88] and wind turbines, and for transportation purposes, electrolysers for fuel cells. The latter is an electrochemical device that relies on the oxidation of a fuel, such as methanol, at a working electrode (anode), while the protons liberated act as a reducing agent to oxygen in the cathodic part of the fuel cell. Research into proton exchange membrane (PEM) fuel cells, in which the oxygen reduction reaction (ORR) occurs, is directed towards improving power output, efficiency, and longevity, such that devices become viable for the transportation fuel cell market.[89]

The ORR occurs at the cathode of PEM fuel cells and has proved to be problematic (dependent upon the catalyst utilised), primarily limiting the lifetimes of devices due to electrode fouling.[90, 69] For example, PEM fuel cell degradation[89] is synonymous with the ORR due to the formation of hydrogen peroxide (H_2O_2) when using catalysts that reduce oxygen *via* a two electron pathway.[91] Furthermore, slow electron transfer kinetics during the ORR can potentially result in a 50% voltage loss and reduce the performance of a PEM fuel cell.[89, 92] There are also problems related to the relative costs of fuel cell catalysts, with platinum (Pt)[93] favoured due to its direct four electron pathway that does not produce harmful by-products such as H_2O_2.[94] The exact mechanism for H_2O_2 poisoning of the cathode is unclear with direct and indirect attack mechanisms proposed in the literature.[95, 96] The ORR processes in acidic media is as follows:[91]

$O_2 + 4H^+ + 4e^- \rightarrow 2H_2O$ direct (4 electron pathway)

$O_2 + 2H^+ + 2e^- \rightarrow H_2O_2$ indirect (2 electron pathway)

$H_2O_2 + 2H^+ + 2e^- \rightarrow 2H_2O$

Consequently, research is directed towards discovering cheaper nonprecious metal catalysts[97] and more pertinently, metal-free carbon materials. Of note, carbon based electrodes have been explored as potential metal-free electrocatalysts for the ORR with limited success given that processes proceed *via* the unfavourable two electron pathway (producing H_2O_2).[91]

With the above insights in mind, the ORR is considered using crystalline hexagonal 2D-hBN, a 2D nanomaterial comprising equal boron and nitrogen atoms arranged in a similar hexagonal structure in crystalline form to that of graphene (thus referred to as 'white graphene').[56] 2D-hBN is found in amorphous and crystalline forms,[59] with crystalline 2D-hBN containing strong σ bonds and weak van der Waals forces,[60] resulting in a range of favourable thermal, mechanical, and chemical properties.[61] Resultantly, 2D-hBN has been widely researched in the field of electrochemistry for applications such as composites, dielectrics and optics.[60] However, note that the bonding of 2D-hBN is covalent[60] and the electrons in the σ bond are localised towards nitrogen,[60] whereas the π bonding present involves an empty p-orbital of boron and a filled p-orbital of nitrogen, with the nitrogen π electrons delocalised.[60] Such an electronic structure allows 2D-hBN to be a good insulator in its solid form.[62]

Considering PEM fuel cells, it has recently been reported that a 2D-hBN membrane allows protons through whilst simultaneously reducing fuel crossover.[70] This effect is highly desirable and may help to improve fuel cell lifetime. However,

the report does not consider that 2D-hBN *per se* may be useful as a catalytic material for fuel cell cathodes. In this regard, there have been limited investigations of 2D-hBN as an electrode material. Koitz *et al*.[98] computationally investigated the ORR with 2D-hBN supported upon Co, Ni, and Cu and found that the underlying metal support highly influenced the reaction energetics, with 2D-hBN/Cu showing a particularly low potential for the ORR to occur. Furthermore, Lyalin *et al*.[71] found *via* density functional theory (DFT) calculations that an inert 2D-hBN monolayer can become catalytically active upon nitrogen doping, whilst Studt *et al.*[72] explored the effects of nitrogen doped graphene towards the ORR with DFT calculations and found the intermediates involved in the reaction bind to the carbon atom next to the nitrogen dopant. In other work, Uosaki *et al.*[69] experimentally investigated the ORR and immobilised 2D-hBN upon gold substrates/electrodes. Their work demonstrated an excellent 2D-hBN|gold interaction due to the binding of the 2D-hBN monolayer with transition metal surfaces given that the N-p_z and B-p_z orbitals of 2D-hBN mix with d_z^2 metal orbitals.[69] Thus upon modification of a gold electrode with 2D-hBN, the potential required for the ORR was reduced by *ca.* 0.27 V compared to a bare gold electrode (although unfortunately the modified electrode followed the two electron pathway, producing H_2O_2).[69] This example shows that 2D-hBN potentially possesses an electrocatalytic behaviour towards the ORR on this substrate. However, gold is a precious metal with a high cost, making it an expensive substrate and therefore not highly desirable in the design, commercialisation and mass-production of fuel cells.[69]

Investigations of 2D-hBN immobilised on carbon-based substrates is perhaps a more pertinent research direction for this material, as is the theme of this chapter. To the best of my knowledge, 2D-hBN has yet to be reported to exhibit an

electrocatalytic behaviour (or an improved electrochemical response) when immobilised upon a carbon substrate towards the ORR.[69, 99] Previous reports have failed to identify 2D-hBN masses that give rise to beneficial voltammetric behaviours (limited to metallic surfaces),[4, 98, 100] nor have they considered several underlying/supporting carbon species in terms of their electrical anisotropy or surface roughness (and substrate effects).[69] it is noted that Uosaki *et al.*[69] investigated 2D-hBN using a glassy carbon based substrate and observed little (*no real*) electrocatalytic effect towards the ORR.[69] This chapter takes a novel approach and investigates the electrocatalytic performance of different pristine 2D-hBN coverages immobilised upon a range of carbon-based substrates (namely; glassy carbon (GC), boron doped-diamond (BDD), and screen-printed graphitic electrodes (SPEs)) towards the ORR. The results to other 2D materials and noble metal electrodes such as platinum and gold for the ORR are compared. This chapter investigates pristine 2D-hBN, which has, to date, not been reported as a beneficial ORR material when supported upon *carbon substrates*; thus, this work provides a high level of novelty.

4.2 Experimental Details

For experimental procedures/tests investigating the electrochemical detection of oxygen, sulfuric acid solutions utilised were of the highest grade available from Sigma-Aldrich (99.999%, double distilled for trace metal analysis) and was used at a concentration of 0.1 M. To oxygenate the solution, it was subject to rigorous bubbling of 100% medicinal grade oxygen through 100 mL of the solution for 45 minutes, assuming this to be a completely saturated solution at room temperature as

described by Gara.[91] The concentration of oxygen was assumed to be 0.9 mM according to previous reports using the same method. [91, 94]

4.3 Results and Discussion

The electrochemical characterisation of pristine 2D-hBN is considered using the outer-sphere redox probe, hexaammineruthenium (III) chloride, as a model electrochemical system. This simple one electron redox couple is used to understand its fundamental interaction with simple redox systems prior to closer examination with a more complex electrode process (ORR). Figure 4.1A depicts the cyclic voltammograms obtained using pristine 2D-hBN modified SPEs, where evidently the bare electrode exhibits a peak-to-peak separation (ΔE_P) of 105 mV. It is observed that the ΔE_P incrementally shifts from *ca*. 105 to 195 mV with increasing pristine 2D-hBN modifications from 10.8 to 324 ng.

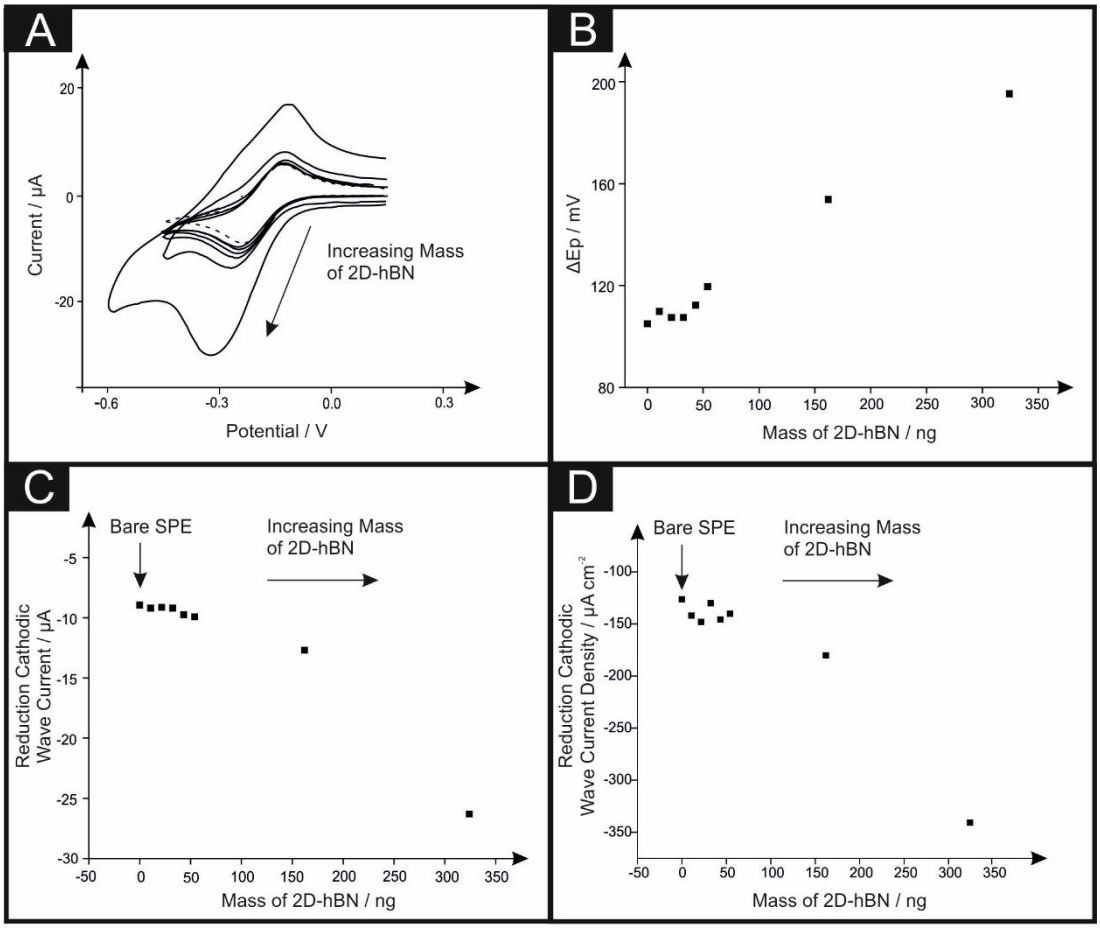

Figure 4.1: Typical cyclic voltammograms (A) recorded in 1 mM $[Ru(NH_3)_6]^{2+/3+}$ / 0.1 M KCl with pristine 2D-hBN masses of: 10.8, 21.6, 32.4, 43.2, 54, 162 and 324 ng immobilised upon SPEs. The dotted line represents an unmodified (bare) SPE. Also shown are the analysis of the voltammograms presented in Figure 4.1A in the form of peak-to-peak separation (ΔE_P) vs. mass of pristine 2D-hBN (B), 'reduction cathodic wave current' against mass of pristine 2D-hBN (C) and 'reduction cathodic wave current density' against mass of pristine 2D-hBN (D) . Scan rate: 100 mV s^{-1} (vs. SCE).

Using the linear gradient plotted in Figure 4.1B, (ΔEp / mV = 0.2892x + 102.91), it is found that 50 ng of 2D-hBN increases the ΔE_P on average by 14.5 mV.

It is important to determine the effective HET rate constant, k^o_{eff}, and how modification of SPEs with different masses of 2D-hBN affects the electron transfer process occurring. The k^o_{eff} values were found to correspond to: 3.1×10^{-3} cm s^{-1}

(unmodified SPE); 2.6×10^{-3} cm s^{-1} (54 ng 2D-hBN modified SPE); 1.5×10^{-3} cm s^{-1} (162 ng 2D-hBN modified SPE); and 1.1×10^{-3} cm s^{-1} (324 ng 2D-hBN modified SPE). It is noted the k^{o}_{eff} values are calculated utilising the Nicholson method. The HET reduces as a function of pristine 2D-hBN mass immobilisation, indicating that the electrochemical process is less favourable at the pristine 2D-hBN modified SPEs in comparison to the underlying (bare) electrode. Despite the above observation, it is clearly visible in Figure 4.1A that the modification of pristine 2D-hBN upon SPEs creates an increase in the observed peak currents. Figure 4.1C shows that 2D-hBN increases the cathodic (reduction) wave current by *ca*. 2.15 μA per 50 ng (mass), with Figure 4.1D showing this trend further towards increased current density. The increased peak current, perhaps because of an increased surface area, is an exciting observation that may be useful for improving the current density of PEM fuel cells.

Next considered is the immobilisation of high masses of 2D-hBN upon SPEs, and the effect upon the electrochemical process of hexaammineruthenium (III) chloride. Figure 4.2A depicts typical cyclic voltammetric profiles of a 324 ng pristine 2D-hBN modified SPE, with Figure 4.2B depicting a plot of 'peak height' *vs.* 'square root of the voltammetric scan rate'. Analysis of Figure 4.2B reveals a linear response, demonstrating a diffusional process in accordance with the Randles–Ševčík equation (see equation 1.21, chapter 1). Furthermore, analysis of 'log peak height' (I_p) *vs.* 'log scan rate' (v) is shown in Figure 4.2C and reveals a gradient of 0.56 (N = 3), indicating the absence of any thin layer effects (where the analyte of interest is trapped on the surface of the electrode giving rise to false electrocatalysis due to negating the process of diffusion) and that the process is predominantly diffusional controlled.[101, 102]

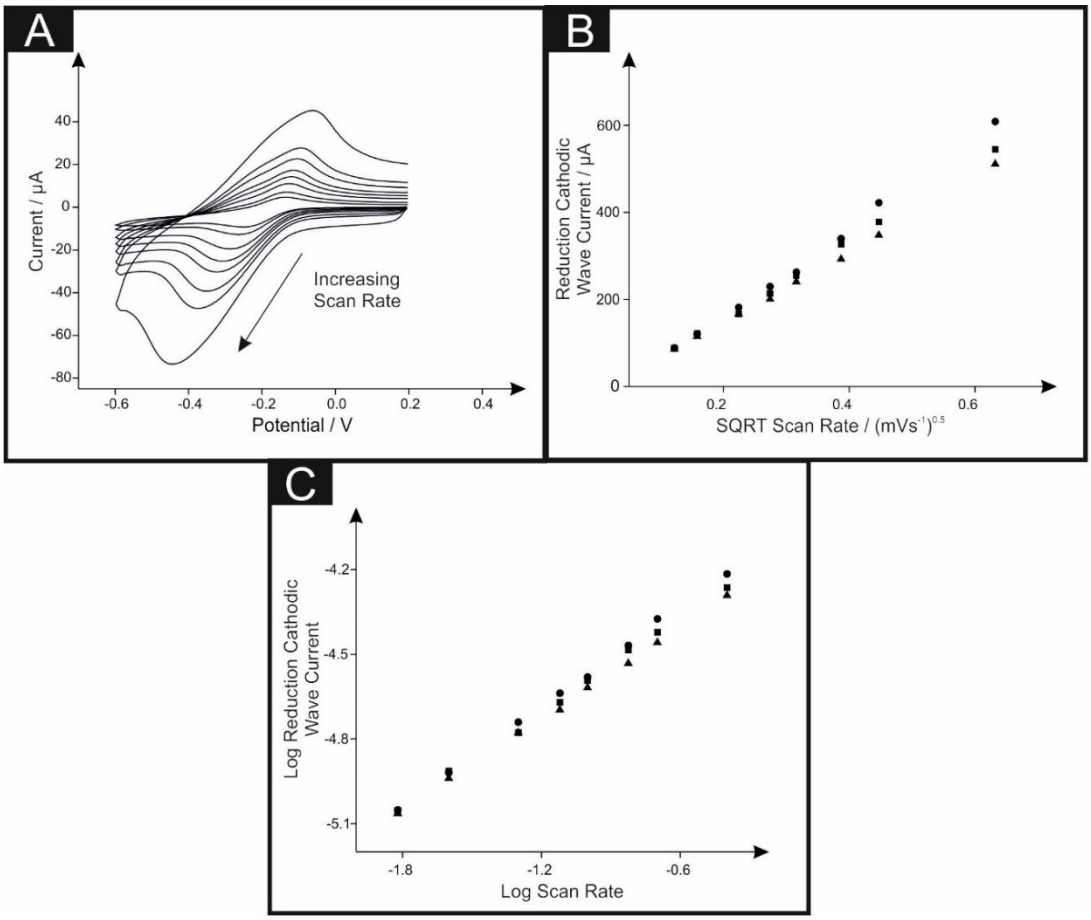

Figure 4.2: Typical cyclic voltammograms (A) recorded in 1 mM $[Ru(NH_3)_6]^{2+/3+}$ / 0.1 M KCl with pristine 2D-hBN mass of 324 ng immobilised upon SPEs. Also shown are analysis of the voltammograms presented in Figure 4.2A in the form of 'reduction cathodic wave current' vs. 'square root scan rate' (B) and 'log reduction cathodic wave curren't vs. 'log of scan rate' (C). Scan rates present in (A): 15, 25, 50, 75, 100, 150, 200 and 400 mV s^{-1} (vs. SCE).

A further consideration is the stability of the pristine 2D-hBN modified layer(s) upon the electrode surface. This is addressed *via* the implementation of a stability experiment in which a 162 ng pristine 2D-hBN modified SPE was subjected to 100 repeated cycles/scans in a hexaammineruthenium (III) chloride (0.1 M KCl) solution at 100 mV s^{-1}. This experiment simulates and recreates the appropriate timescale(s) of the voltammetric tests utilised within this work and shows that the

cathodic I_p and potential remained stable, with only small (*ca*. 1.93 µA and *ca*. 0.01 V respectively) alterations occurring in the recorded signal over 100 cycles (see Figure 4.3 and Table 4.1). Clearly, at this representative coverage, the pristine 2D-hBN modified layer(s) are stable on the electrode surface and do not appear to fall off the electrode into the solution. It is noted that a 100 cycle study is not suitable for fuel cell analysis, with 10,000 cycles being more appropriate.

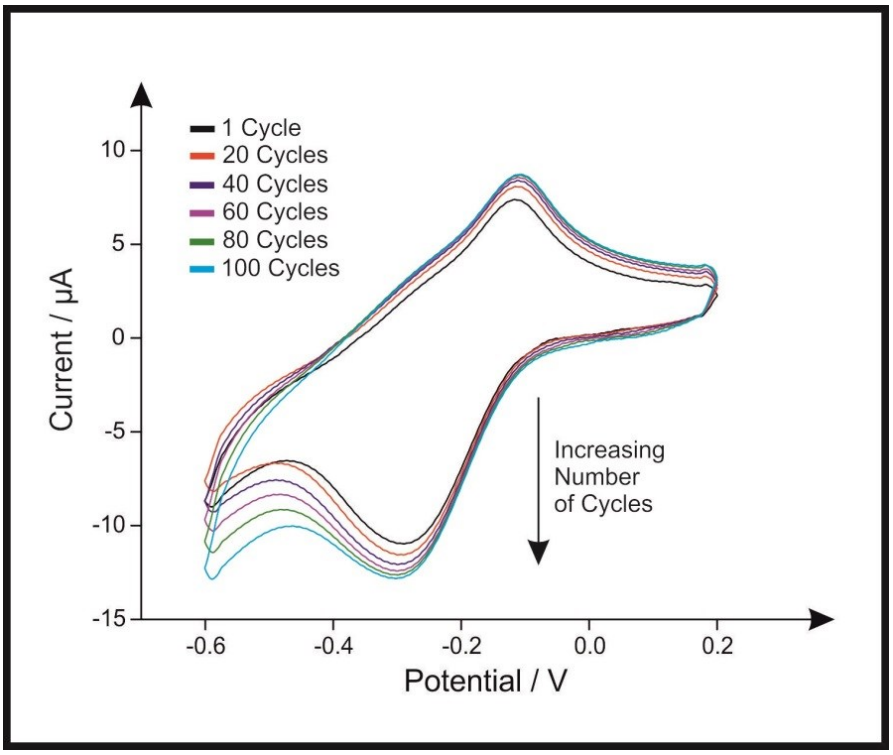

Figure 4.3: Cyclic voltammograms recorded in 1 mM $[Ru(NH_3)_6]^{2+/3+}$ / 0.1 M KCl using a 162 ng pristine 2D-hBN modified SPE. Repeat scans were performed up to 100 cycles. Scan rate: 100 mV s^{-1} (vs. SCE).

Cycle Number	Cathodic Peak (Reduction) Current (µA)	Cathodic Peak (Reduction) Potential (V)	
1	11.20	-0.296	(± 0.002)
20	11.72	-0.296	(± 0.002)
40	12.22	-0.296	(± 0.002)
60	12.41	-0.296	(± 0.002)
80	12.72	-0.300	(± 0.002)
100	13.13	-0.303	(± 0.002)

Table 4.1: Analysis of voltammograms presented in Figure 4.3. Table exhibits the effects of increasing voltammetric cycle number upon the 'cathodic peak current' (µA) and 'cathodic peak potential' (V) when utilising a 162 ng pristine 2D-hBN modified SPE.

Next, a range of carbon-based electrodes are explored as underlying substrates for pristine 2D-hBN immobilisation, with assessment of the resultant electrochemical performances. As presented in Figure 4.4, the optimally pristine 2D-hBN modified GC electrode exhibited a minimal increase in cathodic wave current, with the highest pristine 2D-hBN modification (324 ng) resulting in a decreased cathodic wave current compared to that of previous modifications.

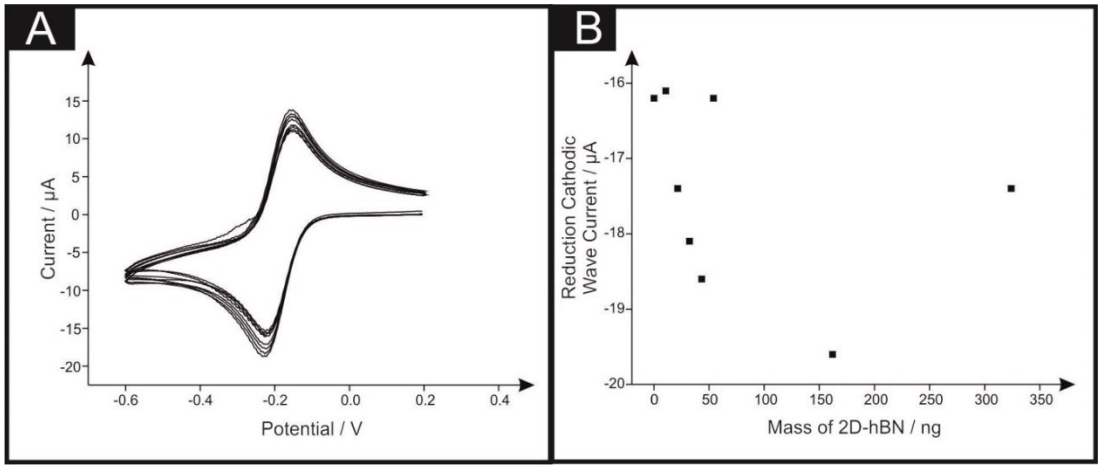

Figure 4.4: Typical cyclic voltammograms (A) recorded in 1 mM $[Ru(NH_3)_6]^{2+/3+}$ / 0.1 M KCl with pristine 2D-hBN masses of: 10.8, 21.6, 32.4, 43.2, 54, 162 and 324 ng immobilised upon a GC electrode. The dotted line represents an unmodified (bare) GC electrode. Also shown are the analysis of the voltammograms presented in Figure 4.4A in the form 'reduction cathodic wave current' against 'mass of 2D-hBN' (B). Scan rate: 100 mV s^{-1} (vs. SCE).

This trend can also be observed in Figure 4.5 for the case of a BDD electrode, as initial pristine 2D-hBN deposition upon this electrode resulted in an increase in the cathodic wave current, from –16.1 µA (unmodified) to –20.1 µA (162 ng pristine 2D-hBN), after which deposition of 324 ng pristine 2D-hBN on the BDD electrode gives rise to a decrease of 2.5 µA in the cathodic wave current.

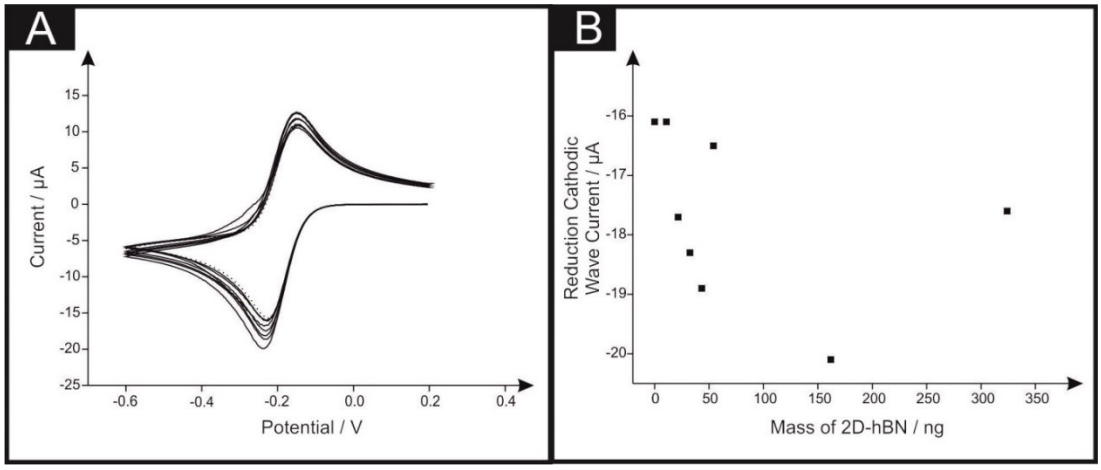

Figure 4.5: Typical cyclic voltammograms (A) recorded in 1 mM $[Ru(NH_3)_6]^{2+/3+}$ / 0.1 M KCl with pristine 2D-hBN masses of: 10.8, 21.6, 32.4, 43.2, 54, 162 and 324 ng immobilised upon a BDD electrode. The dotted line represents an unmodified (bare) BDD electrode. Also shown are the analysis of the voltammograms presented in Figure 4.5 A in the form 'reduction cathodic wave current' against 'mass of pristine 2D-hBN' (B). Scan rate: 100 mV s^{-1} (vs. SCE).

Interestingly, a different scenario was observed for an EPPG electrode (see Figure 4.6). The two highest modifications displayed the lowest observable peak currents in this case, indicating that the electrocatalytic ability of pristine 2D-hBN is dependent upon the underlying electrode substrate.

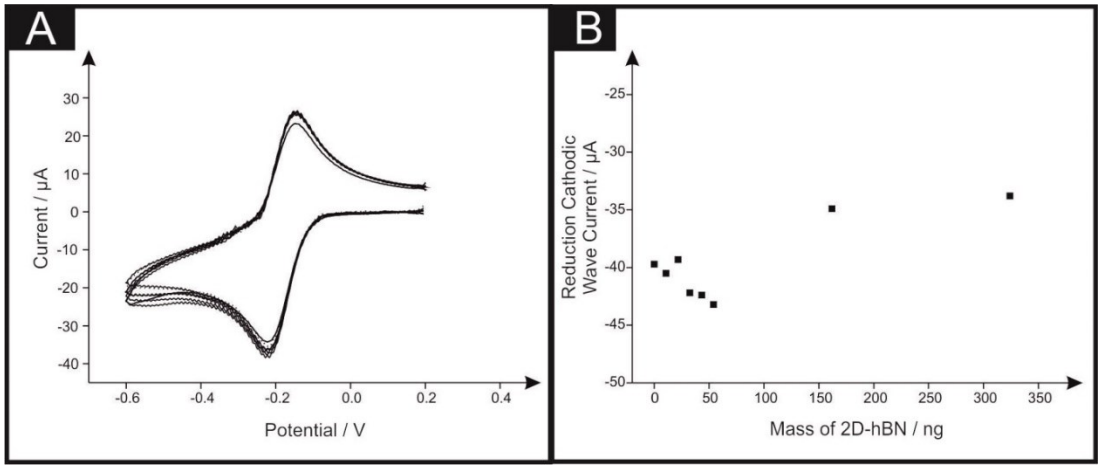

Figure 4.6: Typical cyclic voltammograms (A) recorded in 1 mM $[Ru(NH_3)_6]^{2+/3+}$ / 0.1 M KCl with pristine 2D-hBN masses of: 10.8, 21.6, 32.4, 43.2, 54, 162 and 324 ng immobilised upon a EPPG electrode. The dotted line represents an unmodified (bare) EPPG electrode. Also shown are the analysis of the voltammograms presented in Figure 4.6A in the form 'reduction cathodic wave' current 'against mass of pristine 2D-hBN' (B). Scan rate: 100 mV s^{-1} (vs. SCE).

The data presented within this section shows that the underlying electrode substrate must be considered when utilising pristine 2D-hBN as an electrode material and potential electrocatalyst, particularly in the case of smaller pristine 2D-hBN modifications where the underlying substrate is likely to have a significant effect upon the observed electrochemistry. Above, it has been demonstrated that carbon based substrates, such as SPEs, may exhibit a synergistic effect when pristine 2D-hBN is introduced on to their surface. It is thought that the interaction of pristine 2D-hBN is a dominant factor in its ability to 'link' a substrate to a solution-based redox reaction, and that a ridged surface may be more favourable for this. Indeed, the evidence presented in this section shows that smooth support surfaces, such as GC electrodes, exhibit minimal increases in the cathodic wave current when pristine 2D-

hBN is introduced. Conversely, when using rougher, more ridged surfaces such as a SPE, the cathodic current increases significantly upon pristine 2D-hBN addition. Furthermore, changes are exhibited in the electrode kinetics where differing trends are observed towards the ΔE_P upon pristine 2D-hBN immobilisation on rough and smooth substrates. Therefore, it is important to note that one must take into account not only the quantity of pristine 2D-hBN utilised, but also the underlying electrode substrate itself.

As previously indicated in chapter 3, Figure 3.3, SEM images have been provided which appear to support the aforementioned theory. To gain further insights however, the roughness factor (R_F) values for unmodified and pristine 2D-hBN modified SPEs and GC electrodes were calculated using the double layer capacitance technique as described by Shin *et al*.[103] First, unmodified, 108, 216 and 324 ng pristine 2D-hBN modified SPEs were investigated in 0.1 M H_2SO_4 *via* cyclic voltammetry at various scan rates using a potential range of 0.01 to 0.11 V (due to this being the non-Faradaic potential window). The resultant voltammograms are presented in Figure 4.7, with the corresponding analysis, as shown in Figure 4.8, illustrating a plot of 'the difference between the anodic and cathodic current at 0.06 V' against 'the applied voltammetric scan rate'. The slope obtained is proportional to a value double that of the double layer capacitance,[103] with the absolute calculated double layer capacitance values found to be 2.4, 77.2, 96.0 and 121.7 μF cm^{-2} for SPEs modified with 0, 108, 216 and 324 ng pristine 2D-hBN. The respective R_F values are 1.0, 31.6, 39.4 and 49.9 for the 0, 108, 216 and 324 ng pristine 2D-hBN modified SPEs. It is noted the data points do not go through the origin since there is always a capacitive charge on the electrode. This has been shown in previous

literature.[103] Clearly, the roughness factor significantly increases following pristine 2D-hBN modification on SPEs.

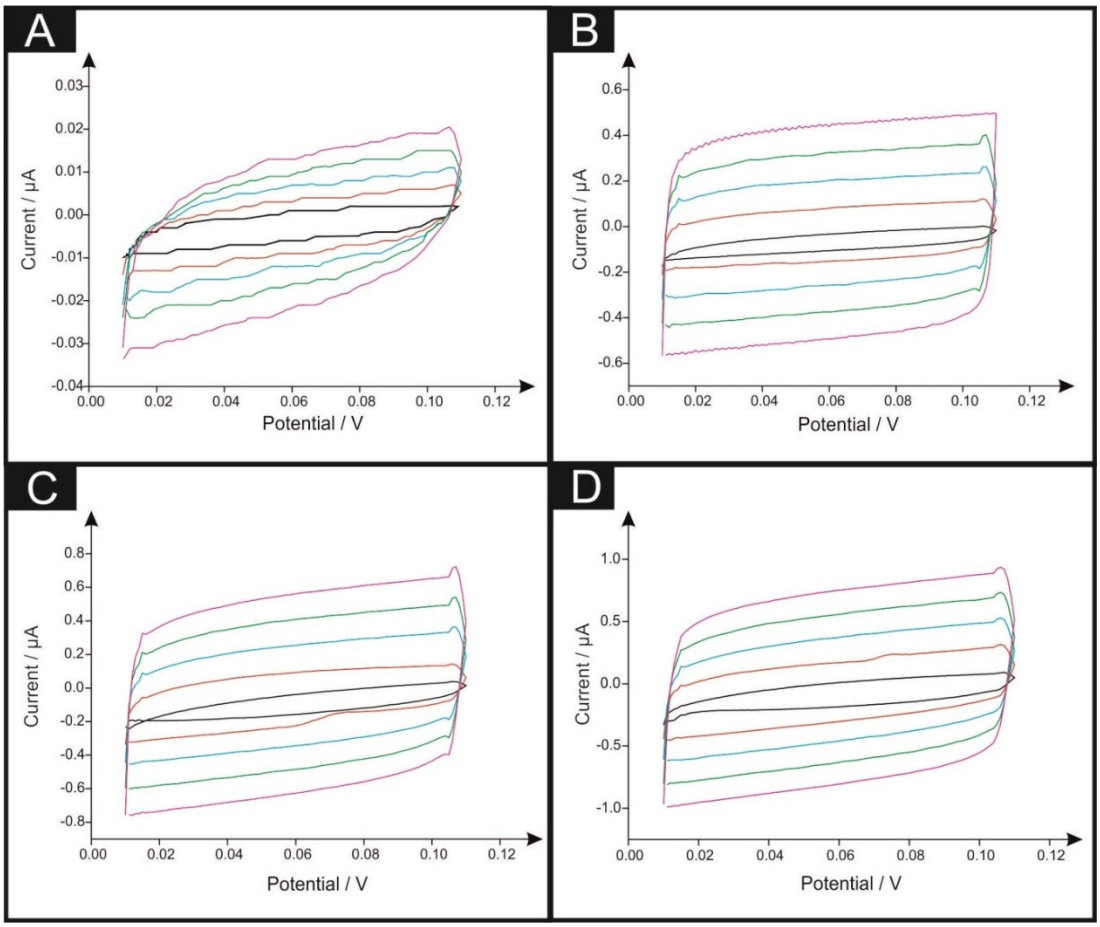

Figure 4.7: Cyclic voltammograms recorded in 0.1 M H_2SO_4 solution for SPEs modified with varying amounts of pristine 2D-hBN. Modifications; (A) 0, (B) 108, (C) 216, (D) 324 ng. Scan rate: 20 (black), 40 (red), 60 (blue), 80 (green) and 100 mV s^{-1} (pink) (vs. SCE).

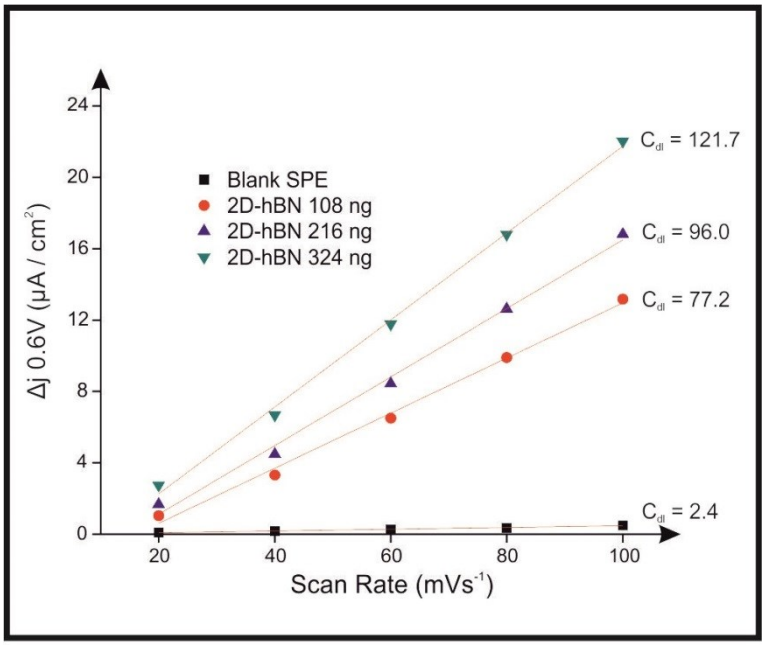

Figure 4.8: The difference in anodic and cathodic current density for unmodified and pristine 2D-hBN modified SPEs taken at +0.06 V vs. scan rate (mV s^{-1}) (see Figure 4.7). The slope of the linear regression indicates the value of double layer capacitance (C_{dl}).

Comparatively, the R_F values obtained for unmodified and pristine 2D-hBN modified GC electrodes significantly differ. Figure 4.9 illustrates the double layer capacitance voltammograms obtained, with corresponding analysis in Figure 4.10. Double layer capacitance values were found to be 12.9, 18.6, 25.7 and 14.5 μF cm^{-2} for 0, 108, 216 and 324 ng 2D-hBN modified GC electrodes, with the corresponding R_F values of 1.0, 1.4, 2.0 and 1.1.

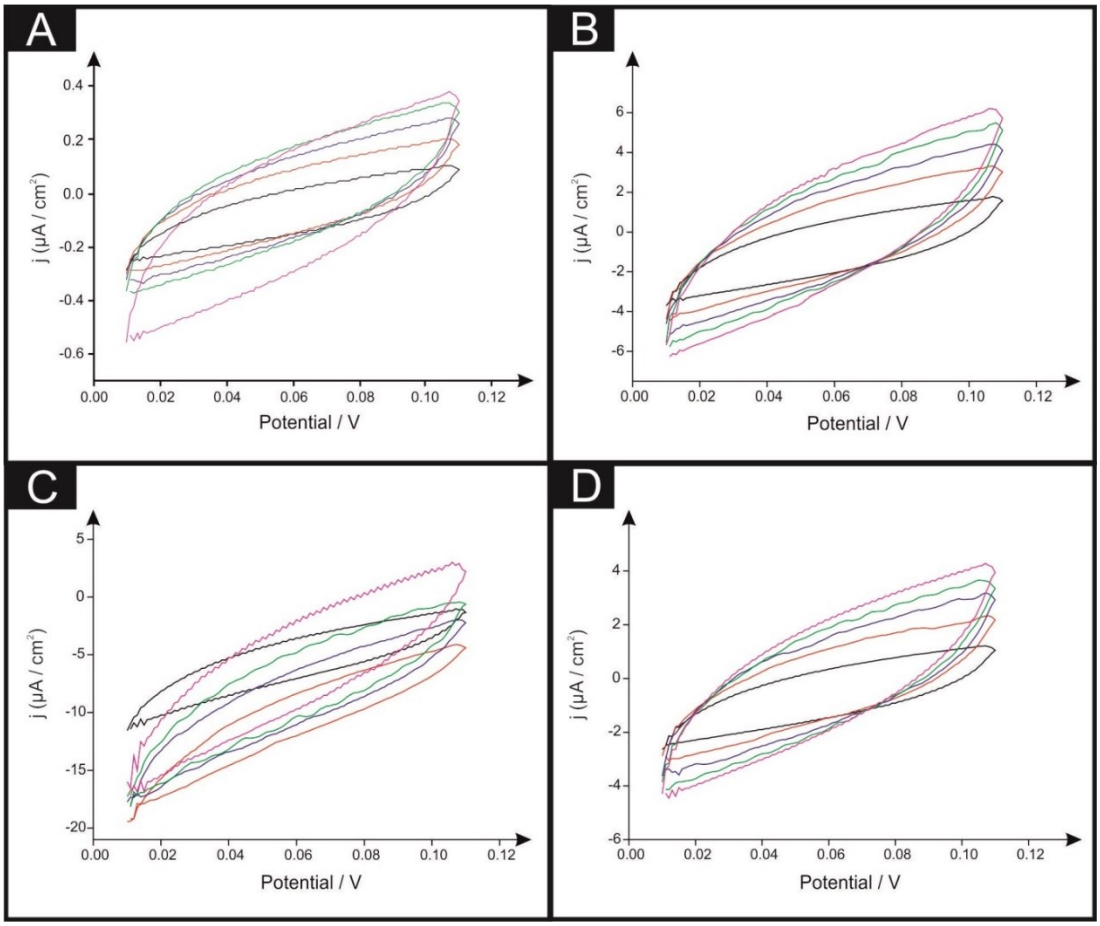

Figure 4.9: Cyclic voltammograms recorded in 0.1 M H_2SO_4 solution for a GC electrode modified with varying amounts of pristine 2D-hBN. Modifications; (A) 0, (B) 108, (C) 216, (D) 324 ng. Scan rate: 20 (black), 40 (red), 60 (blue), 80 (green) and 100 mV s^{-1} (pink) (vs. SCE).

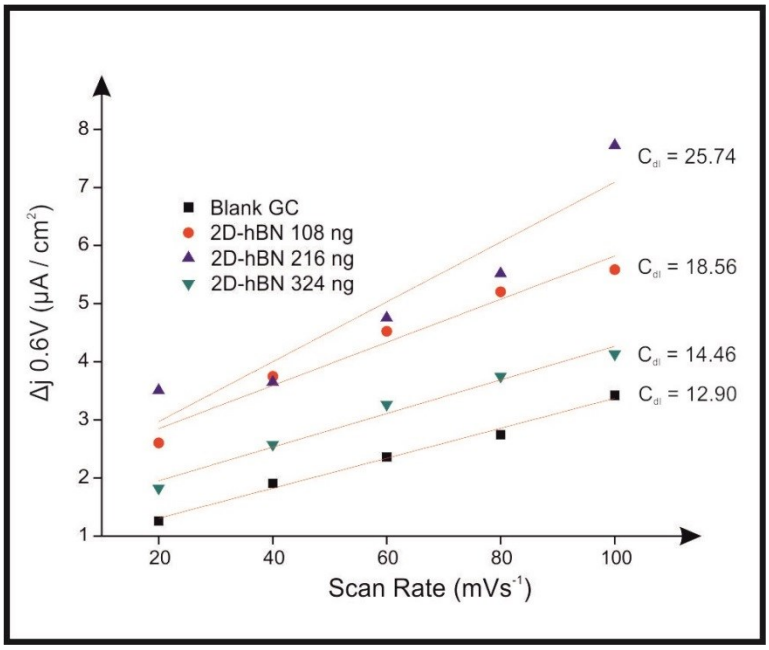

Figure 4.10: The difference in anodic and cathodic current density for an unmodified and 2D-hBN modified GC electrode taken at +0.06 V vs. scan rate (mV s^{-1}) (see Figure 4.9). The slope of the linear regression indicates the value of double layer capacitance (C_{dl}).

Given the above insights concerning the electrochemical roughness of pristine 2D-hBN modified SPE and GC electrodes, it is noted that pristine 2D-hBN adherence with a GC electrode is significantly lower in comparison to an SPE (in terms of alterations in the R_F values calculated following modification). This adds further evidence towards suggesting that a smooth surface, such as a GC electrode, would be less likely to form strong interactions with pristine 2D-hBN, whereas a rougher surface, like that of the SPE, may increase the substrate interaction and in doing so can potentially create a larger (more accessible) electrode surface area. Such an alteration upon the immobilisation of pristine 2D-hBN may prove to be beneficial and agrees with observations reported in Figure 4.1 and Figure 4.2.

Finally, white light profilometry was utilised to compare the surface topography of a range of substrates, namely GC, polished SPEs and unpolished

SPEs. The surface of an unpolished SPE was observed to be significantly rougher (with a root mean squared value of the heights over the whole surface (SQ) of 1338.8 nm) than that of GC and polished SPEs, which had the SQ values of 7.6 and 806.6 nm respectively (see Figure 4.11). Consequently, the effect of pristine 2D-hBN modification was considered with respect to the underlying electrode's surface topography. Figure 4.11D illustrates that immobilisation of 108 ng pristine 2D-hBN upon a GC electrode results in the surface becoming rougher, with a new SQ value of 35.1 nm, indicating an increase of 27.5 nm. Comparatively, 108 ng pristine 2D-hBN modification onto a polished SPE (Figure 4.11E) increases the SQ value from 806.6 nm to 842.4 nm, an increase of 35.8 nm. Evidently, a minimal increase in surface roughness is observed when utilising smooth underlying surfaces, namely polished SPEs and GC electrodes. Conversely, immobilisation of 108 ng pristine 2D-hBN upon an unpolished SPE (Figure 4.11F) resulted in the SQ value increasing from 1338.8 nm (unmodified SPE) to 1752.9 nm. This represents a significant increase of 414.1 nm at the unpolished (rough) SPE, which is distinct from that observed using smooth surfaces. This observation agrees well with the R_F values obtained earlier and suggests that pristine 2D-hBN likely adheres more favourably to a rough surface than that of a smooth/polished surface. Whatever the cause of this observation, the phenomena is highly fascinating and will likely require further in-depth study that is outside the scope of this thesis.

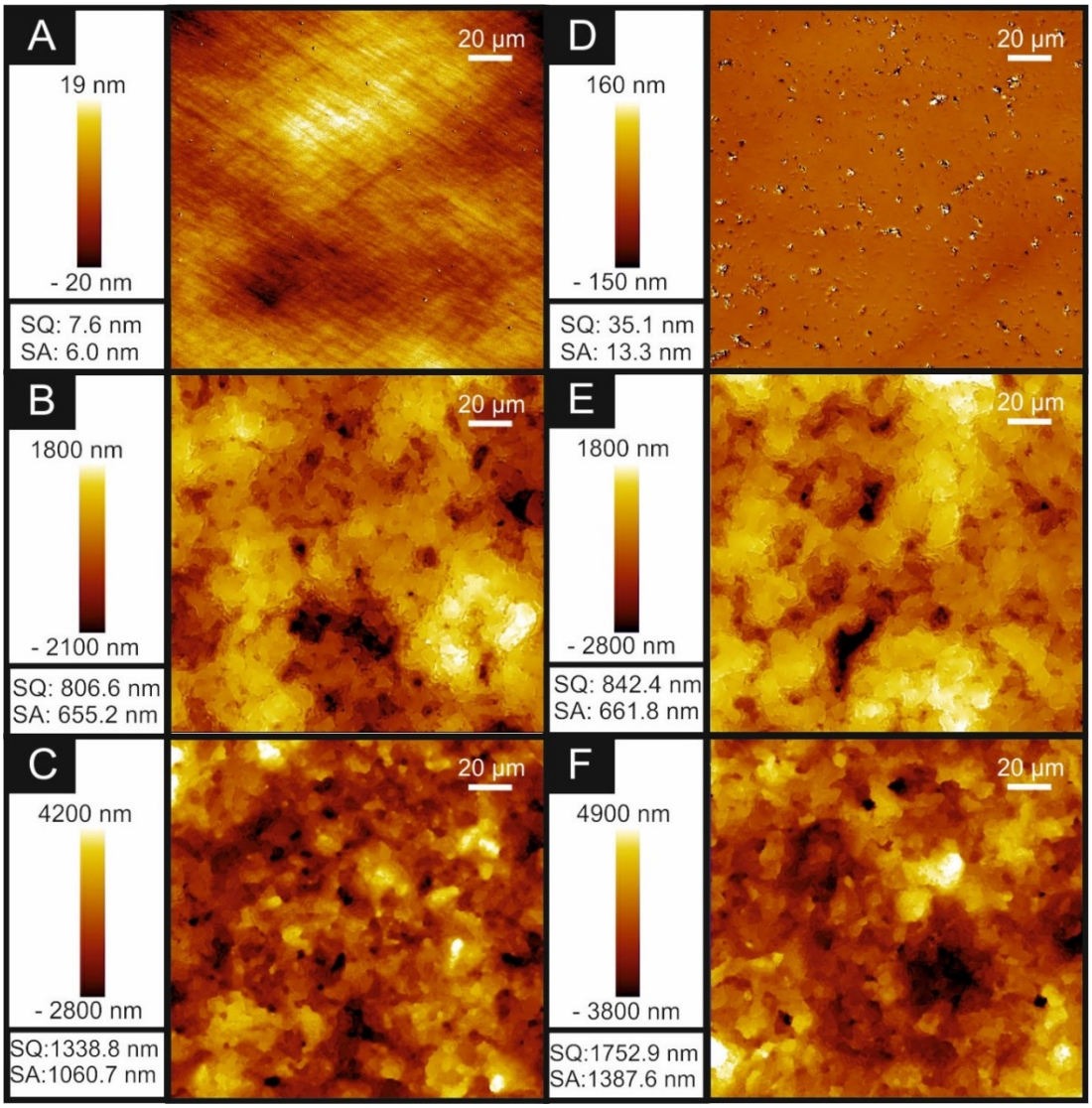

Figure 4.11: White light profilometry, giving surface topography maps of an unmodified GC electrode (A), a polished SPE (B) and an unpolished SPE (C). Also shown (D, E and F) are the respective electrodes (GC/polished SPE/unpolished SPE) following modification with 108 ng pristine 2D-hBN. It is evident that the surface roughness significantly increases with pristine 2D-hBN immobilisation upon unpolished SPEs in comparison to the same conditions when utilising a polished or initially smooth substrate.

The Oxygen Reduction Reaction: pristine 2D-hBN modified Carbon Electrodes

Attention is now turned to exploring the ORR using pristine 2D-hBN modified SPEs, GC, and BDD electrodes, where the underlying electrodes serve to

electrochemically "wire" the pristine 2D-hBN. First, unmodified SPEs, GC and BDD electrodes were explored towards the ORR within 0.1 M H_2SO_4 and scan rate studies were performed where the voltammetric peak height (I_p) was monitored as a function of scan rate (v). As depicted in Figure 4.12, the reduction peak potential for the ORR using SPEs ranges from –0.82 V to –1.41 V at scan rates between 15 – 400 mV s^{-1}, showing an increase with scan rate that is indicative of a relatively slow electrode process.

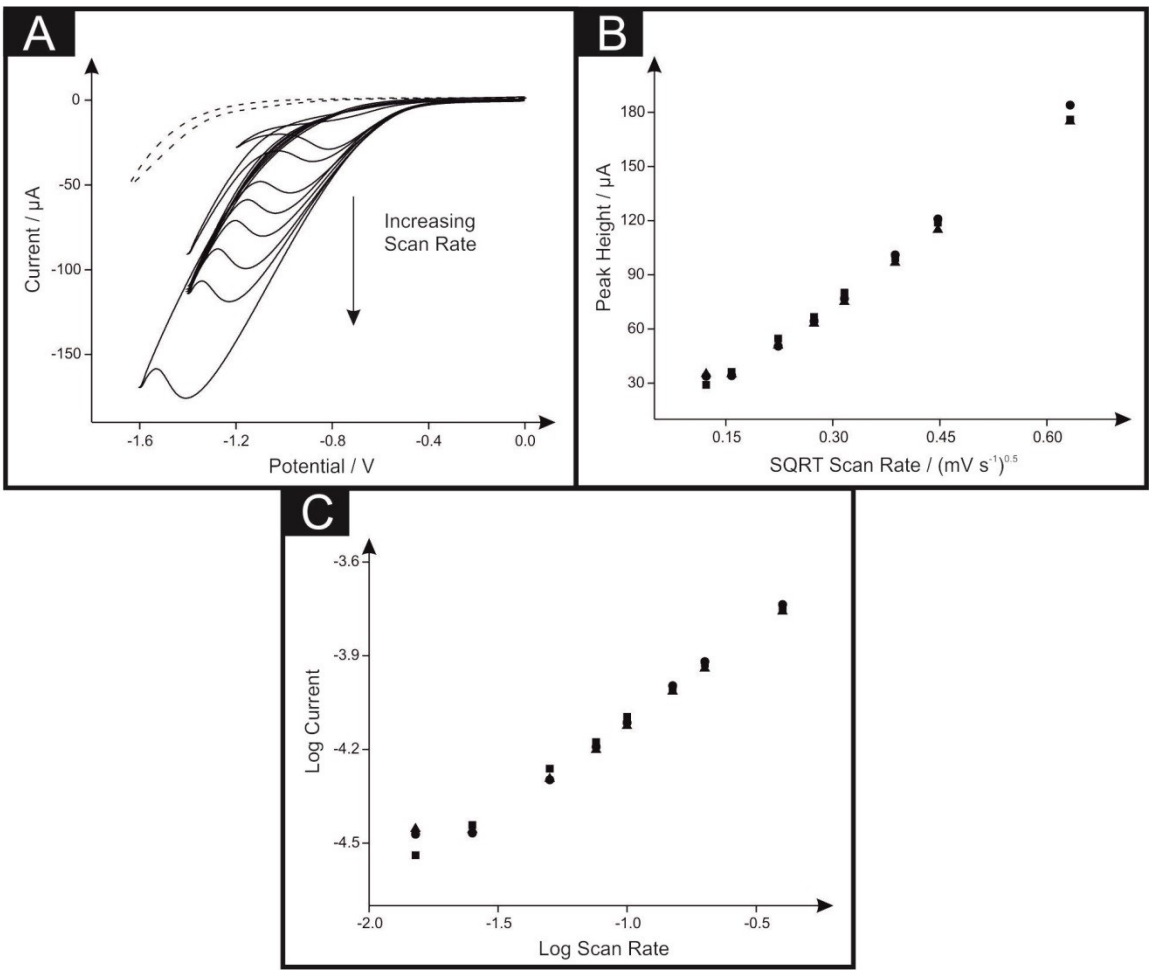

Figure 4.12: Cyclic voltammetry scan rate study recorded in oxygen saturated 0.1 M H_2SO_4 utilising an unmodified SPE (A). Scan rates: 15, 25, 50, 75, 100, 150, 200 and 400 mV s^{-1} (vs. SCE). Also

shown are plots of peak height vs. square root scan rate (B) and log peak height vs. log of scan rate (C).

In the case of a GC electrode, the peak potential required for the ORR to occur ranges from –0.63 V to –0.87 V at scan rates between 15 – 400 mV s^{-1} (see Figure 4.13), which is considerably less than the case of SPEs.

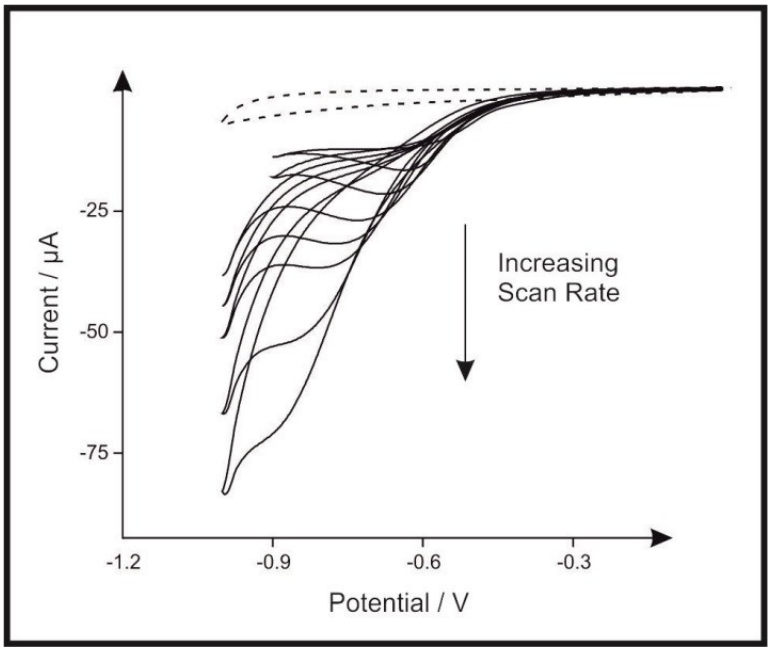

Figure 4.13: Cyclic voltammetry scan rate study recorded in oxygen saturated 0.1 M H_2SO_4 utilising an unmodified GC electrode. Scan rates: 10, 25, 50, 75, 100, 200 and 400 mV s^{-1} (vs. SCE).

Furthermore, Figure 4.14 shows the use of unmodified BDD electrodes towards the ORR results in the absence of an observed oxygen peak, which is in agreement with previous literature.[91] Yano *et al.*[104] suggest that the ORR on BDD only begins upon pre-treatment of positive potentials greater than +1.4 V (*vs.* Ag/AgCl) given that the sp^2 hybridised carbon species become oxidised and mediate

the ORR, with the most likely location for the sp^2 species being the grain boundaries of the sp^3 diamond structure.[91, 104]

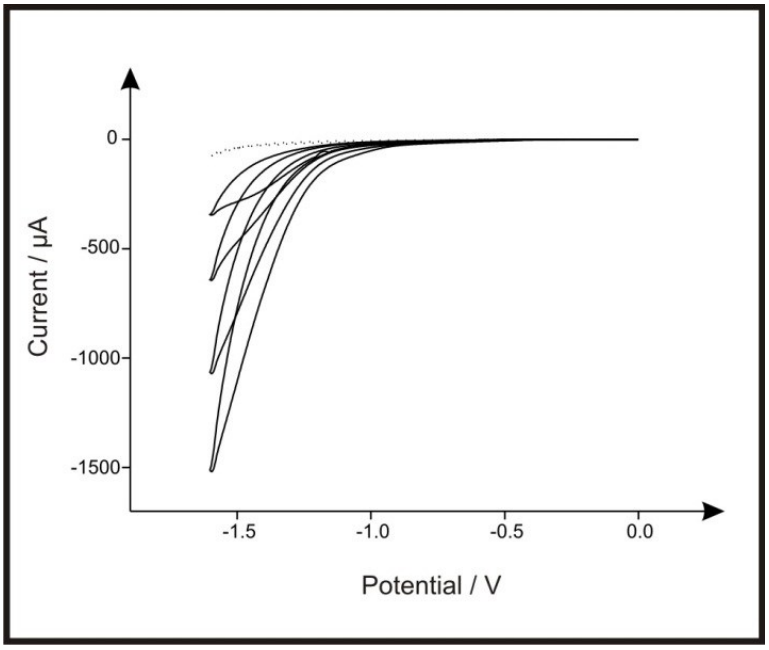

Figure 4.14: Cyclic voltammetry scan rate study recorded in an oxygen saturated 0.1 M H_2SO_4 utilising an unmodified BDD electrode. Scan rates: 25, 50, 100, and 200 mV s^{-1} (vs. SCE).

The effect of pristine 2D-hBN immobilisation towards the ORR utilising the above noted electrodes is next considered. Figure 4.15B illustrates that a 108 ng pristine 2D-hBN modified SPE exhibits an improvement (decrease) in the overpotential required for the ORR to occur compared to the bare/underlying electrode (as shown in Figure 4.15A). This is evidenced by the overpotential required for the ORR to occur shifting from –1.09 to –0.96 V (*vs*. SCE); hence a overpotential reduction of 0.13 V for the ORR to occur is observed (scan rate of 100 mV s^{-1}).

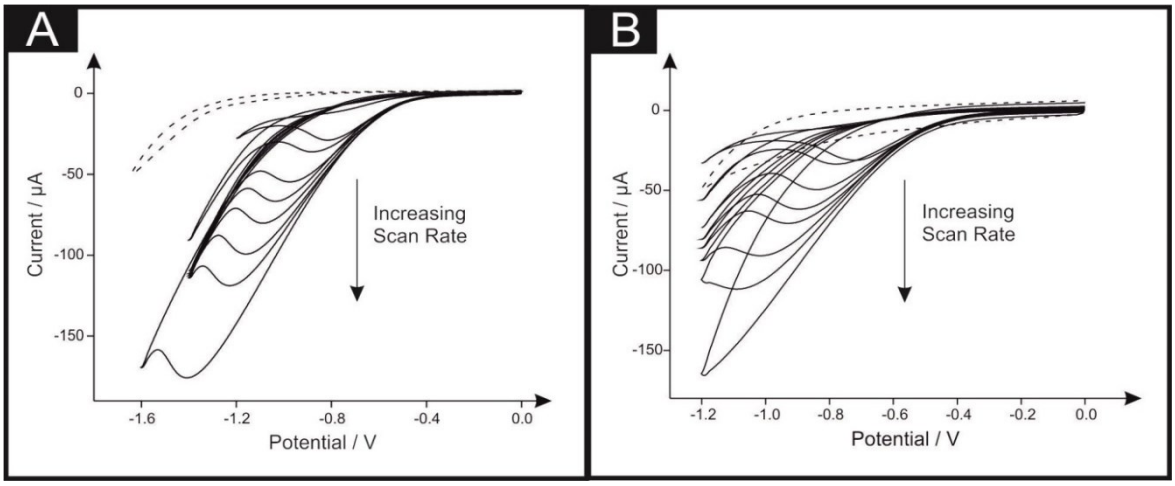

Figure 4.15: Typical cyclic voltammograms recorded in oxygen saturated 0.1 M H_2SO_4 with an unmodified SPE (A) and a 108 ng pristine 2D-hBN modified SPE (B). The dotted line depicts a deoxygenated SPE equivalent in each case. Scan rates: 15, 25, 50, 75, 100, 150, 200 and 400 mV s^{-1} (vs. SCE).

Interestingly, GC electrodes display a detrimental effect upon immobilisation with pristine 2D-hBN, with an increase in the overpotential required for the ORR to occur (see Figure 4.16A). In this case, the overpotential required for the ORR to occur shifts from –0.78 V for an unmodified GC electrode to –0.99 V for a 108 ng 2D-hBN modified GC electrode (at 100 mV s^{-1} *vs*. SCE). This represents an increase of 0.19 V, inferring that 2D-hBN is not an electrocatalytic material towards the ORR when immobilised upon GC.

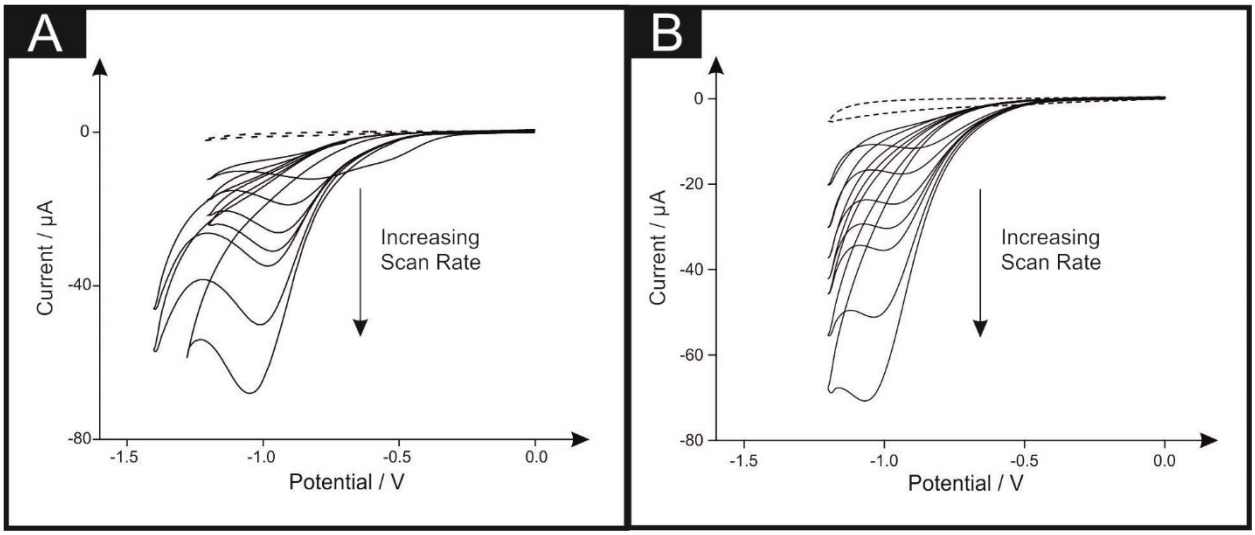

Figure 4.16: Typical cyclic voltammograms recorded in oxygen saturated 0.1 M H_2SO_4 using a 108 ng pristine 2D-hBN (A) and a 324 ng pristine 2D-hBN (B) modified GC electrode. The dotted line depicts a deoxygenated GC electrode equivalent in each case. Scan rates: 10, 25, 50, 75, 100, 200 and 400 mV s^{-1} (vs. SCE).

Additionally, in the case of a 108 ng pristine 2D-hBN modified BDD electrode, initiation of the ORR was again not observed (Figure 4.17A). From these experiments, it is clear that there is a dependency of pristine 2D-hBN towards the ORR upon the supporting electrode substrate – something which has been overlooked in the literature.

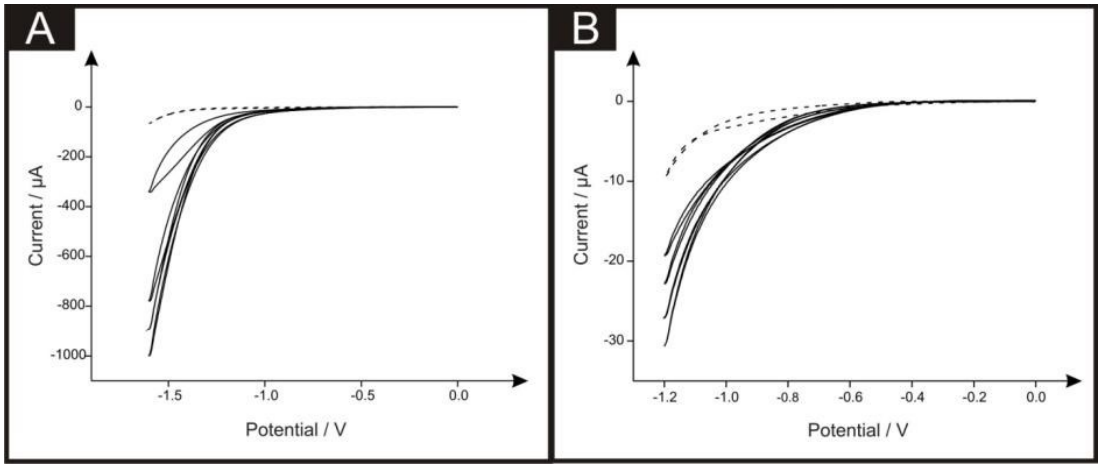

Figure 4.17: Typical cyclic voltammograms recorded in oxygen saturated 0.1M H_2SO_4 using a pristine 108 ng 2D-hBN (A) and a pristine 324 ng 2D-hBN (B) modified BDD electrode. The dotted line depicts a deoxygenated equivalent BDD electrode in each case. Scan rates: 25, 50, 100 and 200 mV s^{-1} (vs. SCE).

Next considered is the diffusion occurring at a pristine 2D-hBN modified substrate to ensure that the responses observed above (and later) are due only to changes in the electrode kinetics and that no mass transport alterations are convoluting the observed electrochemistry. Returning to the case of pristine 2D-hBN modified SPEs as a representative example, Figure 4.18 displays voltammetric curves for a 108 ng pristine 2D-hBN modified SPE with peak analysis shown in Figure 4.18B. A plot of 'peak height' *vs.* 'square-root of the scan rate' reveals a linear above a certain scan rate response, demonstrating a diffusional process. Figure 4.18C shows analysis of 'log I_p' *vs.* 'log v', where a linear gradient of 0.534 ($N = 3$) indicates the absence of any thin layer effects and represents a response that is purely diffusional.[101]

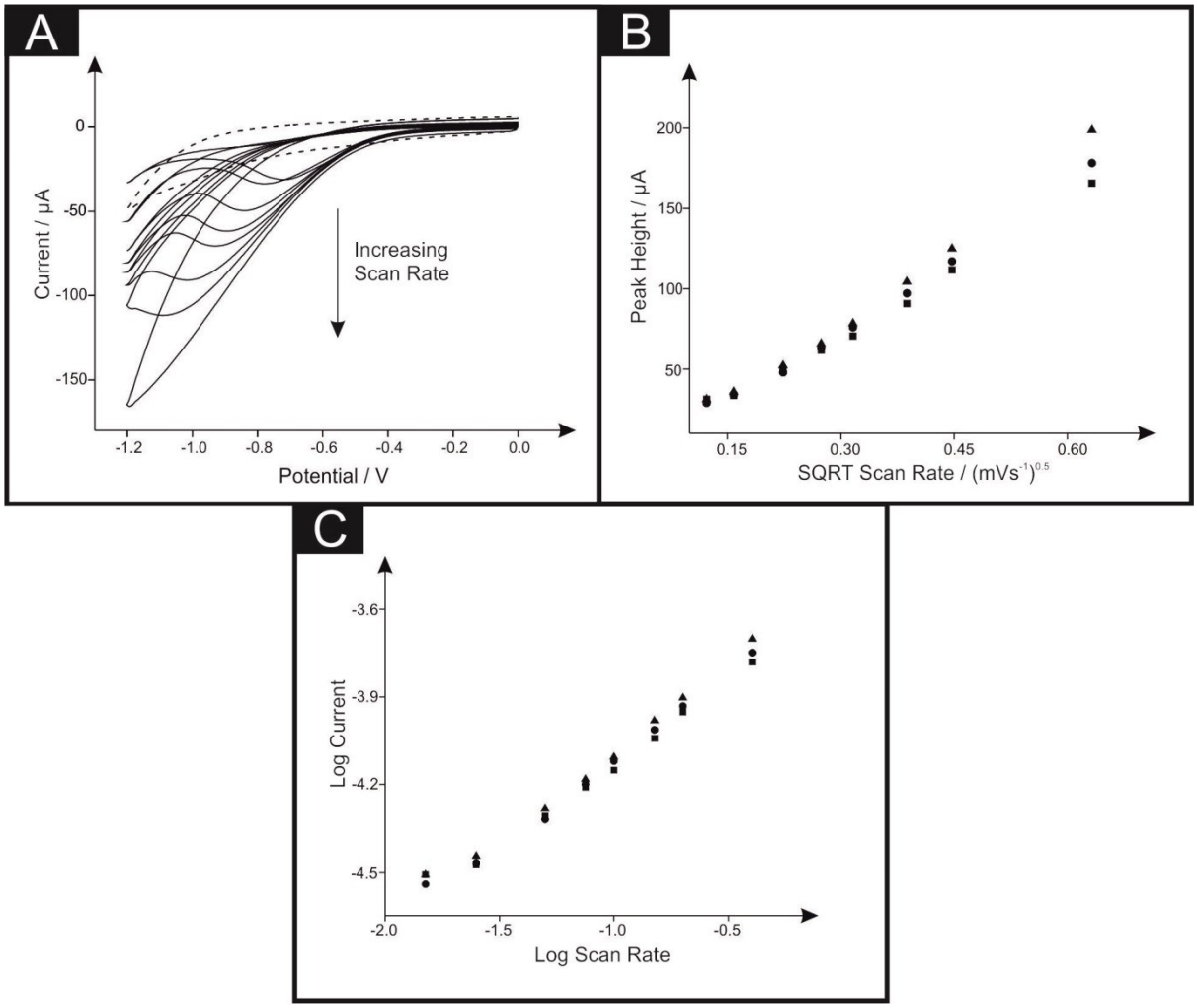

Figure 4.18: Typical cyclic voltammogram (A) recorded in oxygen saturated 0.1 M H_2SO_4 with a 108 ng pristine 2D-hBN modified SPE. The dotted line depicts a deoxygenated unmodified SPE. Also shown are analysis of the peaks presented in Figure 4.18A in the form of 'peak height' vs 'square root scan rate' (B) and 'log peak height' vs. 'log of scan rate' (C). Scan rates: 15, 25, 50, 75, 100, 150, 200 and 400 mV s^{-1} (vs. SCE).

Next explored is the deposition of various masses of pristine 2D-hBN immobilised on SPE, GC, and BDD electrodes and the effect of this is considered towards the ORR. The exploration of different masses/coverages is an overlooked parameter which is not explored in the academic literature. SPEs were modified with pristine 2D-hBN masses ranging from 54 ng to 324 ng and Figure 4.19 illustrates the

voltammetric response obtained. Analysis of these voltammograms is shown in Figure 4.19 inset with a plot of the 'oxygen reduction peak potential' *vs.* the 'mass of immobilised pristine 2D-hBN'. It is observed that an increased mass of pristine 2D-hBN deposited upon SPEs leads to a decrease in the overpotential required for the ORR to occur (a beneficial response), with a linear trend observed: E_p/V = 9.0×10^{-4} mV ng^{-1} –1.072 mV; N = 5; R^2 = 0.976. This was especially prevalent when high masses of pristine 2D-hBN were deposited upon SPEs. The 324 ng pristine 2D-hBN modification upon a SPE resulted in the ORR peak potential shifting from –1.09 V to –0.81 V (*vs*. SCE) at a scan rate of 100 mV s^{-1}, which is a overpotential shift of 0.28 V and indicates a significant reduction in the activation potential for the ORR. This reduction in activation overpotential clearly demonstrates the potential electrocatalytic behaviour of pristine 2D-hBN when using underlying electrode substrates with rough surface morphologies (SPEs).

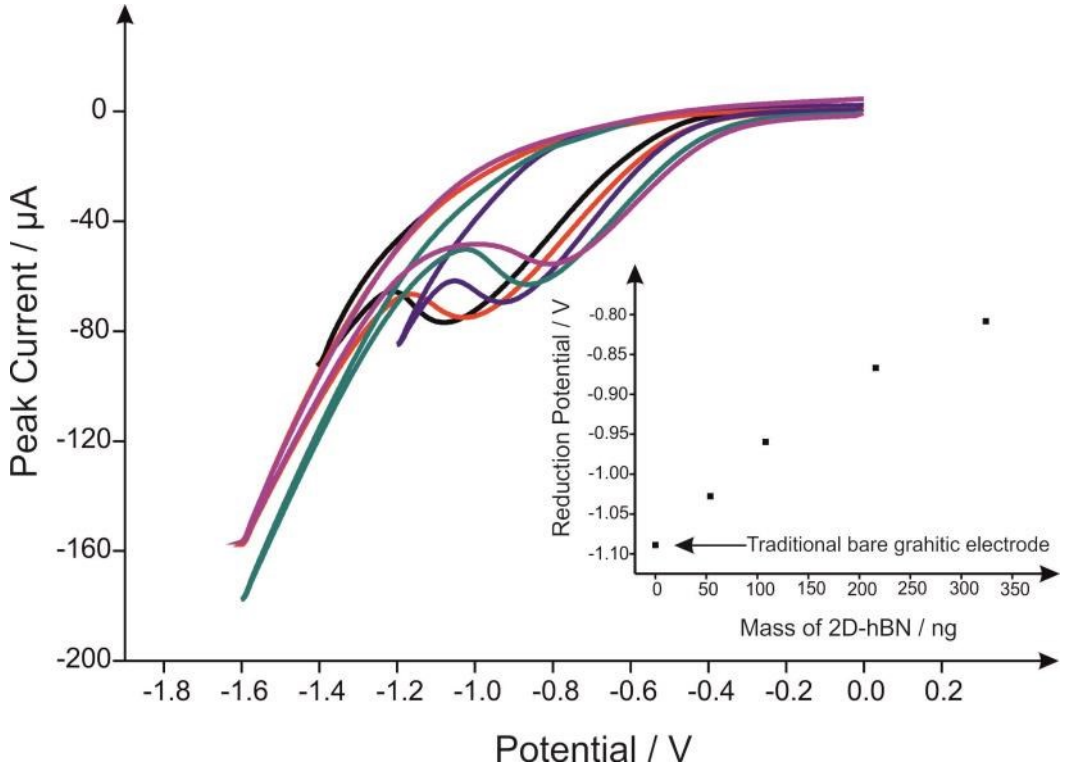

Figure 4.19: Typical cyclic voltammograms recorded in an oxygen saturated 0.1 M H_2SO_4 solution using unmodified (black line), 54 ng (red line), 108 ng (blue line), 216 ng (green line) and 324 ng (pink line) pristine 2D-hBN modified SPEs. Shown in the inset is analysis of cyclic voltammograms obtained in an oxygen saturated 0.1 M H_2SO_4 solution in the form of a plot of oxygen reduction peak potential vs. mass of pristine 2D-hBN electrically wired upon SPEs. Scan rate: 100 mV s^{-1} (vs. SCE).

In contrast, immobilisation of higher masses of pristine 2D-hBN upon a GC electrode leads to a detrimental electrochemical response, with an increasing peak potential for the ORR evident when contrasted to the unmodified electrode. This indicates that a smoother supporting electrode surface does not exhibit a favourable interaction with 2D-hBN. For example, Figure 4.16B illustrates that the deposition of 324 ng pristine 2D-hBN upon a GC electrode increases the overpotential required for the ORR to occur, with a shift from –0.78 V to –1.00 V (*vs*. SCE; scan rate:100 mV s^{-1}), an overall unfavourable increase of 0.22 V. The SEM images in chapter 3, Figure 3.3 and white light profilometry (Figure 4.11) support this inference. Of note,

Figure 4.17B illustrates the 324 ng 2D-hBN modified BDD electrode, resulting in no forthcoming oxygen peak and thus BDD is no longer considered within this work.

Considering the above, the voltammetric curves presented in Figure 4.20 demonstrate that the surface roughness has a significant bearing upon ORR performance when using pristine 2D-hBN as a potential electrocatalyst. A smooth/polished bare SPE gives rise to a voltammetric peak at –0.77 V for the ORR, whereas a rougher, non-polished electrode exhibits a voltammetric potential of –1.16 V under identical conditions. However, in both cases the immobilisation of 324 ng pristine 2D-hBN to the SPE surface results in a significant decrease in activation overpotential, and a decrease in peak current, particularly in the case of the unpolished electrode. Interestingly, in the polished (smooth) case a reduced peak potential of 0.15 V is observed, whereas the unpolished (rough) case reduces the peak potential by 0.24 V. This compliments Figure 3.3 and Figure 4.11, adding evidence to the argument that pristine 2D-hBN interacts more favourably with a rougher electrode surface. This further demonstrates that pristine 2D-hBN is not electrocatalytic for the ORR when immobilised upon a smoother substrate such as GC, which is in agreement with previous literature using gold electrodes and 2D-hBN.[69]

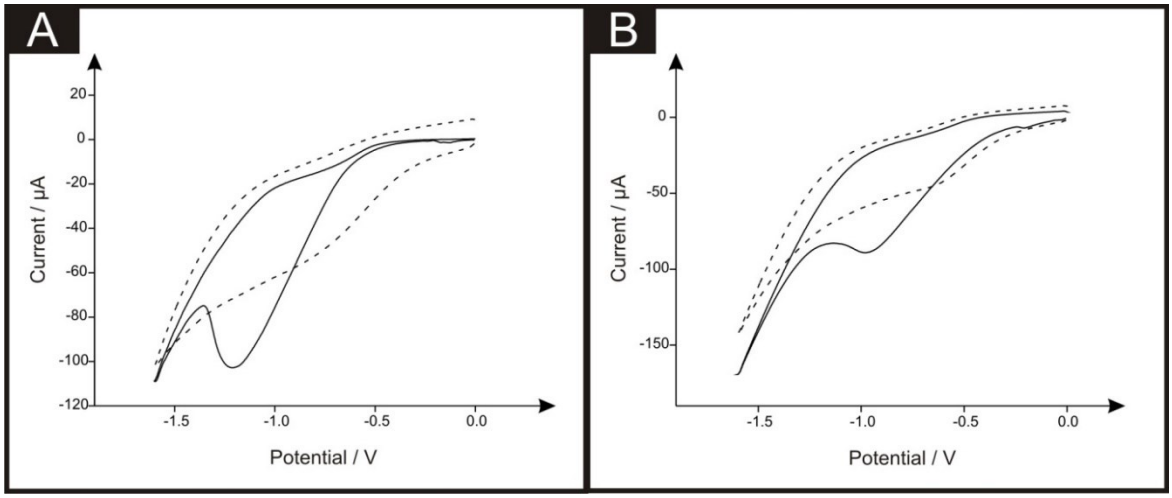

Figure 4.20: Cyclic voltammograms recorded in an oxygen saturated 0.1 M H_2SO_4 solution using unmodified (A) and 324 ng pristine 2D-hBN modified SPEs (B). The 'solid line' depicts an unpolished SPE and the 'dashed line' illustrates the response of a polished SPE. Scan rate: 100 mV s^{-1} (vs. SCE).

The electrocatalytic improvement of SPEs suggests pristine 2D-hBN modified SPEs are comparable to unmodified GC electrodes for the ORR, which proceeds at *ca*. –0.78 V. This represents a valuable and important observation given that SPEs are comparatively more reproducible, cheaper to make and more readily applicable in the field than the alternative bulky GC electrode.

It is clear that the overpotential and performance of the ORR is dependent upon both the mass of pristine 2D-hBN present and the roughness and electrochemical properties of the underlying electrode substrate. In prior literature where pristine 2D-hBN was immobilised upon gold substrates, it is has been demonstrated that the exposed edge regions of 2D-hBN are the active sites at which the ORR occurs.[4] In this case, rough surfaces likely expose more edge regions (and *vice versa* for the smooth surface) and are the expected origin of the apparent electrocatalytic responses observed towards the ORR. Also, note that previous reports suggest the effect of other 2D materials (namely graphene) is dependent upon

the underlying electrode,[48] with this clearly being the cases herein. However, this chapter explores the potential electrocatalytic response of pristine 2D-hBN towards the ORR and it is on this that attention is focused upon.

To gain insights into the electrochemical mechanism, Tafel analysis was performed for unmodified and pristine 2D-hBN modified SPEs, ranging from 108 – 324 ng pristine 2D-hBN. A plot of 'ln current (I)' *vs*. 'E_p' was constructed from analysis of the voltammograms corresponding to the electrochemical reduction of oxygen given by:

$$\frac{\delta \ln I}{\delta E} = \frac{(\alpha n')F}{RT} \qquad (4.1)$$

The slope corresponds to $\delta \ln I / \delta E_p$, α is the electron transfer coefficient, F is the Faraday constant and n' is the number of electrons transferred in the rate determining step, R is the universal gas constant and T is the absolute temperature. The tafel plots corresponding to unmodified, 108, 216 and 324 ng pristine 2D-hBN modified SPEs is shown in Figure 4.21.

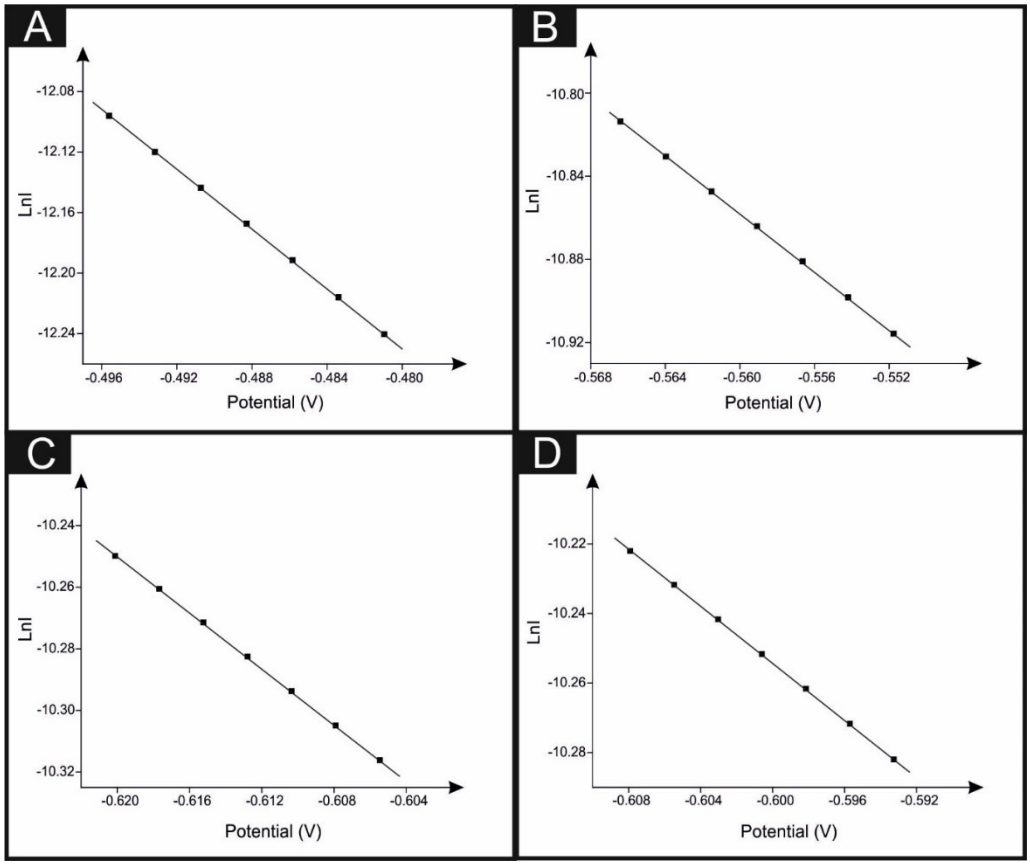

Figure 4.21: Illustrates Tafel plots for unmodified (A), 108 (B), 216 (C) and 324 ng (D) pristine 2D-hBN modified SPEs.

For an unmodified SPE (Figure 4.21A) , the $\alpha n'$ value obtained was 0.25. Within the Tafel region, the Nernstian potential was found to increase by 165.8 mV for every order of magnitude of current. Conversely, for 108, 216 and 324 ng 2D-hBN, $\alpha n'$ values of 0.17, 0.11 and 0.11 were obtained (Figures 4.21B, C and D respectively) with a Nernstian potential increase of 113.47, 75.63 and 69.22 mV per order of magnitude of current respectively. This infers that more current flows using a pristine 2D-hBN modified electrode than at the bare/unmodified SPE. Hence it is proposed that the transfer of the first electron is electrochemically irreversible, so n' = 1 and α values of 0.25 and 0.17, 0.12 and 0.11 are obtained for the unmodified and 108, 216, 324 ng pristine 2D-hBN modified SPEs respectively. The low α values obtained may be due to the high level of irreversibility of the ORR, induced further

by the drop-casting technique of 2D-hBN utilised. The number of electrons transferred overall, *n*, was deduced using the following Randles-Ševćik equation for an irreversible electrochemical process:

$$I_p = -0.496\, n\, (\propto n')^{\frac{1}{2}}\, FA\, [O_2](FvD/RT)^{\frac{1}{2}} \qquad (4.2)$$

where a literature value of 0.9 mM is anticipated for the saturated oxygen solution,[94, 105] and a literature diffusion coefficient value of 2.0×10^{-5} cm^2 s^{-1} is utilised.[106] A value of n = 2.73 for an unmodified SPE was obtained, whereas values of n = 2.45, 2.15 and 1.90 were deduced for 108, 216 and 324 ng pristine 2D-hBN modified SPEs respectively. Unfortunately, these values suggest that the electrochemical reduction of oxygen using unmodified and pristine 2D-hBN modified SPEs produces hydrogen peroxide (H_2O_2) and therefore although the addition of pristine 2D-hBN onto the SPEs improve the electrochemical response, this material cannot be defined as an electrocatalyst in this case. Previous studies by Uosaki *et al* [69] reported that pristine 2D-hBN followed the two electron pathway mechanism and formed H_2O_2 when immobilised upon a gold substrate for the ORR. Confirming this work, where the average number of electrons transferred is two, forming H_2O_2, indicating there is a similar mechanism for the ORR when utilising other 2D materials (graphene).[94]

Hydrogen peroxide (H_2O_2) yields were estimated for representative examples. First, the capacitance of an electrochemical process is estimated utilising: $C = \mathrm{I}/v$, where C is the capacitance, I is the observed peak current at a certain potential and v is the scan rate. Next, the charge is calculated using: $Q = CV$, where Q is the charge and V is the potential. Resultantly, $Q = nFN$ enables the amount of oxygen electrolysed in the reaction to be calculated, where n is the number of

electrons transferred, F is the Faraday constant and N is the number of moles of oxygen electrolysed. There is a 1 : 1 stoichiometric ratio of oxygen produced to H_2O_2, thus the concentration of oxygen electrolysed is theoretically the same as the concentration of H_2O_2 produced in the electrochemical reaction. Therefore, the estimated H_2O_2 yields were calculated for an oxygenated 0.1 M H_2SO_4 solution at a fixed volume of 10 mL utilising unmodified and pristine 2D-hBN modified SPEs of masses ranging from 108 – 324 ng at a scan rate of 100 mV s^{-1}. It was estimated that the concentration of H_2O_2 electrolysed when utilising unmodified SPEs was 2.51 nM, whereas pristine 2D-hBN modified SPEs resulted in 2.78, 3.01 and 3.22 nM of H_2O_2 being produced for 108, 216 and 324 ng pristine 2D-hBN respectively, thus an increase. This agrees with the Tafel analysis and suggests that 2D-hBN modified SPEs follow a similar mechanism to unmodified SPEs towards the ORR (given that the difference in H_2O_2 yields is minimal).

A key factor in terms of the analytical performance of sensors and energy devices is the inherent reproducibility of the response. The reproducibility of the electrode materials of interest was thus explored in acidic conditions with different masses of pristine 2D-hBN deposited on the SPEs. A % Relative Standard Deviation (% RSD) in the analytical signal of 9.40 % was observed for the unmodified SPE (N = 3) at a scan rate of 100 mV s^{-1}. This level of reproducibility is common for printed substrates and is a drawback for SPEs as reproducibility is slightly compromised for mass production. The 54, 108, 216, and 324 ng pristine 2D-hBN modified SPE (N = 3; 100 mV s^{-1}) gave % RSD values in the analytical signal of 1.81, 8.96, 3.45, and 12.59%, respectively. The low % RSD measurements, at lower masses, obtained for the modified electrodes highlight the reproducibility of the drop-casting method at lower masses for pristine 2D-hBN upon SPEs.

Comparison to the Literature

Table 4.2 overviews current literature reports concerning the effect of 2D nanomaterials towards the ORR when supported upon different graphitic substrates. Randviir *et al*.[94] found that 20 ng modified pristine graphene immobilised upon substrates such as EPPG and the basal plane of HOPG (BPPG) resulted in an increased activation overpotential for the ORR under acidic conditions. In the case of the EPPG electrode, the ORR activation overpotential shifts from –575 mV (unmodified) to –1015 mV (20 ng pristine graphene modified), whereas the BPPG shifts from –950 mV (unmodified) to –1080 mV(20 ng pristine graphene modified). However, Qazzazie *et al*.[107] found nitrogen doped graphene (GN) modified GC electrodes resulted in a decrease in activation overpotential for the ORR in alkali conditions. The overpotential at which the ORR occurs shifts from –250 mV to –160 mV upon GN modification.[107] Other 2D materials such as MoS_2 have been utilised for the ORR. Zhao *et al.* [60] have demonstrated that MoS_2 modified GC electrodes result in the ORR occurring at –420 mV in alkaline conditions. GN modified GC electrodes resulted in the ORR occurring at –310 mV.[60] The lowest overpotential for the ORR to occur was observed when utilising MoS_2 and GN combined, resulting in an activation overpotential of –230 mV.[60] In this chapter, pristine 2D-hBN immobilised upon SPEs reduces the overpotential required for the ORR to occur from -1090 mV to -810 mV, thus a greater improvement is observed in this system when contrasted/compared to those reported in the literature (that are summarised in Table 1). However, this chapter finds that pristine 2D-hBN deposition upon GC electrodes increases the ORR activation overpotential from –780 mV to –1000 mV and thus it is important to consider the effect and influence of different underlying

support substrates. Note, the literature imp tented is utilised due to its similarity with the work within thesis when modifying the underlying substrate with the 2D materials of interest.

2D material	Underlying substrate / support material	Substrate ORR potential	2D modified substrate ORR potential	Further comments	Ref.
Pristine Graphene (monolayer platelets suspended in ethanol)	EPPG	-575 mV	-1015 mV upon 20 ng addition	Cyclic Voltammetry, scan rate 100 mV s^{-1} O_2 saturated 0.1 M H_2SO_4	94
Pristine Graphene (monolayer platelets suspended in ethanol)	BPPG	-950 mV	-1080 mV upon 20 ng addition	Cyclic Voltammetry, scan rate 100 mV s^{-1} O_2 saturated 0.1 M H_2SO_4	94
Quasi-Graphene	EPPG	-575 mV	-535 mV	Cyclic Voltammetry, scan rate 100 mV s^{-1} O_2 saturated 0.1 M H_2SO_4	94
Quasi-Graphene	BPPG	-950 mV	-910 mV	Cyclic Voltammetry , scan rate 100 mV s^{-1} O_2 saturated 0.1 M H_2SO_4	94
Thermally reduced Graphene Oxide (TRGO)	GC	-250 mV	-175 mV	Cyclic Voltammetry, O_2 saturated 0.1 M KOH rotating disc 1600 rpm	107
Nitrogen doped Graphene (GN)	GC	-250 mV	-160 mv	Cyclic Voltammetry , O_2 saturated 0.1 M KOH rotating disc 1600 rpm	107
MoS_2	GC	Not available	-420 mV	Cyclic Voltammetry O_2 saturated 0.1 M KOH	60

MoS_2 / Nitrogen doped Graphene (GN)	GC	Not available	-230 mV	Cyclic Voltammetry O_2 saturated 0.1M KOH	[60]
Nitrogen doped graphene (GN)	GC	Not available	-310 mV	Cyclic Voltammetry O_2 saturated 0.1M KOH	[60]
Hexagonal boron nitride (2D-hBN)	GC	-780 mV	-1000 mV upon 324 ng 2D-hBN addition	Cyclic Voltammetry, scan rate 100 mV s^{-1} O_2 saturated 0.1 M H_2SO_4	This work
Hexagonal boron nitride (2D-hBN)	SPE	-1090 mV	-810 mV upon 324 ng 2D-hBN addition	Cyclic Voltammetry, scan rate 100 mV s^{-1} O_2 saturated 0.1 M H_2SO_4	This work

Table 4.2: Comparison of 2D nanomaterials that have been utilised for the ORR.

The Oxygen Reduction Reaction - Metallic Electrodes; Comparison to the Literature

The effect of pristine 2D-hBN towards the ORR was next considered utilising gold and platinum supporting electrodes. Unmodified gold and platinum electrodes were first investigated towards the ORR in acidic conditions, where in Figure 4.22A it is evident that the overpotential required for the ORR to occur using an unmodified gold electrode is –0.35 V (at a scan rate of 100 mV s^{-1}). This differs greatly compared to GC electrodes and SPEs, which exhibit ORR overpotentials of –0.78 V and –1.09 V, respectively.

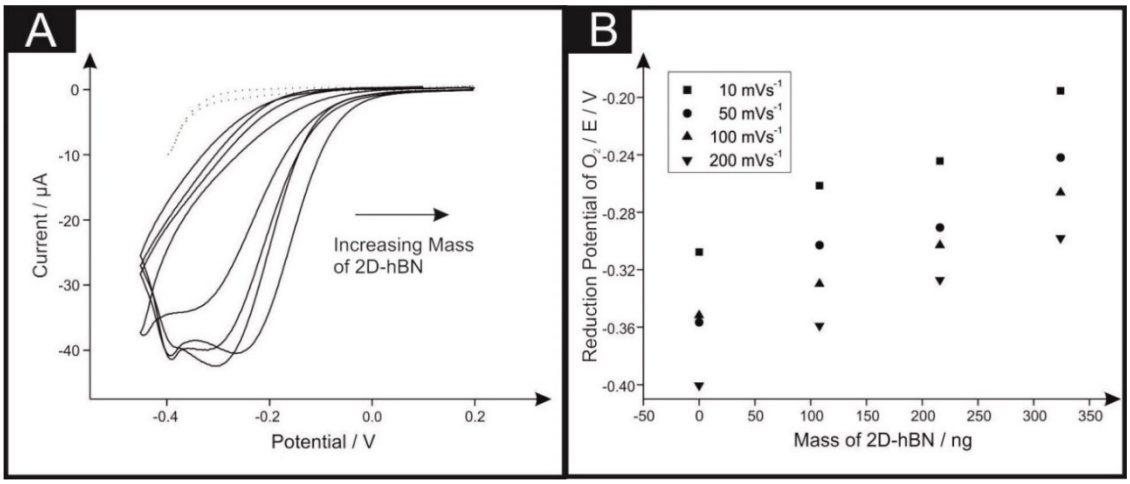

Figure 4.22: Typical cyclic voltammograms (A) recorded in in oxygen saturated 0.1 M H_2SO_4 for an unmodified and a 108, 216 and 324 ng pristine 2D-hBN modified gold electrode. The dotted line represents a deoxygenated unmodified gold electrode. Scan rate: 100 mV s^{-1} (vs. SCE). Also shown are the analysis of the voltammograms at different scan rates in the form of oxygen reduction potential vs mass of pristine 2D-hBN deposited upon a gold electrode (B). Scan rates: 10, 50, 100 and 200 mV s^{-1} (vs. SCE).

Comparatively, Figure 4.23A shows that the activation overpotential required for the ORR to occur utilising an unmodified Pt electrode is 0.02 V, at a scan rate of 100 mV s^{-1}. This greatly differs to gold, GC and SPEs. Thus, platinum is the optimum unmodified electrode material for the ORR in comparison to the other electrodes described within this chapter.

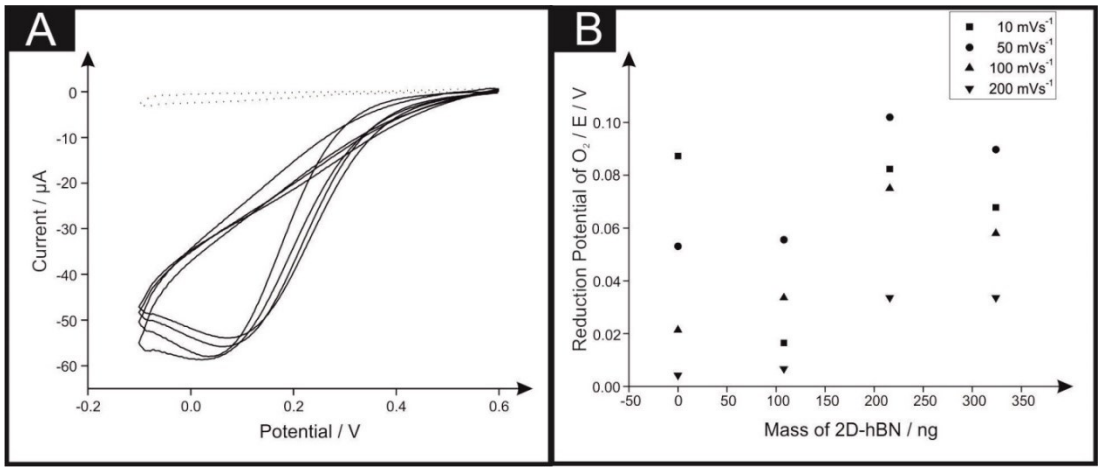

Figure 4.23: Typical cyclic voltammograms (A) recorded in in oxygen saturated 0.1 M H_2SO_4 for unmodified and a 108, 216 and 324 ng pristine 2D-hBN modified platinum electrode. The dotted line represents a deoxygenated unmodified (bare) platinum electrode. Scan rate: 100 mV s^{-1} (vs. SCE). Also shown are the analysis of the voltammograms at different scan rates in the form of oxygen reduction potential vs. mass of pristine 2D-hBN deposited upon a platinum electrode (B). Scan rates: 10 mV s^{-1}, 50 mV s^{-1} 100 mV s^{-1} and 200 mV s^{-1} (vs. SCE).

Attention was turned towards the deposition of various masses of pristine 2D-hBN upon gold and Pt electrodes and its effects upon the ORR. Figure 4.22A depicts cyclic voltammograms of pristine 2D-hBN modified gold electrodes at a scan rate of 100 mV s^{-1}. Upon the 108 ng pristine 2D-hBN modification of the gold macroelectrode the peak potential shifts from –0.35 V to –0.32 V. Thus, a small

overpotential reduction towards the ORR of 0.03 V. Comparably, the 108 ng 2D-hBN modified Pt electrodes displayed an increase in the activation overpotential for the ORR of 0.01 V, as seen in Figure 4.23A. These results suggest that metallic electrode substrates interact with pristine 2D-hBN in a different way to that of graphitic electrodes. The hexagonal orientation of carbon materials may be conducive towards catalytic effects if the pristine 2D-hBN orients itself upon edge planes or rough edges and defects, whereas basal planes may not electrically wire the pristine 2D-hBN to the electrode properly and create an insulating effect. The addition of pristine 2D-hBN has little or no effect upon the activation overpotential of the ORR for both metallic substrates (at this coverage), inferring that the metallic response dominates the electrochemistry in both cases.

The effect of pristine 2D-hBN coverage is next explored to further investigate the effects of pristine 2D-hBN upon gold and Pt electrodes for the ORR. Figure 4.22B exhibits a plot of oxygen reduction overpotential *vs.* mass deposited, where it is observed that as the mass of pristine 2D-hBN deposited upon the gold electrode increases, the overpotential required for the ORR to occur reduces, with a linear trend observed, inferring that pristine 2D-hBN makes the electrode processes more favourable from a thermodynamic point of view. A gold electrode with a 324 ng pristine 2D-hBN modification displayed overpotential reduction from –0.35 V to –0.27 V (*vs*. SCE) for the ORR, demonstrating the electrocatalytic ability of pristine 2D-hBN and this is in good agreement with previous reports.[69] Comparatively using Pt electrodes, it is observed that as the mass of pristine 2D-hBN deposited upon the platinum electrode increases, the overpotential required for the ORR increases (Figure 4.23B), which is in agreement to previous reports.[99] A platinum electrode with a 324 ng pristine 2D-hBN modification displays a potential shift from 0.02 V to

0.05 V (*vs*. SCE) for the ORR. This is a small increase in the potential required for the ORR to occur, whereas under the same conditions pristine 2D-hBN modification upon a gold electrode reduced the ORR activation potential by 0.08 V. These changes are not thought to be statistically significant, especially considering that the large pristine 2D-hBN modification exhibited a % RSD of over 12 %.

4.4 Conclusions

This chapter has demonstrated, for the first time, that pristine 2D-hBN exhibits an improved electrochemical response towards the ORR when immobilised / electrically wired upon graphitic substrates. A reduction in the ORR potential of 280 mV has been demonstrated in the best case using SPEs. Pristine 2D-hBN's beneficial electrochemistry was shown to be highly dependent upon both the underlying support substrate and the mass/coverage utilised. Given that the electrochemical response/performance of pristine 2D-hBN is significantly influenced by the former two considerations, it is important that future research incorporating this novel nanomaterial implements control measures to ascertain pristine 2D-hBN's dependence on mass/coverage and the underlying substrate before claiming "beneficial electrocatalysis" in other pertinent systems. For example, if a researcher has picked a smooth electrode only, such as a GC, it would appear that pristine 2D-hBN is *NOT* beneficial - *a false result.* In this chapter it has been demonstrated that only rough electrode surfaces give rise to beneficial/improved ORR responses, since this likely makes the morphology of pristine 2D-hBN upon electrode surfaces such that edge regions/sites are predominantly exposed which are the active sites[4] for the ORR.

Furthermore, Tafel analysis has been performed showing, for the first time, that when pristine 2D-hBN is supported upon graphitic substrates it undergoes a 2-electron transfer process/pathway (range: 1.90 – 2.45) towards the ORR, producing predominately hydrogen peroxide. Unfortunately, due to the pathway of pristine 2D-hBN, this material cannot be defined as an electrocatalyst towards the ORR for use in fuel cells. Although the pristine 2D-hBN is not as active as platinum towards the ORR, this work demonstrates that pristine 2D-hBN does have potential as an electrode material, which has never before considered as a catalyst *per se*. It is noted that researchers will deliberately dope carbon nanotubes with (separately) Boron and Nitrogen atoms; pristine 2D-hBN offers a readily available "doped" material and as shown in this work, can provide electrochemically useful responses. This work indicates the potential for pristine 2D-hBN to be utilised as a beneficial and novel electrode material towards a range of applications.

Chapter 5 : Pristine 2D Hexagonal Boron Nitride (2D-hBN) Explored for the Electrochemical Sensing of Dopamine

Continuing with observations and conclusions from chapter 4, where pristine 2D-hBN was explored towards the ORR, a biological approach is now taken where pristine 2D-hBN nanosheets are explored as a potential electrocatalyst towards the electroanalytical sensing of dopamine (DA) and common interferents ascorbic acid (AA) and uric acid (UA). Pristine 2D-hBN nanosheets are electrically wired *via* a drop-casting modification process onto a range of commercially available carbon supporting electrodes, including glassy carbon (GC), boron-doped diamond (BDD) and screen-printed graphitic electrodes (SPEs). Pristine 2D-hBN has not previously been explored towards the electrochemical detection / electrochemical sensing of DA, AA and UA. The potential electrocatalytic performance of 2D-hBN modified electrodes is critically evaluated along with the effect of supporting carbon electrode platforms and the effect of 'mass coverage' (which is commonly neglected in the 2D material literature) towards the detection of DA, AA and UA. This chapter contains work that has been peer-reviewed and published in the academic literature.[2]

5.1 Introduction

Dopamine (DA) is a catecholamine that plays a vital role in the functioning of numerous biological systems.[108-111] Studies suggest abnormal levels of DA can lead to neurological disorders such as Parkinson's disease and Schizophrenia.[108, 112] There have been numerous efforts directed towards the electrochemical detection of

[2] A. F. Khan, D. A. C. Brownson, E. P. Randviir, G. C. Smith and C. E. Banks, *Anal. Chem.*, 2016, **88**, 9729-9737.

DA.[113-115] However, DA tends to co-exist alongside ascorbic acid (AA), which leads to overlapping voltammetric signals, giving rise to limitations when detecting these compounds.[116] Resultantly, current research is focused on improving the analytical sensitivity and selectivity for these two important compounds.[117, 118]

Research using gold (Au), platinum (Pt) and glassy carbon (GC) electrodes does not allow the sufficient differentiation between the anodic oxidation peak potentials of DA and AA.[119] Furthermore, due to the oxidised species of DA and AA residing on the electrode surface, these electrodes are prone to fouling, leading to reduced sensitivity, inhibited linear ranges, and inadequate electroanalytical capabilities.[119] As such, an electrode material that improves the electrochemical detection capabilities of DA is highly sought, particularly whilst resisting both chemical and electrochemical surface fouling,[120] and in the case of applied sensors, where AA and uric acid (UA) are commonly found to co-exist within sample matrixes.[121] The structures of said compounds (DA, AA and UA) are shown in Figure 5.1

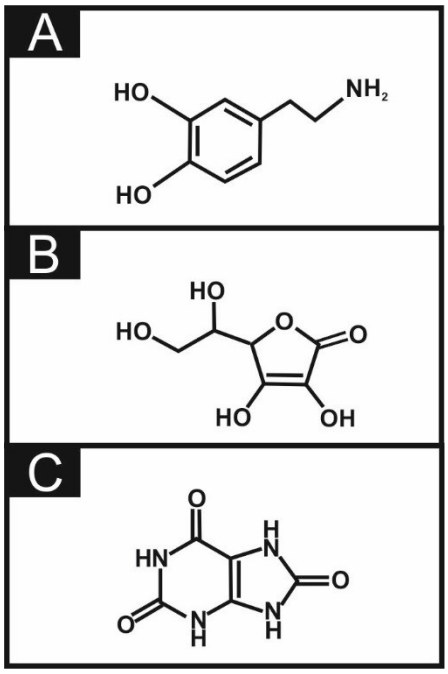

Figure 5.1: Structures of DA (A), AA (B) and UA (C) are shown.[122-124]

In previous research, Deng *et al*.[119] showed that AA and DA activation potentials could be distinguished through manipulation of GC electrodes using boron–doped carbon nanotubes (BCNTs), resulting in an anodic peak separation for AA and DA of *ca*. 238 mV. This was highly beneficial in comparison to a 'regular' carbon nanotube (CNT) modified GC electrode, that exhibited a peak separation of *ca*. 122 mV.[119] This enhanced response with BCNTs was attributed to the edge plane sites of the CNTs and a change in electronic structure, with boron-doping improving the electron transfer kinetics of the CNTs.[33, 119, 125] Similarly, Medeiros *et al*.[116] conducted studies towards the simultaneous detection of DA and AA utilising carbon nitride electrodes (CN_x) and observed an anodic peak separation of *ca*. 330 mV, attributed to the anodic pre-treatment (APT) of the CN_x in an alkaline medium.[116] Furthermore, Wang *et al*.[126] reported highly sensitive methods for the detection of DA, using Nafion/carbon nanotube coated poly(3-nethylthiophene) modified

electrodes.[126] Such methods require extensive sample pre-treatment and use complex electrode composites, but are promising nevertheless. An overview of the different materials utilised in the simultaneous detection of DA, AA and UA can be found in Table 5.1, which compares the electrochemical detection methods similar to that utilised within this thesis. It is noted nanomolar detection of DA, AA and UA is applicable *via* electrochemical impedance spectroscopy and amperometry techniques[127-129]

Electrode Material	Electrocatalytic (with regards to)	Dopamine LOD (μM)	Explored in the presence of:	Electrochemical method	Ref.
Nitrogen doped graphene	GC	0.25	UA, AA	DPV	130
Chitosan–graphene	GC	1.00	UA, AA	DPV	131
Carbon Ionic Liquid Electrode	CPE	1.00	UA, AA	DPV	132
AuNPs@MoS_2	GC	0.05	UA, AA	DPV	133
Pt–Au hybrid	GC	24.0	UA, AA	DPV	134
Poly(Evans blue)	GC	0.25	UA, AA	DPV	135
AuNPs–β-CD–Graphene	GC	0.15	UA, AA	SWV	136
Ordered mesoporous carbon / Nafion composite film	GC	0.50	UA, AA	DPV	137
Functionalised graphene	Bare graphite	0.25	UA, AA	DPV	138

Pristine 2D-hBN	SPE	0.65	UA, AA*	DPV	This Work

Table 5.1: A comparison of various electrode materials utilised towards the detection of DA in the presence of UA and AA. ***Key:*** *AuNP@MoS_2, Gold nanoparticle modified molybdenum disulfide; AuNPs–β-CD–Graphene, Gold nanoparticles–β-cyclodextrin–graphene; 2D-hBN, 2D hexagonal boron nitride; GC, Glassy carbon electrode; CPE, Carbon paste electrode; functionalised graphene synthesised by solvothermal reduction of colloidal dispersions of graphite oxide; UA, Uric Acid; AA, Ascorbic Acid DPV, Differential Pulse Voltammetry; SWV, Square Wave Voltammetry.*

** DA and AA signal de-convolution is not possible upon simultaneous detection.*

Numerous newly-emerged 2D nanomaterials have been considered for the detection of DA in recent years, such as graphene,[32, 115, 139] molybdenum disulphide (MoS_2),[133] and MoS_2 decorated with gold nanoparticles.[133] However, a lesser researched nanomaterial is crystalline hexagonal boron nitride (2D-hBN). Crystalline 2D-hBN is a 2D material comprising equal quantities of boron and nitrogen atoms arranged in a hexagonal structure; similar to graphene, hence it is referred to as 'white graphene'.[56] 2D-hBN contains strong σ bonds and weak van der Waals forces,[60] resulting in a nanomaterial that displays high thermal conductivity, is mechanically strong, and yet lubricating.[61] 2D-hBN has been utilised as an electrocatalyst in applications such as the oxygen reduction reaction (ORR),[140] and in solar energy conversion by photo-redox catalysis.[141] This reported electrocatalytic performance might prove beneficial for separating the voltammetric signals of DA, AA and UA; such an application has not previously been considered for this novel 2D material.

In this chapter, for the first time, pristine 2D-hBN is explored as a potential electrocatalyst towards the detection of DA when immobilised upon a range of commercially available graphitic electrodes/substrates whilst producing multiple mass-related coverage studies (commonly overlooked in the literature). This work then considers pristine 2D-hBN modified graphitic substrates towards the improved simultaneous detection of DA, AA and UA .Pristine 2D-hBN has not previously been reported as a beneficial electrocatalytic material when immobilised upon carbon or any other platforms applied towards the electrochemical detection of DA (and in the presence of AA and UA). This research provides new insights into the exploration of pristine 2D-hBN's electrochemical properties, performance and applicability.

5.2 Results and Discussion

Dopamine Electrochemistry

The electron transfer reactions between pristine 2D-hBN and DA were first studied using unmodified SPEs, GC and BDD electrodes in order to benchmark the system. Figure 5.2 depicts the respective cyclic voltammograms obtained towards the oxidation of 1 mM DA in a pH 7.4 phosphate buffer solution PBS (commonly utilised within the literature.)[142] It is also noted DA detection is possible at different ranges of pH.[143] The anodic oxidation potential utilising SPEs is obtained at +0.37 V, corresponding to the electrochemical oxidation of DA, which agrees well with previous literature.[75] Comparatively, the GC electrode exhibits an observed peak at +0.31 V, and the BDD electrode at +0.45 V, with both in agreement with previous studies.[144, 145] These findings indicate that the GC electrode exhibits the lowest (most beneficial) potential required for the electrochemical oxidation of DA. However, the SPEs exhibits a greater peak current, offering a more favourable peak for electroanalytical application and thus potentially higher sensitivity at lower concentrations. The BDD electrode exhibits the highest potential and lowest peak current towards the detection of DA, as one would expect due to the chemical nature and reactivity of the BDD electrode.[33, 146, 147] It is noted upon carrying out the oxidation of DA, the solution often changes colour from colourless to black, which may indicate polymerisation.

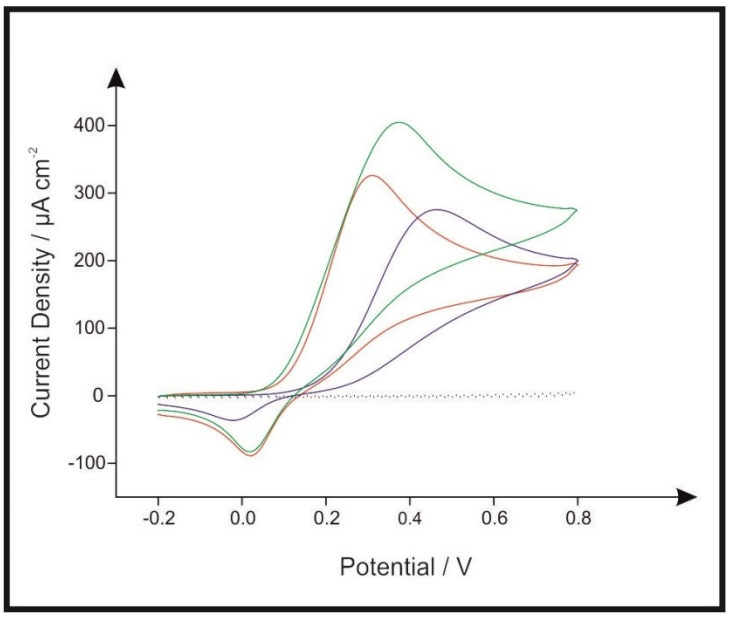

Figure 5.2: Typical cyclic voltammograms recorded in a 1 mM DA solution (PBS, pH 7.4) utilising a bare/unmodified SPE (green), GC (red) and BDD (blue) electrode. The dashed line depicts respective pH 7.4 PBS blanks. Scan rate: 100 mV s^{-1} (vs. SCE).

The electrochemical oxidation of DA was next considered using electrodes modified with increasing pristine 2D-hBN masses (a coverage study), ranging from 108 to 324 ng. Figure 5.3A depicts typical cyclic voltammograms towards DA detection using pristine 2D-hBN modified SPEs, where it is evident that increasing pristine 2D-hBN additions upon the SPE's surface beneficially lowers the potential required to electrochemically oxidise DA (a catalytic response). The observed peak currents also increase, however, this occurs until a mass of 324 ng pristine 2D-hBN is reached and thus is mass/coverage dependent. Analysis of these voltammograms is presented in Figure 5.3C, where overall, a decrease in oxidation potential required for DA is observed of up to 90 mV (compared to the bare electrode) upon modification of a SPE with 324 ng pristine 2D-hBN; suggesting that pristine 2D-hBN exhibits electrocatalytic activity towards DA. Previous studies using 2D nanomaterials (such as graphene modified EPPG and BPPG electrodes) towards DA

detection have shown the activation potential increases, indicating not such a beneficial response, contrary to what is observe herein.[48, 148, 149]

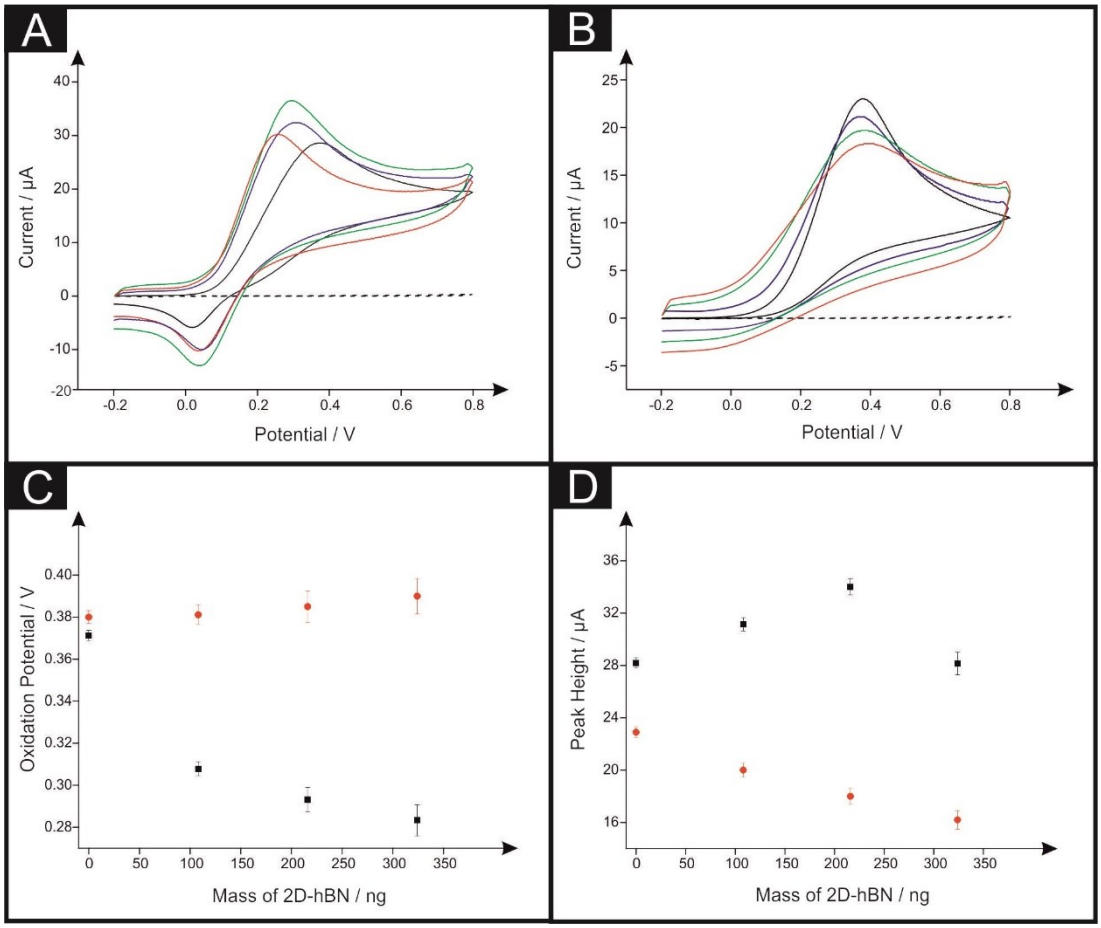

*Figure 5.3: Typical cyclic voltammograms recorded in (A) 1 mM DA and (B) 1 mM ascorbic acid, pH 7.4 PBS with unmodified SPEs (black) and pristine 2D-hBN modified electrodes. Masses of modification as follows: 108 (blue), 216 (green) and 324 ng (red) immobilised. The dashed line represents the PBS blank respectively. Analysis of the cyclic voltammograms is presented in the form of plot (C) illustrating oxidation potential of DA (black square) and AA (red circle) vs. mass of pristine 2D-hBN immobilised and plot (D) depicting peak current of DA (black square) and AA (red circle) vs. mass of pristine 2D-hBN immobilised. Scan rate: 100 mV s^{-1} (vs. SCE). Each data point (C and D) is the average and standard deviation (*N = 3*).*

Figure 5.3D depicts the effect of pristine 2D-hBN deposition upon a SPE when considering the peak current/height observed for DA. An increase in the peak current is observed in contrast to the unmodified SPE, with an overall increase of from 28.2 to 34.0 μA evident when immobilising 216 ng of 2D-hBN. However, upon the highest deposition of 324 ng of pristine 2D-hBN, a decreased peak current is observed (to 28.1 μA); one reported explanation for this response is that a 'critical mass' of modification is achieved and surpassed whereby the pristine 2D-hBN nanosheets can no longer support themselves upon the electrode surface and delaminate/detach when utilised.[150, 151] However, given that the potential continues to decrease (thus a continued electrocatalytic response), this may not be the case herein and this response is considered in more detail later.

Next considered is the electrochemical implications of modifying pristine 2D-hBN onto smooth underlying electrode surfaces. In contrast to pristine 2D-hBN modified SPEs, the effect of pristine 2D-hBN deposition upon GC and BDD electrodes towards the oxidation of DA was found to differ significantly. Figure 5.4A depicts cyclic voltammograms for unmodified and pristine 2D-hBN modified GC electrodes towards DA oxidation. It is evident that the activation potential required for DA increases and that the anodic peak current decreases upon pristine 2D-hBN additions onto the GC electrode. This is displayed quantitatively in Figure 5.4B, where it can be observed that immobilisation of 108 ng pristine 2D-hBN upon the GC electrode shifts the DA oxidation activation potential from +0.31 V (unmodified GC) to +0.34 V. 216 ng pristine 2D-hBN modification results in a further increase in DA activation potential to +0.38 V and the highest modification of 324 ng pristine 2D-hBN gives rise to the greatest potential of +0.39 V. Therefore,

in contrast to pristine 2D-hBN modified SPEs, which give rise to a beneficial response and decreased the DA activation/potential by up to 90 mV. Conversely, pristine 2D-hBN modified GC electrodes increase the activation/potential by 80 mV. It is evident that the electrocatalytic effect of pristine 2D-hBN is dependent upon the underlying support substrate (as discussed previously in chapter 4). In this case SPEs have a rough surface and it is suggested that pristine 2D-hBN preferentially binds to the ridges of the SPE (see chapter 3, Figure 3.3), while pristine 2D-hBN binding less successfully to a smoother polished surface of the SPE, which is like that of the GC electrode in this case. Previous studies have investigated the use of 2D materials to improve the activation potential of DA when utilising GC electrodes. Sun *et al*.[133] utilised the 2D material MoS_2 decorated with gold nanoparticles modified upon a GC electrode, and found DA, AA and UA could be differentiated. In particular, the DA and AA oxidation peaks were separated by 151 mV.[133] Evidently, MoS_2 decorated with gold nanoparticles displayed an electrocatalytic effect in the oxidation of DA and AA; however, pristine 2D-hBN does not display this effect when immobilised upon a GC electrode, it does however when immobilised upon a SPE.

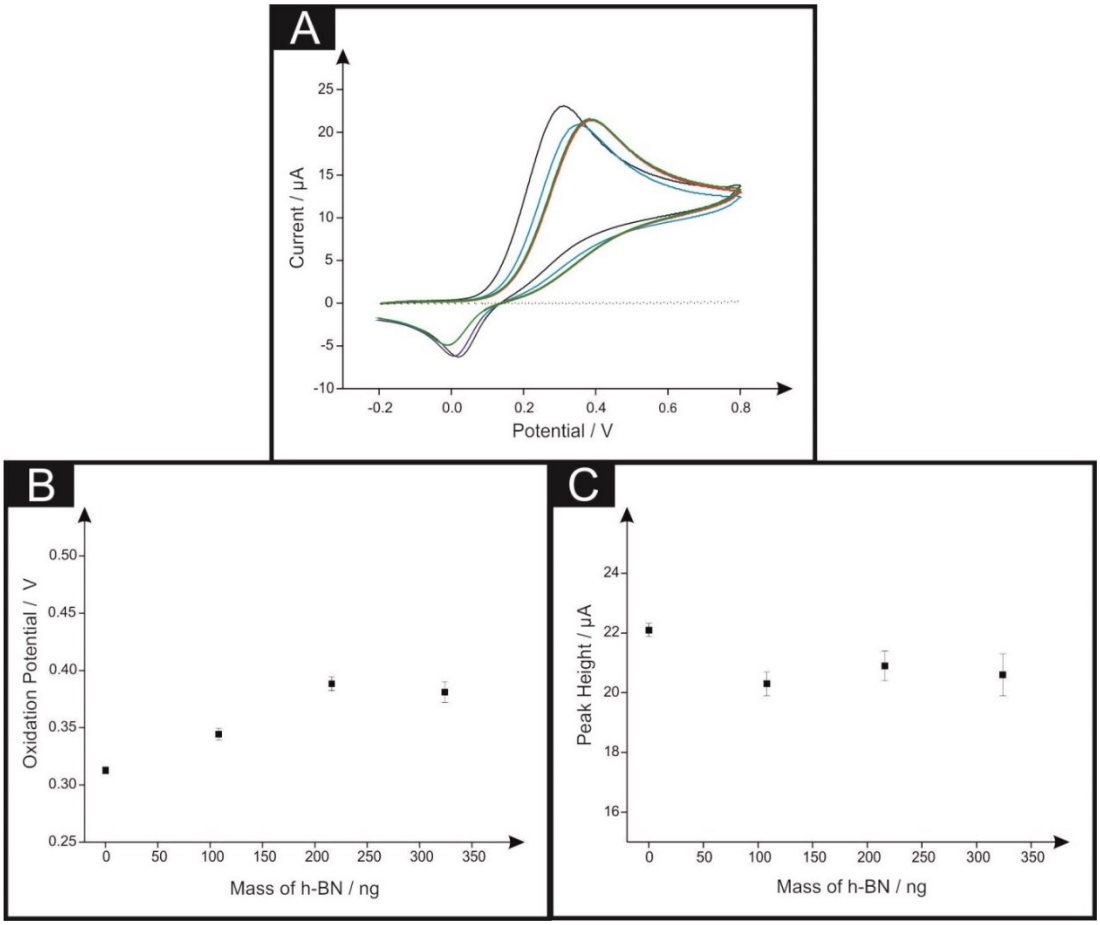

*Figure 5.4: Typical cyclic voltammograms (A) recorded in 1 mM DA (PBS pH 7.4) using an unmodified GC electrode (black) and a GC electrode following modification with various pristine 2D-hBN masses of 108 (blue), 216 (green) and 324 ng (red). The dashed line depicts the PBS blank for the GC electrode. Analysis of cyclic voltammograms for the unmodified and pristine 2D-hBN modified GC electrode is presented in the form of plot (B) illustrating DA oxidation potential vs. mass of pristine 2D-hBN deposited, and plot (C) depicting peak current vs. mass of pristine 2D-hBN immobilised upon a GC electrode. Scan rate: 100 mV s^{-1} (vs. SCE). Each data point (B and C) is the average and standard deviation (*N = *3).*

Next, pristine 2D-hBN modified BDD electrodes were utilised to observe if any change in peak potential or current was possible for the electrochemical oxidation of DA. Figure 5.5A depicts cyclic voltammograms obtained for unmodified and pristine 2D-hBN modified BDD electrodes. Upon pristine 2D-hBN

modification of the BDD electrode, the activation potential for DA increases. Analysis is depicted in Figure 5.5B, where it can be seen that immobilisation of pristine 2D-hBN (108 ng) upon the BDD electrode shifts the DA oxidation potential from +0.44 V (unmodified BDD) to +0.50 V; to +0.55 V for 216 ng and to +0.54 V for the 324 ng pristine 2D-hBN modified BDD electrode. Hence, it is observed that pristine 2D-hBN is not electrocatalytic towards the electrochemical oxidation of DA when supported upon a BDD electrode. Figure 5.5C illustrates the effect of pristine 2D-hBN modified BDD electrodes towards DA peak current. Again (as with the case for the GC electrode), the peak current decreases from 19.4 (unmodified BDD) to 18.7 μA upon the addition of 108 ng of 2D-hBN, to 19.2 μA with 216 ng and to 18.9 μA upon 324 ng pristine 2D-hBN modification of the BDD electrode.

In both cases (GC and BDD), pristine 2D-hBN increases the oxidation potential required for the detection of DA and lowers the observed peak currents. It is inferred that the observed 'potential' electrocatalytic effect of pristine 2D-hBN is dependent on the underlying support surface, and more specifically surface roughness. Evidently, pristine 2D-hBN modified SPEs (with rough surface morphologies) exhibit an electrocatalytic effect towards DA oxidation in comparison to unmodified SPEs. In contrast, modifications of pristine 2D-hBN upon smooth electrodes (GC and BDD) exhibit an increased (detrimental) potential for DA oxidation and decreased peak currents. This indicates that a smoother supporting electrode surface does not exhibit the same favourable interaction with pristine 2D-hBN as noted above (for the SPE), resulting in poor electrochemical performance (a phenomena observed in chapter 4). This likely originates as a result of pristine 2D-hBN detaching from the polished GC/BDD electrode surface given the unfavourable interaction, reducing the sensitivity of DA detection. Whatever the cause of this

observation, the phenomena is highly fascinating and will likely require further in-depth study that is outside the scope of this thesis.

To offer some insight into the above phenomena, SEM images were obtained to assess how the pristine 2D-hBN platelets prefer to reside upon smooth and rough SPE surfaces. Chapter 3, Figures 3.3A and 3.3B depict the surface morphology of unpolished and polished SPEs. It is evident that the polishing process produces a smoother electrode surface *via* reducing the number of contours and ridges present,[152] with a decrease in the quantity of the small binder particles covering the surface (used in the fabrication procedure to adhere the graphite-ink/paste together). Figures 3.3C–F show how changes in the SPE's morphology alters how pristine 2D-hBN rests upon the surface. In Figure 3.3C, the pristine 2D-hBN platelets are visible and appear as discs that collect preferentially around contours and ridges on the rough SPE surface. Conversely, Figure 3.3D shows the platelets on a smooth surface collect in similar areas, but also indicates large areas of underlying substrate where the platelets have not rested (in this case the surface is apparently not favourable to pristine 2D-hBN interaction). With Figures 3.3E and 3.3F highlighting this phenomenon further, it appears that pristine 2D-hBN prefers to reside upon a rougher electrode surface (as previously described in chapter 4).

To further validate these inferences regarding the effectiveness of pristine 2D-hBN interaction on rough and smooth electrode surfaces, the roughness factor (R_F) values for unmodified and pristine 2D-hBN modified SPEs and GC electrodes were calculated using a double layer capacitance technique as previously described in chapter 4.[150, 103] Figures 4.7 and 4.8 depict the analysis of unmodified, 108, 216 and 324 ng pristine 2D-hBN modified SPEs were the R_F values obtained are 1, 31.6, 39.4 and 49.9 respectively. It is clear that the roughness factor significantly increases

following pristine 2D-hBN modification of SPEs. Thus, it is revealed that pristine 2D-hBN modification of SPEs exhibits excellent adherence upon the electrode surface, likely due to SPEs providing a high level of surface roughness, which may prove to be beneficial.

Comparatively, the R_F values obtained for unmodified and pristine2D-hBN modified GC electrodes significantly differ. Figures 4.9 and 4.10 present the analysis of unmodified, 108, 216 and 324 ng pristine 2D-hBN modified GC electrodes, revealing the R_F values of 1, 1.36, 2.0 and 1.12 respectively. It is clear that pristine 2D-hBN adherence with a GC electrode is significantly lower when contrasted to an SPE. This adds further weight towards the inference that a smooth surface, such as a GC electrode, would be less likely to form strong interactions with pristine 2D-hBN, whereas the rough/ridged surface of a SPE may increase the substrate interaction and thus appears to be beneficial.

White light profilometry was utilised to compare the surface topography of GC and both polished/unpolished SPE substrates. The surface of an unpolished SPE exhibited a root mean squared value of the heights over the whole surface (SQ) of 1338.8 nm, which was significantly rougher than that of the GC (7.6 nm) and polished SPE (806.6 nm) alternatives, see Figure 4.11. Surface topography was also explored following modification with 108 ng of pristine 2D-hBN upon the said electrodes (Figure 4.11). Immobilisation of pristine 2D-hBN upon the GC electrode resulted in a rougher surface, with an increased SQ value of 35.1 nm. This was also the case utilising the polished SPE, with an increased SQ value of 842.4 nm compared to the unmodified surface. Interestingly, pristine 2D-hBN immobilisation upon an unpolished SPE resulted in a significantly larger SQ value increase, from 1338.8 nm (unmodified) to 1752.9 nm. Clearly, although a minimal increase in

roughness is observed with the addition of pristine 2D-hBN onto GC and polished SPEs (smooth surfaces); immobilisation upon an unpolished SPE (an initially rough surface) gives rise to a substantial increase in surface roughness. This observation confirms insight gained through the R_F values and SEMs (Figure 3.3) analysed above and strengthens the inference that pristine 2D-hBN adheres much more readily to a rougher underlying surface (contrary to a smooth surface) an effect previously exhibited in chapter 4.

The above observations suggests that, in contrast to GC and BDD alternatives, modification of pristine 2D-hBN onto SPEs gives rise to the most synergistic and resultantly beneficial electrocatalytic response towards the oxidation of DA (with an increased peak current and a reduction of up to 90 mV in the peak potential). Given this result, focus is now turned towards exploring the clear electrocatalytic effect exhibited when immobilising pristine 2D-hBN onto a SPE as an underlying supporting surface and aim to obtain a favourable analytical response.

Ascorbic Acid and Dopamine Electrochemistry

The electrochemical detection of 1 mM ascorbic acid (AA) in pH 7.4 PBS was explored utilising cyclic voltammetry at pristine 2D-hBN modified SPEs. Inspection of Figure 5.3B reveals that an unmodified SPE activates the oxidation potential of AA at +0.38 V, with a peak current of 22.9 μA. Upon modification of the SPE with pristine 2D-hBN (range: 108 to 324 ng; see Figure 5.3B), it is clear that there is no significant alteration/change in the resulting oxidation potential of AA, however, a notable decrease in the peak current is evident (see Figures 5.3C and 5.3D). Thus, unlike the response obtained towards DA, pristine 2D-hBN does not significantly/beneficially alter the oxidation potential of AA and inversely a

detrimental effect on the peak current is evident (which may be due to an insulating effect of pristine 2D-hBN towards AA). Furthermore, it has previously been shown that the oxidation mechanism of AA on carbon-based electrodes is invoked at specific functionalities and oxygenated surface sites.[55] In the case reported herein, it is likely that such sites are present on the underlying electrode material and that pristine 2D-hBN blocks/covers these upon its immobilisation, resulting in the observed decline in AA peak currents. For the case of DA, the introduction of pristine 2D-hBN will also reduce the presence of such oxygenated sites;[25] however, clearly, pristine 2D-hBN possesses sites that support DA oxidation. This is consistent with decreasing AA oxidation currents with the increased mass deposition (surface coverage) of pristine 2D-hBN, whilst an improved electrochemical response towards DA is observed.

Next considered is the separation/resolution of DA and AA oxidation potentials at pristine 2D-hBN modified SPEs (in separate solutions). Figure 5.5 depicts cyclic voltammograms of AA and DA utilising unmodified and 324 ng pristine 2D-hBN modified SPEs. Utilising the unmodified SPE, the peak potentials for DA and AA correspond to *ca*. +0.37 and +0.38 V respectively, indicating that these electrodes cannot significantly differentiate the potentials of DA and AA.[16, 39] Likewise, the pristine 2D-hBN modified SPEs exhibit the peak potentials for DA and AA at *ca*. +0.28 and +0.39 V respectively, with the beneficially reduced potential of DA and increased potential of AA resulting in a separation of 110 mV. Given the beneficial catalytic response of pristine 2D-hBN modified SPEs towards DA and their inhibiting of AA, it is next considered if this scenario can be utilised advantageously in the simultaneous detection of DA and AA.

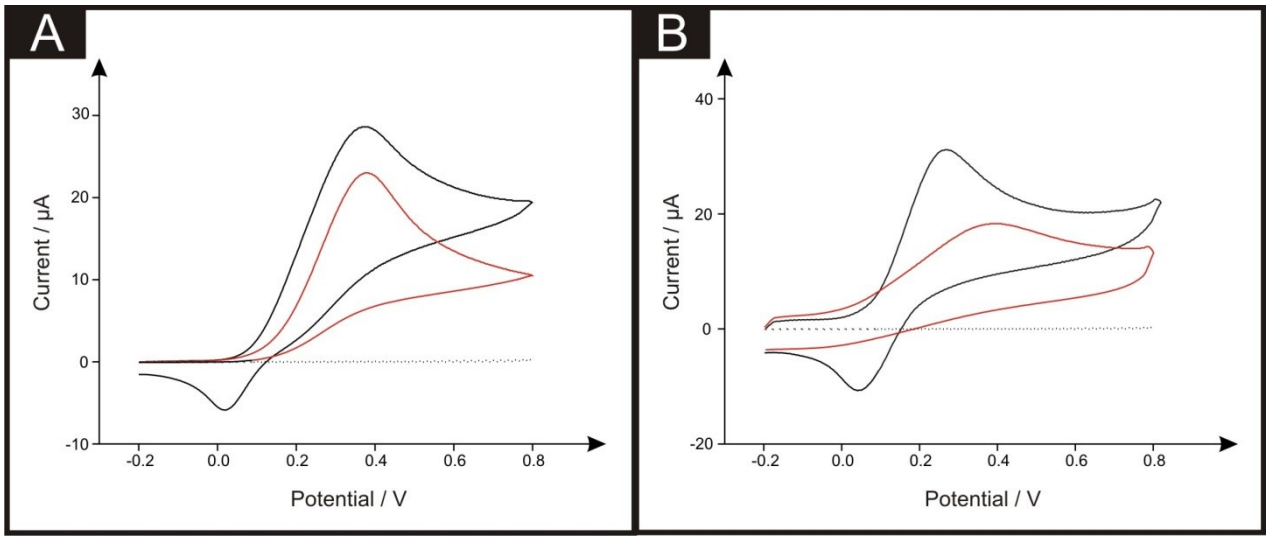

Figure 5.5: Typical cyclic voltammograms recorded in 1 mM DA (black) and 1 mM AA (red) pH 7.4 PBS. The response of the unmodified SPEs are utilised in (A) and 324 ng pristine 2D-hBN modified SPEs in (B).The 'dashed line' depicts the blank response in the absence of the analyte. Scan rate: 100 mV s^{-1} (vs. SCE).

Differential pulse voltammetry (DPV) was utilised to explore the simultaneous detection of DA and AA, with aliquots of DA added (representing, 3 – 75 µM) into a 0.1 mM AA solution. Figure 5.6A shows the observed voltammetry at unmodified SPEs, where upon additions of DA an increase in the current relating to the DA oxidation peak is observed (accompanying a small displacement of peak potential to more electro-negative regions). Evidently, the simultaneous detection of DA and AA is not observed. Next utilised were SPEs with 108 ng 2D-hBN immobilised, where (as observed in Figure 5.6B) additions of DA result in a further increase in the current obtained at the DA oxidation peak. In this latter case, again, only a single peak is observed, indicating the incapability of simultaneous detection utilising these electrodes. When comparing the linear calibration curves reported in

Figure 5.6C, which represent the sensitivity towards the detection of DA, it is interesting to note that the analytical sensitivity of the pristine 2D-hBN modified SPE is significantly increased over that of the unmodified alternative (from 4.0×10^{-9} $\mu A\ \mu M^{-1}$, to 2.0×10^{-8} $\mu A\ \mu M^{-1}$ respectively). Furthermore, for interested readers, Figure 5.6D illustrates that the DA oxidation potential does not significantly differ upon DA additions when utilising a 108 ng pristine 2D-hBN SPE, contrary to that observed at an unmodified SPE, which continually shifts more electro-negative. Suggesting that pristine 2D-hBN is less susceptible to oxidised species adsorbing onto its surface.

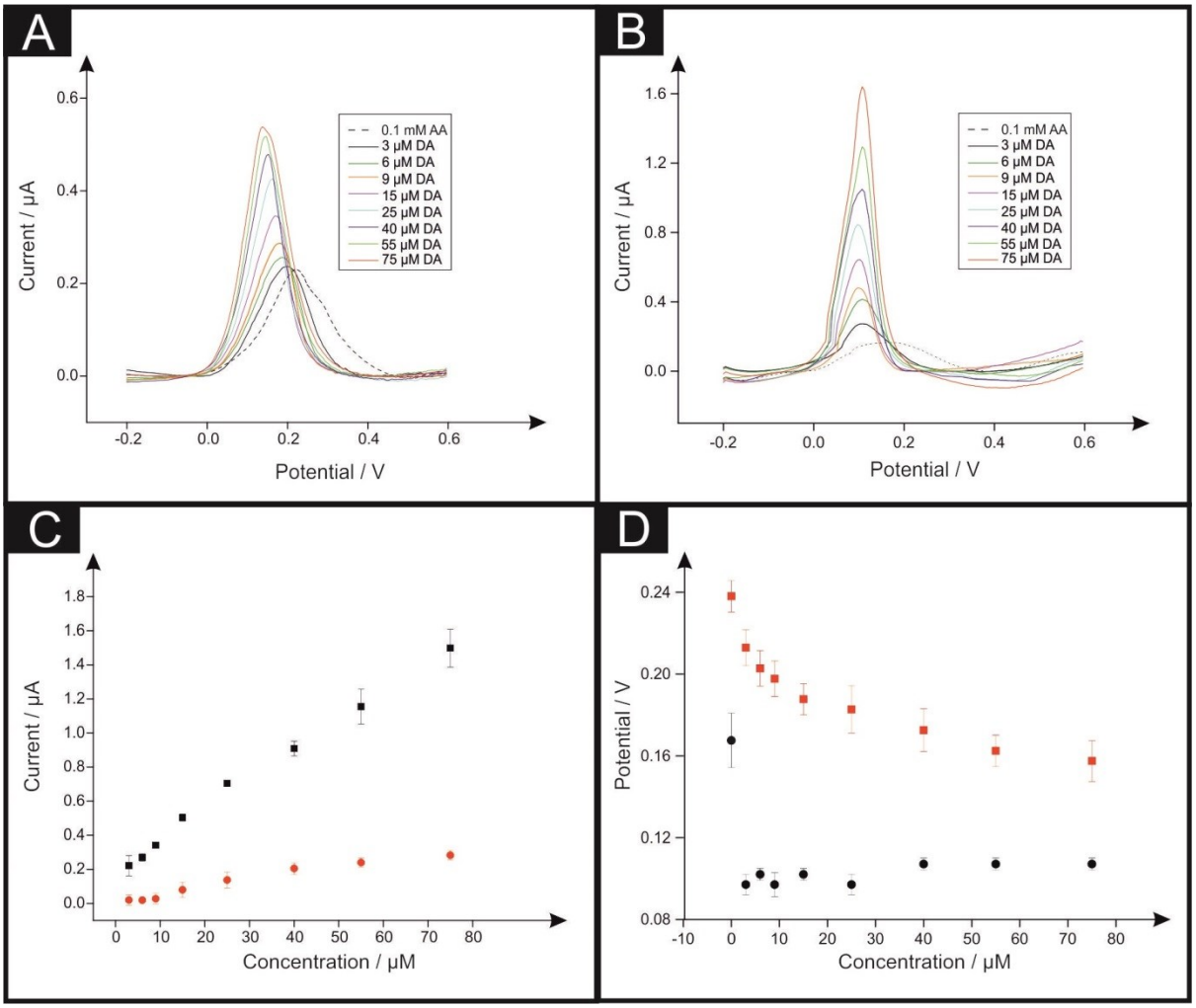

Figure 5.6: Typical DPVs obtained utilising unmodified SPEs (A) and 108 ng pristine 2D-hBN modified SPEs (B) by adding aliquots of DA at concentrations in the range of 3 – 75 µM into a 0.1 mM AA solution (pH 7.4 PBS); the dotted line represents 0.1 mM AA. Analytical curve (C) obtained utilising unmodified (red) and 108 ng pristine 2D-hBN modified SPEs (black) corresponding to the anodic peak current for the oxidation of DA over the concentration range. Also shown is the correlation/curve (D) utilising unmodified (red) and 108 ng pristine 2D-hBN modified SPEs (black) corresponding to the anodic peak potential for the oxidation of DA and how this changes over the concentration range. Conditions as follows: E*-pulse, 20 mV;* t*-pulse, 200 ms; equivalent scan rate, 10 mV* s^{-1}*; (vs. SCE). Each data point (C and D) is the average and standard deviation (*N *= 3).*

Although the simultaneous DPV detection of DA and AA is not viable, with only a single peak observed, it is clearly shown that pristine 2D-hBN modified SPEs

(which are cheap, reproducible, portable, and analytically competitive)[27, 75] could potentially be considered as an alternative/new sensor, exhibiting enhanced electroanalytical signals towards the detection of DA.

Uric Acid and Dopamine Electrochemistry

The electrochemical detection of 1 mM uric acid (UA) in pH 7.4 PBS was explored utilising cyclic voltammetry at pristine 2D-hBN modified SPEs. Inspection of Figure 5.7A reveals that an unmodified SPE activates the oxidation potential of UA at +0.49 V, with a typical peak current of *ca*. 21.1 μA. Upon modification of the SPE with pristine 2D-hBN (range: 108 to 324 ng; see Figure 5.7), it is clear that a significant alteration/change occurs in the resulting oxidation potential of UA, with an overall reduction in the activation potential of 50 mV towards the electro-negative region. Furthermore, the addition of pristine 2D-hBN gives rise to an increase in the observed peak current.

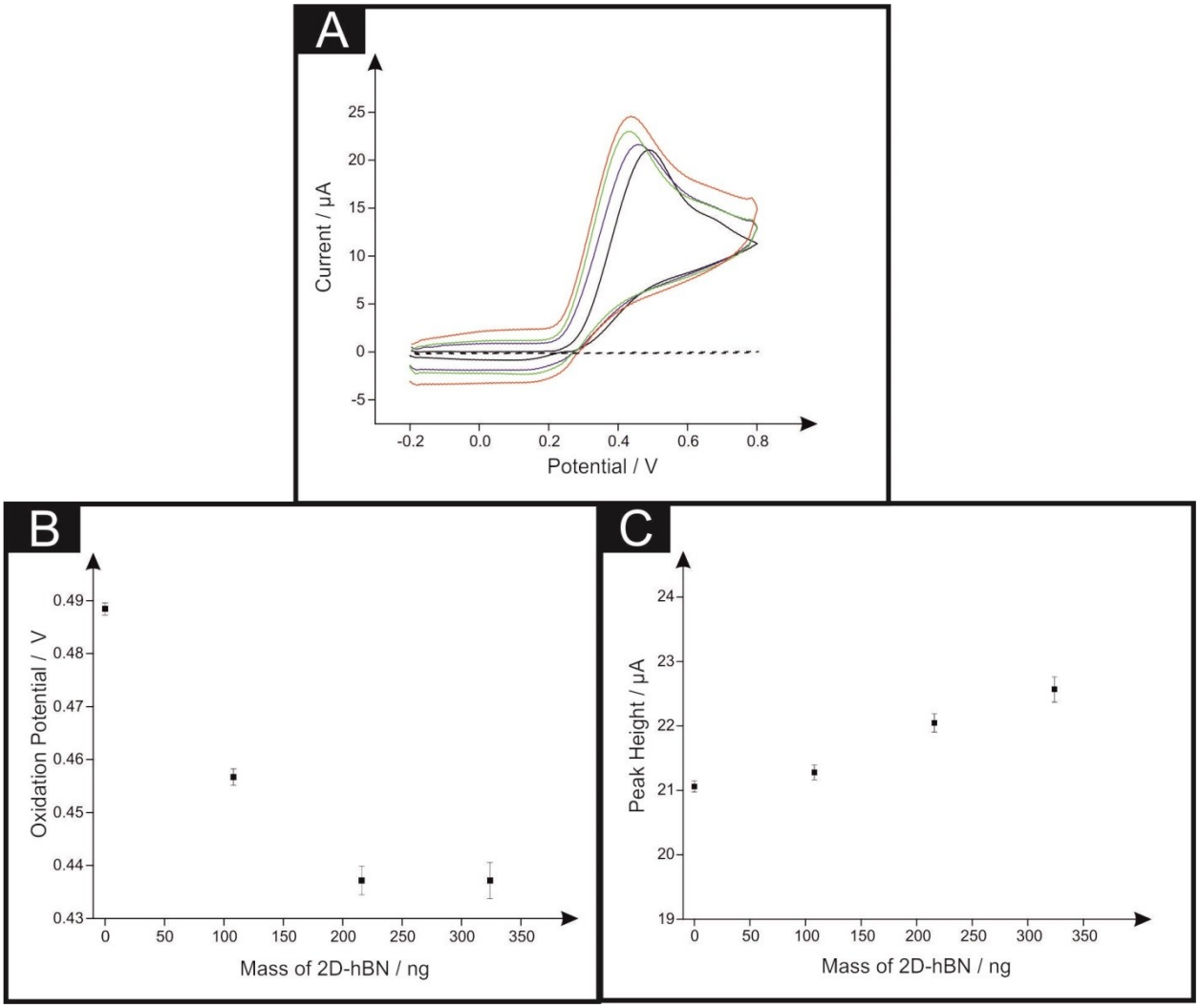

*Figure 5.7: Typical cyclic voltammograms recorded in 1 mM UA in pH 7.4 PBS utilising an unmodified SPE (black) and SPEs following modification with pristine 2D-hBN masses of 108 (blue), 216 (green) and 324 ng (red). The dashed line depicts the PBS blank. Analysis of cyclic voltammograms for the unmodified and pristine 2D-hBN modified SPE's is presented in the form of plot (B) illustrating UA oxidation potential vs. mass of pristine 2D-hBN and plot (C) depicting peak current vs. mass of pristine 2D-hBN immobilised upon a SPE. Scan rate: 100 mV s^{-1} (vs. SCE). Each data point (B and C) is the average and standard deviation (*N = *3).*

Next, the simultaneous detection of UA and DA was investigated *via* cyclic voltammetry by adding equal aliquots of UA and DA at a concentration of 0.5 mM into a pH 7.4 PBS. Unmodified SPEs were utilised and as evident in Figure 5.8A, the

simultaneous detection of UA and DA is viable, with the respective oxidation peaks observed at *ca*. +0.28 and +0.49 V. Modification of the SPE with pristine 2D-hBN (range: 108 to 324 ng; see Figure 5.8A) results in a reduced peak potential for DA oxidation (+0.19 V), whilst also beneficially reducing the peak potential at which the oxidation of UA occurs (+0.45 V) and resultantly enhancing peak separation between DA and UA by *ca*. 50 mV. Furthermore, the peak currents recorded for DA and UA were both found to increase upon the utilisation of pristine 2D-hBN. It is clear that pristine 2D-hBN modified SPEs display favourable electrocatalytic behaviour towards the simultaneous detection of DA and UA, with the possibility of improved analytical sensitivity.

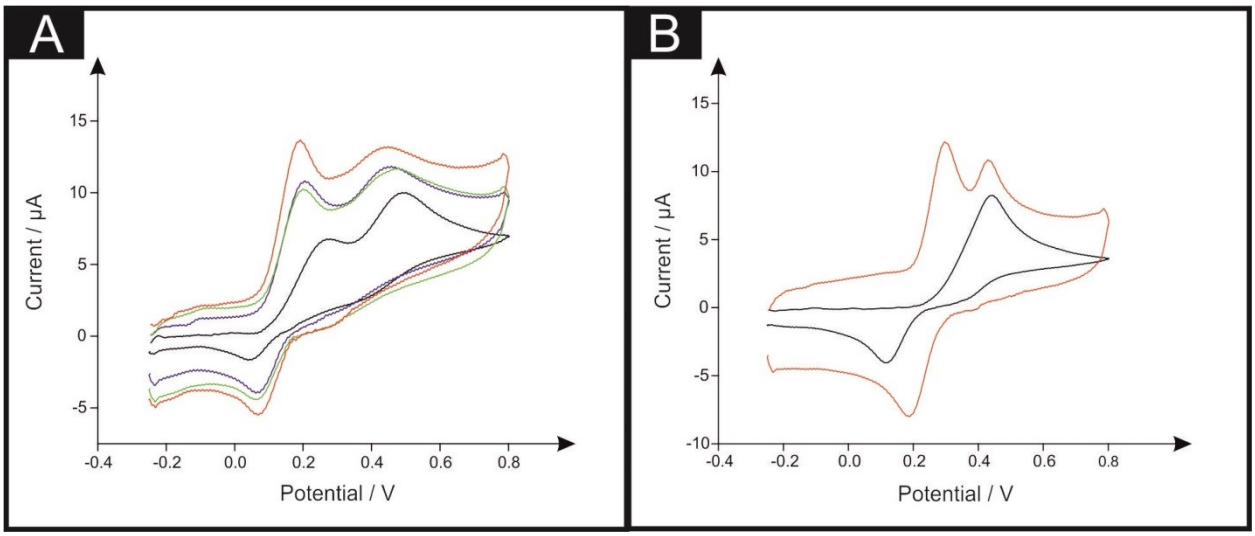

Figure 5.8: Typical cyclic voltammograms (A) recorded in 0.5 mM DA and 0.5 mM UA (PBS pH 7.4) with an unmodified SPE (black) and pristine 2D-hBN modified SPEs at masses of 108 (blue), 216 (green) and 324 ng (red). Figure B depicts voltammograms recorded in 0.5 mM DA and 0.5 mM UA (in a pH 5 acetate buffer) at an unmodified SPE (black) and a 324 ng (red) pristine 2D-hBN modified SPE. Scan rate: 100 mV s^{-1} (vs. SCE).

Next considered was the effect of carrying out the simultaneous detection of DA and UA at pH 5.0, a study frequently conducted within the literature.[153-155]

For a pH 5.0 solution (see Figure 5.8B) the voltammetric scan using an unmodified SPE shows only one oxidation peak (in agreement with previous literature),[156] which is likely due to the oxidation of UA.[157,158] However, the utilisation of a 324 ng pristine 2D-hBN modified SPE, results in the appearance of two oxidation peaks in pH 5.0 (at +0.33 V and +0.46 V for DA and UA respectively). Evidently, the utilisation of a pristine 2D-hBN modified SPE results in the simultaneous detection of UA and DA at pH 5.0, further demonstrating the electrocatalytic effect of pristine 2D-hBN modified SPEs towards the detection of DA in the presence of common interferents. Upon comparison of the peaks in Figures 5.8A and 5.8B, the peaks at pH 5.0 appear sharper, and exhibit improved peak resolution than the case of pH 7.4, where the peaks are broader and less defined. The electroanalytical experiments henceforth were conducted at pH 5.0.

DPV was utilised to explore the simultaneous detection of DA and UA at pH 5.0, with aliquots of DA added (representing, 3 – 75 μM) into a 0.1 mM UA (in acetate buffer) solution. Figure 5.9A shows the observed voltammetry at unmodified SPEs, where upon additions of DA, a corresponding weak signal at *ca*. +0.33 V is revealed (increasing in peak height respective to further additions) alongside the UA oxidation peak (+0.40 V). It is notable however, that such signal is only visible upon higher additions of DA.

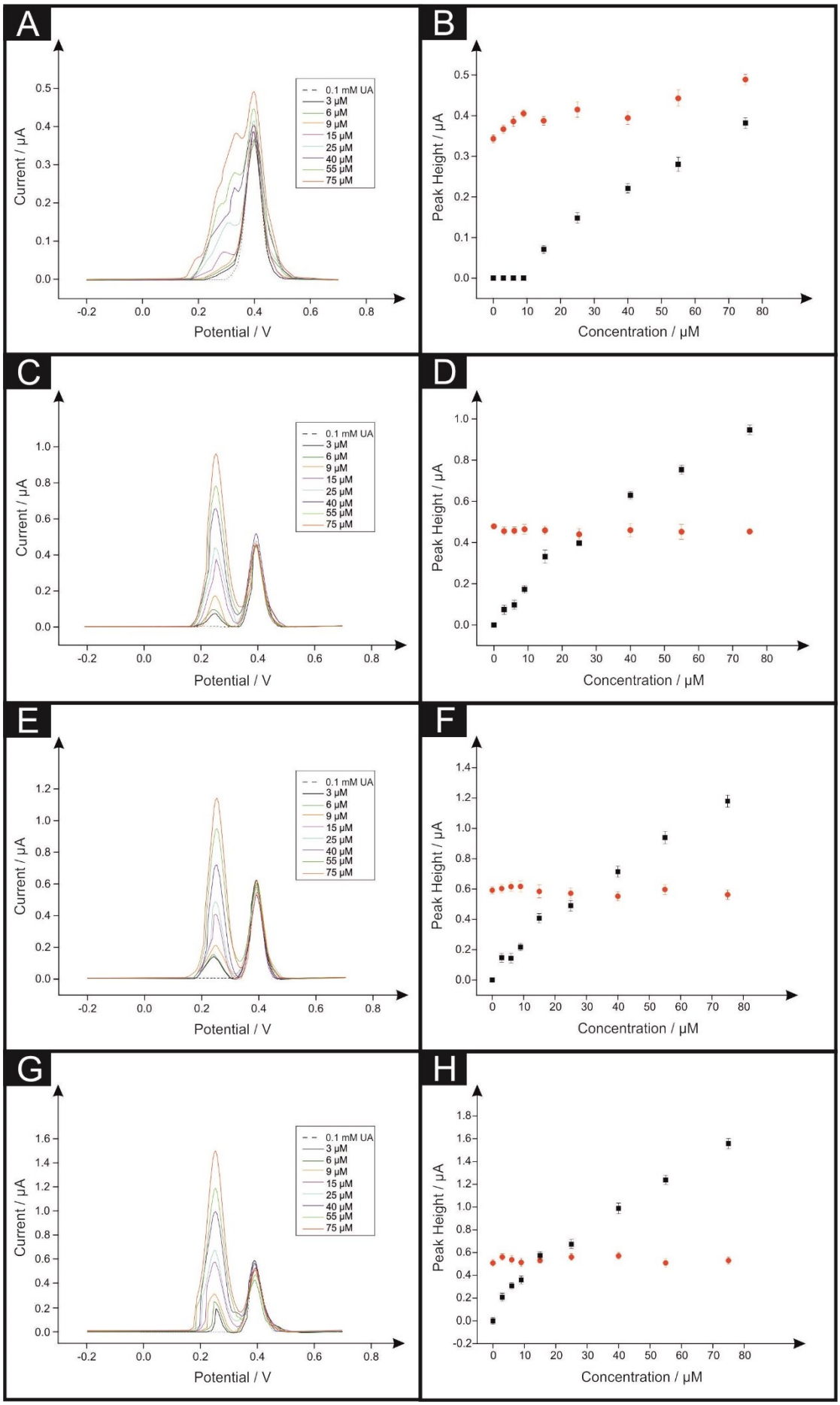
A
Current / µA
Potential / V
0.1 mM UA
3 µM
6 µM
9 µM
15 µM
25 µM
40 µM
55 µM
75 µM
B
Peak Height / µA
Concentration / µM
C
Current / µA
Potential / V
D
Peak Height / µA
Concentration / µM
E
Current / µA
Potential / V
F
Peak Height / µA
Concentration / µM
G
Current / µA
Potential / V
H
Peak Height / µA
Concentration / µM

Figure 5.9: Typical DPVs (A, C, E and G) recorded by adding aliquots of DA at concentrations in the range of 3–75 μM (in 0.1 mM UA in pH 5.0 acetate buffer) utilising an unmodified SPE and a SPE following modification with 108, 216 and 324 ng pristine 2D-hBN. Dotted line represents 0.1 mM UA blank. Additionally, corresponding analytical curves of the simultaneous oxidation of DA (black squares) and UA (red circle) over the concentration ranges utilising unmodified SPEs (Figure B) and 108 ng (Figure D), 216 ng (Figure F), 324 ng (Figure H) pristine 2D-hBN modified SPEs are shown. Conditions as follows: E*-pulse, 20 mV;* t*-pulse, 200 ms; equivalent scan rate, 10 mV* s^{-1}*; (vs. SCE). Each data point (B, D, F and H) is the average and standard deviation (*N *= 3).*

Next, pristine 2D-hBN modified SPEs (range: 108, 216 and 324 ng) were utilised towards the simultaneous detection of DA and UA at pH 5.0. Figure 5.9 depicts the voltammetry when utilising pristine 2D-hBN modified SPEs, where two clearly separated oxidation peaks are visible at each of the modification masses utilised. Specifically, when compared to the unmodified SPE, which exhibits the oxidation potentials for DA and UA at ca. +0.33 and +0.40 V respectively, the 2D-hBN modified SPEs decrease (improve) the value corresponding to DA oxidation to ca. +0.25 V whilst not altering the potential at which UA oxidation is observed. In terms of the electroanalytical response, with each increased mass immobilisation of pristine 2D-hBN it is clear through examination of Figure 5.9 that there is a significant enhancement of the peak current relating to the oxidation of DA, whilst the peak current corresponding to UA is unaffected. The values/equations of the linear calibration curves relating to the increased analytical sensitivity towards DA detection (see Figure 5.9) that are observed at each of the pristine 2D-hBN modified SPEs are as follows: unmodified SPE, $I_p/\mu A = 5.46\times10^{-9}\ \mu A\ \mu M^{-1} - 1.58\times10^{-8}\ \mu A$; N = 3; $R^2 = 0.982$; 108 ng pristine 2D-hBN modified SPE, $I_p/\mu A = 1.26\times10^{-8}\ \mu A\ \mu M^{-1} + 5.91\times10^{-8}\ \mu A$; N = 3; $R^2 = 0.977$; 216 ng pristine 2D-hBN modified SPE, $I_p/\mu A =$

1.44×10^{-8} μA μM^{-1} + 1.16×10^{-7} μA; N = 3; R^2 = 0.983; 324 ng pristine 2D-hBN modified SPE, $I_p/\mu A = 1.94\times10^{-8}$ μA μM^{-1} + 1.63×10^{-7} μA; N = 3; R^2 = 0.976.

In terms of the analytical utility of 2D-hBN, the 324 ng pristine 2D-hBN modified SPE exhibited a limit of detection (LOD, based on three-sigma) for DA (in the presence of UA) of 0.65 μM, which is highly competitive with the literature, as evident in Table 5.1. Thus, this thesis has shown proof of concept. Conversely, the unmodified SPE possesses a LOD of 2.73 μM.

It has been shown, for the first time, the utilisation of pristine 2D-hBN modified SPEs (in pH 5.0) allows for the simultaneous detection of UA and DA. Figure 5.8 depicts enhanced peak separations (*ca*. 70 mV) and increased peak currents relating to the detection of DA (when compared to an unmodified SPE). This further suggests that pristine 2D-hBN modified SPEs are an effective electrocatalytic material when utilised towards the electroanalytical sensing of DA and demonstrate a continued electrocatalytic effect in the presence of UA. The observed beneficial effect is clearly dependent upon the supporting surface of pristine 2D-hBN and in the case of modified SPEs is likely due to the favourable interaction of pristine 2D-hBN with the rough surface morphology (see Figure 3.3 and 4.11) enabling the effective 'electrical wiring' of pristine 2D-hBN onto the electrode surface.

Given the apparent benefits, it is interesting to consider the future potential applications of pristine 2D-hBN in the field of electroanalysis. A pertinent research question would be to extend the work reported herein towards 'real' and more complex sample matrixes, such as in urine and cerebrospinal fluid. Moreover, fundamental studies investigating the effect of pristine 2D-hBN lateral grain sizes on the observed electrochemistry could potentially result in defining the underlying

electron transfer mechanism and the origin of this behaviour, knowledge that no doubt would lead to targeted beneficial applications. Currently, with the prominent deliberate doping of graphene (and other carbon-based electrodes) with (separately) Boron and Nitrogen atoms within the literature towards the detection of various analytes (namely, Glucose, Hydrogen Peroxide, Cocaine, and (as explored herein) AA, DA and UA);[14] pristine 2D-hBN offers a readily available 'doped' material, which as shown in this work, can provide electrochemically useful responses. Consequently, there is clear scope to benefit multiple areas of electroanalysis through the inclusion of pristine 2D-hBN. Furthermore, surfactants such as Nafion are widely implemented within electroanalysis to impart improvements upon fabricated sensor devices. However, it has previously been shown that such surfactants strongly influence the underlying electrochemistry,[56] thus it would be beneficial for future work to consider the effects/influence of various surfactants upon the electrochemistry of pristine 2D-hBN (explored in later chapters). With further reference to following the course of doped carbon materials, explorations of pristine 2D-hBN's performance as a material component within supercapacitors may also lead to new and fascinating discoveries (see chapter 6).

5.3 Conclusions

This chapter has reported, for the first time, the electrocatalytic behaviour of pristine 2D-hBN towards the electrochemical detection of DA. A simple drop-casting method was implemented and the catalytic effect of pristine 2D-hBN was shown to be dependent upon *both* the mass/coverage *and* substrate utilised (particularly the roughness of the underlying supporting electrode surface). Given the excellent electrocatalytic oxidation of DA observed, pristine 2D-hBN modified

SPEs were shown to possess the ability to de-convolute the signals of DA and two commonly reported interferents: AA (by *ca*. 110 mV in separate solutions) and UA (by *ca*. 70 and 50 mV simultaneously at pH 5.0 and pH 7.4 respectively). The pristine 2D-hBN modified SPEs exhibited a competitive LOD value of 0.65 μM and as such offer a viable means towards the detection of DA in the presence of common interferents. Evidently, this chapter has shown promise for future exploration of this novel nanomaterial pristine 2D-hBN ('*an initially unlikely*' candidate) as a beneficial electrode material, which may prove highly pertinent in the field of electrochemistry.

In order to understand the role of the fabrication process upon the observed electrochemistry of 2D-hBN towards the applications investigated herein (chapters 4 and 5), the following chapters (6 and 7) focus upon the utilisation of surfactants (commonly employed in 2D materials electrochemical studies) in the fabrication of 2D-hBN and implement this approach towards said applications.

Chapter 6 : Surfactant-Exfoliated 2D Hexagonal Boron Nitride (2D-hBN): role of surfactant upon the electrochemical reduction of oxygen and capacitance applications

In this chapter, surfactant-exfoliated 2D hexagonal boron nitride (2D-hBN) nanosheets are fabricated using the surfactant sodium cholate in aqueous media (see chapter 3.4.3) and are explored towards the electrochemical reduction of oxygen (oxygen reduction reaction) within acidic media for the first time. The surfactant-exfoliated 2D-hBN nanosheets are immobilised upon graphitic screen-printed electrodes (SPEs) with mass coverage studies performed and the observed electrochemical response is compared to the surfactant-free pristine 2D-hBN approach (see chapter 4). Also investigated for the first time is the effectiveness of surfactant-exfoliated 2D-hBN as an electrochemical supercapacitor material. In both examples the effect of the fabrication process of 2D-hBN is de-convoluted through the utilisation of control experiments in the form of surfactant modified graphite electrodes. This chapter contains work that has been peer-reviewed and published in the academic literature.[3]

6.1 Introduction

The continuing depletion of natural energy resources has resulted in the need to find alternative means of energy production.[37, 159, 160] Reassuringly, reliance upon finite sources of energy is reducing and alternative means of energy generation are

[3] A. F. Khan, M. P. Down, G. C. Smith, C. W. Foster and C. E. Banks, *J. Mater. Chem. A*, 2017, 5, 4103-4113.

highly sought. One such example is the proton exchange membrane (PEM) fuel cell, in which the oxygen reduction reaction (ORR) occurs,[161] and this technology currently leads the transportation fuel cell market. However, an increase in the efficiency of PEM fuel cells is highly desirable, therefore research efforts are directed towards improving their performance in terms of power output, efficiency, and longevity.[162]

A significant drawback of PEM fuel cells is the ORR, which can limit fuel cell lifetimes in many devices due to electrode fouling.[69] The ORR occurs at the cathode of PEM fuel cells, where fuel cell degradation[89] is synonymous with the ORR due to the formation of hydrogen peroxide (H_2O_2) when using catalysts that reduce oxygen *via* the two electron pathway.[91] Thus, a platinum (Pt) [93] electrocatalyst is commonly employed as its mechanism for the reduction is a direct four electron pathway that does not produce harmful by-products such as H_2O_2 (see chapter 4).[94, 162, 163] However, due to Pt being sparse and expensive,[69] it is unsuitable for mass production as a fuel cell catalyst. Consequently, research is directed towards cheaper nonprecious metal catalysts[97] and more pertinently, metal-free carbon based materials.[94]

Previous studies have utilised 2D materials towards the ORR**.** [107] [164] Zhao *et al.* [165] have demonstrated that MoS_2 modified GC electrodes result in the ORR occurring at –420 mV within alkaline conditions. The same report also demonstrated GN GC electrodes resulted in the ORR occurring at –310 mV.[165] The lowest overpotential for the ORR to occur was observed when MoS_2 and GN combined resulting in an activation overpotential for the ORR of –230 mV.[165]

A lesser researched material is 2D hexagonal boron nitride (2D-hBN). Zhao *et al*.[166] studied the ORR and computationally demonstrated *via* density functional

theory (DFT) that carbon-singly doped into *h*-BN nanosheets can cause high spin density and charge density resulting in the enhancement of O_2 adsorption.[166] Uosaki *et al.*[69] investigated the ORR and immobilised 2D-hBN upon gold substrates/electrodes where the overpotential required for the ORR was reduced by *ca.* 0.27 V.[69] This thesis has previously shown (chapter 4) that surfactant-free (pristine) 2D-hBN nanosheets exhibit an electrocatalytic behaviour towards the ORR when immobilised upon SPEs.[86] Pristine 2D-hBN reduced the overpotential required for the ORR to occur by *ca*. 0.28 V in comparison to unmodified/underlying SPEs.[86] Interestingly, no such beneficial response was observed for pristine 2D-hBN when it was modified/supported on GC and boron doped diamond (BDD) underlying electrodes.[86] The observed beneficial response at pristine 2D-hBN modified SPEs was attributed to the interaction between 2D-hBN and the roughness of the underlying SPE, whereas the comparatively smooth surface of a GC electrode hindered this.[86]

Another key area in the energy sector is improving the overall power of energy storage devices. A fundamental high power solution is to utilise advanced electrode materials within supercapacitor devices. Supercapacitors are passive and static electrical energy storage devices, utilised in applications from portable electronics to hybrid cars. They are typically seen as a viable future solution in the search for greener and higher powered electronics. Furthermore, supercapacitors are required to store energy whilst offering transient, but extremely high powers, delivered over a short period of time.[167, 168] Thus, developing an improved capacitor performance and a greater understanding/insight into their fabrication and mechanism is of extremely high significance.[37, 169]

Current research is directed towards chemically doping novel carbon-based nanomaterials with foreign atoms in order obtain superior properties and impart improved supercapacitor performances. Pertinent materials of note which offer beneficial performances, such as a high a specific capacitance (C_s), include: vertically aligned boron carbon nitride (BCN) nanotubes (*ca.* 321 F g^{-1});[170] three-dimensional Nitrogen and Boron co-doped graphene aerogels (*ca.* 239 F g^{-1}); [171] Nitrogen-doped 2D graphene (*ca.* 220, and *ca.* 197 F g^{-1}); [172, 173] and Boron-doped 2D graphene (*ca.* 173 F g^{-1}).[174] Furthermore Gao *et al*.[60] have utilised h-BN nanoparticles (in bulk) to form a composite supercapacitor material with reduced-graphene oxide (r-GO).[60] Their report showed the h-BN/r-GO composite material offers a C_s value of 140 F g^{-1} when mixed with acetylene black / polyvinylidene fluoride and pressed onto a nickel foam electrode in a 6 M KOH solution. However, 2D-hBN *per se* has yet to be explored as a supercapacitor material.

This chapter considers for the first time 2D-hBN nanosheets fabricated using the surfactant sodium cholate in aqueous media and explores the electrochemical reduction of oxygen (ORR) and capacitive performance within acidic media. Furthermore, control experiments, in the form of surfactant modified graphitic electrodes are implemented in order to deconvolute the true electrochemical response. The effect of surfactant-exfoliated 2D-hBN, has yet to be explored towards the ORR and capacitance applications.

6.2 Experimental Details

For experimental procedures/tests investigating the electrochemical detection of oxygen, sulfuric acid solutions utilised were of the highest grade available from Sigma-Aldrich (99.999%, double distilled for trace metal analysis) and was used at a

concentration of 0.1 M. To oxygenate the solution, it was subject to rigorous bubbling of 100% medicinal grade oxygen through 100 mL of the solution for 45 minutes, assuming this to be a completely saturated solution at room temperature as described by Gara.[91] The concentration of oxygen was assumed to be 0.9 mM according to previous reports using the same method. [91, 94]

6.3 Results and Discussion

The Oxygen Reduction Reaction (ORR)

The oxygen reduction reaction (ORR),[175] is an important reaction that occurs at the cathode of PEM fuel cells. Due to its high kinetic parameter, research is directed towards reducing the peak potential at which the ORR occurs,[176] with particular focus on 2D nanomaterials as a means to do this.[177] Consequently, 2D-hBN is explored towards the ORR using surfactant-exfoliated 2D-hBN immobilised upon SPEs (see Figure 1.11) where the underlying electrode serves to electrically wire/ interconnect the 2D-hBN materials.

First, unmodified, 37.5 ng surfactant-exfoliated 2D-hBN and 10 µg sodium cholate modified SPEs were explored towards the ORR within 0.1 M H_2SO_4. The 10 µg sodium cholate modified SPE is a control experiment, which equates to the same volume of 37.5 ng surfactant 2D-hBN drop-cast upon the electrode surface so that just the effect of the sodium cholate on the ORR can be evaluated. It is important to note that the same sodium cholate was utilised in the exfoliation process of 2D-hBN (see Section 3.4.3). One can observe, through inspection of Figure 6.1 that the reduction overpotential of the ORR using an unmodified SPE occurs at -1.09 V. However, upon immobilisation of 37.5 ng 2D-hBN, a decrease is exhibited in the overpotential required for the ORR to occur, shifting from –1.09 to –0.59 V (*vs*. SCE); hence an overpotential reduction of 0.50 V for the ORR to occur is observed (scan rate: 100 mV s^{-1}), compared to the response of the bare underlying electrode. Next, control experiments were performed utilising sodium cholate modified SPEs towards the ORR to understand the role of surfactants in the electrochemical process. As a result, 10 µg sodium cholate modified SPEs were utilised towards the ORR, and the voltammogram shown in Figure 6.1 illustrates the overpotential required for

the ORR to occur is – 0.65 V (*vs*. SCE); thus a reduction in the overpotential for the ORR to occur of 0.44 V is observed (scan rate: 100 mV s^{-1}) in comparison to an unmodified SPE. Hence, it is clear sodium cholate has a dominant role in the electrocatalytic effect shown towards the ORR upon the use of surfactant-exfoliated 2D-hBN modified SPEs, given the reduction in the overpotential of 0.44 V when utilising a sodium cholate modified SPE.

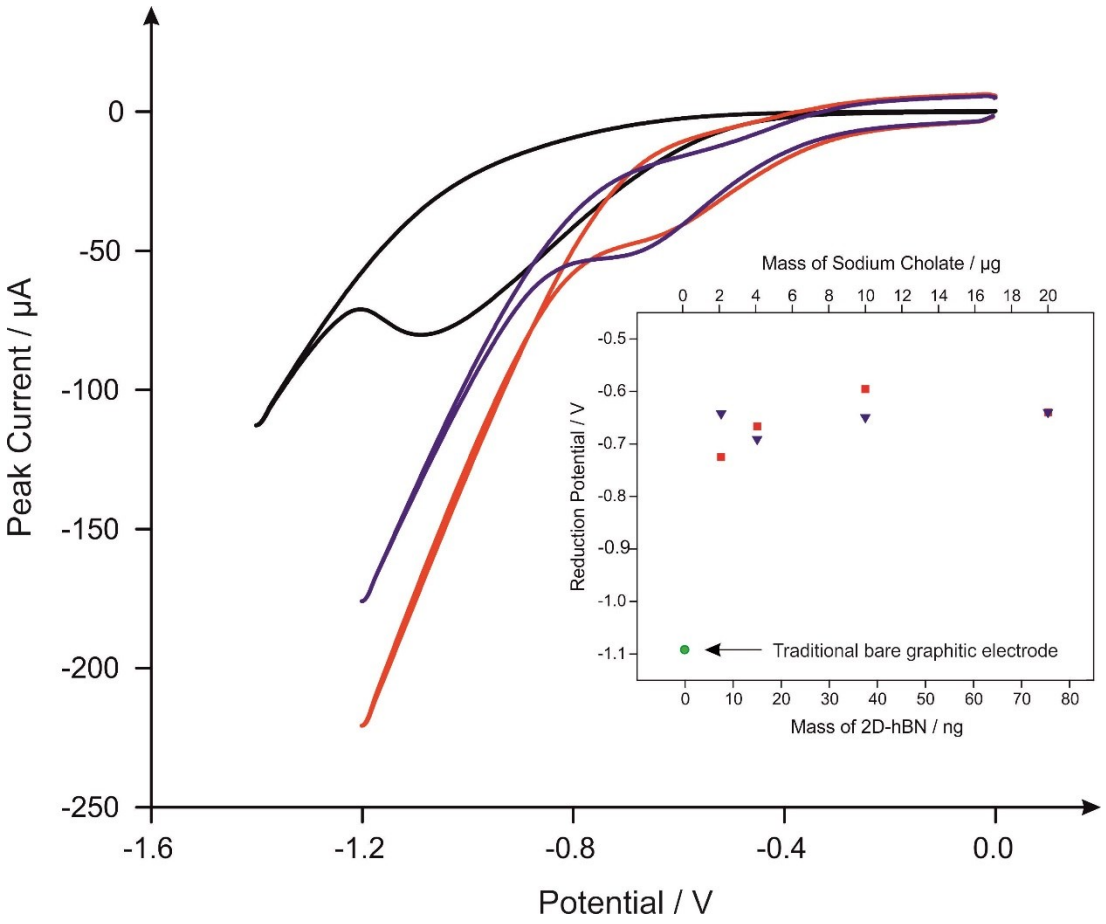

Figure 6.1: Typical cyclic voltammograms recorded in an oxygen saturated 0.1 M H_2SO_4 solution using unmodified (black line), 37.5 ng surfactant-exfoliated 2D-hBN (red line) and 10 µg sodium cholate (on its own as a control, blue line) modified SPEs. Shown in the inset is analysis of the cyclic voltammograms in the form of a plot of oxygen reduction potential vs. mass of 2D-hBN (red squares)

and sodium cholate (blue triangles) electrically wired upon SPEs. The green circle depicts an unmodified (bare) SPE. Scan rate: 100 mV s^{-1} (vs. SCE).

Corresponding voltammograms of nitrogen saturated 0.1 M H_2SO_4 utilising unmodified, 37.5 ng surfactant-exfoliated 2D-hBN and 10 µg sodium cholate modified SPEs are exhibited in Figure 6.2A, where the absence of an oxygen signal is clearly apparent and the process observed in Figure 6.1 is due to the electrochemical reduction of oxygen.

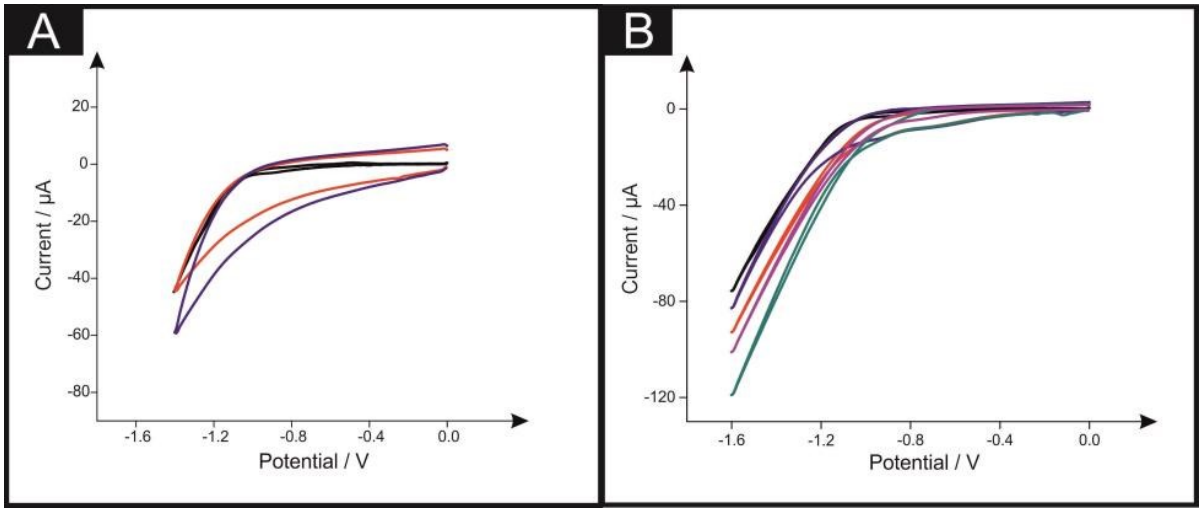

Figure 6.2: Typical cyclic voltammograms (A) recorded in nitrogen saturated 0.1 M H_2SO_4 solution using unmodified (black line), 37.5 ng surfactant-exfoliated 2D-hBN (red line) and 10 µg sodium cholate (blue line) modified SPEs. Also shown are cyclic voltammograms (B) recorded in nitrogen saturated 0.1 M H_2SO_4 with unmodified (black line), 54 ng (red line), 108 ng (blue line), 216 ng (green line) and 324 ng (pink line) pristine 2D-hBN modified SPEs. Scan rate: 100 mV s^{-1} (vs. SCE).

Following this, the deposition of various masses of surfactant-exfoliated 2D-hBN immobilised on SPEs and the effect upon the ORR is explored; again sodium

cholate control investigations are also implemented (equating to the same volume of surfactant-exfoliated 2D-hBN drop-cast onto the electrode surface). The effect of different masses and coverages is an overlooked parameter in the academic literature. As a result, SPEs were modified with surfactant-exfoliated 2D-hBN masses ranging from 7.5 - 75 ng; inset of Figure 6.1 depicts a plot of the oxygen reduction peak potential *vs.* the mass of immobilised surfactant-exfoliated 2D-hBN. It is observed that increased amounts of surfactant-exfoliated 2D-hBN deposited upon SPEs leads to a decrease in the overpotential required for the ORR to occur in comparison to an unmodified SPE, with the activation peak potential shifting from -1.09 V to -0.73 V, -0.67 V, -0.59 V and -0.64 V for 7.5, 15, 37.5 and 75 ng surfactant-exfoliated 2D-hBN modified SPEs respectively. Thus, a significant reduction in the activation overpotential for the ORR to occur is shown at various masses of immobilised surfactant-exfoliated 2D-hBN, with highest reduction (0.50 V) exhibited at 37.5 ng modified 2D-hBN. Furthermore, sodium cholate control coverage studies were performed with the data presented in the inset of Figure 6.1 which shows that the overpotential required for the ORR shifts from -1.09 V to -0.64 V, -0.69 V, -0.65 V and -0.64 V for , 2, 4, 10 and 20 μg sodium cholate modified SPEs respectively. This further demonstrates the dominant nature of the sodium cholate surfactant when utilised towards the ORR, which exhibits a similar electrocatalytic effect to that of the surfactant-exfoliated 2D-hBN. Thus, it is suggested the significant electrocatalytic response obtained when utilising surfactant-exfoliated 2D-hBN towards the ORR, is inherently due to the surfactant, sodium cholate; such observations have not been reported before. The above data with surfactant-exfoliated 2D-hBN agrees with previous studies carried out by Brownson *et al,*[49] whom observed that the electrocatalytic response of 2D materials such as

graphene in various electroanalytical applications, should not assumed to be solely due to graphene itself, rather the effect of surfactants, such as sodium cholate, in the production of graphene dominate its electroanalytical response.[49, 169]

Next considered is the effect of surfactant-free (pristine) 2D-hBN electrically wired upon SPEs towards the ORR, previously explored in chapter 4. Figure 4.19 illustrates the voltammetric response obtained for pristine 2D-hBN modified SPEs (within 0.1 M H_2SO_4), where it is clear that increasing immobilisation of pristine 2D-hBN upon SPEs, of masses ranging from 54 ng to 324 ng, reduces the overpotential required for the ORR to occur. Analysis of this is shown in Figure 4.19 inset, where it is revealed the overpotential required for the ORR to occur shifts from -1.09 V (unmodified SPE) to -0.81 V (*vs*. SCE) at a scan rate of 100 mV s^{-1} upon increasing additions of pristine 2D-hBN, with the highest modification of 324 ng pristine 2D-hBN, demonstrating a overpotential shift of 0.28 V. Thus, it is clear, pristine 2D-hBN exhibits electrocatalytic-type behaviour towards the ORR, however it is significantly inferior to that of surfactant-exfoliated 2D-hBN, where a 0.5 V decrease in overpotential is observed. Therefore, it is inferred the surfactant, sodium cholate, utilised in the exfoliation of 2D-hBN significantly enhances its electrochemical response. Corresponding voltammograms of nitrogen saturated 0.1 M H_2SO_4 utilising unmodified and 54 – 324 ng pristine 2D-hBN modified SPEs are exhibited in Figure 6.2B, where the absence of an oxygen signal is clearly apparent and the process observed in Figure 4.19 is due to the electrochemical reduction of oxygen.

A further consideration is the stability of the various 2D-hBN modified layer(s) upon the electrode surface. This is addressed *via* the implementation of a stability experiment in which a 37.5 ng surfactant-exfoliated 2D-hBN, a 324 ng

pristine 2D-hBN and a 10 µg sodium cholate modified SPE was subjected to 10 repeated cycles/scans in a 0.1 M H_2SO_4 solution at 100 mV s^{-1}. This experiment simulates and recreates the appropriate timescale(s) of the voltammetric tests utilised within this work and shows that the cathodic I_p and potential remained stable, with only small alterations occurring in the recorded signal over 10 cycles (see Figure 6.3 and Table 6.1), for the case of all modified electrodes. Clearly, at these representative coverages, the modified layer(s) are stable on the electrode surface and do not appear to fall off the electrode into the solution.

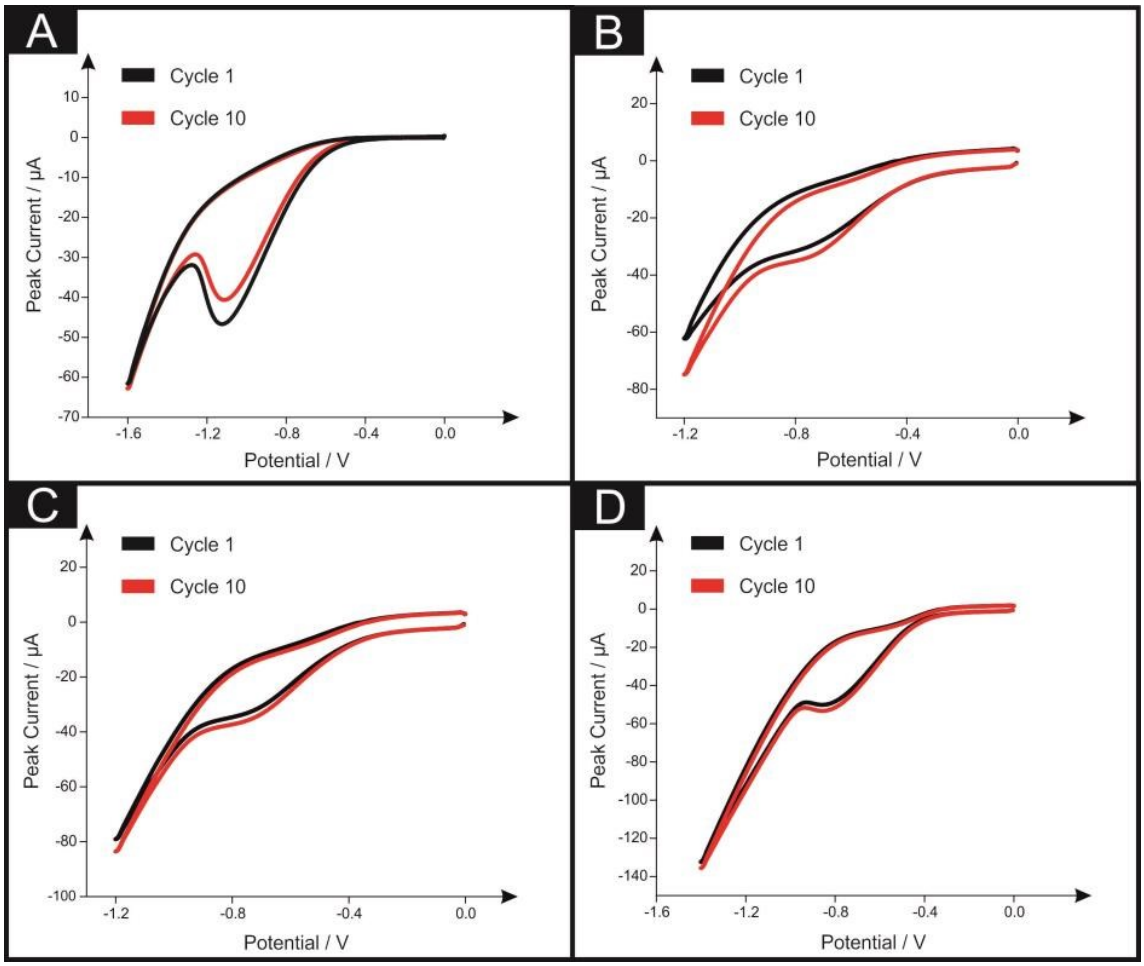

Figure 6.3: Cyclic voltammograms recorded in 0.1 M H2SO4 using; (A) an unmodified SPE, (B) a 37.5 ng surfactant-exfoliated 2D-hBN modified SPE, (C) a 10 µg sodium cholate modified SPE and

(D) a 324 ng pristine 2D-hBN modified SPE. Repeat scans were performed up to 10 cycles. Scan rate: 100 mV s^{-1} (vs. SCE).

Electrode Material	Cycle 1		Cycle 10	
	Cathodic Peak (Reduction) Current (µA)	Cathodic Peak (Reduction) Potential (V)	Cathodic Peak (Reduction) Current (µA)	Cathodic Peak (Reduction) Potential (V)
37.5 ng surfactant-exfoliated 2D-hBN modified SPE	-28.80	-0.71	-32.20	-0.71
10 µg sodium cholate modified SPE	-30.70	-0.71	-32.50	-0.70
324 ng pristine 2D-hBN modified SPE	-50.40	-0.84	-53.20	-0.84
Unmodified SPE	-46.90	-1.12	-40.08	-1.11

Table 6.1: Analysis of voltammograms presented in Figure 6.4. Table exhibits the effects of increasing voltammetric cycle number upon the 'cathodic peak current' (µA) and 'cathodic peak potential' (V) when utilising a 37.5 ng surfactant-exfoliated 2D-hBN, 324 ng pristine 2D-hBN and 10 µg sodium cholate modified SPE.

To gain further insights into the electrochemical mechanism, Tafel analysis was performed for unmodified, surfactant-exfoliated 2D-hBN and sodium cholate modified SPEs, of masses ranging from 7.5ng – 75 ng and 2 – 20 µg respectively.

This analysis has also been performed previously for pristine 2D-hBN modified SPEs (chapter 4) of masses ranging from 108 ng – 342 ng. A plot of natural logarithm of the current (ln *I*) *vs*. E_p was constructed for analysis of the voltammograms corresponding to the electrochemical reduction of oxygen using equation 4.1 found in chapter 4 and the said Tafel plots are shown in Figure 6.4 corresponding to unmodified, 7.5, 7.5, 15, 37.5 and 75 ng surfactant-exfoliated 2D-hBN modified SPEs.

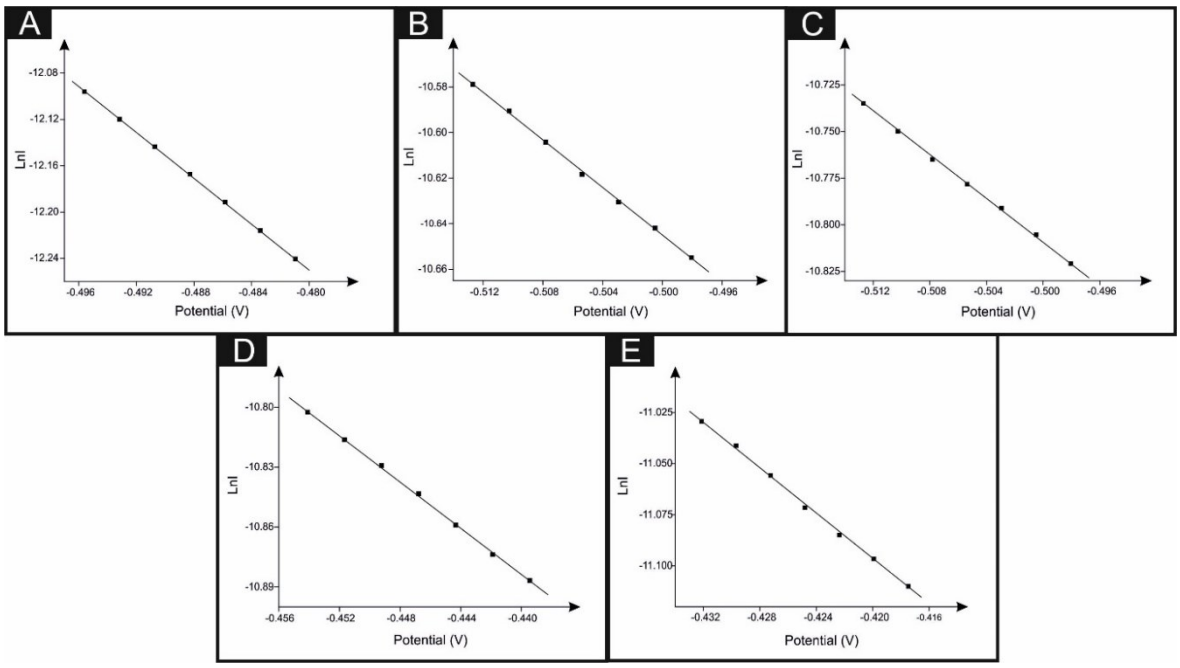

Figure 6.4: Illustrates Tafel plots for unmodified (A), 7.5 (B), 15 (C), 37.5 (D) and 75 ng (E) surfactant-exfoliated 2D-hBN modified SPEs.

For an unmodified SPE (Figure 6.4A), the $\alpha n'$ value obtained was 0.25. Within the Tafel region, the Nernstian potential was found to increase by 163.2 mV for every order of magnitude of current. Conversely, for 7.5, 15, 37.5 and 75 ng surfactant-exfoliated 2D-hBN (Figures 6.4B, C, D, and E repectively), $\alpha n'$ values of 0.14, 0.12,

0.12 and 0.12 were obtained, with a Nernstian potential increase of 93.24, 76.68, 81.13 and 82.12 mV per order of magnitude of current respectively. Whereas Figure 6.5 illustrates Tafel plots for, for 2, 4, 10 and 20 µg sodium cholate modified SPEs.

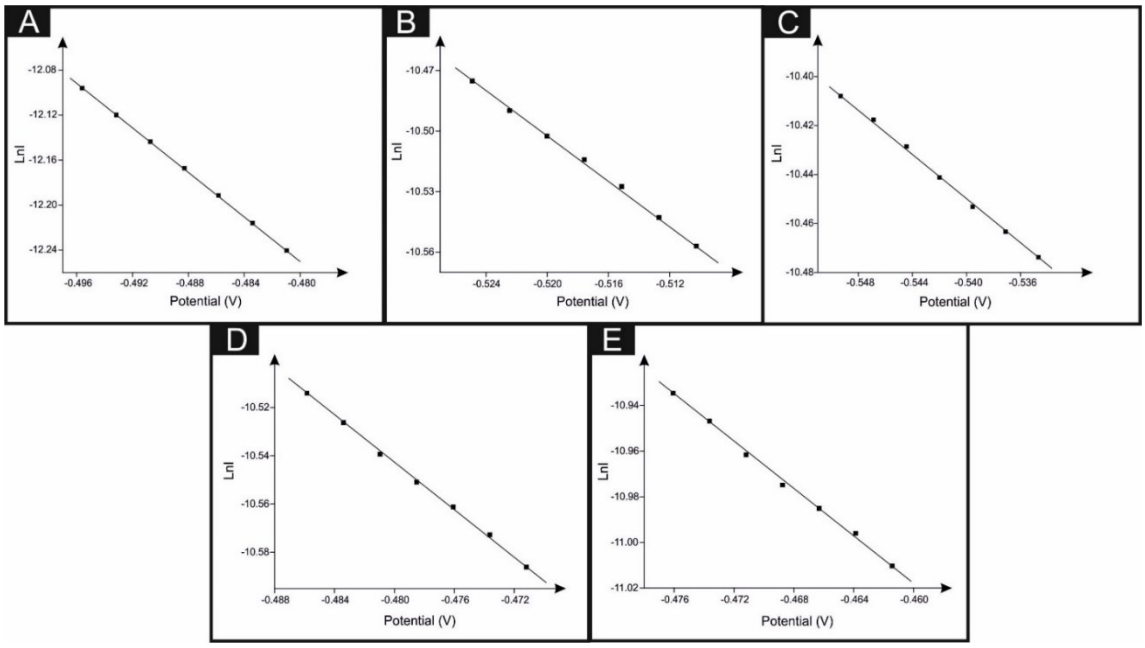

Figure 6.5: Illustrates Tafel plots for unmodified (A), 2 (B), 4 (C), 10 (D) and 20 µg (E) sodium cholate modified SPEs.

Where $\alpha n'$ values of 0.13, 0.15, 0.15 and 0.14 were obtained, with a Nernstian potential increase of 88.37, 96.70, 98.39 and 93.28 mV per order of magnitude of current respectively. In the case of pristine 2D-hBN modified SPEs of masses 108, 216 and 324 ng, $\alpha n'$ values of 0.17, 0.11 and 0.11 were obtained, with a Nernstian potential increase of 113.47, 75.63 and 69.22 mV per order of magnitude of current respectively. This infers that more current flows using surfactant-exfoliated 2D-hBN, sodium cholate and pristine 2D-hBN modified electrodes in comparison to bare SPEs. Hence it is suggested the transfer of the first electron is electrochemically

irreversible, so $n' = 1$ and α values of 0.25 and 0.14, 0.12, 0.12 and 0.12 are obtained for unmodified and 7.5, 15, 37.5 and 75 ng surfactant-exfoliated 2D-hBN modified SPEs respectively. Furthermore, α values of 0.13, 0.15, 0.15 and 0.14 were found to correspond to sodium cholate modified SPEs. Finally, the α values of 108, 216 and 324 ng pristine 2D-hBN modified SPEs corresponded to 0.17, 0.12 and 0.11 respectively. The number of electrons transferred overall, n, was deduced using the Randles-Ševćik equation (4.2) outlined previously in chapter 4 for an irreversible electrochemical process. A literature value of 0.9 mM [94, 105] is assumed for the oxygen saturated solution, and a literature diffusion coefficient value of 2.0×10^{-5} $cm^2\ s^{-1}$.[106] A value of $n = 2.66$ for an unmodified SPE was obtained whereas values of $n = 3.45$, 3.04, 2.91 and 2.53 were deduced for 7.5, 15, 37.5 and 75 ng surfactant-exfoliated 2D-hBN respectively and $n = 2.79$, 2.75 , 2.91 and 2.68 for 2, 4, 10 and 20 μg sodium cholate modified SPEs. Pristine 2D-hBN modified SPEs of masses 108, 216 and 324 ng resulted in values of $n = 2.45$, 2.15 and 1.90 respectively. This suggests the electrochemical reduction of oxygen using an unmodified, surfactant-exfoliated 2D-hBN, sodium cholate and pristine 2D-hBN modified SPEs produces hydrogen peroxide (H_2O_2) rather than the desirable product of H_2O. Previous studies have shown pristine 2D-hBN followed the two electron pathway mechanism and formed H_2O_2 when immobilised upon a gold substrate for the ORR.[69] The observed average number of electrons transferred indicates that there is a similar mechanism for the ORR when utilising other 2D materials (graphene).[94]

Next, hydrogen peroxide (H_2O_2) yields were estimated for unmodified, surfactant-exfoliated 2D-hBN, sodium cholate and pristine 2D-hBN modified SPEs. First, the capacitance of an electrochemical process is estimated utilising: $C = I/v$, where C is the capacitance, I is the observed peak current at a certain potential and v

is the scan rate. Next, the charge is calculated using: $Q = CV$, where Q is the charge and V is the potential. Resultantly, $Q = nFN$ enables the amount of oxygen electrolysed in the reaction to be calculated, where n is the number of electrons transferred, F is the Faraday constant and N is the number of moles of oxygen electrolysed. There is a 1 : 1 stoichiometric ratio of oxygen produced to H_2O_2, thus the concentration of oxygen electrolysed is theoretically the same as the concentration of H_2O_2 produced in the electrochemical reaction. Therefore, the estimated H_2O_2 yields were calculated for an oxygenated 0.1 M H_2SO_4 solution at a fixed volume of 10 mL utilising unmodified, surfactant-exfoliated 2D-hBN, sodium cholate and pristine 2D-hBN modified SPEs of masses ranging from 7.5 – 75 ng, 2 – 20 μg and 108 – 324 ng respectively, at a scan rate of 100 mV s^{-1}. It was estimated that the concentration of H_2O_2 electrolysed when utilising unmodified SPEs was 2.49 nM, whereas the surfactant-exfoliated 2D-hBN modified SPEs resulted in 1.41, 1.12, 0.98 and 0.99 nM of H_2O_2 being produced for 7.5, 15, 37.5 and 75 ng 2D-hBN respectively, thus a decrease. Comparatively, sodium cholate modified SPEs resulted in 1.08, 1.23, 1.20 and 1.09 nM of H_2O_2 being produced for 2, 4, 10 and 20 μg sodium cholate respectively. Finally, pristine 2D-hBN modified SPEs resulted in 2.78, 3.01 and 3.22 nM of H_2O_2 being produced for 108, 216 and 324 ng respectively. This suggests that surfactant-exfoliated 2D-hBN, sodium cholate and pristine 2D-hBN modified SPEs follow a similar mechanism to unmodified SPEs for the ORR, given the minimal changes in peroxide yield.

A key factor in terms of the analytical performance of sensors is the inherent reproducibility of the response. The reproducibility of the electrode materials of interest was thus explored in acidic conditions with different masses of surfactant-exfoliated 2D-hBN, sodium cholate and pristine 2D-hBN deposited on the SPEs. A

percentage relative standard deviation (% RSD) in the analytical signal of 7.30 % was observed for the unmodified SPE (N = 3) at scan rate 100 mV s^{-1}. This level of reproducibility is common for printed substrates and is a drawback for SPEs as reproducibility is slightly compromised for mass production. The 7.5, 15, 37.5, and 75 ng surfactant 2D-hBN modified SPE (N = 3; 100 mV s^{-1}) gave % RSD values in the analytical signal of 0.35, 0.47, 1.21, and 2.08 %, respectively. Furthermore, the 2, 4, 10, and 20 μg sodium cholate modified SPE (N = 3; 100 mV s^{-1}) gave % RSD values in the analytical signal of 0.44, 0.71, 1.09, and 2.33 %, respectively. Finally, the 54, 108, 216, and 324 ng pristine 2D-hBN modified SPE (N = 3; 100 mV s^{-1}) gave % RSD values in the analytical signal of 1.81, 8.96, 3.45, and 12.59 % respectively. The low % RSD measurements obtained for the modified electrodes highlight the reproducibility of the drop-casting method for 2D-hBN and sodium cholate upon SPEs.

If one considers the key observation of 2D-hBN utilised towards the ORR with surfactant fabrication compared to the surfactant-free approach, the former produces a greater reduction in the overpotential towards the ORR. There are two scenarios: the first is that different surface morphologies are evident. That is few layer 2D-hBN *via* the surfactant protocol *vs.* few to multi-layer 2D-hBN, which leads towards its bulk form where the electrochemical properties of bulk h-BN are known to be inferior compared to 2D-hBN.[178] Secondly, the surfactant is contributing to the response, as can be seen from control experiments, the response is due to the combination of the surfactant and 2D-hBN.

6.3.2 Exploring 2D-hBN as a Capacitive Material

Capacitance measurements of the 2D-hBN material was next considered. In order to benchmark this approach, first considered is the cyclic voltammetric responses of the unmodified graphite based electrode material (SPE) utilising a two-electrode system in 0.1 M H_2SO_4 (scan rate 100 m Vs^{-1}) and observe the response exhibited upon immobilisation of pristine and surfactant-exfoliated 2D-hBN masses ranging from 7.5 to 75 ng. A sodium cholate control coverage study of masses ranging from 2 – 20 µg, equating to the same volume of surfactant-exfoliated 2D-hBN drop-cast onto the electrode surface was also performed. Figure 6.6 depicts typical voltammograms obtained, where it is clear the capacitance of pristine 2D-hBN, surfactant-exfoliated 2D-hBN and sodium cholate modified SPEs is greatly superior to that of unmodified SPEs, indicated by the larger current passed.

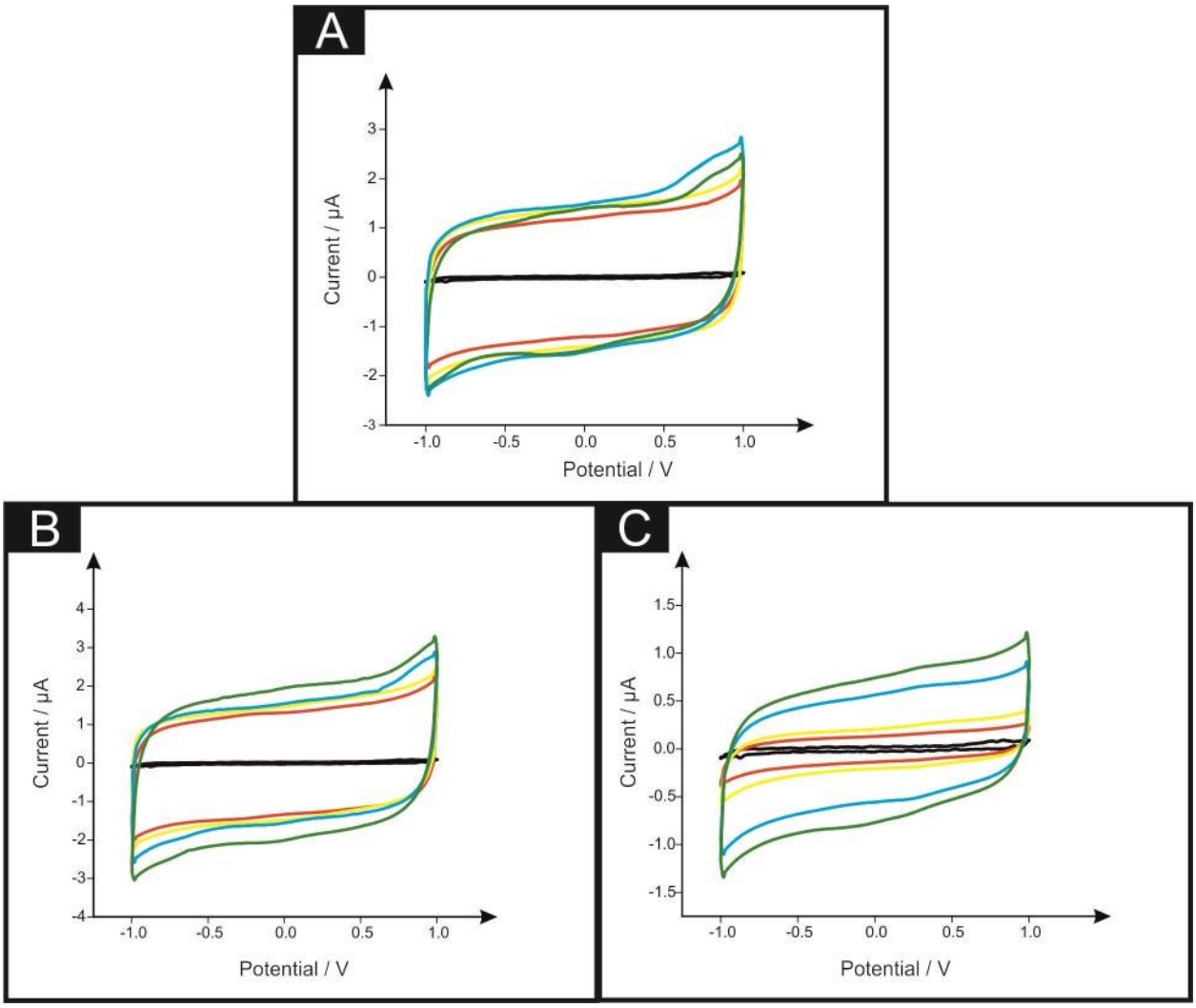

Figure 6.6: Typical cyclic voltammograms recorded in 0.1 M H_2SO_4 with surfactant-exfoliated 2D-hBN masses of: 7.5 (red line), 15 (yellow line), 37.5 (blue line) and 75ng (green line) immobilised upon SPEs (A). Sodium cholate masses of: 2.0 (red line), 4.0 (yellow line), 10.0 (blue line) and 20.0 µg (green line) immobilised upon SPEs (B). Pristine 2D-hBN masses of: 7.5 (red line), 15 (yellow line), 37.5 (blue line) and 75ng (green line) immobilised upon SPEs (C). In all cases, the black line represents an unmodified (bare) SPE. Scan rate: 100 mV s^{-1}.

Analysis of these voltammograms is depicted in Figure 6.7A, where a comparison study between the responses of unmodified, 75 ng pristine 2D-hBN, 75 ng surfactant-exfoliated 2D-hBN and 20 µg sodium cholate modified SPEs is observed.

It is clear that the unmodified SPEs display the lowest capacitance. Whereas immobilisation of 75 ng pristine 2D-hBN upon an SPE increases the observed capacitance (due to an increase in current), comparatively, 75 ng surfactant-exfoliated 2D-hBN immobilised upon an SPE exhibits a far superior capacitance in comparison to the pristine 2D-hBN of the same mass. To rationalise this effect, a control study utilising 20 μg sodium cholate immobilised upon an SPE was carried out, and it is established that sodium cholate modified SPEs *per se* offer the highest capacitance. This suggests the surfactant sodium cholate dominates the response.

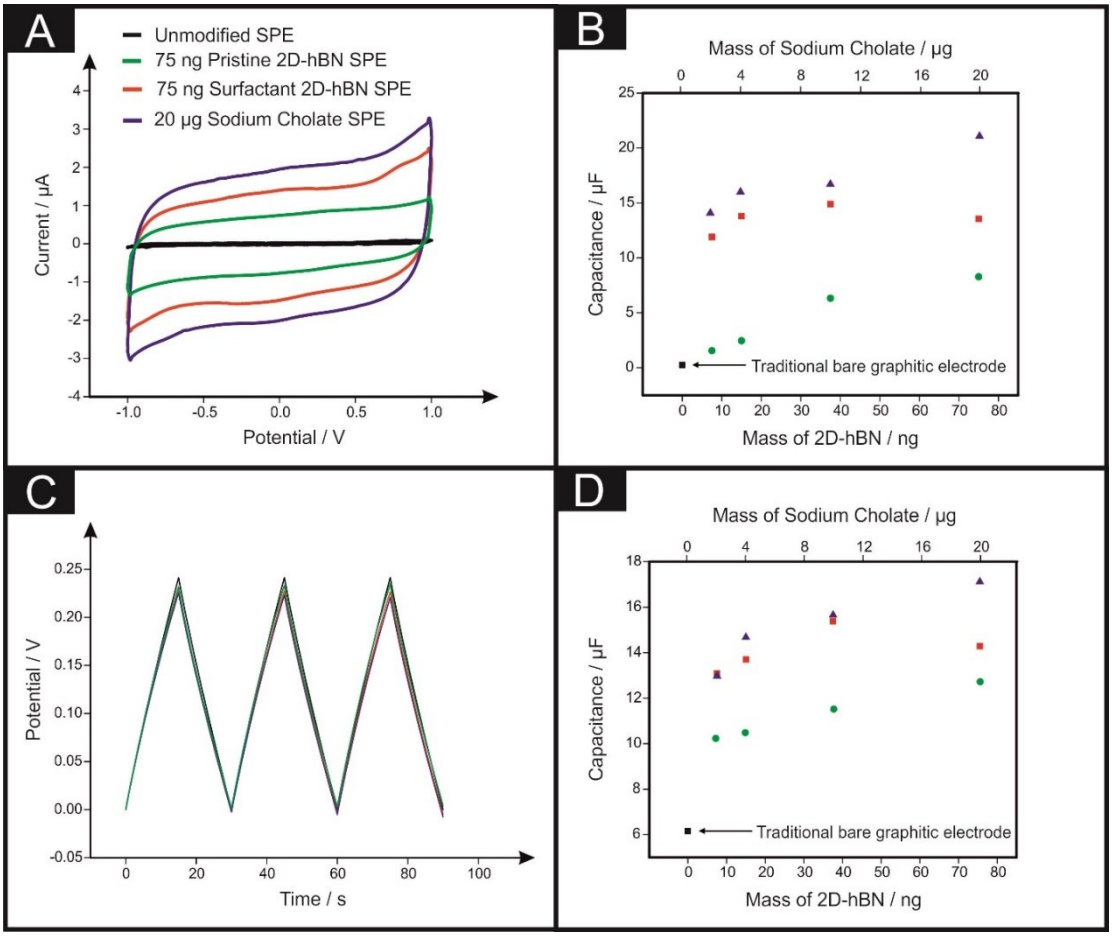

Figure 6.7: Typical cyclic voltammograms (A) recorded in 0.1 M H_2SO_4 with unmodified (black line) and 75 ng pristine 2D-hBN (green line), 75 ng surfactant-exfoliated 2D-hBN (red line) and 20 µg sodium cholate (blue line) modified SPEs. Scan rate: 100 mV s^{-1}. (B) Analysis of voltammograms (Figure 6.6) illustrates the effects of SPEs modified with masses of pristine 2D-hBN (green) and surfactant-exfoliated 2D-hBN (red), mass range: 7.5, 15, 37.5 and 75 ng along with sodium cholate (blue) mass range: 2, 4, 10 and 20 µg vs. the capacitance (µF). (C) Typical charge/discharge profiles recorded in 0.1 M H_2SO_4 with unmodified (black) 75 ng pristine 2D-hBN (green), 75 ng surfactant-exfoliated 2D-hBN (red) and 20 µg sodium cholate (blue) modified SPEs. (D) Analysis of charge/discharge profiles illustrates the effects of SPEs modified with masses of pristine 2D-hBN (green) and surfactant-exfoliated 2D-hBN (red), mass range: 7.5, 15, 37.5 and 75 ng along with sodium cholate (blue) mass range: 2, 4, 10 and 20 µg, vs. the capacitance (µF).

To investigate this further, the capacitance was deduced for unmodified, pristine 2D-hBN, surfactant-exfoliated 2D-hBN and sodium cholate modified SPEs. The capacitance of the working electrode, C_{WE}, was calculated from the

corresponding voltammograms (see Figure 6.6) using the following equation: $C_{WE} = 2\left(\frac{I}{v\Delta V}\right)$ where C_{WE} is the capacitance exhibited by the working electrode, I is the current, v is the scan rate and ΔV is the difference in potential ($V_2 - V_1$) for each scan. Figure 6.7B depicts the values obtained, where an unmodified SPE is found to have a capacitance 0.24 µF, whereas immobilisation of 75 ng pristine 2D-hBN, 75 ng surfactant-exfoliated 2D-hBN and 20 µg sodium cholate upon an SPE increases the capacitance to 8.28, 13.55 and 21.07 µF respectively. Hence, it is clear sodium cholate modified SPEs offer the highest capacitance in contrast to pristine and surfactant-exfoliated 2D-hBN with a significant increase in capacitance observed in comparison to an unmodified SPE in each case. Furthermore, it is evident in Figure 6.7B that the capacitance of surfactant-exfoliated 2D-hBN decreases upon 75 ng 2D-hBN immobilisation on an SPE, with the highest value of 14.9 µF value observed upon 37.5ng 2D-hBN modification. Contrastingly, the capacitance of sodium cholate modified SPEs continue to increase upon each modification. Therefore, the response exhibited when utilising surfactant-exfoliated 2D-hBN modified SPEs, should not assumed to be solely due to 2D-hBN, rather the surfactant used in the production of 2D-hBN is dominating and improving the response of 2D-hBN, an effect comparable to that which was observed previously in the detection of oxygen. A summary of the results are shown in Table 6.2.

Mass of Pristine 2D-hBN ng	Capacitance µF	Mass of Surfactant-exfoliated 2D-hBN ng	Capacitance µF	Mass of Sodium Cholate µg	Capacitance µF
0	0.24	0	0.24	0	0.24
7.50	1.55	7.5	11.90	2.0	14.08
15.0	2.46	15.0	13.80	4.0	16.00
37.5	6.33	37.5	14.90	10.0	16.70
75.0	8.28	75.0	13.55	20.0	21.07

Table 6.2: A summary of the effect of increasing mass immobilisation of pristine 2D-hBN, surfactant-exfoliated 2D-hBN and sodium cholate modified SPEs upon capacitance µF. Note, capacitance values were obtained from cyclic voltammograms

Next, a galvanostatic charge/discharge study was performed using a two-electrode approach to compliment the setup utilised for supercapacitors within the field. Figure 6.7C illustrates the charge/discharge profiles obtained for unmodified, 75ng pristine 2D-hBN, 75 ng surfactant-exfoliated 2D-hBN and 20 µg sodium cholate modified SPEs. Capacitance measurements, utilising a two electrode system, were undertaken *via* a method outlined by Kampouris *et al*.[168] upon utilisation of the circuit with 300 µF parallel capacitors. This was implemented to improve the linearity of the slope of the charge/discharge profiles, thus allowing for a more accurate analysis of the capacitive characteristics to be established.[168, 179] This method is described below.

A systematic approach to characterising the capacitance of an electrode pair in parallel circuit with a capacitor is presented here. In order to best describe the benefit of this approach, the principles of capacitor theory should be understood. A specific example can be used, with three capacitors, which illustrates how utilising a parallel circuit can improve the interpretation of results. In this example three

capacitors of capacitance C_1, C_2 and C_3 are considered. It is assumed that the capacitor C_1 is the supercapacitor such that $C_1 = C_{supercapacitor}$. The first case where the capacitors are connected in parallel, as shown in Figure 6.8.

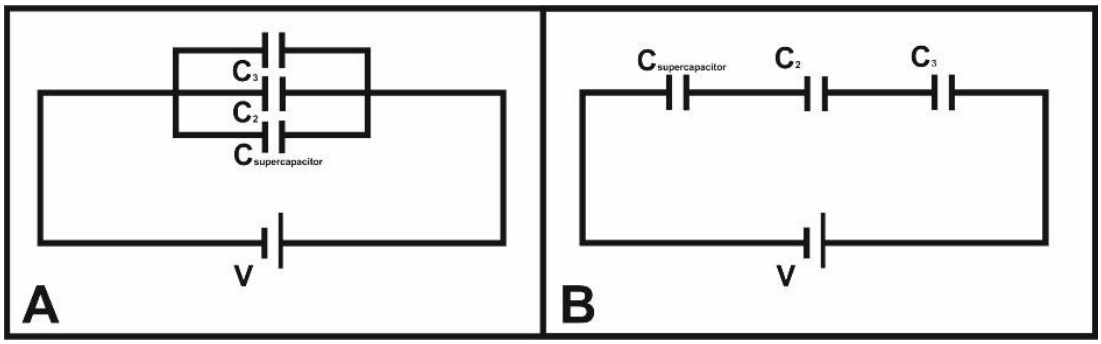

Figure 6.8: Capacitance circuits for the three-capacitor system, A) in parallel and B) in series.

In this case the potential across the capacitors is the same:

$$V = V_2 = V_3 = V_{Supercapacitor} \tag{6.1}$$

and as such the total charge is distributed equally across the capacitors:

$$Q = Q_2 = Q_3 = Q_{Supercapacitor} \tag{6.2}$$

and consequently:

$$C_{total}V = C_2V_2 + C_3V_3 + C_{Supercapacitor}V_{Supercapacitor} \tag{6.3}$$

however from equation 6.1:

$$C_{total}V = C_2V + C_3V + C_{Supercapacitor}V \tag{6.4}$$

and finally

$$C_{total} = C_2 + C_3 + C_{Supercapacitor} \quad (6.5)$$

In this example, the total capacitance of the parallel circuit is the sum of all the capacitances of each of the parallel branches.

The second case is where there are three capacitors in series as shown in Figure 6.8B. In this case the potential is split between each of the components in series:

$$V = V_2 + V_3 + V_{Supercapacitor} \quad (6.6)$$

and

$$V = V_2 + V_3 + V_{Supercapacitor} \quad (6.7)$$

therefore

$$\frac{Q}{C_{total}} = \frac{Q}{C_2} + \frac{Q}{C_3} + \frac{Q}{C_{supercapacitor}} \quad (6.8)$$

and finally

$$\frac{1}{C_{total}} = \frac{1}{C_2} + \frac{1}{C_3} + \frac{1}{C_{supercapacitor}} \quad (6.9)$$

In this case the total capacitance of the series circuit is the sum of the inverse capacitances of the components.

If the effect of this comparison is considered on the analysis of the capacitive properties of the supercapacitor one can see the benefit of analysing the properties in a circuit of know capacitance. Figure 6.9 shows the various arrangements for analysis of the supercapacitor in parallel with a 100 µF capacitor. Either a single 100

µF capacitor is utilised in parallel shown in Figure 6.9B or a variable capacitor system is set to 100 µF in parallel, shown in Figure 6.9A. The effect this has on the observed charging cycle and the interpretation of the *dV/dt* are shown in Figure 6.9C. As a commercial grade capacitor has a nominally linear response, the resulting curve is a combination of a linear curve and the plateauing 'shark-fin' shaped curve that is often seen in experimental supercapacitor characterisation. The resulting curve still presents a relatively curved shape and as such poses the same problem as before, in that the determination of where to take the gradient for the characteristic capacitance is undefined. In order to address this, further evaluations of varying parallel capacitances are investigated.

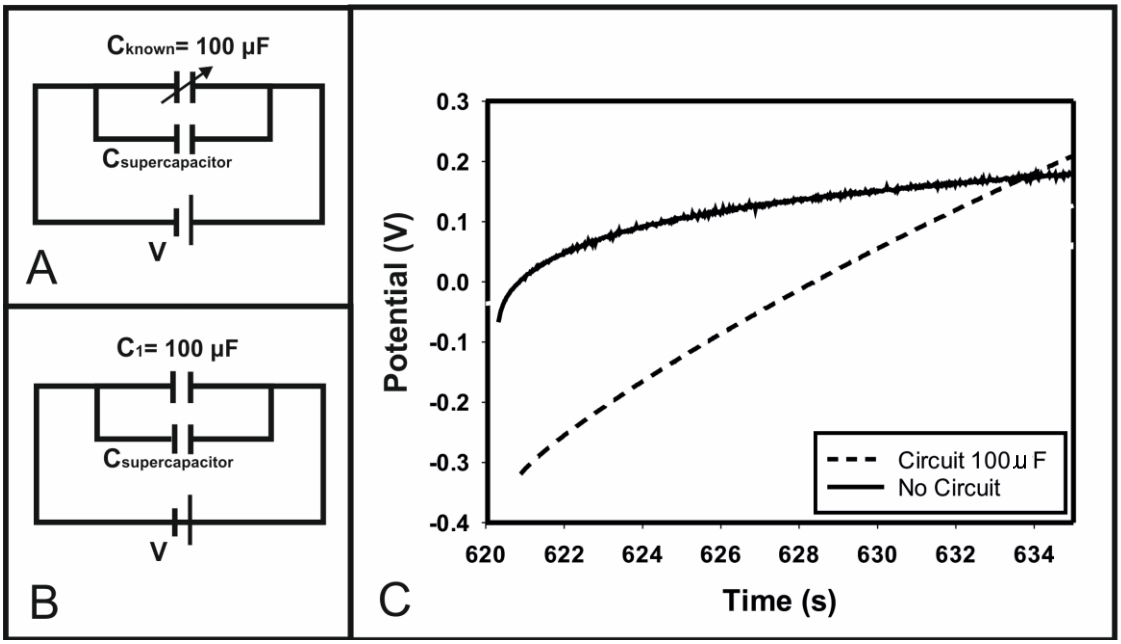

Figure 6.9: Evaluation of the capacitance of the supercapacitor integrated into a parallel circuit for 100 µF

Through increasing the parallel capacitance, the effect on the nominal gradient of the charging cycles can be seen. Figure 6.10 shows the arrangements for measuring in parallel with a 200 µF capacitor, or two 100 µF capacitors, which as shown previously are the same. In this case, the line is significantly smoother still and straighter.

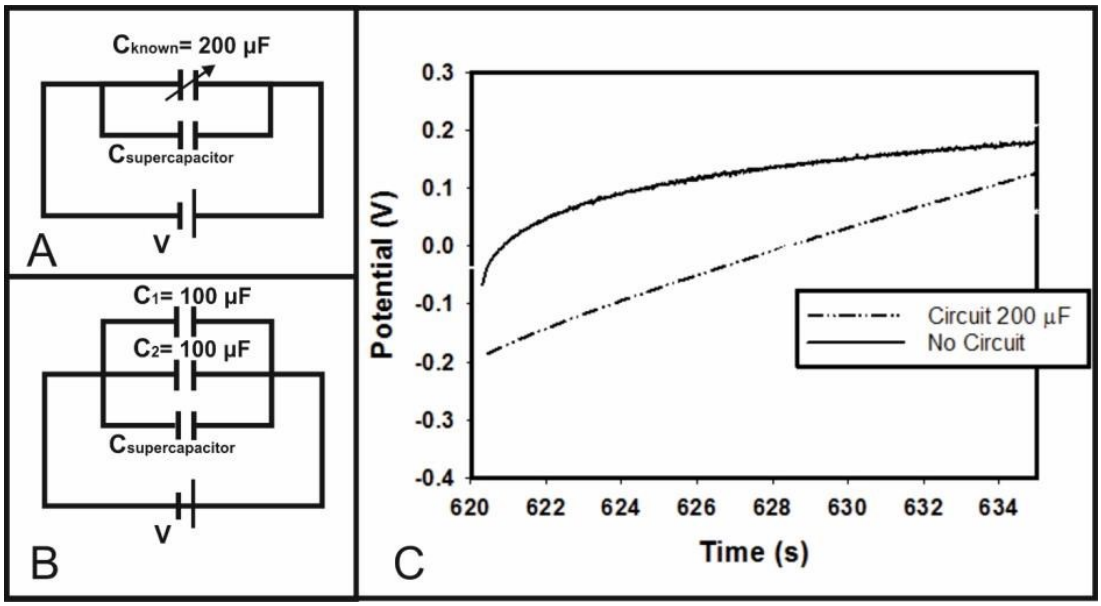

Figure 6.10: Evaluation of the capacitance of the supercapacitor integrated into a parallel circuit for 200 µF.

Increasing the parallel capacitance further still, to 620 µF, shown in Figure 6.11, the charge cycles are near linear in behaviour. As a result, the gradient of the whole line can be utilised to determine the capacitive properties of the system, and equation from the main body of text can be used to interpret the capacitance for the working electrode.

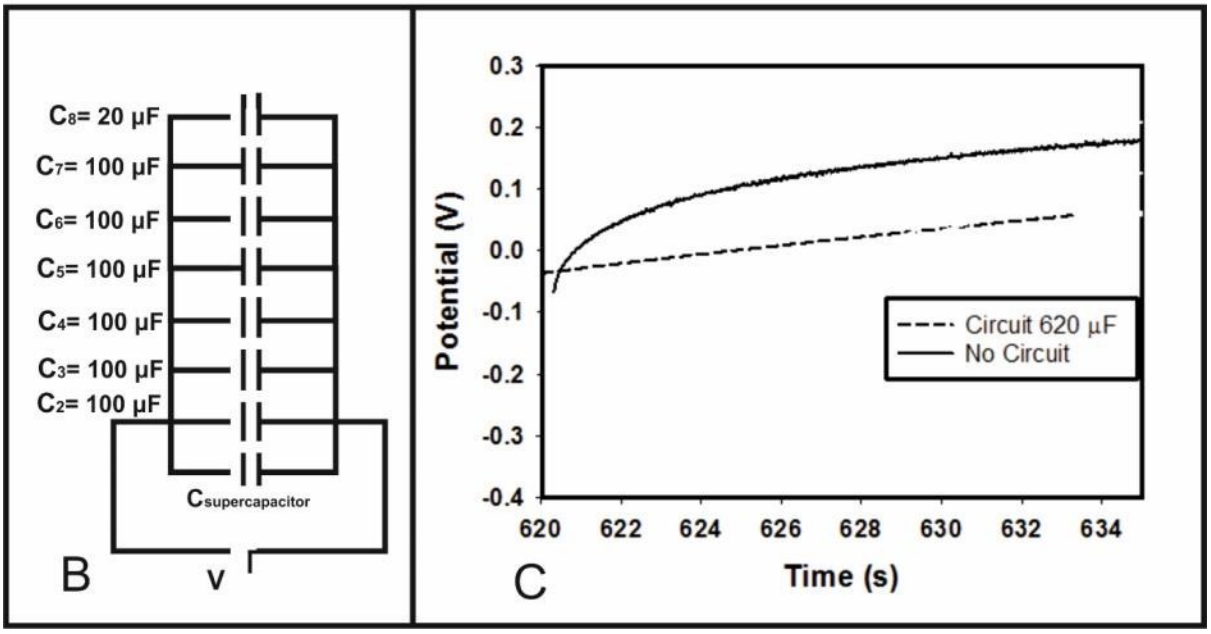

Figure 6.11: Evaluation of the capacitance of the supercapacitor integrated into a parallel circuit for 620 µF.

The result of this analysis is a systematic approach for providing a true value of the capacitance of an electrode without the risk of misinterpretation of the data. Also by utilising the component in a system the approach to the analysis of electrode properties, the set-up is limited to a 2-wire analysis, which is commercially more useful in terms of supercapacitors. This is a benefit, also, as there is yet to be a standardized approach to such analysis. This develops a uniform approach for all researchers, providing a system that improves repeatability and cohesion amongst the field. The approach consists of the following steps;

1) Perform charge/discharge cycles with the system alone, without any parallel capacitance;
2) Interpret the capacitance without the circuit;

3) Insert the variable capacitor/capacitor circuit in parallel with a low capacitance, of the order of the value extracted from the interpretation without the circuit in steps 1) and 2);
4) Re-interpret the capacitance from the resulting charge cycle, with the parallel circuit in place.
5) If the charge properties are still not linear increase the capacitance until a linear signal is achieved;
6) Interpret the *true capacitance* from the resulting linear charge response.

Returning to Figure 6.7C, it is shown that the potential of the charge/discharge profiles incrementally decrease upon immobilisation of 75 ng pristine 2D-hBN, 75 ng surfactant-exfoliated 2D-hBN and the highest reduction is observed upon a 20 µg modified SPE, in comparison to an unmodified SPE, suggesting an increase in capacitance. To evaluate this further, the capacitance, C_{WE}, was calculated from the corresponding galvanostatic charge curve using the following equation:[168] $C_{WE} = \frac{1}{2}\left[\frac{I}{dV/dt} - C_{known}\right]$ where C_{WE} is the capacitance exhibited by the working electrode, I is the current, (dV/dt) is the slope of potential versus time and C_{known} is the capacitance of the parallel circuit.[168, 179] Analysis of charge/discharge profiles of unmodified SPEs, pristine and surfactant-exfoliated 2D-hBN modified SPEs, (masses ranging from 7.5 to 75 ng) and sodium cholate modified SPEs of masses ranging from 2 – 20 µg are exhibited in Figure 6.7D. An unmodified SPE is found to have a capacitance of 6.15 µF, whereas immobilisation of 75 ng pristine 2D-hBN, 75 ng surfactant-exfoliated 2D-hBN and 20 µg sodium cholate upon an SPE increases the capacitance to 12.68, 14.20 and 17.36 µF respectively, at a current of 5.0 µA, (which provided the best signal to noise ratio). Hence, the charge/discharge profiles offer a similar trend to that of the voltammetry method when measuring the

capacitance and it is again clear sodium cholate modified SPEs offer the highest capacitance in contrast to pristine and surfactant-exfoliated 2D-hBN with a significant increase in capacitance observed when compared to an unmodified SPE in each modified case. Furthermore, it is again evident in Figure 6.7D that the capacitance of surfactant-exfoliated 2D-hBN decreases upon 75 ng 2D-hBN immobilisation on an SPE, with the highest value of 15.39 μF value observed upon 37.5ng 2D-hBN modification. Whereas, sodium cholate modified SPEs continue to exhibit an increase in capacitance upon each modification. Pristine 2D-hBN modification offers the least favourable increase in capacitance. Thus, it is established, from charge/discharge profiles and voltammograms, the surfactant, sodium cholate, used in the exfoliation of 2D-hBN is dominating the observed beneficial response towards capacitance measurements and this effect is not due solely to 2D-hBN (a summary of the results are reported in Table 6.3).

	Material					
	Unmodified (bare) SPE	**Pristine 2D-hBN**	**Surfactant 2D-hBN (2D-hBN)**	**Surfactant 2D-hBN (sodium cholate)**	**Surfactant 2D-hBN (2D-hBN + sodium cholate)**	**Sodium Cholate**
Mass	0.00030g	75 ng	75 ng	20 µg	2.0075×10^{-5} g	20 µg
Capacitance C_{WE} (µF)	6.15	12.69	14.15	14.15	14.15	17.36
Specific Capacitance C_S (F g^{-1})						
Method 1	0.02	169.15	188.76	0.71	0.71	0.87
Method 2	N/A	169.13	188.74	0.69	0.68	1.72
Method 3	N/A	87.12	106.73	0.40	0.40	1.12
Areal Capacitance C_A (µF cm^{-2})	87.02	179.44	200.24	200.24	200.24	245.58
Volumetric Capacitance C_V (F cm^{-3})	0.058	387.35	432.26	0.71	2.32	0.86

Table 6.3: A summary of the effect of increasing mass immobilisation of pristine 2D-hBN (75 ng), surfactant-exfoliated 2D-hBN (75 ng) and sodium cholate (20 µg) upon SPEs towards; capacitance (C_{WE}) µF, specific capacitance (C_S) F g^{-1}, areal capacitance (C_A) µF cm^{-2} and volumetric capacitance (C_V) F cm^{-3}. The current is held at 5.0 µA throughout. Note capacitance measurements are obtained from charge/discharge profiles

Additionally, a capacitive retention study over 500 charge/discharge cycles is depicted within Figure 6.12, demonstrating the incorporation of sodium cholate in the fabrication process of 2D-hBN results in a negative effect upon its' cycling stability, with the highest retention shown utilising pristine 2D-hBN.

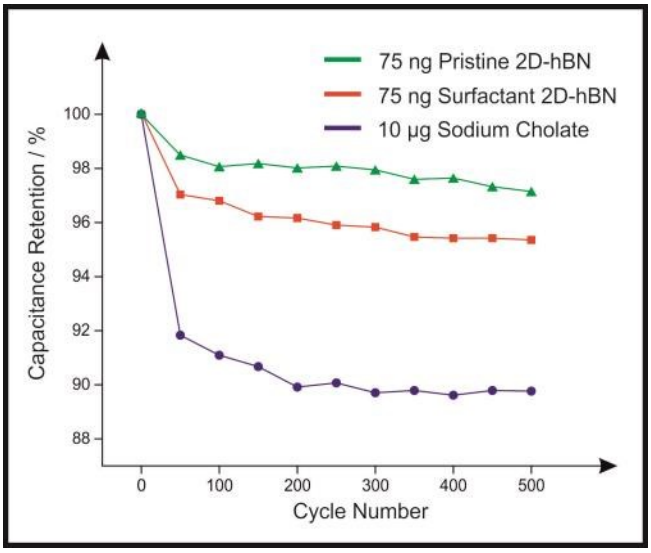

Figure 6.12: Capacitance retention 500 life cycle test obtained from charge/discharge profiles in 0.1M H_2SO_4 utilising a 75 ng pristine 2D-hBN, 75 ng surfactant-exfoliated 2D-hBN and 10 µg sodium cholate modified SPE, at a current of 5.0 µA.

Attention was next turned towards obtaining the specific capacitance (C_S) values of unmodified, pristine 2D-hBN, surfactant-exfoliated 2D-hBN and sodium cholate modified SPEs from said charge/discharge profiles. Current literature utilises an array of methods in the calculation of C_S, however the differences observed for each method are not reported. Thus, in this work a diverse range of methods were utilised to calculate the C_S values and Table 6.3 exhibits the differences observed. Method 1 is the typical analysis of electrode performance, which assumes that all of

the performance is a result of the added material; method 2 evaluates the improved specific capacitance as a result of the material added to the electrode by reducing by the capacitive value of the unmodified electrode; and method 3 indicates the specific capacitance associated with the drop-cast material only. From these equations, $C_{WE\ (modified)}$ is the capacitance (F) of the material immobilised upon an SPE, $C_{WE\ (unmodified)}$ is the capacitance (F) of the unmodified (bare) SPE. Furthermore, m_1 is the mass (g) of material immobilised upon an SPE and m_2 is the mass (g) of an unmodified (bare) SPE.

Method 1:

$$C_s = \frac{C_{WE\ (modified)}}{m_1}$$

Method 2:

$$C_s = \left(\frac{C_{WE\ (modified)}}{m_1}\right) - \left(\frac{C_{WE\ (unmodified)}}{m_2}\right)$$

Method 3:

$$C_s = \frac{C_{WE\ (modified)} - C_{WE\ (umodified)}}{m_1}$$

The hope is that standardisation of measuring the capacitance of materials can been achieved in the academic literature. Table 6.3 exhibits the C_S values obtained for unmodified, 75ng pristine 2D-hBN, 75 ng surfactant-exfoliated 2D-hBN and 20 µg sodium cholate modified SPEs. The C_S values for 75 ng pristine 2D-hBN immobilised upon an SPE obtained are 169.15, 169.13 and 87.12 F g^{-1} when utilising

methods 1, 2 and 3 respectively. Whereas, surfactant-exfolaited 2D-hBN, for which 75 ng 2D-hBN is specifically analysed offers C_s values of 188.76, 188.74 and 106.73 F g^{-1} for methods 1, 2 and 3 respectively. Thus, an increase C_S in comparison to pristine 2D-hBN is observed. Comparatively, when evaluating surfactant-exfoliated 2D-hBN for which 20 µg sodium cholate is specifically analysed, C_S values of 0.71, 0.69 and 0.40 are observed when utilising method 1, 2 and 3 respectively. Thus it is apparent when investigating surfactant-exfoliated 2D-hBN, there is a significant difference in C_S value when analysing either 2D-hBN or sodium cholate. Note each case has the same capacitance value (14.15 µF). The combination of 75 ng 2D-hBN and 20 µg sodium cholate towards obtaining a C_S value for the surfactant-exfoliated 2D-hBN was also investigated. As a result, C_s values of 0.71, 0.68 and 0.40 F g^{-1} are observed when utilising methods 1, 2 and 3 respectively. Thus, due to the lower mass of the 2D-hBN, a higher C_S value is obtained in comparison to the sodium cholate, indicating the importance of evaluating all materials utilised in the exfoliation of 2D-hBN. Finally, a control study utilising 20 µg sodium cholate *per se* was investigated. Table 6.3 exhibits the C_S values obtained of 0.87, 1.72 and 1.12 F g^{-1} for methods, 1, 2 and 3 respectively. These values incrementally increase in comparison to 20 µg sodium cholate in 2D-hBN, due to the higher capacitance (17.36 µF). However, as explained above, due to the higher mass of sodium cholate in comparison to 2D-hBN, a lower *Cs* value is obtained. Therefore, it is important to consider both materials (2D-hBN and sodium cholate) when investigating the C_S values of surfactant-exfoliated 2D-hBN rather than solely 2D-hBN, as it is clear that significant differences are observed due to the mass implemented when calculating the C_S. Indeed, the utilisation of a 7.5 ng surfactant-exfoliated 2D-hBN modified

SPE (lowest mass) results in the highest C_S value (1745 F g^{-1}) see Figure 6.13 and Table 6.4.

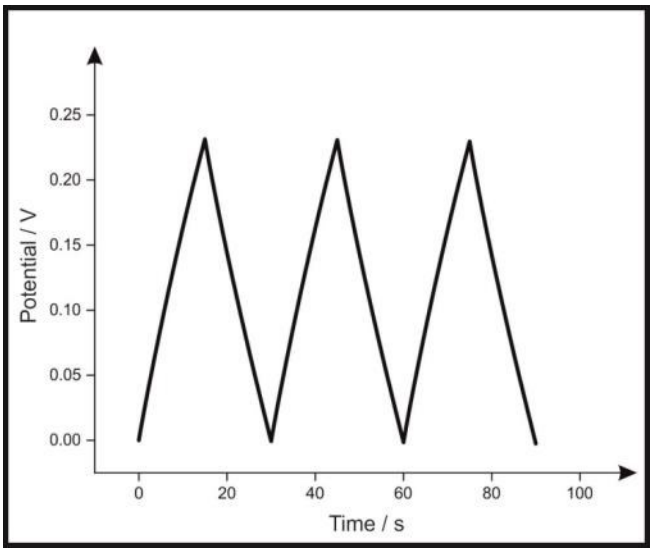

Figure 6.13: Typical charge/discharge profiles recorded in 0.1 M H_2SO_4 with a 7.5 ng surfactant-exfoliated 2D-hBN modified SPE. Note the average slope of the charge profile relates to 0.015329 V s^{-1} (N=3) at a current of 5.0 µA.

Consequently, the comparison of the capacitance (C_{WE}) values alone demonstrate more realistic properties when considering industrial applications. Furthermore, the volumetric and areal capacitance were also calculated for the 75 ng pristine 75 ng 2D-hBN, surfactant-exfoliated 2D-hBN and 20 µg sodium cholate, the values of which can be found in Table 6.3. A full summary for all masses of pristine 2D-hBN, surfactant-exfoliated 2D-hBN and sodium cholate towards measurements of capacitance (C_{WE}), specific capacitance (C_S), volumetric (C_V) and areal capacitance (C_A) are summarized within Table 6.4.

Mass of Pristine 2D-hBN ng	Capacitance µF	Capacitance µF cm^{-2} (C_A)	Capacitance F cm^{-3} (C_V)	Capacitance F g^{-1} (C_S) (method 1)	Capacitance F g^{-1} (C_S) (method 2)	Capacitance F g^{-1} (C_S) (method 3)
0	6.15	87.02	0.058	0.02	N/A	N/A
7.50	10.18	144.00	3108.63	1357.48	1357.46	537.16
15.0	10.43	147.54	1592.50	695.42	695.40	285.26
37.5	11.47	162.20	700.28	305.80	305.78	141.73
75.0	12.69	179.44	387.35	169.15	169.13	87.12
Mass of Surfactant 2D-hBN (2D-hBN ng)	**Capacitance µF**	**Capacitance µF cm^{-2} (C_A)**	**Capacitance F cm^{-3} (C_V)**	**Capacitance F g^{-1} (C_S) (method 1)**	**Capacitance F g^{-1} (C_S) (method 2)**	**Capacitance F g^{-1} (C_S) (method 3)**
0	6.15	87.02	0.058	0.02	N/A	N/A
7.5	13.09	185.09	3995.60	1744.80	1744.78	924.48
15.0	13.70	193.75	2091.27	913.22	913.20	503.06
37.5	15.39	217..65	939.67	410.34	410.32	246.27
75.0	14.15	200.24	432.26	188.76	188.74	106.73
Mass of Surfactant 2D-hBN (Sodium Cholate µg)	**Capacitance µF**	**Capacitance µF cm^{-2} (C_A)**	**Capacitance F cm^{-3} (C_V)**	**Capacitance F g^{-1} (C_S) (method 1)**	**Capacitance F g^{-1} (C_S) (method 2)**	**Capacitance F g^{-1} (C_S) (method 3)**
0	6.15	87.02	0.058	0.02	N/A	N/A
2	13.09	185.09	6.53	6.54	6.53	3.47
4	13.70	193.75	3.42	3.42	3.40	1.89
10	15.39	217..65	1.53	1.54	1.52	0.92
20	14.15	200.24	0.71	0.71	0.69	0.40
Mass of Surfactant 2D-hBN (both components g)	**Capacitance µF**	**Capacitance µF cm^{-2} (C_A)**	**Capacitance F cm^{-3} (C_V)**	**Capacitance F g^{-1} (C_S) (method 1)**	**Capacitance F g^{-1} (C_S) (method 2)**	**Capacitance F g^{-1} (C_S) (method 3)**
0	6.15	87.02	0.116	0.02	N/A	N/A
2.0075×10^{-6}	13.09	185.09	42.80	6.52	6.50	3.45
4.015×10^{-6}	13.70	193.75	22.44	3.41	3.39	1.88
1.00375×10^{-5}	15.39	217..65	10.08	1.53	1.51	0.92
2.0075×10^{-5}	14.15	200.24	4.64	0.71	0.68	0.40
Mass of Sodium Cholate µg	**Capacitance µF**	**Capacitance µF cm^{-2} (C_A)**	**Capacitance F cm^{-3} (C_V)**	**Capacitance F g^{-1} (C_S) (method 1)**	**Capacitance F g^{-1} (C_S) (method 2)**	**Capacitance F g^{-1} (C_S) (method 3)**
0	6.15	87.02	0.058	0.02	N/A	N/A
2.0	13.02	184.09	6.49	6.51	12.99	6.86

4.0	14.73	208.35	3.67	7.37	7.34	4.29
10.0	15.69	221.89	1.56	1.57	3.12	1.91
20.0	17.36	245.58	0.86	0.87	1.72	1.12

Table 6.4: A summary of the effect of increasing mass immobilisation of pristine 2D-hBN (7.5 - 75 ng), surfactant-exfoliated 2D-hBN (7.5 – 75 ng) and sodium cholate (2 -20 µg) modified SPEs towards capacitance (C_{WE}) µF, areal capacitance (C_A) µF cm^{-2}, volumetric capacitance (C_V) F cm^{-3} and specific capacitance (C_S) F g^{-1} . The current is held at 5.0 µA throughout. Note, capacitance values were obtained from charge/discharge profiles.

6.4 Conclusions

In this chapter, it has demonstrated for the first time that surfactant-exfoliated 2D-hBN exhibits an electrocatalytic effect towards the ORR when immobilised upon graphitic substrate (SPE). A potential reduction of *ca*. 0.50 V was observed upon immobilisation of 37.5 ng surfactant-exfoliated 2D-hBN on an SPE, in comparison to its bare equivalent. However, through the utilisation of control coverage studies, the large electrocatalytic effect is highly dependent upon the surfactant (sodium cholate) utilised, with a potential reduction of *ca.* 0.44 V observed when utilising *just* sodium cholate (no 2D-hBN) modified SPEs.

Furthermore, it was demonstrated for the first time surfactant-exfoliated 2D-hBN is an effective electrochemical supercapacitor material, with a specific capacitance value of up to 1745 F g^{-1} obtained for 7.5 ng surfactant-exfoliated 2D-hBN modified SPEs (Figure 6.13 and Table 6.4). Furthermore, a diverse range of methods are introduced and utilised to calculate the specific capacitance, a substantially overlooked and misinterpreted parameter within the literature allowing standardisation in the academic literature to be achieved.

In both electrochemical systems, the surfactant was the overall dominating factor in the observed 2D-hBN electrocatalytic and capacitive (μF) response. Thus, future research involving surfactant-exfoliated 2D-hBN should consider the electrochemical behaviour of the surfactant alone to allow the true de-convolution of the electrochemical response of 2D-hBN; without this control experiment, 2D-hBN can be wrongly attributed to electrochemically catalytic/active when actually it is the surfactant itself being the more active material.

The following chapter continues to investigate the effect of the fabrication process towards the observed electrochemistry of 2D-hBN. A biological approach is

considered in the sensing of dopamine (DA) and its common interferents ascorbic acid (AA) and uric acid (UA), first studied in chapter 5.

Chapter 7 : Surfactant-Exfoliated 2D hexagonal Boron Nitride (2D-hBN) Explored as a Potential Electrochemical Sensor for Dopamine: surfactants significantly influence sensor capabilities

In this chapter, surfactant exfoliated 2D hexagonal Boron Nitride (2D-hBN) nanosheets are explored as a potential electrochemical sensing platform and evaluated towards the electroanalytical sensing of dopamine (DA) in the presence of the common interferents, ascorbic acid (AA) and uric acid (UA). Surfactant exfoliated 2D-hBN nanosheets fabricated using sodium cholate in aqueous media are electrically wired *via* a drop-casting modification process onto disposable screen-printed graphite electrodes (SPEs). The performance of these 2D-hBN modified SPEs are critically evaluated and the effect of 'mass coverage' towards the detection of DA, AA and UA is demonstrated. Previous studies utilising surfactant-free (pristine) 2D-hBN modified SPEs (see chapter 5) have shown a beneficial effect towards the detection of DA, AA and UA when compared to the underlying/unmodified graphite-based electrode. Thus the effect of fabrication process of 2D-hBN towards DA, AA and UA is considered with control experiments performed in order to de-convolute the electrochemical response and effectively evaluate the 'underlying surface / surfactant / 2D materials' electrocatalytic[4]

[4] A. F. Khan, D. A. C. Brownson, C. W. Foster, G. C. Smith and C. E. Banks, *Analyst*, 2017, **142**, 1756-1764

contribution. This chapter contains work that has been peer-reviewed and published in the academic literature.[4]

7.1.1 Introduction

Dopamine (DA), a catecholamine that exists in the extracellular fluid of the central nervous system, as previously described in chapter 5.[108, 109, 133, 180, 181] Irregular levels of this compound can lead to neurological disorders such as Schizophrenia, attention deficit hyperactivity disorder (ADHD) and Parkinson's disease.[108, 112, 182] Moreover, as previously described in chapter 5 electrochemical sensors are continuously developed for DA due to their many advantages.[183, 184] Resultantly, numerous efforts towards the electrochemical detection of DA are undertaken,[113-115] however as described in chapter 5, DA's co-existence with ascorbic acid (AA) often results in overlapping voltammetric signals and complicated voltammetry, hindering detection.[116] Thus, research is currently focused on imparting improved analytical responses for these two compounds.[117, 118] Furthermore, in certain sample matrixes, uric acid (UA) is also problematic.[119,121] As such, an electrode material that improves the electrochemical detection capabilities of DA, whilst efficiently differentiating the peaks of common interferents and that is not prone to surface fouling, is highly sought.[120]

Previous studies have utilised 2D materials towards the detection of DA, AA and UA (see Figure 5.1 for structures of said compounds).[40, 130, 133, 136] Han *et al*.[40] observed that a GC electrode modified with chitosan-graphene allowed for the simultaneous detection of DA, AA and UA. They reported three distinct oxidation peaks at *ca*. 0.12, 0.24 and 0.33 V, which were attributed to AA, DA and UA respectively.[40] Conversely, an unmodified GC electrode exhibited a convoluted

single peak at *ca*. 0.49 V. In other research, Sheng *et al*.[130] found the simultaneous detection of DA, AA and UA was viable when utilising nitrogen-doped graphene modified upon a GC electrode, whilst Tian *et al*.[136] explored the simultaneous detection of AA, DA and UA utilising a GC electrode after modification with graphene (decorated with gold nanoparticles) and found the simultaneous detection of these compounds was also viable (at oxidation potentials of *ca*. 0.22, 0.43 and 0.55 V respectively). Such a response is significantly beneficial over that of a bare/unmodified GC electrode, where a single oxidation peak was observed at *ca*. 0.35 V. Moreover, Sun *et al*.[133] utilised gold nanoparticle decorated MoS_2 nanosheet modified GC electrodes and reported the peak separation between DA/AA and DA/UA at *ca*. 0.15 and 0.14 V respectively; thus allowing for the simultaneous detection of these compounds, which is not possible at the unmodified GC electrode. A summary of the different 2D materials utilised in the detection of DA can be found in table 7.1.

Electrode Material	Electrocatalytic (with regards to)	Dopamine LOD (μM)	Explored in the presence of:	Electrochemical method	Ref.
AuNPs@MoS_2	GC	0.05	UA, AA	DPV	133
Chitosan–graphene	GC	1.00	UA, AA	DPV	40
AuNPs–β-CD–Graphene	GC	0.15	UA, AA	SWV	136
Functionalised graphene	Bare graphite	0.25	UA, AA	DPV	138
PtNPs@MoS_2	GC	0.17	UA	DPV	185
Nitrogen doped graphene	GC	0.25	UA, AA	DPV	130
AuNPs@MoS_2	GC	0.08	AA	DPV	186
Graphene	GC	2.64	AA	DPV	187
GNS-CNTs/MoS_2	GC	0.05	_	DPV	188
MoS_2-RGO	GC	0.94	AA	DPV	189
Pristine 2D-hBN	SPE	0.65	UA, AA*	DPV	190

Surfactant Exfoliated 2D-hBN	SPE	1.57	UA, AA*	DPV	This work

Table 7.1: A comparison of various 2D materials utilised towards the detection of DA. ***Key:*** *PtNP@MoS2, Platinum nanoparticle modified molybdenum disulfide;AuNP@MoS_2, GNS-CNTs/MoS_2, Molybdenum disulfide flowers placed on graphene nanosheets and multiwalled carbon nanotubes; MoS_2-RGO, Molybdenum disulphide – reduced graphene oxide; Gold nanoparticle modified molybdenum disulfide; AuNPs–β-CD–Graphene, Gold nanoparticles–β-cyclodextrin–graphene; 2D-hBN, 2D hexagonal boron nitride; GC, Glassy carbon electrode; CPE, Carbon paste electrode; functionalised graphene synthesised by solvothermal reduction of colloidal dispersions of graphite oxide; UA, Uric Acid; AA, Ascorbic Acid DPV, Differential Pulse Voltammetry; SWV, Square Wave Voltammetry.*

** DA and AA signal de-convolution is not possible upon simultaneous detection.*

What is evident from examination of previous literature, is that researchers often neglect two serious considerations that are vital to understanding the true performance of a given nanomaterial towards the resulting sensor: i) the implications that the fabrication route may impart onto the observed voltammetry; ii) the effects of the novel material's 'mass coverage' on their chosen supporting material.

It has previously been reported in this thesis (chapter 5) that surfactant-free (pristine) 2D hexagonal Boron Nitride (2D-hBN) nanosheets exhibit an electrocatalytic behaviour towards the sensing of DA when immobilised upon screen-printed graphite electrodes (SPEs).[190] Pristine 2D-hBN reduced the potential required for the electrochemical oxidation of by *ca*. 90 mV and increased the peak current/signal in comparison to unmodified/underlying SPEs.[190] Although the simultaneous detection of DA and AA was not viable, the simultaneous detection of DA and UA was achieved with this novel approach utilising pristine 2D-hBN as the sensing platform.[190] When utilising the pristine 2D-hBN modified SPEs, a beneficial increase in the peak separation between DA and UA was reported (*ca.* 50 mV increase *vs*. unmodified) whilst the pristine 2D-hBN based sensor offered improved peak currents/signal in contrast to an unmodified SPE.[190] Interestingly, no such beneficial response was observed for pristine 2D-hBN when it was modified/supported on GC and boron doped diamond (BDD) underlying electrodes. The observed beneficial response at 2D-hBN modified SPEs was attributed to the interaction between 2D-hBN and the roughness of the underlying SPE, whereas the comparatively smooth surface of a GC electrode hindered this.[190] This initial work demonstrated the importance of considering the influence of additional factors (other than that of the 2D material chosen) and their contribution to the observed

electrochemical response. There are now many routes to fabricate 2D materials, and surfactant exfoliation is a common and favourable approach due to its simplicity.[187]

Surfactant-exfoliated 2D-hBN has yet to be explored towards the detection of DA in the presence of AA and UA. As such, it is essential to demonstrate that care needs to be taken, not only with the choice of 2D material chosen, but also when considering its fabrication route, which can dramatically affect the electrochemical performance.

Herein, this chapter considers for the first time, the electrochemical oxidation of DA, AA and UA utilising surfactant (sodium cholate) exfoliated 2D-hBN nanosheet modified SPEs. Furthermore, control experiments, in the form of surfactant modified (in the absence of 2D-hBN) graphitic electrodes and mass-coverage studies are implemented in order to de-convolute the true electrochemical response, such that fundamental knowledge is uncovered concerning the influence of both the surfactant and surface coverage on the resulting electrochemical properties of the material under investigation. The effect of surfactant-exfoliated 2D-hBN has not yet been explored in this manner. Thus, herein proof of concept is shown.

7.2 Results and Discussion

Surfactant exfoliated 2D-hBN utilised towards the electrochemical detection of DA, AA and UA

The electron transfer reactions between surfactant-exfoliated 2D-hBN and DA, AA and UA were first studied separately using unmodified SPEs in order to benchmark the electrochemical system. Figure 7.1B, C and D depicts typical cyclic voltammograms obtained towards the electrochemical oxidation of 1 mM DA, AA and UA respectively (separately in pH 7.4 phosphate buffer solution (PBS)). When

utilising unmodified/bare SPEs, the anodic oxidation potentials are observed at +0.36 V, +0.38V and +0.49 V respectively for the electrochemical oxidation of DA, AA and UA. This agrees well with previous literature.[75]

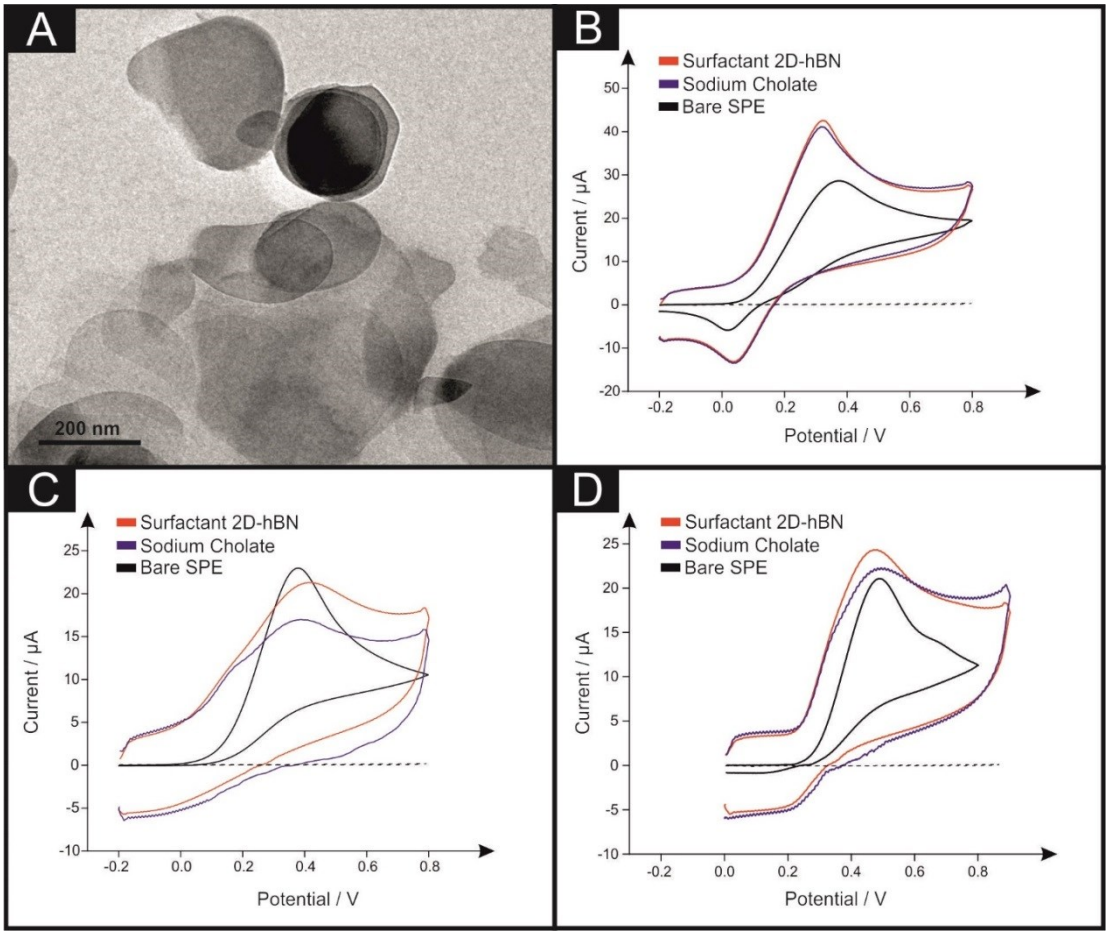

Figure 7.1: Typical TEM image of surfactant-exfoliated 2D-hBN after deposition onto a holey carbon film supported upon a Cu TEM grid (A). Also shown are typical cyclic voltammograms recorded in pH 7.4 PBS with (B) 1 mM DA, (C) 1 mM AA and (D) 1mM UA when utilising unmodified SPEs (black), and 150 ng surfactant exfoliated 2D-hBN (red) and 40 µg sodium cholate (blue) modified SPEs. The dashed line represents the blank PBS respectively. Scan rate: 100 mV s^{-1} (vs. SCE). Note that full coverage study data of the modified electrodes is presented in Figure 7.2 and Table 7.2

The electrochemical oxidation of DA, AA and UA was next considered using SPEs modified with increasing masses of surfactant-exfoliated 2D-hBN (a coverage study), ranging from 7.5 to 300 ng. Figure 7.1B depicts typical cyclic voltammograms obtained towards DA electrochemical oxidation at 150 ng surfactant-exfoliated 2D-hBN modified SPEs, where the potential required for oxidation decreases upon immobilisation of surfactant-exfoliated 2D-hBN when compared to the response at an unmodified SPE. Analysis of these voltammograms is presented in Figure 7.2A and Table 7.2, where an overall decrease in DA oxidation potential of *ca.* 40 mV (compared to an unmodified SPE) is exhibited. Furthermore, the observed peak currents evidently improve upon the immobilisation of increasing surfactant-exfoliated 2D-hBN masses (Figure 7.2B and Table 7.2). Specifically, the current increases from 28.0 μA (unmodified SPE) to 35.8 μA at a surfactant-exfoliated 2D-hBN modification mass of 150 ng. Note, the peak currents observed herein (measured at the baseline of each voltammogram respectively), are not as a result of increased capacitance upon the utilisation of surfactant-exfoliated 2D-hBN modified SPEs, which is discussed later.

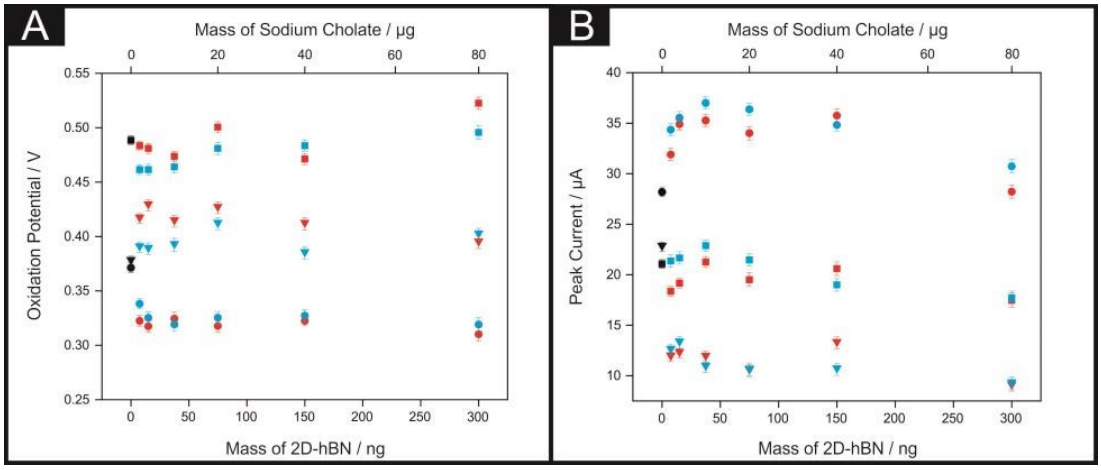

Figure 7.2: Analysis of the cyclic voltammograms of 7.5 – 300 ng surfactant-exfoliated 2D-hBN and (separately) 2 – 80 µg sodium cholate modified SPEs is presented in the form of plot (A), illustrating the oxidation potential of DA (circle), AA (inverted triangle) and UA (square) vs. mass of surfactant-exfoliated 2D-hBN immobilised (red) and equivalently oxidation potential of DA (circle), AA (inverted triangle) and UA (square) vs. mass of sodium cholate immobilised (blue). Plot (B) depicts the peak current of DA (circle), AA (inverted triangle) and UA (square) vs. mass of surfactant-exfoliated 2D-hBN immobilised (red) and equivalently peak current of DA (circle), AA (inverted triangle) and UA (square) vs. mass sodium cholate immobilised (blue). In plots A and B, the black circle, inverted triangle and square represent the unmodified SPE towards DA, AA and UA respectively. Scan rate: 100 mV s^{-1} (vs. SCE). Each data point (A and B) is the average and standard deviation (N = 3).

Electrode Material	Mass (ng)	Oxidation potential DA (V)	Oxidation potential AA (V)	Oxidation potential UA(V)	Oxidation Current DA (μA)	Oxidation Current AA (μA)	Oxidation Current UA (μA)
Surfactant-exfoliated 2D-hBN	0	0.36	0.38	0.49	28.0	22.9	21.1
	7.5	0.32	0.42	0.48	31.9	12.0	18.4
	15	0.32	0.43	0.48	34.9	12.4	19.2
	37.5	0.32	0.42	0.47	35.3	12.0	21.3
	75	0.32	0.42	0.50	34.0	10.6	19.5
	150	0.32	0.41	0.47	35.8	13.4	20.6
	300	0.31	0.40	0.52	28.2	9.1	17.5
Electrode Material	Mass (μg)	Oxidation potential DA (V)	Oxidation potential AA (V)	Oxidation potential UA (V)	Oxidation Current DA (μA)	Oxidation Current AA (μA)	Oxidation Current UA (μA)
Sodium cholate	0	0.36	0.38	0.49	28.0	22.9	21.1
	2	0.33	0.39	0.46	34.3	12.7	21.4
	4	0.33	0.39	0.46	35.5	13.4	21.7
	10	0.32	0.39	0.46	37.0	11.0	22.9
	20	0.33	0.41	0.48	36.4	10.7	21.5

40	0.33	0.39	0.48	34.8	10.8	19.0
80	0.32	0.40	0.50	30.7	9.4	17.7

Table 7.2: Tabulated data shown from Figure 7.2.

Interestingly, it has been shown previously in chapter 5, that surfactant-free (pristine) 2D-hBN immobilised upon SPEs offers a greater, more beneficial response towards DA oxidation, reducing the potential by *ca.* 90 mV.[190] Thus, to rationalise the observed difference in the DA anodic oxidation potentials and increased peak currents, control experiments were performed utilising sodium cholate modified SPEs (in the *absence* of 2D-hBN) towards DA oxidation in order to understand and de-convolute the role said surfactant, which may potentially, partake in the electrochemical process. Figure 7.1B depicts a typical cyclic voltammogram of a 20 μg sodium cholate modified SPE utilised towards DA oxidation. It is important to note that (throughout this study), the volume of surfactant utilised equates to the identical volume present within the specific and comparative surfactant-exfoliated 2D-hBN modification that was drop-cast onto the electrode surface, such that the *true* effect of the sodium cholate can be evaluated. The sodium cholate utilised for control experiments and exfoliation was also identical (see section 3.4.3). Returning to the observed electrochemical response, it is apparent within Figure 7.1B that a similar voltammetric signature towards DA oxidation (*ca.* 0.32 V) is observed at both the 150 ng surfactant-exfoliated 2D-hBN and the equivalent sodium cholate (with *no 2D-hBN present*) modified SPEs. Detailed analysis is presented in Figure 7.2 and Table 7.2 (coverage study), where SPEs modified with sodium cholate (mass range: 2 – 80 μg) give rise to similar electrochemical oxidation potentials and peak currents towards DA detection as the equivalent surfactant-exfoliated 2D-hBN modified SPEs. This is a significant observation, which suggests that the surfactant (sodium cholate) has a dominant role in the observed voltammetry recorded towards DA oxidation. Thus it is suggested the improved peak currents of DA in the anodic region and the increased capacitive response when utilising surfactant exfoliated 2D-

hBN and its sodium cholate modified SPE equivalent (in comparison to unmodified SPEs) is likely due to the oxidation of cyclohexanol (hydroxyl groups) of the surfactant *itself* (Figure 7.1B, Figure 7.2 and Table 7.2). Interestingly, in this case (given the 'greater' beneficial response recorded at pristine 2D-hBN with no surfactant present), the incorporation of the surfactant has an inhibiting effect on the electrochemistry of 2D-BN, as evidenced by the response shown upon the utilisation of pristine 2D-hBN modified SPEs upon direct comparison with the use of surfactant-exfoliated 2D-hBN modified SPEs.[190]

Equivalent studies to the aforementioned oxidation of DA were carried out towards the detection of AA and UA, utilising a range of equivalent surfactant exfoliated 2D-hBN (7.5 – 300 ng) and sodium cholate (2 – 80 μg) modified SPEs. Inspection of Figure 7.1C and 7.1D reveals that a 150 ng surfactant exfoliated 2D-hBN modified SPE increases the electrochemical oxidation potential of AA by *ca.* 30 mV and decreases the peak potential of UA by *ca.* 20 mV, whilst the peak currents decrease to 13.4 μA and increase to 20.6 μA respectively (when compared to the unmodified SPEs, *vide supra*). Detailed analysis is shown in Figure 7.2A, 7.2B and Table 7.2 where coverage studies reveal the inhibitory/detrimental effect of utilising surfactant- exfoliated 2D-hBN modified SPEs towards the detection of AA and UA. It has previously been reported in chapter 5 that pristine 2D-hBN modified SPEs exhibit a detrimental effect towards the detection of AA; inferred due to the oxidation mechanism of AA on carbon-based electrodes being invoked at specific functionalities and oxygenated surface sites (which 2D-hBN likely blocks).[190, 191] However, the case of UA detection was somewhat different, with pristine 2D-hBN modified SPEs exhibiting a beneficial response in terms of the potential required for its anodic oxidation (with a decrease of up to *ca.* 50 mV shown).[190] To de-convolute

the inhibitory response of surfactant-exfoliated 2D-hBN modified SPEs, control studies in the form of equivalent sodium cholate modified SPEs were carried out. It is clear, as previously observed with DA oxidation, that similar anodic peak potentials and currents are exhibited at the surfactant modified SPEs when compared directly to the surfactant-exfoliated 2D-hBN equivalents. This work suggests that the sodium cholate is interfering and potentially dominating the electrochemical response in the former case (when present with the 2D-hBN), thus resulting in 2D-hBN's *apparent* not so beneficial response.

Next, the simultaneous detection of DA and AA was investigated *via* cyclic voltammetry by adding equal aliquots of DA and AA at the equal concentration of 0.5 mM into a pH 7.4 PBS. First, unmodified SPEs were utilised and the observed response is depicted in Figure 7.3A. It is clear that in this case the simultaneous detection of DA and AA is not viable, with a single oxidation peak observed at *ca*. +0.32 V (peak current: 15.7 μA). Modification of the SPE with 150 ng surfactant exfoliated 2D-hBN results in an increased peak current of 24.5 μA and a reduced peak potential for the DA and AA oxidations (*ca*. +0.25 V), however the simultaneous detection is again not viable. A similar response towards the simultaneous detection of DA and AA was reported previously when utilising pristine 2D-hBN (no surfactant) modified SPEs, suggesting that 2D-hBN *itself* blocks the oxidation mechanism of AA when it is immobilised upon carbon-based electrodes.[190, 191] To confirm this insight, a control experiment was performed utilising a 40 μg sodium cholate modified SPE (equivalent surfactant content as per the surfactant exfoliated 2D-hBN). As evident within Figure 7.3A, a similar response is observed towards the simultaneous detection of DA and AA at both the surfactant exfoliated 2D-hBN and the surfactant (control: *no* 2D-hBN present) modified SPE.

Specifically, a single peak is depicted at *ca*. 0.24 V and a maximum current of 22.5 µA (40 µg sodium cholate modified SPE). Evidently, the surfactant present interferes and dominates the electrochemical response observed when utilising 2D-hBN.

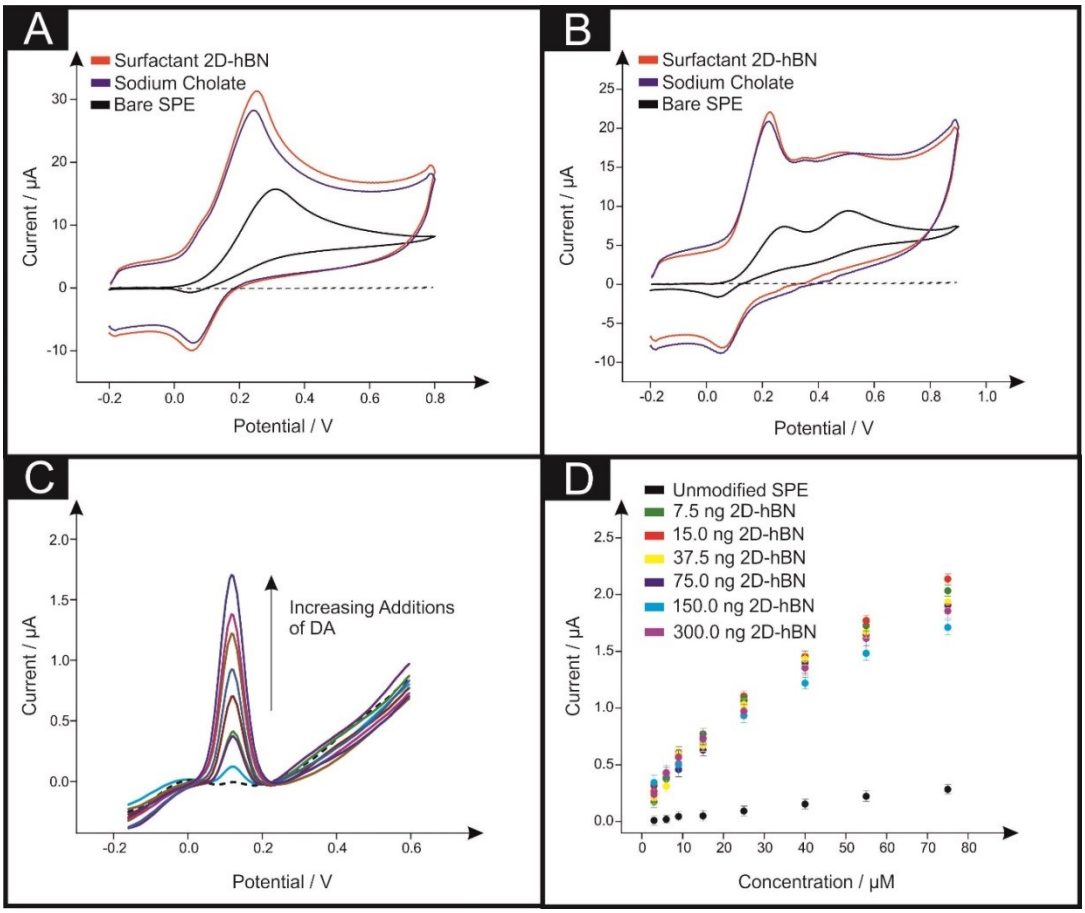

Figure 7.3: ***A:*** *Typical cyclic voltammograms recorded in 0.5 mM DA and 0.5 mM AA (PBS pH 7.4) using an unmodified (black), 150 ng surfactant-exfoliated 2D-hBN (red) and 40 µg sodium cholate (blue) modified SPEs.* ***B:*** *Voltammograms recorded in 0.5 mM DA and 0.5 mM UA (PBS pH 7.4) at unmodified (black), 150 ng surfactant-exfoliated 2D-hBN (red) and 40 µg sodium cholate (blue) modified SPEs. A and B were recorded utilising a scan rate of 100 mV s^{-1} (vs. SCE).* ***C:*** *Typical DPVs obtained by adding aliquots of DA at concentrations in the range of 3 – 75 µM into a 0.1 mM AA*

solution (pH 7.4 PBS) utilising a 150 ng surfactant-exfoliated 2D-hBN modified SPE; the dashed line represents 0.1 mM AA with no DA present. ***D:*** *Analytical curves corresponding to the anodic peak current for the oxidation of DA over the concentration range studied, obtained utilising unmodified and surfactant-exfoliated 2D-hBN (mass range: 7.5 – 300 ng) modified SPEs. DPV conditions:* E-*pulse, 20 mV;* t-*pulse, 10 mV* s^{-1}*; (vs. SCE). Each data (D) is the average deviation (N = 3)*

This is investigated further and attention is turned towards the simultaneous detection of DA and UA. Cyclic voltammetry was performed after adding equal aliquots of DA and UA (at a concentration of 0.5 mM) into a pH 7.4 PBS. Figure 7.3B shows that the simultaneous detection of DA and UA is viable when utilising an unmodified SPE, with the respective oxidation peaks observed at *ca*. +0.28 (7.48 μA) and +0.51 V (9.36 μA). Modification of the SPEs with 150 ng surfactant-exfoliated 2D-hBN results in a lower (less electro-positive, *i.e.* beneficial response) oxidation peak potential of +0.22 V, with an increased peak current of 16.7 μA for DA (when compared to that of an unmodified SPE). However, a detrimental response is observed in the case of UA, with a similar peak potential exhibited (+0.50 V) and a lower peak current (7.28 μA), suggesting a decrease in sensitivity. This observation differs considerably to the previous work in chapter 5 that utilised pristine 2D-hBN towards the simultaneous detection of DA and UA, where the peak separation/resolution of both anodic oxidation peaks was enhanced with the inclusion of pristine 2D-hBN.[190] To de-convolute the response, an equivalent sodium cholate control study was performed with a 40 μg modified SPE. Figure 7.3B depicts the response obtained towards DA and UA oxidation, demonstrating a similar response to exhibited at the 150 ng surfactant-exfoliated 2D-hBN modified SPE, with respective oxidation peaks observed at *ca*. +0.22 V (14.9 μA) and +0.52 V (7.11 μA). Evidently, the inclusion of the surfactant does not offer a favourable

interaction between the analyte of interest and the electrode surface, resulting in the significantly inhibited electrochemical oxidation process of UA.[49] It is clear that the surfactant utilised in the exfoliation of 2D-hBN hinders the observed electrochemical response towards the simultaneous detection of DA and UA, where, given the previous reports at pristine 2D-hBN modified SPE (chapter 5), the electrocatalytic effect of 2D-hBN is masked. Evidently, the response observed herein (and in other reports within the literature that utilise similar surfactants) should not be assumed to be due solely to 2D-hBN itself, but rather due to the effect of the surfactant present (sodium cholate) or other contributing factors incorporated as part of the fabrication process of 2D-hBN (and other novel 2D materials), that, as this chapter has shown, can *contribute to* and *dominate* the electrochemical response.

Note that there is significant signal overlap of DA and AA and therefore the simultaneous detection of all three analytes (DA, AA and UA) is not viable with this approach. Resultantly, the case of all three compounds are not considered, rather the focus herein is upon the simultaneous detection of DA in the presence of AA and UA separately.

Differential pulse voltammetry (DPV) was next utilised to further scrutinise the simultaneous detection of DA and AA, with aliquots of DA added (representing, 3 – 75 μM) into a 0.1 mM AA solution. Figure 7.4A shows the observed voltammetry at unmodified SPEs, where upon additions of DA an increment in the current relating to the oxidation of DA is observed (with a small displacement of peak potentials to more electro-negative regions). Again, the simultaneous detection of DA and AA is not observed when utilising an unmodified/bare SPE.

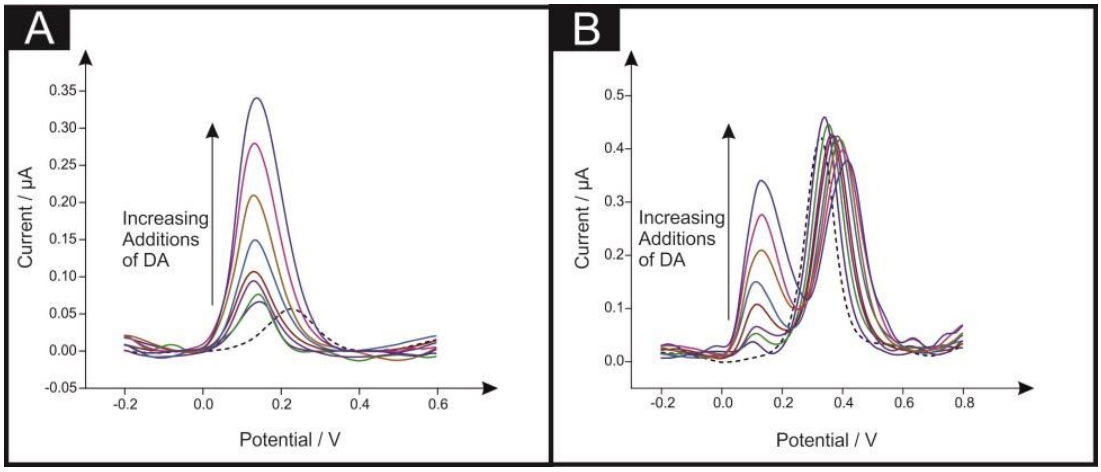

Figure 7.4: Typical DPVs (A) for the simultaneous detection of DA and AA utilising unmodified/bare SPEs by adding aliquots of DA at concentrations in the range of 3 – 75 µM into a 0.1 mM AA solution (pH 7.4 PBS); the dashed line represents the 0.1 mM AA scan in the absence of DA. (B) illustrates typical DPVs for the simultaneous detection of DA and UA utilising unmodified SPEs by adding aliquots of DA at concentrations in the range of 3 – 75 µM into a 0.1 mM UA solution (pH 7.4 PBS); the dashed line represents 0.1 mM UA scan in the absence of DA. Conditions as follows: E*-pulse, 20 mV;* t*-pulse, 200 ms; equivalent scan rate, 10 mV* s^{-1}*; (vs. SCE).*

Next, a range of surfactant exfoliated 2D-hBN masses (7.5 – 300 ng) were immobilised upon SPEs. Figure 7.3C depicts typical DPVs obtained towards the attempted simultaneous detection of DA and AA utilising 150 ng surfactant-exfoliated 2D-hBN modified SPEs. In this case, additions of DA resulted in a significant increase in the peak current obtained for DA oxidation when compared to an unmodified SPE. However, again, a single oxidation peak is evident, indicating the unviability of simultaneous DA and AA detection. Of note however is that the oxidation potential does not differ upon DA additions in this latter case, contrasting the behaviour observed at unmodified SPEs. This suggests that the electrode (following modification of the surface with surfactant-exfoliated 2D-hBN) is less

susceptible to oxidised species adsorbing onto its surface. Further analysis of this is depicted in Figure 7.3D, with a range of surfactant-exfoliated 2D-hBN modified SPEs (7.5 – 300 ng) illustrating the differences exhibited in the linear calibration curves at these modified SPEs. What is clear through inspection of Figure 7.3D, is that immobilisation of surfactant-exfoliated 2D-hBN increases the analytical sensitivity towards the detection of DA (when compared to the unmodified SPE). Interestingly however, when further additions are employed, the beneficial response reduces after a mass of 150 ng is utilised. The R^2 values of the linear calibration curves relating to the increased analytical sensitivity towards DA detection (see Figure 7.3D) that are observed at each of the unmodified and surfactant-exfoliated 2D-hBN modified SPEs (7.5 – 300 ng) are as follows: 0.984, 0.955, 0.978, 0.940, 0.944, 0.963, 0.954 and 0.963. Previous studies (chapter 5) utilising pristine 2D-hBN modified SPEs towards the simultaneous detection of DA and AA gave rise to a similar response, suggesting that 2D-hBN is not a viable candidate for the simultaneous detection of DA and AA, although it does offer improved electroanalytical signals towards DA.[190] To rationalise this further, a sodium cholate control study was carried out (see Figure 7.5) which demonstrated a similar response to that obtained at the surfactant-exfoliated 2D-hBN modified SPEs. The R^2 values of the linear calibration curves relating to the increased analytical sensitivity towards DA detection (see Figure 7.5B) that are observed at each of the unmodified and sodium cholate modified SPEs 2 – 80 μg) are as follows: 0.977, 0.964, 0.968, 0.957, 0.939, 0.975, 0.954 and 0.963. Again, it is suggested that sodium cholate (the surfactant utilised) is likely dominating the observed electrochemical response. Insight is offered into the possible mechanism of this response below (*vide infra*). Likely due to either favourable surface charges or the oxidation of cyclohexanol on

the surfactant structure,[49-51, 192] where in the case of the electrochemical oxidation of DA there could be a favourable interaction between the electrochemical product formed and the surfactant itself, which may be the opposite case for AA where no such beneficial effect is exhibited.

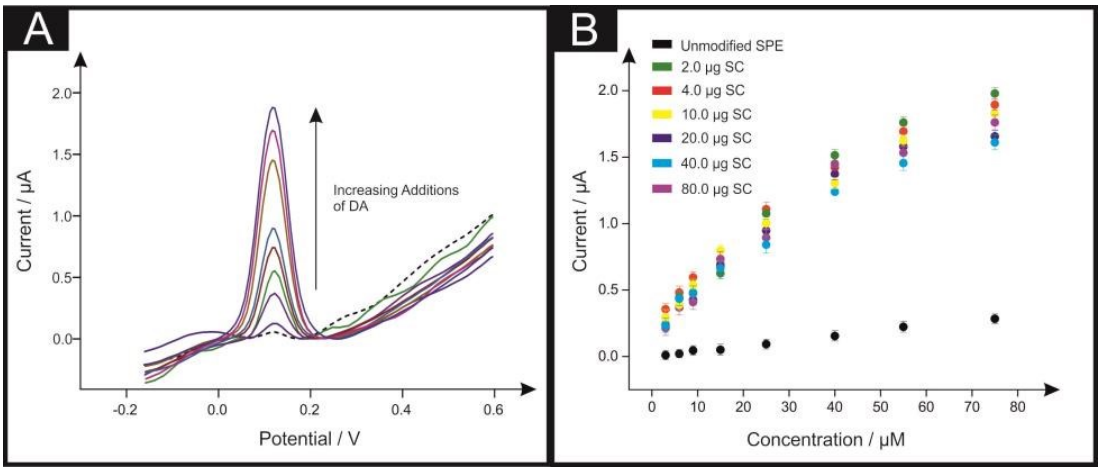

Figure 7.5: DPVs obtained utilising (A), 40 µg sodium cholate modified SPEs by adding aliquots of DA at concentrations in the range of 3 – 75 µM into a 0.1 mM AA solution (pH 7.4 PBS); the dashed line represents 0.1 mM AA scan in the absence of DA. Analytical curves (B) obtained utilising unmodified and sodium cholate modified SPEs of masses ranging from 2 – 80 µg corresponding to the anodic peak current for the oxidation of DA over the concentration range. Conditions as follows: E-*pulse, 20 mV;* t-*pulse, 200 ms; equivalent scan rate, 10 mV* s^{-1}*; (vs. SCE). Each data point (B) is the average and standard deviation (N = 3).*

Finally, attention was directed towards the simultaneous detection of DA and UA when utilising DPV, with aliquots of DA added (representing, 3 – 75 µM) into a 0.1 mM UA solution. Figure 7.4B shows the observed voltammetry at unmodified SPEs, where upon additions of DA an increase in the current relating to the oxidation of DA is observed, with a signal for UA oxidation also apparent. Accordingly, the

simultaneous of detection of DA and UA is viable at unmodified SPEs. Therefore the utilisation of 150 ng surfactant-exfoliated 2D-hBN modified SPEs is considered. Figure 7.6A depicts the voltammograms obtained with additions of DA resulting in a significant increase in the peak current obtained corresponding to the oxidation of DA (when contrasted to an unmodified SPE). However, interestingly, it is apparent that in the case of utilising surfactant-exfoliated 2D-hBN, increasing additions of DA results in a reduced peak current observed for UA. Further analysis of this is presented in Figure 7.6B and 7.6C, where a range of surfactant-exfoliated 2D-hBN masses (7.5 – 300 ng) were immobilised upon SPEs and explored towards the simultaneous detection of DA and UA. It is clear the lowest mass immobilisation of surfactant-exfoliated 2D-hBN (7.5 ng) offers the greatest beneficial response corresponding to peak height. With further increases in the mass of surfactant-exfoliated 2D-hBN immobilised upon an SPE decreasing the peak currents observed, whilst simultaneously consistently reducing the peak currents of UA. This suggests improved sensitivity towards the electrochemical oxidation of DA in comparison to an unmodified SPE, whereas the opposite is evident towards UA detection. The R^2 values of the linear calibration curves relating to the increased analytical sensitivity towards DA detection (see Figure 7.3D) that are observed at the unmodified and each of the surfactant-exfoliated 2D-hBN modified SPEs (7.5 – 300 ng) are as follows: 0.971, 0.965, 0.961, 0.949, 0.934, 0.957, 0.954 and 0.970.

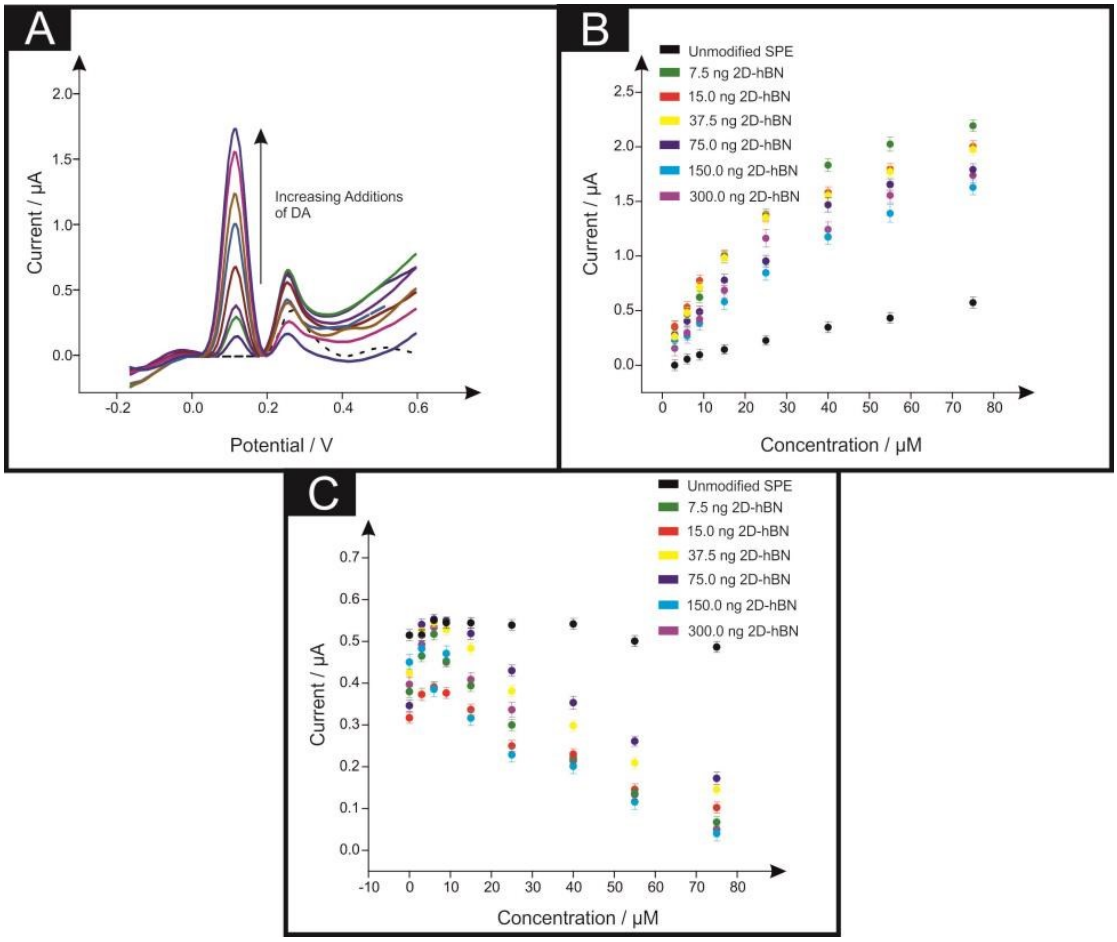

Figure 7.6: DPVs obtained utilising (A), 150 ng surfactant-exfoliated modified SPEs by adding aliquots of DA at concentrations in the range of 3 – 75 µM into a 0.1 mM UA solution (pH 7.4 PBS); the dashed line represents 0.1 mM UA. Analytical curves (B) obtained utilising unmodified and surfactant- exfoliated 2D-hBN modified SPEs of masses ranging from 7.5 – 300 ng corresponding to the anodic peak current for the oxidation of DA over the concentration range. (C) analytical curves obtained utilising unmodified and surfactant-exfoliated 2D-hBN modified SPEs of masses ranging from 7.5 – 300 ng corresponding to the anodic peak current for the oxidation of UA over the concentration range. Conditions as follows: E*-pulse, 20 mV;* t*-pulse, 200 ms; equivalent scan rate, 10 mV* s^{-1}*; (vs. SCE). Each data point (B and C) is the average and standard deviation (N = 3).*

Further analysis of this behaviour was carried out in the form of sodium cholate control coverage studies (2 – 80 μg), which are shown in Figures 7.7A, 7.7B and 7.7C, demonstrating a similar trend to that of the surfactant-exfoliated 2D-hBN modified SPEs. The R^2 values of the linear calibration curves relating to the increased analytical sensitivity towards DA detection (see Figure 7.5B) that are observed at each of the unmodified and sodium cholate modified SPEs 2 – 80 μg) are as follows: 0.961, 0.952, 0.959, 0.971, 0.964, 0.956, 0.961 and 0.968. It has previously been shown that the use of pristine 2D-hBN improves the peak separation/resolution towards the simultaneous detection of DA and UA (chapter 5).[190] With this in mind, it is clear upon the utilisation of surfactant-exfoliated 2D-hBN modified SPEs, that a detrimental effect towards the said detection is exhibited, particularly in the case of UA. Therefore, it is inferred that the exfoliation process of 2D-hBN (*i.e.* the use of surfactants) is the origin of the distinct change in behaviour. Clearly, it is of vital importance to consider the surfactant utilised in the exfoliation of 2D-hBN in order to de-convolute the true electrochemical response of this material.

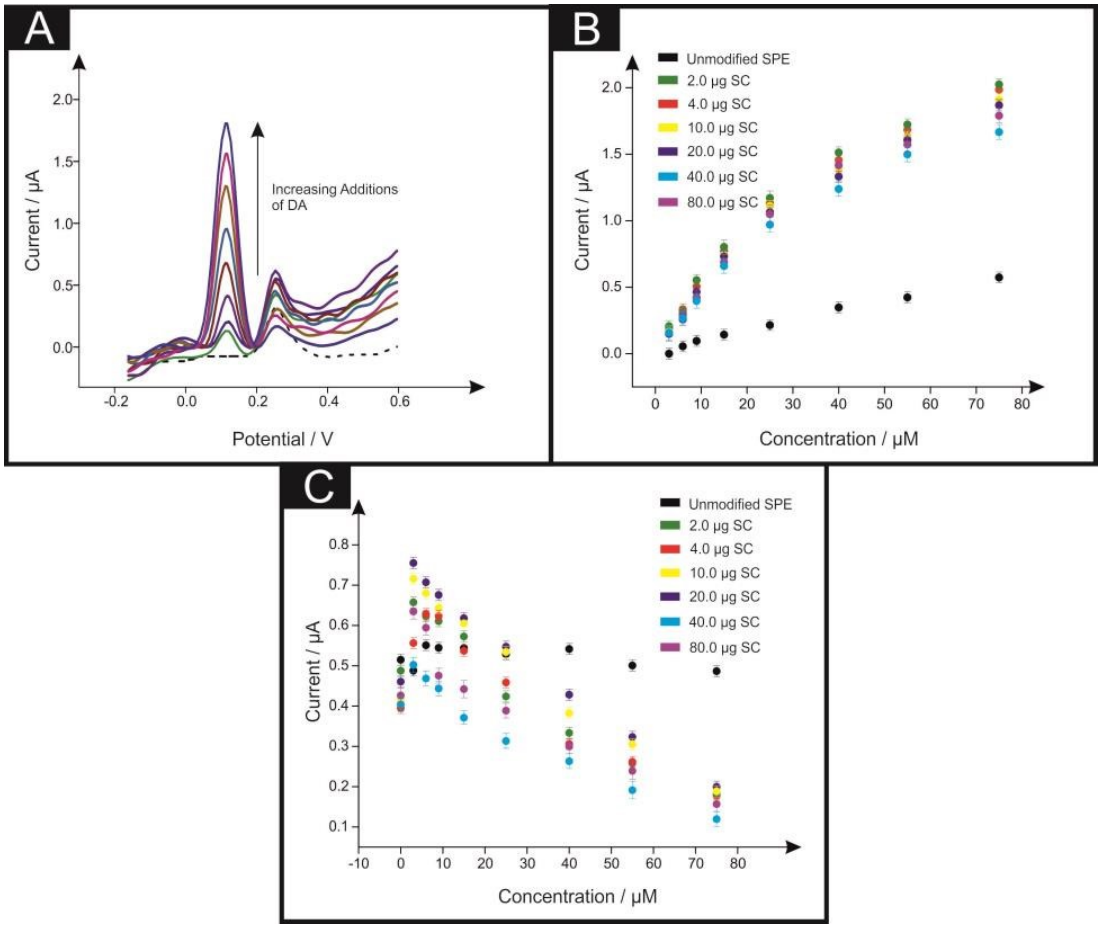

Figure 7.7: DPVs obtained utilising (A), 40 µg sodium cholate modified SPEs by adding aliquots of DA at concentrations in the range of 3 – 75 µM into a 0.1 mM UA solution (pH 7.4 PBS); the dashed line represents 0.1 mM UA. Analytical curves (B) obtained utilising unmodified and sodium cholate modified SPEs of masses ranging from 2 – 80 µg corresponding to the anodic peak current for the oxidation of DA over the concentration range. (C) analytical curves obtained utilising unmodified and sodium cholate modified SPEs of masses ranging from 2 – 80 µg corresponding to the anodic peak current for the oxidation of UA over the concentration range. Conditions as follows: E*-pulse, 20 mV;* t*-pulse, 200 ms; equivalent scan rate, 10 mV* s^{-1}*; (vs. SCE). Each data point (B and C) is the average and standard deviation (N = 3).*

Next, the limit of detection (LOD, based on three-sigma) for surfactant-exfoliated 2D-hBN was calculated and the 300 ng 2D-hBN modified SPE exhibited a LOD for DA (in the presence of UA) of 1.57 µM, which is higher than that of the

previously studied pristine 2D-hBN (0.65μM), suggesting the surfactant utilised in the exfoliation of 2D-hBN can hinder its analytical utility. A full comparison with other 2D materials is shown in Table 7.1. On the other hand; the unmodified SPE possesses a LOD of 2.89 μM.

Interestingly, sodium cholate has been utilised previously towards the surfactant based exfoliation of graphene, where subsequent studies demonstrated that, *when present*, the surfactant contributes to (and in some cases dominates) the observed electrochemistry.[49-51] In the aforementioned studies, the surfactant (sodium cholate) was shown to be electroactive, in that it gave rise to an electrochemical oxidation peak at *ca*. +0.30 V when modified onto SPEs and cyclic voltammetry was performed in blank buffers.[49] Based upon the chemical structure (see Figure 3.8), it is surmised that the electrochemical response is due to the oxidation of cyclohexanol (hydroxyl groups), *via* an equal proton/electron transfer process (which is likely to be 2). Thus, in this chapter, where an improved peak current is observed in the anodic region, it is likely that oxidation of the surfactant *itself* contributes to this increment. However, the effects of surfactants are complicated and a variety of different responses are observed when utilising distinct analytes (*i.e.* DA, UA and AA). In other studies, the charges present on various surfactants (including sodium cholate) have been shown to interfere with the observed electrochemical response;[50, 192] for example, inhibiting metal sensing and alternatively improving aerometric biosensors. It is likely that the influence of surface charges (and/or potentially a change in hydrophilicity) on the electrode surface is contributing to the response observed in this work, which are (in this case) detrimental and thus inferred to result in unfavourable interactions between the electrochemical analyte/product with that of the surfactant/electrode surface. The effect of surfactants on electrochemical

processes are not completely understood and more work is needed to elucidate the exact mechanism.[49, 193, 194] What is clear however, is that the surfactant utilised in the exfoliation of 2D-hBN contributes to (and in some cases dominates) the observed electrochemical response. Thus, as reported herein, when utilising surfactant exfoliated-2D-hBN, the electrochemical response should not be assumed to be due solely to 2D-hBN itself, but rather due to the effect of surfactant (sodium cholate) incorporated as part of the fabrication process, that can *contribute to* and *dominate* the electrochemical response. This applies also to or other newly emerging novel 2D materials *and* to other contributing factors incorporated as part of the fabrication process. Researchers in this field should be cautious (particularly before reporting beneficial electrocatalysis) and ensure that diligent control experiments (such as those reported herein), are performed.

7.3 Conclusions

This chapter has explored, for the first time, the use of surfactant-exfoliated 2D-hBN nanosheets immobilised upon a supporting SPE surface as a potential electrochemical sensing platform towards the simultaneous detection of DA, AA and UA. The effects of 'mass coverage' was explored on the 2D-hBN's electrochemical behaviour and was shown to be an essential consideration when investigating novel nanomaterials that should be implemented as routine protocols to fully understand and ascertain the *true* properties. Furthermore, through the implementation of diligent control experiments (in the form of equivalently modified surfactant electrodes, with *no* 2D-hBN present), it is found that the fabrication route utilised to prepare said 2D-hBN is a vital experimental consideration that is often overlooked within the literature. It has been shown that the surfactant utilised in the exfoliation

of 2D-hBN *contributes* to (and *dominates*) the observed electrochemical response. When utilising surfactant- exfoliated 2D-hBN, researchers within the field are urged to consider a contribution from the inherent surfactant. It is inferred that the electrochemical response should not be assumed to be due solely to 2D-hBN itself, but rather due to the effect of surfactant (in this case, sodium cholate) incorporated as part of the fabrication process. Given the wide variety of ionic and non-ionic surfactants that are utilised in the manufacture of novel 2D materials, these findings should be applied to other newly emerging 2D materials (and the various surfactants utilised) and should serve as an important warning when considering other contributing factors incorporated as part of the various fabrication processes.[49] It is likely that different surfactant and 2D material combinations will give rise to distinct relationships and as such, the electrochemical performance/properties will be affected in different ways, either beneficially or detrimentally.[49] Critically, when investigating the electrochemical properties/performance of such materials, researchers should exercise caution (particularly before reporting beneficial electrocatalysis) and ensure that diligent control experiments (such as those reported herein), are performed in order to effectively de-convolute the observed response and correctly attribute the individual contributions. The significance here is not in the material *itself*, but the fundamental knowledge that the surfactant (preparation/synthesis method) and surface coverage utilised changes the electrochemical properties of the material under investigation.

The following chapter investigates a new approach for producing 2D-hBN SPEs in order to replace the less-reproducible and time-consuming drop casting technique of 2D-hBN utilised in previous chapters.

Chapter 8 : 2D Hexagonal Boron Nitride Screen-Printed Electrode Platforms Explored Towards the Oxygen Reduction Reaction

This chapter considers a new fabrication approach for producing 2D-hBN SPEs in order to replace the less-reproducible and time-consuming drop-casting technique of 2D-hBN utilised throughout chapters 4-7. As such, a low cost and reproducible approach for producing 2D Hexagonal Boron Nitride (2D-hBN) electrochemical screen-printed platforms (hBN-SPEs) is revealed. These novel hBN-SPEs are explored as a potential electrocatalyst towards the oxygen reduction reaction (ORR) within acidic media and their performance towards the ORR are critically evaluated. This approach allows the fabrication of highly reproducible and mass producible hBN-SPEs and this fabrication approach readily allows the surface coverage (mass) of hBN to be readily changed and controlled. This fabrication approach replaces the less-reproducible and time-consuming drop casting technique of hBN (see chapters 3 and 5) offering an alternative beneficial approach to produce novel electrode platforms that can be utilised towards a range of applications.

8.1 Introduction

Proton exchange membrane (PEM) fuel cells in which the oxygen reduction reaction (ORR) occurs,[161] is considered a viable alternative means of storing and transporting energy that has potential to replace fossil fuel energy. Nevertheless, efforts towards enhancing PEM fuel cell performance in terms of power output, and longevity are greatly desired.[162] The ORR has proven to be a substantial shortcoming

for PEM fuel cell technology, since it can reduce fuel cell lifetimes and performance where fuel cell degradation at the cathode, in which the ORR occurs, results in the formation of hydrogen peroxide (H_2O_2) upon the utilisation of catalysts that reduce oxygen *via* the two electron pathway.[91] Therefore to overcome this issue, platinum (Pt)[93] electrocatalysts are frequently utilised since they follow the direct four electron pathway mechanism in the reduction of oxygen, resulting in the production of only H_2O (see chapter 4).[94, 162, 163] However, due to Pt being limited in availability and highly expensive,[69] it is unsuitable for mass production as a fuel cell catalyst. Consequently, research is directed towards cheaper nonprecious metal catalysts[97] and more pertinently, metal-free carbon based materials.[94]

Of late, interest has veered towards utilising novel 2D materials as electrocatalysts for the ORR with materials such as 2D-MoS_2,[164] 2D-$MoSe_2$[195, 196] and 2D-WSe_2 all employed towards this application.[195, 196] 2D hexagonal boron nitride (2D-hBN), a previously overlooked electrocatalytic 2D material, has recently been investigated towards the ORR, exhibiting beneficial results. Indeed, Uosaki *et al*.[69] immobilsed 2D-hBN upon gold substrates/electrodes [69] and demonstrated that the overpotential required for the ORR to occur was reduced by *ca.* 270 mV compared to the unmodified gold substrate. Their diligent study also found 2D-hBN had no beneficial effect towards the ORR when immobilised upon a carbon substrate.[69] It has however been demonstrated within this thesis that 2D-hBN is electrocatalytic towards the ORR when drop-cast upon a SPE, [197] an electrode surface significantly overlooked (chapter 4). Indeed, upon the utilisation of surfactant-free (pristine) 2D-hBN the overpotential required for the ORR to occur reduced by *ca*. 280 mV. This beneficial effect was attributed to the interaction between the rough SPE surface and the edge sites of 2D-hBN.[197] Moreover, it has

also been shown within this thesis that surfactant-exfoliated 2D-hBN exhibited an electrocatalytic effect towards the ORR when drop-cast upon an SPE.[198] An overpotential reduction of *ca*. 500 mV was observed upon immobilisation of 37.5 ng surfactant-exfoliated 2D-hBN upon an SPE, in comparison to its bare equivalent, significantly greater than the surfactant-free approach.[198] However, through the utilisation of control coverage studies, the large electrocatalytic effect was shown to be highly dependent upon the surfactant (sodium cholate) utilised,[198] with a overpotential reduction of *ca.* 440 mV observed when utilising *just* sodium cholate (no 2D-hBN) modified SPEs.[198]

A common approach in the modification of supporting electrode platforms is the drop-casting technique (utilised in the above studies), in which a fixed volume of liquid (containing the electrocatalyst) is immobilised onto an electrode surface utilising a pipette. This convenient technique is prominent in the literature due to the ease of implementation, allowing for the catalytic performance of various materials to be tested. However, disadvantages of this technique include limited reproducibility, uneven dispersion of material and it can be highly time consuming. Thus, an alternative method is necessary and one potential technique is the use of screen-printed electrodes (SPEs), whereby the material of interest is directly incorporated into the SPE ink and printed.

This chapter reports for the first time, the facile low cost production of hBN screen-printed electrode platforms and benchmark these new electrochemical platforms towards the ORR. An array of differing coverages (mass) of 2D-hBN can be readily incorporated into these platforms. Thus, this fabrication approach replaces the less-reproducible and time-consuming drop casting technique of 2D-hBN and other 2D materials utilised previously, offering a rapid and ready-to-use alternative.

Hence, this beneficial approach enables the production of novel electrode platforms that can be employed towards a range of applications.

8.2 Experimental Details

For experimental procedures/tests investigating the electrochemical detection of oxygen, sulfuric acid solutions utilised were of the highest grade available from Sigma-Aldrich (99.999%, double distilled for trace metal analysis) and was used at a concentration of 0.1 M. To oxygenate the solution, it was subject to rigorous bubbling of 100% medicinal grade oxygen through 100 mL of the solution for 45 minutes, assuming this to be a completely saturated solution at room temperature as described by Gara.[91] The concentration of oxygen was assumed to be 0.9 mM according to previous reports using the same method. [91, 94]

8.3 Results and Discussion

It has previously show within this thesis (chapters 4 and 6) that 2D-hBN exhibits a beneficial electrocatalytic effect towards the ORR when drop-cast upon a screen-printed graphitic electrodes (SPEs).[197, 198] However this method has various disadvantages (see introduction). Thus, to alleviate the said disadvantages, novel 2D-hBN conductive inks have been produced in which the 2D-hBN (1, 5, 10 and 15%) is incorporated within graphitic ink using the method outlined in the experimental section (chapter 3). This has enabled the production of hBN-SPEs upon the implementation of the screen-printing fabrication methodology (see experimental section). Hence these newly fabricated electrodes are now utilised towards the ORR.

First, the ORR system was benchmarked utilising an unmodified SPE within 0.1 M H_2SO_4 and Figure 8.1 depicts the cyclic voltammogram obtained. It is evident that the peak potential required for the ORR to occur at an unmodified SPE is -1.09 V, which is in good agreement to previous literature.[197, 198] Next, of range hBN-SPEs (1, 5, 10, and 15%) were explored towards the ORR. Figure 8.1 illustrates the overpotential required for the ORR to occur reduces upon the employment of hBN-SPEs, in comparison to the unmodified equivalent. This trend is clearly exhibited in Figure 8.1 inset, where a plot of the oxygen reduction peak potential *vs.* the (% mass) of incorporated 2D-hBN is shown where the ORR activation potential shifts from -1.09 V to -0.94 V, -0.89 V, -0.96 V and -1.03 V for 1, 5, 10 and 15 % hBN-SPEs respectively. Thus, a clear reduction in the activation overpotential for the ORR to occur is shown at various percentages of hBN-SPEs, with the highest reduction, 200 mV exhibited at 5% hBN-SPEs, demonstrating the electrocatalytic effect of the novel 2D-hBN ink produced. However, as the percentage mass of 2D-hBN incorporated within SPEs increases, there is a decrease in the observed beneficial

effect of these novel electrodes towards the ORR peak potential, with 10 and 15% hBN-SPEs specifically exhibiting this trend. Thus, it is suggested, higher percentages of hBN-SPEs, may create an insulating effect towards the ORR, owing to an agglomeration of the material forming bulk h-BN.

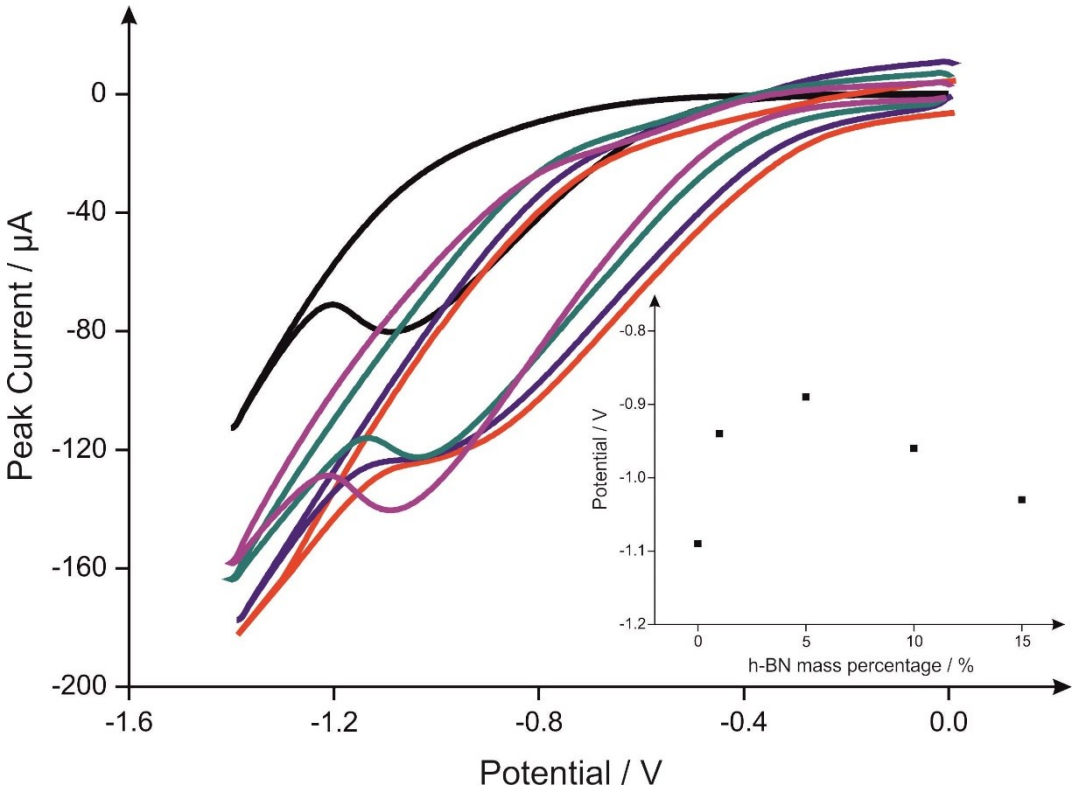

Figure 8.1: Typical cyclic voltammograms recorded in an oxygen saturated 0.1 M H_2SO_4 solution using unmodified (black line), 1% 2D-hBN (blue line), 5% 2D-hBN (red line), 10% 2D-hBN (green line) and 15% 2D-hBN (pink line) incorporated SPEs. Shown in the inset is analysis of the cyclic voltammograms in the form of a plot of oxygen reduction potential vs. % incorporation of 2D-hBN. Scan rate: 100 mV s^{-1} (vs. SCE).

To explore this phenomenon further, SEM images of the hBN-SPEs at the various percentage 2D-hBN incorporations (1-15%) were obtained. Figure 8.2A illustrates that at 1% hBN-SPEs, small amounts of 2D-hBN are visible as disc like

shapes approximately 200 nm in size. Figure 8.2B depicts this further, however there is a clear increase in the amount 2D-hBN located upon the graphitic sites of the SPE. This trend significantly increases at higher percentage masses of hBN-SPEs (10 and 15%) where there is a substantial agglomeration of 2D-hBN upon the surface of the SPE (Figure 8.2C and 8.2D) and it is apparent the size of the 2D-hBN discs increase from *ca.* 200 nm to *ca.* 500 nm. Thus, as stated previously, the electrocatalytic effect of hBN-SPEs towards the ORR is hindered at higher 2D-hBN masses which may be due to the observed agglomeration of 2D-hBN (Figure 8.2C and 8.2D) causing an insulating effect. However, it is clear the novel 2D-hBN ink formulated at lower percentages, offers a beneficial effect towards the ORR when incorporated into a SPE.

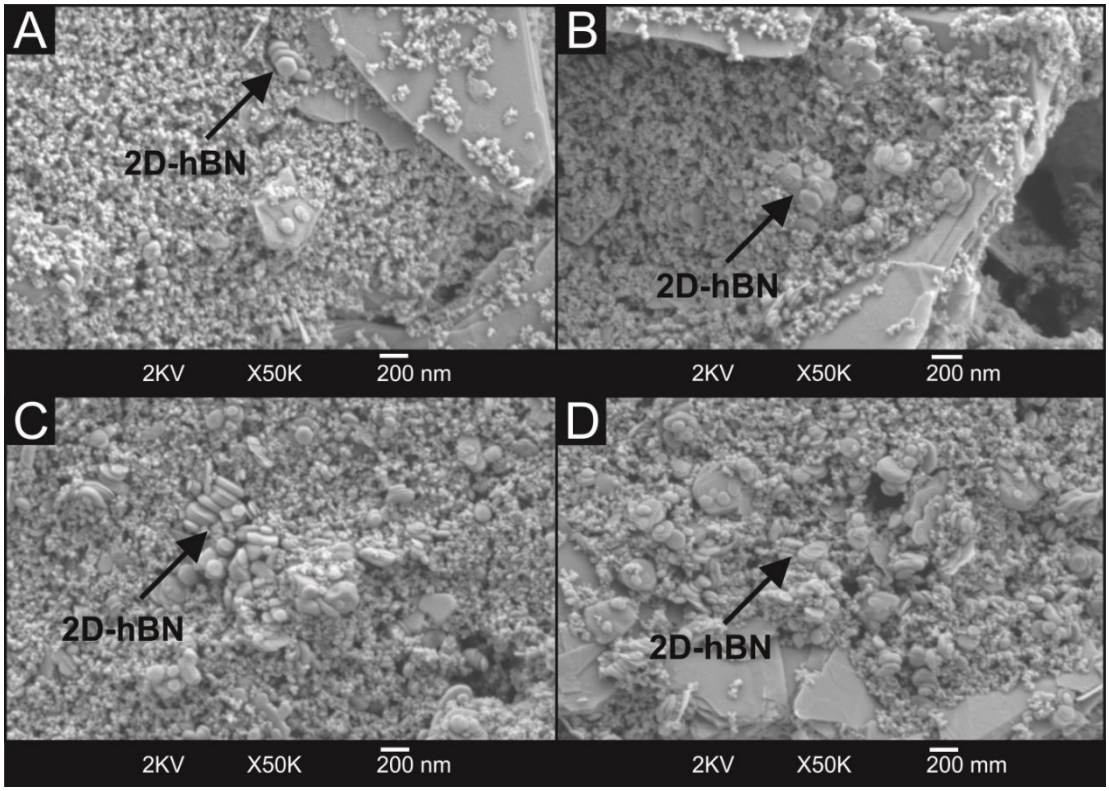

Figure 8.2: Typical SEM images for SPE with 1% 2D-hBN (A), 5% 2D-hBN (B), 10% 2D-hBN (C) and 15% 2D-hBN (D). 2D-hBN platelets are evident as disc-like shapes approximately 200 nm in size.

Next the electrocatalytic effect of hBN-SPEs is compared to the current drop-casting technique utilised within the literature. This thesis has previously demonstrated that surfactant-free (pristine) 2D-hBN nanosheets exhibited electrocatalytic behaviour towards the ORR when drop-cast upon SPEs, with a 280 mV reduction in the potential required for the ORR to occur, when compared to unmodified SPEs (chapter 4).[197] This beneficial effect was attributed to the interaction between the rough SPE surface and the edge sites of pristine 2D-hBN.[197] Furthermore, this thesis has also shown surfactant-exfoliated 2D-hBN exhibited an

electrocatalytic effect towards the ORR with an overpotential reduction of *ca*. 500 mV observed when 37.5 ng surfactant-exfoliated 2D-hBN was drop-cast upon an SPE, in comparison to its bare equivalent (chapter 6).[198] However, control coverage studies, illustrated the large electrocatalytic effect was highly dependent upon the surfactant (sodium cholate) utilised, with an overpotential reduction of *ca.* 440 mV observed when utilising sodium cholate *per se* (no 2D-hBN) modified SPEs.[198] Thus, the fabrication process of 2D-hBN significantly influenced its electrochemical response. The drop-casting technique offers a more beneficial electrocatalytic response towards the ORR in comparison to the hBN-SPEs utilised in this paper. However, the said novel approach of fabricating hBN-SPEs offers reduced overpotentials towards the ORR in comparison to unmodified SPEs, which has yet to be reported. Hence, due to their ease of fabrication, cost and the potential to be mass produced hBN-SPEs offer a facile alternative to current graphitic SPEs, with the prospect of improving/enhancing other electrochemical applications in which said unmodified graphitic SPEs are frequently utilised.

Next, the effect of hBN-SPEs towards ORR peak currents was investigated. A plot of the oxygen reduction peak current *vs.* the (%) of incorporated 2D-hBN is shown (Figure 8.3A) and it is revealed there is an increase of up to 65.0 μA (85.4 %) upon the utilisation of said hBN-SPEs in contrast to unmodified SPEs. Such responses are compared the drop-casting technique in which pristine and surfactant-exfoliated 2D-hBN modified SPEs are employed (Figures 8.3B and 8.3C respectively). Upon examination of these figures, it is revealed the ORR peak currents for pristine and surfactant exfoliated 2D-hBN reduce by 20.5 and 38.5 μA respectively in comparison to the bare underlying SPE. Thus, it is clear, hBN-SPEs offer significantly higher peak currents for the ORR, in comparison the drop-casting

technique involving pristine and surfactant exfoliated 2D-hBN. The vastly superior response of hBN-SPEs towards the ORR peak current in comparison the drop-casted 2D-hBN and unmodified graphite SPEs suggests said hBN-SPEs could offer an alternative approach which significantly improves sensitivity. This increased performance of hBN-SPEs, perhaps due to an increase in surface area, is an exciting property and the said electrodes may become a powerful tool in the investigation of other pertinent electrochemical systems understanding of 2D-hBN electrochemistry.

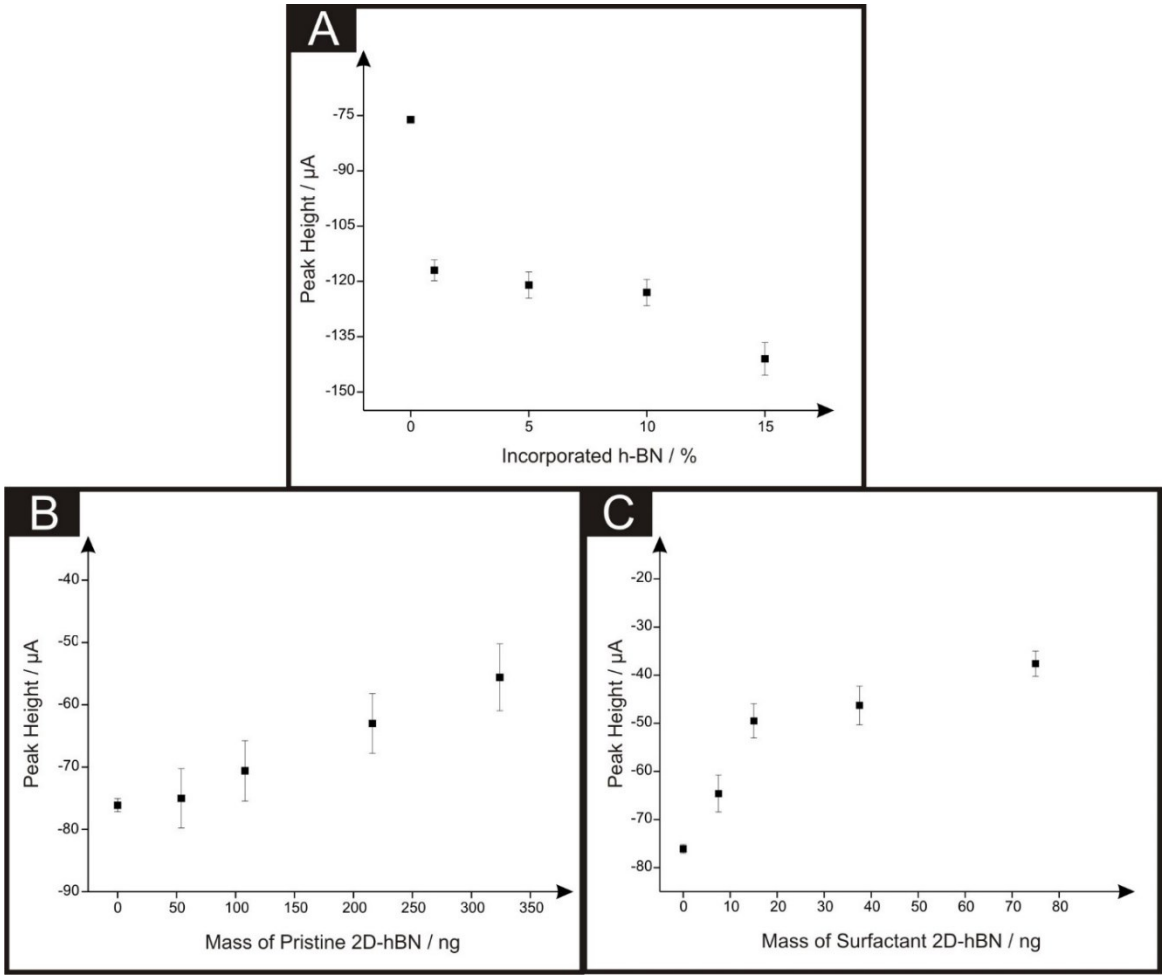

*Figure 8.3: Analysis of cyclic voltammograms obtained in an oxygen saturated 0.1 M H_2SO_4 solution in the form of a plot of oxygen reduction peak current vs. incorporated 2D-hBN % (A), peak current vs. mass of pristine 2D-hBN (B) and peak current vs. mass of surfactant-exfoliated 2D-hBN deposited upon SPEs, recorded in oxygen saturated 0.1 M H_2SO_4. Scan rate: 100 mV s^{-1} (vs. SCE). Each data point (A, B & C) is the average and standard deviation (*N = *3).*

To understand the electrochemical mechanism of the ORR, Tafel analysis was performed for unmodified and hBN-SPEs, ranging from 1 – 15 %. A plot of 'ln current (I)' *vs*. 'E_p' was constructed from analysis of the voltammograms corresponding to the electrochemical reduction of oxygen using Equation 4.1

(chapter 4). Tafel plots are shown in Figure 8.4 Which correspond to unmodified, 1, 5, 10 and 15% hBN-SPEs.

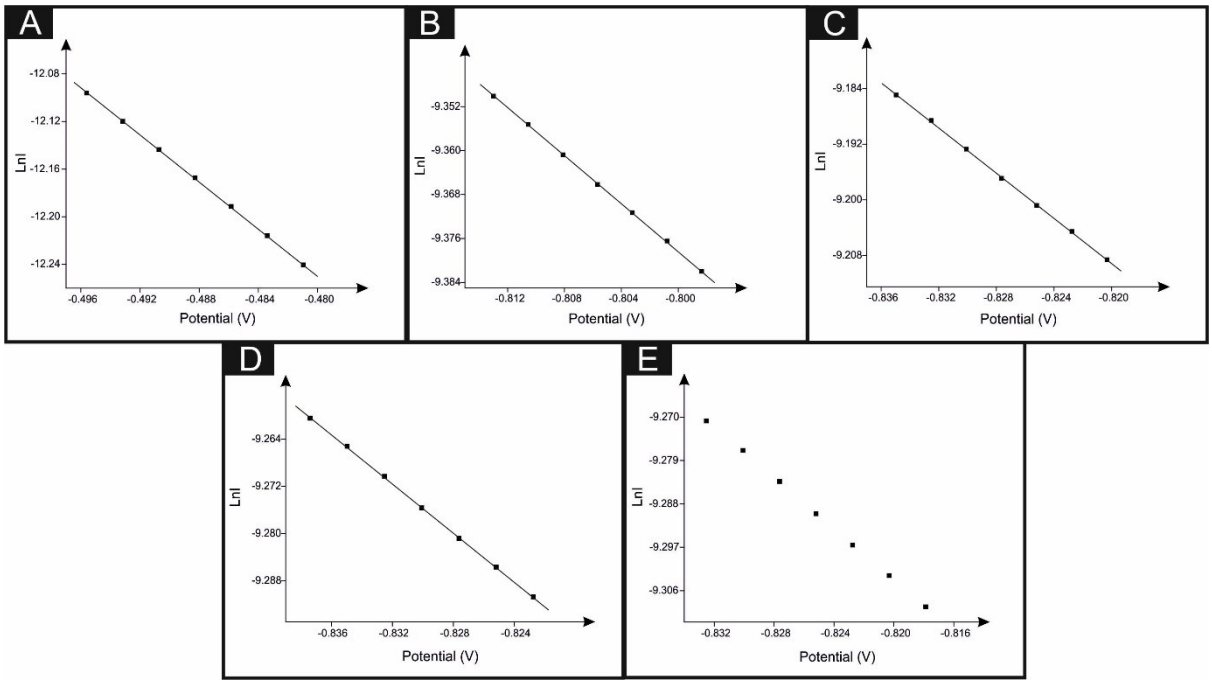

Figure 8.4: Illustrates Tafel plots for unmodified (A), 1 (B), 5 (C), 10 (D) and 15% (E) hBN-SPEs.

Where $\alpha n'$ values of 0.25, 0.06, 0.04, 0.05 and 0.07 were obtained corresponding to Figures 8.4A, B, C, D and E respectively. Next the number of electrons transferred in the reaction was deduced utilising the Randles-Ševćik equation (4.2) outlined previously in chapter 4 for an irreversible electrochemical process. The slope corresponds to $\delta \ln I / \delta E_p$, α is the electron transfer coefficient, F is the Faraday constant and n' is the number of electrons transferred in the rate determining step, R is the universal gas constant and T is the absolute temperature. Thus, the number of electrons transferred overall, n, could be found. A value of n = 2.70 for an unmodified SPE was obtained, whereas values of n = 1.47, 1.71, 1.61 and 1.58 were deduced for 1, 5, 10 and 15% hBN-SPEs. These values suggest that the

electrochemical reduction of oxygen using unmodified and hBN-SPEs produces hydrogen peroxide (H_2O_2). Previous chapters demonstrated pristine 2D-hBN (chapter 4) and surfactant-exfoliated 2D-hBN (chapter 6) followed the two electron pathway and produced H_2O_2. Furthermore, Previous studies by Uosaki *et al* [69] reported that 2D-hBN followed the two electron pathway upon the utilisation of a gold substrate, similar to this work.

Hydrogen peroxide (H_2O_2) yields were next estimated for unmodified and hBN-SPEs. First, the capacitance of an electrochemical process is estimated utilising: $C = \mathrm{I}/v$, where C is the capacitance, I is the observed peak current at a certain potential and v is the scan rate. Next, the charge is calculated using: $Q = CV$, where Q is the charge and V is the potential. Resultantly, $Q = nFN$ enables the amount of oxygen electrolysed in the reaction to be calculated, where n is the number of electrons transferred, F is the Faraday constant and N is the number of moles of oxygen electrolysed. There is a 1 : 1 stoichiometric ratio of oxygen produced to H_2O_2, therefore the concentration of oxygen electrolysed is theoretically the same as the concentration of H_2O_2 produced in the electrochemical reaction. Therefore, the estimated H_2O_2 yields were calculated for an oxygenated 0.1 M H_2SO_4 solution at a fixed volume of 10 mL utilising unmodified and hBN-SPEs of percentages ranging from 1 – 15 % at a scan rate of 100 mV s^{-1}. It was estimated that the concentration of H_2O_2 electrolysed when utilising unmodified SPEs was 2.51 nM, whereas hBN-SPEs resulted in 8.74, 4.89, 4.72, and 5.95 nM of H_2O_2 being produced for 1, 5, 10 and 15% h-BN respectively, hence there is an increase in quantity of H_2O_2 produced when utilising hBN-SPEs.

A key factor in terms of the analytical performance of sensors is the inherent reproducibility of the response. The reproducibility of the electrode materials of

interest was thus explored in acidic conditions with different masses of 2D-hBN incorporated into SPEs. A percentage relative standard deviation (% RSD) in the analytical signal of 4.30 % was observed for the unmodified SPE ($N = 3$) at scan rate 100 mV s^{-1}. The 1, 5, 10, and 15 % hBN-SPEs ($N = 3$; 100 mV s^{-1}) gave rise to % RSD values in the analytical signal of 3.03, 3.23, 3.82, and 3.46 %, respectively. Thus, in comparison to the drop casting technique, in which the % RSD values are significantly affected upon increasing immobilisation of any 2D-hBN material (pristine or surfactant exfoliated), 2D-hBN impregnated SPEs offer consistently low % RSD values at the different 2D-hBN incorporations.

The results presented herein illustrate the utilisation of 2D-hBN inks when fabricated and implemented within an SPE offer a beneficial alternative approach towards the ORR in comparison to the current drop-casting technique. The said hBN-SPEs offer a competitive reduction in the overpotential required for the ORR to occur in comparison to the drop-casting technique, whilst significantly enhancing the peak current - a detrimental feature of the drop-casting technique. Thus, these hBN-SPEs could be an attractive tool for researchers, giving rise to a potentially sensitive, selective, experimentally simple, portable low cost electrode.

8.4 Conclusions

It has been demonstrated for the first time, the facile production and implementation of a 2D-hBN ink within a SPE system (hBN-SPE) offers an improved, highly reproducible electrochemical response towards the ORR in comparison to an unmodified graphitic SPE equivalent. A reduction in the ORR potential of up to 200 mV is exhibited when using 5% hBN-SPEs in comparison to a bare SPE. The observed reduction in ORR peak potential is less significant than the

previously explored pristine 2D-hBN (chapter 4) or surfactant exfoliated 2D-hBN modified SPEs (chapter 6) which utilised the drop-casting technique. However, hBN-SPEs significantly increase the peak current of the ORR (up to 85.4 %) when compared to an unmodified SPE. Comparatively, the drop-casting technique involving pristine and surfactant-exfoliated 2D-hBN offers a detrimental effect towards the ORR peak current, with a reduction of 20.5 and 38.5 μA observed respectively in comparison to an unmodified SPE. Thus, the hBN-SPE fabrication approach offers an experimentally simple, portable low cost electrode platform which can be easily manufactured opening new possibilities for those seeking to utilise 2D materials towards electrochemical applications. Moreover, due the fabrication methodology, an array of 2D materials can be implemented within this approach.

Chapter 9 : Conclusions and Future Work

9.1 Overall Conclusions

This thesis has contributed to the understanding of 2D hexagonal boron nitride (2D-hBN) electrochemistry and its application as an electrode material, when it was previously considered non-electroactive. Thus, the aims and objectives of thesis have been met.

This thesis has demonstrated for the first time, that pristine 2D-hBN exhibits an improved electrochemical response towards the ORR when immobilised / electrically wired upon graphitic substrates. A reduction in the ORR potential of 280 mV has been shown when using 2D-hBN modified SPEs. Pristine 2D-hBN's beneficial electrochemistry was shown to be highly dependent upon both the underlying support substrate and the mass/coverage utilised. It has been demonstrated that only rough electrode surfaces give rise to beneficial/improved ORR responses, since this likely makes the morphology of pristine 2D-hBN upon electrode surfaces such that edge regions/sites are predominantly exposed which are the active sites[4] for the ORR. This work demonstrates that pristine 2D-hBN does have potential as an electrode material, which has never before considered as a catalyst *per se*.

Building upon this work, pristine 2D-hBN has been utilised as a sensing platform. It has been reported, for the first time, the electrocatalytic behaviour of pristine 2D-hBN towards the detection of dopamine (DA). A simple drop-casting method was implemented and the catalytic effect of pristine 2D-hBN was shown again to be dependent upon *both* the mass/coverage *and* substrate utilised (particularly the roughness of the underlying supporting electrode surface) as

mentioned above. Given the excellent electrocatalytic oxidation of DA observed, pristine 2D-hBN modified SPEs were shown to possess the ability to de-convolute the signals of DA and two commonly reported interferents: AA (by *ca*. 110 mV in separate solutions) and UA (by *ca*. 70 and 50 mV simultaneously at pH 5.0 and pH 7.4 respectively), offering a viable means towards the detection of DA in the presence of common interferents.

The effect of changing the fabrication process in the production of 2D-hBN was also considered. It was demonstrated for the first time that surfactant-exfoliated 2D-hBN exhibits an electrocatalytic effect towards the ORR when immobilised upon graphitic substrate (SPE). A potential reduction of *ca*. 500 mV was observed upon immobilisation of 37.5 ng surfactant-exfoliated 2D-hBN on an SPE, in comparison to its bare equivalent. Thus, a significant improvement in comparison to the utilisation of pristine 2D-hBN. However, through the utilisation of control coverage studies, the large electrocatalytic effect was shown to be highly dependent upon the surfactant (sodium cholate) utilised, with a potential reduction of *ca.* 440 mV observed when utilising *just* sodium cholate (no 2D-hBN) modified SPEs. Furthermore, it was demonstrated for the first time surfactant-exfoliated 2D-hBN is an effective electrochemical supercapacitor material, with a specific capacitance value of up to 1745 F g^{-1} obtained for 7.5 ng surfactant-exfoliated 2D-hBN modified SPEs. In both electrochemical systems, the surfactant was the overall dominating factor in the observed 2D-hBN electrocatalytic and capacitive (μF) response. Furthermore, the effect of surfactants in the fabrication of 2D-hBN towards the detection of DA and its common interferents (AA and UA) was also considered. It was again shown through control experiments that the surfactants contribute to the observed electrochemical response.

Thus, when considering the above cases, it has been shown that the surfactant utilised in the exfoliation of 2D-hBN *contributes* to (and *dominates*) the observed electrochemical response. When utilising surfactant-exfoliated 2D-hBN, researchers within the field are urged to consider a contribution from the inherent surfactant. It is inferred that the electrochemical response should not be assumed to be due solely to 2D-hBN itself, but rather due to the effect of surfactant (in this case, sodium cholate) incorporated as part of the fabrication process. Critically, caution should be exercised before reporting beneficial electrocatalysis diligent control experiments (such as those reported herein), are performed in order to effectively de-convolute the observed response and correctly attribute the individual contributions. The significance here is not in the material *itself*, but the fundamental knowledge that the surfactant (preparation/synthesis method) and surface coverage utilised changes the electrochemical properties of the material under investigation.

Finally, it was demonstrated, for the first time the utilisation of facile low cost produced 2D-hBN incorporated SPEs (hBN-SPEs) exhibit an improved electrochemical response towards the ORR. A reduction in the ORR potential of up to 200 mV is exhibited when using 5% hBN-SPEs in comparison to its bare equivalent. Furthermore, a significant increase in peak current upon the utilisation of 2D-hBN impregnated SPEs was seen, (up to 85.4 %) when compared to an unmodified SPE. However, the observed reduction in ORR peak potential is not as significant as the previously explored pristine 2D-hBN or surfactant-exfoliated 2D-hBN modified SPEs. Nevertheless, it clearly offers the greatest peak current in comparison to the said studies. Thus, due to the ease of manufacture and possible increase in sensitivity, 2D-hBN impregnated SPEs could be a viable alternative, with further applications also possible.

9.2 Suggestions for Future Work

Future work continuing the work in this thesis is as follows:

1) The utilisation of 2D-hBN incorporated SPEs towards the detection of dopamine and its common interferents in order to evaluate any beneficial effect observed in comparison to the drop-casting technique utilised in this thesis.

2) The possibility of employing pristine and surfactant-exfoliated 2D-hBN modified SPEs along with 2D-hBN incorporated SPEs towards the hydrogen evolution reaction (HER). The HER (along with ORR) is an important reaction that occurs within fuel cells, thus further investigation into this may be of interest.

3) Modify a range of metallic electrodes with pristine and surfactant-exfoliated 2D-hBN in order to compare the effects of 2D-hBN and its fabrication process upon non-carbon substrates towards the ORR and the detection of dopamine and its common interferents.

4) Implement the use of pristine and surfactant-exfoliated 2D-hBN modified SPEs along with 2D-hBN incorporated SPEs towards heavy metal sensing, such as the separation of lead and arsenic.

Publications arising from this Thesis

1) 2D Hexagonal Boron Nitride (2D-hBN) Explored as a Potential Electrocatalyst for the Oxygen Reduction Reaction, A. F. Khan, E. P. Randviir, D. A. C. Brownson, X. Ji, G. C. Smith and C. E. Banks, Electroanalysis, 29, 622.

   Contributions: Electrochemical measurements, data analysis and writing of the peer-reviewed article.

2) 2D Hexagonal Boron Nitride (2D-hBN) Explored for the Electrochemical Sensing of Dopamine, A. F. Khan, D. A. C. Brownson, E. P. Randviir, G. C. Smith and C. E. Banks, Analytical Chemistry, 88, 9729.

   Contributions: Electrochemical measurements, data analysis and writing of the peer-reviewed article.

3) Surfactant-exfoliated 2D hexagonal boron nitride (2D-hBN): role of surfactant upon the electrochemical reduction of oxygen and capacitance applications, A. F. Khan, M. P. Down, G. C. Smith, C. W. Foster and C. E. Banks, Journal of Materials Chemistry A, 5, 4103.

   Contributions: Fabrication of 2D-hBN, electrochemical measurements, data analysis and writing of the peer-reviewed article.

4) Surfactant exfoliated 2D hexagonal Boron Nitride (2D-hBN) explored as a potential electrochemical sensor for dopamine: surfactants significantly

influence sensor capabilities, A. F. Khan, D. A. C. Brownson, C. W. Foster G. C. Smith and C. E. Banks, Analyst, 142, 1756.

Contributions: Fabrication of 2D-hBN, electrochemical measurements, data analysis and writing of the peer-reviewed article.

References

1. A. J. Bard and L. R. Faulkner, *Electrochemical Methods*, 2nd Ed., Wiley, New York, 2001.
2. A. C. Fisher, *Electrode Dynamics*, Oxford University Press, New York, 2009.
3. J. Wang, *Analytical Electrochemistry*, 2nd Ed., Wiley-VCH, New York, 2000.
4. R. G. Compton and C. E. Banks, *Understanding Voltammetry*, Imperial College Press, London, Second edn., 2011.
5. D. A. C. Brownson and C. E. Banks, *Handbook of Graphene Electrochemistry*, Springer, 2014.
6. C. G. Zoski, *Handbook of Electrochemistry*, Elsevier, Oxford, First edn., 2007.
7. F. Scholz, *Electroanalytical Methods*, Springer-Verlag Berlin Heidelberg, Second edn., 2010.
8. A. Kaifer and M. Gómez-Kaifer, *Fundamentals of Electrochemical Theory*, WileyVCH Verlag GmbH, Germany, 2007.
9. Z. Galus, *Fundamentals of Electrochemical Analysis*, Polish Scientific Publishers PWN, Warsaw, Second edn., 1994.
10. R. S. Nicholson, *Anal. Chem.*, 1965, **37**, 1351-1355.
11. J. P. Metters, S. M. Houssein, D. K. Kampouris and C. E. Banks, *Anal. Methods*, 2013, **5**, 103-110.
12. I. Lavagnini, R. Antiochia and F. Magno, *Electroanalysis*, 2004, **16**, 505-506.
13. R. J. Klingler and J. K. Kochi, *The Journal of Physical Chemistry*, 1981, **85**, 1731-1741.
14. H. Matsuda and Y. Ayabe, *Z. Elektrochemie*, 1955, **59**, 494.
15. S. Shahrokhian and E. Asadian, *Electrochim. Acta*, 2010, **55**, 666-672.
16. F. Béguin, V. Presser, A. Balducci and E. Frackowiak, *Adv. Mater.*, 2014, **26**, 2219-2251.
17. M. Rajkumar, C.-T. Hsu, T.-H. Wu, M.-G. Chen and C.-C. Hu, Prog. Nat. Sci., 2015, **25**, 527-544.
18. H. Helmholtz, *Ann. Phys.*, 1853, **165**, 211-233.
19. K. K. Cline, M. T. McDermott and R. L. McCreery, *The Journal of Physical Chemistry*, 1994, **98**, 5314-5319.
20. R. L. McCreery, *Chem. Rev.*, 2008, **108**, 2646-2687.
21. P. Chen and R. L. McCreery, *Anal. Chem.* , 1996, **68**, 3958-3965.
22. H. O. Pierson, *Handbook of Carbon, Graphite, Diamonds and Fullerenes*, Noyes Publications, USA, 1994.
23. C. E. Banks and R. G. Compton, *Analyst*, 2005, **130**, 1232-1239.
24. C. E. Banks, A. Crossley, C. Salter, S. J. Wilkins and R. G. Compton, *Angew. Chem. Int. Ed.*, 2006, **45**, 2533-2537.
25. J. H. T. Luong, K. B. Male and J. D. Glennon, *Analyst*, 2009, **134**, 1965-1979.
26. A. Noorbakhsh and A. Salimi, *Biosens. Bioelectron.*, 2011, **30**, 188-196.
27. J. P. Metters, R. O. Kadara and C. E. Banks, *Analyst*, 2011, **136**, 1067-1076.
28. N. R. Gall, E. V. Rut'kov and A. Y. Tontegode, *Int. J. Mod. Phys. B*, 1997, **11**, 1865-1911.
29. H. P. Boehm, R. Setton and E. Stumpp, *Carbon*, 1986, **24**, 241-245.
30. C. Soldano, A. Mahmood and E. Dujardin, *Carbon*, 2010, **48**, 2127-2150.

31. A. K. Geim and K. S. Novoselov, *Nat Mater*, 2007, **6**, 183-191.
32. E. P. Randviir, D. A. C. Brownson and C. E. Banks, *Mater. Today*, 2014, **17**, 426-432.
33. D. A. C. Brownson, D. K. Kampouris and C. E. Banks, *Chem. Soc. Rev.*, 2012, **41**, 6944-6976.
34. K. S. Novoselov, D. Jiang, F. Schedin, T. J. Booth, V. V. Khotkevich, S. V. Morozov and A. K. Geim, *Proc. Natl. Acad. Sci. U.S.A.*, 2005, **102**, 10451-10453.
35. Y. Zhu, S. Murali, W. Cai, X. Li, J. W. Suk, J. R. Potts and R. S. Ruoff, *Adv. Mater.*, 2010, **22**, 3906-3924.
36. D. A. C. Brownson and C. E. Banks, *Analyst*, 2010, **135**, 2768-2778.
37. D. A. C. Brownson, D. K. Kampouris and C. E. Banks, *J. Power Sources*, 2011, **196**, 4873-4885.
38. M. Pumera, *The Chemical Record*, 2009, **9**, 211-223.
39. X. Wang, L. Zhi and K. Müllen, *Nano Lett.*, 2008, **8**, 323-327.
40. C. Liu, S. Alwarappan, Z. Chen, X. Kong and C.-Z. Li, *Biosens. Bioelectron.*, 2010, **25**, 1829-1833.
41. K. S. Novoselov, A. K. Geim, S. V. Morozov, D. Jiang, Y. Zhang, S. V. Dubonos, I. V. Grigorieva and A. A. Firsov, *Science*, 2004, **306**, 666-669.
42. D. Chen, L. Tang and J. Li, *Chem. Soc. Rev.*, 2010, **39**, 3157-3180.
43. U. Khan, A. O'Neill, M. Lotya, S. De and J. N. Coleman, *Small*, 2010, **6**, 864-871.
44. X. Li, W. Cai, L. Colombo and R. S. Ruoff, *Nano Lett.*, 2009, **9**, 4268-4272.
45. X.-m. Chen, G.-h. Wu, Y.-q. Jiang, Y.-r. Wang and X. Chen, *Analyst*, 2011, **136**, 4631-4640.
46. W.-J. Lin, C.-S. Liao, J.-H. Jhang and Y.-C. Tsai, *Electrochem. Commun.*, 2009, **11**, 2153-2156.
47. A. Ambrosi, A. Bonanni, Z. Sofer, J. S. Cross and M. Pumera, *Chemistry – A European Journal*, 2011, **17**, 10763-10770.
48. D. A. C. Brownson, L. J. Munro, D. K. Kampouris and C. E. Banks, *RSC Adv.*, 2011, **1**, 978-988.
49. D. A. C. Brownson, J. P. Metters, D. K. Kampouris and C. E. Banks, *Electroanalysis*, 2011, **23**, 894-899.
50. D. A. C. Brownson and C. E. Banks, *Analyst*, 2011, **136**, 2084-2089.
51. D. A. C. Brownson and C. E. Banks, *Chem. Comm.*, 2012, **48**, 1425-1427.
52. D. Voiry, H. Yamaguchi, J. Li, R. Silva, D. C. B. Alves, T. Fujita, M. Chen, T. Asefa, V. B. Shenoy, G. Eda and M. Chhowalla, *Nat Mater*, 2013, **12**, 850-855.
53. C. Tan and H. Zhang, *Chem. Soc. Rev.*, 2015, **44**, 2713-2731.
54. A. B. Laursen, S. Kegnaes, S. Dahl and I. Chorkendorff, *Energy Environ. Sci.*, 2012, **5**, 5577-5591.
55. Q. Lu, Y. Yu, Q. Ma, B. Chen and H. Zhang, *Adv. Mater.*, 2016, **28**, 1917-1933.
56. H. Zeng, C. Zhi, Z. Zhang, X. Wei, X. Wang, W. Guo, Y. Bando and D. Golberg, *Nano Lett.*, 2010, **10**, 5049-5055.
57. Doc Brown, http://www.docbrown.info, accessed; 10/03/2018).
58. P.Atkins, T.Overton, J.Rourke, M.Weller and F.Armstrong, *Inorganic Chemistry Fourth Edition*, Oxford, 2006.
59. M. Kawaguchi, S. Kuroda and Y. Muramatsu, *J. Phys. Chem. Solids*, 2008, **69**, 1171-1178.

60. T. Gao, L.-j. Gong, Z. Wang, Z.-k. Yang, W. Pan, L. He, J. Zhang, E.-c. Ou, Y. Xiong and W. Xu, *Mater. Lett.*, 2015, **159**, 54-57.
61. Q. Xu, L. Cai, H. Zhao, J. Tang, Y. Shen, X. Hu and H. Zeng, *Biosens. Bioelectron.*, 2015, **63**, 294-300.
62. L. Britnell, R. V. Gorbachev, R. Jalil, B. D. Belle, F. Schedin, M. I. Katsnelson, L. Eaves, S. V. Morozov, A. S. Mayorov, N. M. R. Peres, A. H. Castro Neto, J. Leist, A. K. Geim, L. A. Ponomarenko and K. S. Novoselov, *Nano Lett.*, 2012, **12**, 1707-1710.
63. L. H. Li, Y. Chen, G. Behan, H. Zhang, M. Petravic and A. M. Glushenkov, *J. Mater. Chem.*, 2011, **21**, 11862-11866.
64. D. Pacilé, J. C. Meyer, Ç. Ö. Girit and A. Zettl, *Appl. Phys. Lett.*, 2008, **92**, 133107.
65. C. Jin, F. Lin, K. Suenaga and S. Iijima, *Phys. Rev. Lett.*, 2009, **102**, 195505.
66. A. Nag, K. Raidongia, K. P. S. S. Hembram, R. Datta, U. V. Waghmare and C. N. R. Rao, *ACS Nano*, 2010, **4**, 1539-1544.
67. L. Song, L. Ci, H. Lu, P. B. Sorokin, C. Jin, J. Ni, A. G. Kvashnin, D. G. Kvashnin, J. Lou, B. I. Yakobson and P. M. Ajayan, *Nano Lett.*, 2010, **10**, 3209-3215.
68. L. Ci, L. Song, C. Jin, D. Jariwala, D. Wu, Y. Li, A. Srivastava, Z. F. Wang, K. Storr, L. Balicas, F. Liu and P. M. Ajayan, *Nat Mater*, 2010, **9**, 430-435.
69. K. Uosaki, G. Elumalai, H. Noguchi, T. Masuda, A. Lyalin, A. Nakayama and T. Taketsugu, *J. Am. Chem. Soc.*, 2014, **136**, 6542-6545.
70. S. Hu, M. Lozada-Hidalgo, F. C. Wang, A. Mishchenko, F. Schedin, R. R. Nair, E. W. Hill, D. W. Boukhvalov, M. I. Katsnelson, R. A. W. Dryfe, I. V. Grigorieva, H. A. Wu and A. K. Geim, *Nature*, 2014, **516**, 227-230.
71. A. Lyalin, A. Nakayama, K. Uosaki and T. Taketsugu, *Phys. Chem. Chem. Phys.*, 2013, **15**, 2809-2820.
72. F. Studt, *Catal. Lett.*, 2013, **143**, 58-60.
73. N. A. Choudry, D. K. Kampouris, R. O. Kadara and C. E. Banks, *Electrochem. Commun.*, 2010, **12**, 6-9.
74. M. Khairy, D. K. Kampouris, R. O. Kadara and C. E. Banks, *Electroanalysis*, 2010, **22**, 2496-2501.
75. E. P. Randviir, D. A. C. Brownson, J. P. Metters, R. O. Kadara and C. E. Banks, *Phys. Chem. Chem. Phys.*, 2014, **16**, 4598-4611.
76. J. P. Metters, R. O. Kadara and C. E. Banks, *Sens. Actuators, B*, 2012, **169**, 136-143.
77. F. E. Galdino, C. W. Foster, J. A. Bonacin and C. E. Banks, *Anal. Methods*, 2015, **7**, 1208-1214.
78. E. P. Randviir, D. A. C. Brownson, J. P. Metters, R. O. Kadara and C. E. Banks, *Phys. Chem. Chem. Phys*, 2014, **16**, 4598-4611.
79. S. J. Rowley-Neale, C. W. Foster, G. C. Smith, D. A. C. Brownson and C. E. Banks, *Sustainable Energy Fuels*, 2017, **1**, 74-83.
80. Graphene Supermarket, https://graphene-supermarket.com, accessed; 04/01/2013.
81. G. R. Bhimanapati, D. Kozuch and J. A. Robinson, *Nanoscale*, 2014, **6**, 11671-11675.
82. R. V. Gorbachev, I. Riaz, R. R. Nair, R. Jalil, L. Britnell, B. D. Belle, E. W. Hill, K. S. Novoselov, K. Watanabe, T. Taniguchi, A. K. Geim and P. Blake, *Small*, 2011, **7**, 465-468.

83. R. Kurapati, C. Backes, C. Ménard-Moyon, J. N. Coleman and A. Bianco, *Angew. Chem. Int. Ed.*, 2016, **55**, 5506-5511.
84. J. Tauc, R. Grigorovici and A. Vancu, *Physica Status Solidi B Basic Solid State Physics*, 1966, **15**, 627-637.
85. T. T. Tran, K. Bray, M. J. Ford, M. Toth and I. Aharonovich, *Nat Nano*, 2016, **11**, 37-41.
86. A. F. Khan, E. P. Randviir, D. A. C. Brownson, X. Ji, G. C. Smith and C. E. Banks, *Electroanalysis*, 2017, **29**, 622-634.
87. S. Yuan, B. Toury, S. Benayoun, R. Chiriac, F. Gombault, C. Journet and A. Brioude, *Eur. J. Inorg. Chem.*, 2014, **2014**, 5507-5513.
88. X. Luo, J. Wang, M. Dooner and J. Clarke, *Appl. Energy*, 2015, **137**, 511-536.
89. O. T. Holton and J. W. Stevenson, *Platinum Metals Rev,*, 2013, **57**.
90. S. K. Bikkarolla, P. Cumpson, P. Joseph and P. Papakonstantinou, *Faraday Discuss.*, 2014, **173**, 415-428.
91. M. Gara and R. G. Compton, *New J. Chem.*, 2011, **35**, 2647-2652.
92. W. Sheng, H. A. Gasteiger and Y. Shao-Horn, *J. Electrochem. Soc.*, 2010, **157**, B1529-B1536.
93. C. Song and J. Zhang, in *PEM Fuel Cell Electrocatalysts and Catalyst Layers*, ed. J. Zhang, Springer London, 2008, DOI: 10.1007/978-1-84800-936-3_2, ch. 2, pp. 89-134.
94. E. P. Randviir and C. E. Banks, *Electroanalysis*, 2014, **26**, 76-83.
95. F. Jaouen, E. Proietti, M. Lefevre, R. Chenitz, J.-P. Dodelet, G. Wu, H. T. Chung, C. M. Johnston and P. Zelenay, *Energy Environ. Sci.*, 2011, **4**, 114-130.
96. S. M. Dockheer, L. Gubler, A. Wokaun and W. H. Koppenol, *Phys. Chem. Chem. Phys.*, 2011, **13**, 12429-12434.
97. U. Kramm, in *Encyclopedia of Applied Electrochemistry*, eds. G. Kreysa, K.-i. Ota and R. Savinell, Springer New York, 2014, DOI: 10.1007/978-1-4419-6996-5_204, ch. 204, pp. 909-918.
98. R. Koitz, J. K. Norskov and F. Studt, *Phys. Chem. Chem. Phys.*, 2015, **17**, 12722-12727.
99. G. Elumalai, H. Noguchi and K. Uosaki, *Phys. Chem. Chem. Phys.*, 2014, **16**, 13755-13761.
100. A. Lyalin, A. Nakayama, K. Uosaki and T. Taketsugu, *The Journal of Physical Chemistry C*, 2013, **117**, 21359-21370.
101. I. Streeter, G. G. Wildgoose, L. Shao and R. G. Compton, *Sens. Actuators, B*, 2008, **133**, 462-466.
102. D. A. C. Brownson, A. C. Lacombe, M. Gomez-Mingot and C. E. Banks, *RSC Adv.*, 2012, **2**, 665-668.
103. S. Shin, Z. Jin, D. H. Kwon, R. Bose and Y.-S. Min, *Langmuir*, 2015, **31**, 1196-1202.
104. T. Yano, E. Popa, D. A. Tryk, K. Hashimoto and A. Fujishima, *J. Electrochem. Soc.*, 1999, **146**, 1081-1087.
105. T. Kaskiala, *Miner. Eng.*, 2002, **15**, 853-857.
106. P. Han and D. M. Bartels, *The Journal of Physical Chemistry*, 1996, **100**, 5597-5602.
107. D. Qazzazie, M. Beckert, R. Mülhaupt, O. Yurchenko and G. Urban, *J. Phys. Conf. Ser.*, 2014, **557**, 012009.
108. P. Wang, Y. Li, X. Huang and L. Wang, *Talanta*, 2007, **73**, 431-437.

109. B. A. J. Larkin, M. El-Sayed, D. A. C. Brownson and C. E. Banks, *Anal. Methods*, 2012, **4**, 721-729.
110. Y. Yang, P. Qi, Y. Ding, M. F. Maitz, Z. Yang, Q. Tu, K. Xiong, Y. Leng and N. Huang, *J. Mater. Chem. B*, 2015, **3**, 72-81.
111. A. Pandikumar, G. T. Soon How, T. P. See, F. S. Omar, S. Jayabal, K. Z. Kamali, N. Yusoff, A. Jamil, R. Ramaraj, S. A. John, H. N. Lim and N. M. Huang, *RSC Adv.* , 2014, **4**, 63296-63323.
112. S. R. Ali, Y. Ma, R. R. Parajuli, Y. Balogun, W. Y. C. Lai and H. He, *Anal. Chem.*, 2007, **79**, 2583-2587.
113. L. C. S. Figueiredo-Filho, D. A. C. Brownson, O. Fatibello-Filho and C. E. Banks, *Electroanalysis*, 2014, **26**, 93-102.
114. K. Jackowska and P. Krysinski, *Anal. Bioanal.Chem.*, 2012, **405**, 3753-3771.
115. D. A. C. Brownson, L. C. S. Figueiredo-Filho, B. L. Riehl, B. D. Riehl, M. Gomez-Mingot, J. Iniesta, O. Fatibello-Filho and C. E. Banks, *J. Mater. Chem.* , 2016, **4**, 2617-2629.
116. R. A. Medeiros, A. Benchick, R. C. Rocha-Filho, O. Fatibello-Filho, B. Saidani, C. Debiemme-Chouvy and C. Deslouis, *Electrochem. Commun.*, 2012, **24**, 61-64.
117. Y. Wang and Y. Xiao, *Microchim Acta*, 2012, **178**, 123-130.
118. R. A. Medeiros, R. Matos, A. Benchikh, B. Saidani, C. Debiemme-Chouvy, C. Deslouis, R. C. Rocha-Filho and O. Fatibello-Filho, *Anal. Chim. Acta*, 2013, **797**, 30-39.
119. C. Deng, J. Chen, M. Wang, C. Xiao, Z. Nie and S. Yao, *Biosens. Bioelectron.*, 2009, **24**, 2091-2094.
120. M. D. Hawley, S. V. Tatawawadi, S. Piekarski and R. N. Adams, *J. Am. Chem. Soc.*, 1967, **89**, 447-450.
121. H. Filik, A. A. Avan and S. Aydar, *Arabian J. Chem.*, 2016, **9**, 471-480.
122. D. Vallone, R. Picetti and E. Borrelli, *Neurosci. Biobehav. Rev.*, 2000, **24**, 125-132.
123. G. A. F. Roberts, *J. Chem. Soc., Perkin Trans. 1*, 1979, DOI: 10.1039/p19790000603, 603-605.
124. D. Yasuda, K. Takahashi, T. Kakinoki, Y. Tanaka, T. Ohe, S. Nakamura and T. Mashino, *MedChemComm*, 2013, **4**, 527-529.
125. T. J. Davies, R. R. Moore, C. E. Banks and R. G. Compton, *J. Electroanal. Chem.*, 2004, **574**, 123-152.
126. H.-S. Wang, T.-H. Li, W.-L. Jia and H.-Y. Xu, *Biosens. Bioelectron.*, 2006, **22**, 664-669.
127. S. Saha, P. Sarkar and A. P. F. Turner, *Electroanalysis*, 2014, **26**, 2197-2206.
128. Y. Ferry and D. Leech, *Electroanalysis*, 2005, **17**, 113-119.
129. F. Shang, L. Zhou, K. A. Mahmoud, S. Hrapovic, Y. Liu, H. A. Moynihan, J. D. Glennon and J. H. T. Luong, *Anal. Chem.*, 2009, **81**, 4089-4098.
130. Z.-H. Sheng, X.-Q. Zheng, J.-Y. Xu, W.-J. Bao, F.-B. Wang and X.-H. Xia, *Biosens. Bioelectron.*, 2012, **34**, 125-131.
131. D. Han, T. Han, C. Shan, A. Ivaska and L. Niu, *Electroanalysis*, 2010, **22**, 2001-2008.
132. A. Safavi, N. Maleki, O. Moradlou and F. Tajabadi, *Anal. Biochem.*, 2006, **359**, 224-229.
133. H. Sun, J. Chao, X. Zuo, S. Su, X. Liu, L. Yuwen, C. Fan and L. Wang, *RSC Adv.*, 2014, **4**, 27625-27629.
134. S. Thiagarajan and S.-M. Chen, *Talanta*, 2007, **74**, 212-222.

135. L. Lin, J. Chen, H. Yao, Y. Chen, Y. Zheng and X. Lin, *Bioelectrochemistry*, 2008, **73**, 11-17.
136. X. Tian, C. Cheng, H. Yuan, J. Du, D. Xiao, S. Xie and M. M. F. Choi, *Talanta*, 2012, **93**, 79-85.
137. D. Zheng, J. Ye, L. Zhou, Y. Zhang and C. Yu, *J. Electroanal. Chem.*, 2009, **625**, 82-87.
138. M. Mallesha, R. Manjunatha, C. Nethravathi, G. S. Suresh, M. Rajamathi, J. S. Melo and T. V. Venkatesha, *Bioelectrochemistry*, 2011, **81**, 104-108.
139. Y. Wang, Y. Li, L. Tang, J. Lu and J. Li, *Electrochem. Commun.*, 2009, **11**, 889-892.
140. K. Uosaki, G. Elumalai, H. Noguchi, T. Masuda, A. Lyalin, A. Nakayama and T. Taketsugu, *J. Am. Chem. Soc.*, 2014, **136**, 6542-6545.
141. C. Huang, C. Chen, M. Zhang, L. Lin, X. Ye, S. Lin, M. Antonietti and X. Wang, *Nat Commun*, 2015, **6**.
142. S. Sansuk, E. Bitziou, M. B. Joseph, J. A. Covington, M. G. Boutelle, P. R. Unwin and J. V. Macpherson, *Anal. Chem.*, 2013, **85**, 163-169.
143. M. Amiri, E. Amali, A. Nematollahzadeh and H. Salehniya, *Sens. Actuators, B*, 2016, **228**, 53-58.
144. J. Zhou, M. Sheng, X. Jiang, G. Wu and F. Gao, *Sensors*, 2013, **13**, 14029.
145. A. N. Patel, S.-y. Tan, T. S. Miller, J. V. Macpherson and P. R. Unwin, *Anal. Chem.*, 2013, **85**, 11755-11764.
146. D. A. C. Brownson, S. A. Varey, F. Hussain, S. J. Haigh and C. E. Banks, *Nanoscale*, 2014, **6**, 1607-1621.
147. D. A. C. Brownson, P. J. Kelly and C. E. Banks, *RSC Adv.*, 2015, **5**, 37281-37286.
148. D. A. C. Brownson, C. W. Foster and C. E. Banks, *Analyst*, 2012, **137**, 1815-1823.
149. D. A. C. Brownson, M. Gomez-Mingot and C. E. Banks, *Phys. Chem. Chem. Phys.*, 2011, **13**, 20284-20288.
150. S. J. Rowley-Neale, D. A. C. Brownson, G. C. Smith, D. A. G. Sawtell, P. J. Kelly and C. E. Banks, *Nanoscale*, 2015, **7**, 18152-18168.
151. S. J. Rowley-Neale, J. M. Fearn, D. A. C. Brownson, G. C. Smith, X. Ji and and C. E. Banks, *Nanoscale*, 2016, DOI: 10.1039/C6NR04073**J**.
152. L. R. Cumba, C. W. Foster, D. A. C. Brownson, J. P. Smith, J. Iniesta, B. Thakur, D. R. do Carmo and C. E. Banks, *Analyst*, 2016, DOI: 10.1039/C6AN00167J.
153. Y. Wu, Z. Dou, Y. Liu, G. Lv, T. Pu and X. He, *RSC Adv.*, 2013, **3**, 12726-12734.
154. C. Liu, G. Lu, L. Jiang, L. Jiang and X. Zhou, *Electroanalysis*, 2006, **18**, 291-297.
155. Y. Zhang, W. Lei, Y. Xu, X. Xia and Q. Hao, *Nanomaterials*, 2016, **6**, 178.
156. P. Kalimuthu and S. A. John, *Talanta*, 2010, **80**, 1686-1691.
157. H. N. Po and N. M. Senozan, *J. Chem. Educ.*, 2001, **78**, 1499.
158. T. C. Ngo and D. G. Assimos, *Reviews in Urology*, 2007, **9**, 17-27.
159. D.-W. Wang and D. Su, *Energy Environ. Sci.*, 2014, **7**, 576-591.
160. D. Higgins, P. Zamani, A. Yu and Z. Chen, *Energy Environ. Sci.*, 2016, **9**, 357-390.
161. H. Jin, H. Zhang, H. Zhong and J. Zhang, *Energy Environ. Sci.*, 2011, **4**, 3389-3394.

162. A. Morozan, B. Jousselme and S. Palacin, *Energy Environ. Sci.*, 2011, **4**, 1238-1254.
163. D. Geng, Y. Chen, Y. Chen, Y. Li, R. Li, X. Sun, S. Ye and S. Knights, *Energy Environ. Sci.*, 2011, **4**, 760-764.
164. S. J. Rowley-Neale, J. M. Fearn, D. A. C. Brownson, G. C. Smith, X. Ji and C. E. Banks, *Nanoscale*, 2016, **8**, 14767-14777.
165. K. Zhao, W. Gu, L. Zhao, C. Zhang, W. Peng and Y. Xian, *Electrochim. Acta*, 2015, **169**, 142-149.
166. J. Zhao and Z. Chen, *The Journal of Physical Chemistry C*, 2015, **119**, 26348-26354.
167. C.-C. Hu, K.-H. Chang, M.-C. Lin and Y.-T. Wu, *Nano Lett.*, 2006, **6**, 2690-2695.
168. D. K. Kampouris, X. Ji, E. P. Randviir and C. E. Banks, *RSC Adv.*, 2015, **5**, 12782-12791.
169. D. A. C. Brownson and C. E. Banks, *Chem. Commun.*, 2012, **48**, 1425-1427.
170. E. Iyyamperumal, S. Wang and L. Dai, *ACS Nano*, 2012, **6**, 5259-5265.
171. Z.-S. Wu, A. Winter, L. Chen, Y. Sun, A. Turchanin, X. Feng and K. Müllen, *Adv. Mater.*, 2012, **24**, 5130-5135.
172. K. Wang, L. Li, T. Zhang and Z. Liu, *Energy*, 2014, **70**, 612-617.
173. V. Sahu, S. Grover, B. Tulachan, M. Sharma, G. Srivastava, M. Roy, M. Saxena, N. Sethy, K. Bhargava, D. Philip, H. Kim, G. Singh, S. K. Singh, M. Das and R. K. Sharma, *Electrochim. Acta*, 2015, **160**, 244-253.
174. L. Niu, Z. Li, W. Hong, J. Sun, Z. Wang, L. Ma, J. Wang and S. Yang, *Electrochim. Acta*, 2013, **108**, 666-673.
175. S. Gadipelli, T. Zhao, S. A. Shevlin and Z. Guo, *Energy Environ. Sci.*, 2016, **9**, 1661-1667.
176. I. E. L. Stephens, A. S. Bondarenko, U. Gronbjerg, J. Rossmeisl and I. Chorkendorff, *Energy Environ. Sci.*, 2012, **5**, 6744-6762.
177. L. Lai, J. R. Potts, D. Zhan, L. Wang, C. K. Poh, C. Tang, H. Gong, Z. Shen, J. Lin and R. S. Ruoff, *Energy Environ. Sci.*, 2012, **5**, 7936-7942.
178. Y. Xue, Q. Liu, G. He, K. Xu, L. Jiang, X. Hu and J. Hu, *Nanoscale Res. Lett.*, 2013, **8**, 1-7.
179. M. P. Down, C. W. Foster, X. Ji and C. E. Banks, *RSC Adv.*, 2016, **6**, 81130-81141.
180. W. Yang, Y. Yu, Y. Tang, K. Li, Z. Zhao, M. Li, G. Yin, H. Li and S. Sun, *Nanoscale*, 2017, **9**, 1022-1027.
181. V. Vinoth, J. J. Wu and S. Anandan, *Anal. Methods*, 2016, **8**, 4379-4390.
182. A. Pandikumar, G. T. Soon How, T. P. See, F. S. Omar, S. Jayabal, K. Z. Kamali, N. Yusoff, A. Jamil, R. Ramaraj, S. A. John, H. N. Lim and N. M. Huang, *RSC Adv.*, 2014, **4**, 63296-63323.
183. L. C. S. Figueiredo-Filho, D. A. C. Brownson, O. Fatibello-Filho and C. E. Banks, *Analyst*, 2013, **138**, 4436-4442.
184. H.-X. Zhao, H. Mu, Y.-H. Bai, H. Yu and Y.-M. Hu, *J. Pharm. Anal.*, 2011, **1**, 208-212.
185. J. Chao, X. Han, H. Sun, S. Su, L. Weng and L. Wang, *Science China Chemistry*, 2016, **59**, 332-337.
186. S. Su, H. Sun, F. Xu, L. Yuwen and L. Wang, *Electroanalysis*, 2013, **25**, 2523-2529.
187. Y.-R. Kim, S. Bong, Y.-J. Kang, Y. Yang, R. K. Mahajan, J. S. Kim and H. Kim, *Biosens. Bioelectron.*, 2010, **25**, 2366-2369.

188. V. Mani, M. Govindasamy, S.-M. Chen, R. Karthik and S.-T. Huang, *Microchim Acta*, 2016, **183**, 2267-2275.
189. K. Pramoda, K. Moses, U. Maitra and C. N. R. Rao, *Electroanalysis*, 2015, **27**, 1892-1898.
190. A. F. Khan, D. A. C. Brownson, E. P. Randviir, G. C. Smith and C. E. Banks, *Anal. Chem.*, 2016, **88**, 9729-9737.
191. I. F. Hu and T. Kuwana, *Anal. Chem.*, 1986, **58**, 3235-3239.
192. D. A. C. Brownson and C. E. Banks, *Electrochem. Commun.*, 2011, **13**, 111-113.
193. M. Pumera, R. Scipioni, H. Iwai, T. Ohno, Y. Miyahara and M. Boero, *Chemistry – A European Journal*, 2009, **15**, 10851-10856.
194. J. F. Rusling, *Colloids Surf., A*, 1997, **123**, 81-88.
195. J. Guo, Y. Shi, X. Bai, X. Wang and T. Ma, *J. Mater. Chem. A*, 2015, **3**, 24397-24404.
196. A. Y. S. Eng, A. Ambrosi, Z. Sofer, P. Šimek and M. Pumera, *ACS Nano*, 2014, **8**, 12185-12198.
197. A. F. Khan, E. P. Randviir, D. A. C. Brownson, X. Ji, G. C. Smith and C. E. Banks, *Electroanalysis*, 2017, DOI: 10.1002/elan.201600462, n/a-n/a.
198. A. F. Khan, M. P. Down, G. C. Smith, C. W. Foster and C. E. Banks, *J. Mater. Chem. A*, 2017, **5**, 4103-4113.